"Computational Chemical Kinetics of Biofuel Combustion Using Ab-Initio Methods and Statistical Rate Theories"

"Computergestützte chemische Kinetik von Biokraftstoffverbrennung mit Ab-initio-Methoden und statistischer Ratentheorien"

Von der Fakultät für Maschinenwesen der Rheinisch-Westfälischen Technischen Hochschule Aachen zur Erlangung des akademischen Grades einer Doktorin der Naturwissenschaften genehmigte Dissertation

vorgelegt von

Prajakta Rajaram Parab

Berichter: Juniorprofessor Dr.-Ing. Karl Alexander Heufer

Honorarprofessor Dr. rer. nat. Ravi Xavier Filipe Fernandes

Tag der mündlichen Prüfung: 16. November 2017

Diese Dissertation ist auf den Internetseiten der Universitätsbibliothek online verfügbar.

Berichte aus der Chemie

Prajakta Rajaram Parab

Computational Chemical Kinetics of Biofuel Combustion Using Ab-Initio Methods and Statistical Rate Theories

Shaker Verlag Aachen 2018

Bibliographic information published by the Deutsche Nationalbibliothek The Deutsche Nationalbibliothek lists this publication in the Deutsche Nationalbibliografie; detailed bibliographic data are available in the Internet at http://dnb.d-nb.de.

Zugl.: D 82 (Diss. RWTH Aachen University, 2017)

Copyright Shaker Verlag 2018
All rights reserved. No part of this publication may be reproduced, stored in a retrieval system, or transmitted, in any form or by any means, electronic, mechanical, photocopying, recording or otherwise, without the prior permission of the publishers.

Printed in Germany.

ISBN 978-3-8440-5708-9 ISSN 0945-070X

Shaker Verlag GmbH • P.O. BOX 101818 • D-52018 Aachen Phone: 0049/2407/9596-0 • Telefax: 0049/2407/9596-9

Internet: www.shaker.de • e-mail: info@shaker.de

Table of Contents

I	Introduction	1
	I.1. Energy and Environment.	1
	i. Biofuels	1
	ii. Tailor Made Fuels from Biomass (TMFB) and Goal of this thesis	2
	I.2. Combustion Chemistry	3
	I.3. Reaction Kinetics	6
	i. Reaction Rate Constant	6
	ii. Transition State Theory	7
	I.4. Thermochemistry	8
	i. Standard Enthalpy of Formation	9
	ii. Entropy	10
	iii. Heat Capacity at Constant Pressure	10
	iv. Statistical Thermodynamics	10
II	Computational Details and Quantum Chemistry	16
	II.1. Computational Chemistry Methods	16
	i. Ab initio Methods	16
	ii. Density Functional Methods	19
	iii. Semi-empirical Methods	20
	iv. Molecular-mechanics Method	20
	II.2. The Schrödinger Equation and the Born-Oppenheimer approximation	20
	II.3. Computational Models and Model Chemistries	21
	i. Basis Set	21
	ii. Gaussian Composite Methods	25
П	Computational Chemistry Tools	28
	III.1. Gaussian software package	28
	III.2. Gaussian Post Processor (GPOP)	31
	i. GPOP Pre-processing Tools	31
	ii. Thermodynamic and Rate Constant Calculations	35
	III.3. Basis-set expansion solver for 1-dimensional Schrödinger Equation	36
	(BEx1D)	50

IV	Results and Discussion	38
	IV.1. Reaction kinetics of the Hydrogen atom abstraction from isopentanol by H	20
	atom and HO 2 radical	38
	i. Reaction Barriers and Energies	43
	ii. High Pressure Limit Rate Constants	45
	IV.2. Theoretical investigation of Intramolecular Hydrogen Shift Reaction in 3-	<i>5</i> 1
	Methyltetrahydrofuran (3-MTHF) Oxidation	51
	i. Thermochemistry	55
	ii. C-H Bond Dissociation Energies	56
	iii. Reaction Barriers and Energies	57
	iv. High Pressure Limit Rate Constants	59
	v. Product Branching Ratio	63
	vi. 3-MTHF H-shift Reaction Comparison with Methylcyclopentane	65
	IV.3. Theoretical Investigation of Intramolecular hydrogen shift Reactions in 2-	70
	Methyltetrahydrofuran (2-MTHF) oxidation	/0
	i. Thermochemistry	72
	ii. C-H Bond Dissociation Energy	72
	iii. Reaction Barriers and Energies	74
	iv. High Pressure Limit Rate Constants	77
	v. Product Branching Ratio	81
	vi. 2-MTHF rate constant comparison with methylcyclopentane and 3-MTHF	83
	IV.4. Theoretical Study on 2-butanone Combustion Reactions	89
	i. C-H bond dissociation energies	92
	ii. Reaction Barriers and Energies	93
	iii. High Pressure Limit Rate Constants	96
	IV.5. Reaction Kinetics and Thermochemistry of the Smallest Ketone: Acetone	102
	i. Thermochemistry	103
	ii. Bond Dissociation Enthalpies	105
	iii. Reaction Barriers and Energies	106
	iv. Rate Constants	108
V	Summary	112
	Bibliography	114
	Appendix	120

Abstract

The main focus of this thesis was on the detailed theoretical understanding of important reactions taking place during the combustion of fuel. Ab initio quantum calculations were performed to understand reactions kinetics of important reactions taking place during combustion. Emphasis has been also put on computing thermodynamic properties of intermediate species formed during fuel combustion. The biofuel candidates considered herein are the ones which are of interest at the cluster of excellence "Tailor Made Fuels from Biomass" at the RWTH Aachen University, Germany. Among alcohols, isopentanol was considered for computing high pressure limit rate constants for the H-atom abstraction reactions from isopentanol by H atom and HO2 radicals. Furthermore, from cyclic oxygenated species 2-and 3-MTHF were of highlight. For these fuels, rate constants were determined for the isomerization reactions (alkylperoxy radical to hydroperoxyalkyl radical). Detail analysis showed that the strength of the C-H bonds, position of the abstracted hydrogen (cis or trans) and the ring size of the transition states affected the reaction kinetics for these isomerization reactions. Lastly, from the ketone family, 2-Butanone and acetone were considered. For 2-BT, high pressure limit rate constants were determined for the H atom abstraction reactions from 2-butanone by methylperoxy (CH₃OO) radical. Also due to high interest in ketonic fuels, the smallest member of the ketone family; acetone was chosen to get insight into its elementary reactions occurring during combustion. The reaction kinetics of O₂ addition to the acetonyl radical, isomerization of acetonylperoxy radical to the corresponding QOOH species and also β -scission reaction in the acetonyl radical were investigated. Overall, the results obtained from these computations are beneficial for the fundamental understandings and also for the development of detail kinetic models.

Zusammenfassung

Der Fokus dieser Dissertation liegt auf dem detaillierten, theoretischen Verständnis wichtiger Reaktionen während der Verbrennung von Kraftstoffen.

Untersuchung Dazu wurden quantenchemische Ab-initio Rechnungen zur Reaktionskinetik zentraler Reaktionen in Verbrennungsvorgängen durchgeführt. Weiterhin wurden die thermodynamischen Eigenschaften von Zwischenprodukten, die während der Kraftstoffverbrennung auftreten. berechnet. Berücksichtigt wurden hierbei Biokraftstoffkandidaten, die innerhalb der Exzellenzinitiative "Maßgeschneiderte Kraftstoffe aus Biomasse" an der RWTH Aachen in Deutschland diskutiert werden.

Aus der Gruppe der Alkohole wurde *iso*-Pentanol betrachtet. Es wurden die Ratenkonstanten der H-Abstraktion durch H-Atome und durch H \dot{O}_2 -Radikale im Hochdrucklimit berechnet.

Zudem wurden 2- und 3-Methyltetrahydrofuran (MTHF) als oxygenierte zyklische Kohlenwasserstoffe untersucht. Für diese Kraftstoffe wurden die Ratenkonstanten der Isomerisationsreaktionen des Alkylperoxy-Radikals zum Hydroperoxyalkyl-Radikal bestimmt. Detaillierte Analysen haben dabei gezeigt, dass die Bindungsstärke der C-H Bindungen, die Position des abstrahierten Wasserstoffs (cis oder trans) sowie die Ringgröße des Übergangszustands die Reaktionskinetik dieser Isomerisationsreaktionen beeinflussen.

Es wurden außerdem 2-Butanon und Aceton als Spezies aus der Gruppe der Ketone berücksichtigt. Für 2-Butanon wurden die Ratenkonstanten der H-Abstraktion durch Methylperoxy-Radikale (CH₃OO) im Hochdrucklimit ermittelt. Aufgrund des hohen Interesses an ketonischen Kraftstoffen wurde Aceton, welches das kleinste Keton darstellt, im Detail untersucht, um einen Einblick in die elementaren Reaktionen während des Verbrennungsvorgangs zu erlangen. Die Reaktionskinetik der O₂-Addition an das Acetonyl-Radikal, der Isomerisation des Acetonylperoxy-Radikals zur entsprechenden QOOH Spezies und der β-Spaltung des Acetonyl-Radikals wurde betrachtet.

Damit sind die Ergebnisse dieser Berechnungen sowohl förderlich für das fundamentale Verständnis von Verbrennungsvorgängen als auch von Nutzen für die Entwicklung detaillierter kinetischer Modelle.

Acknowledgement

First and foremost, I would like to express my sincere gratitude to my supervisor Prof. Dr.-Ing Karl Alexander Heufer for his guidance, support and constant encouragement throughout the research. I am extremely thankful to Prof. Dr. rer. nat. Ravi Fernandes, with whom I had opportunity to begin my doctoral studies in Germany. Thanks to Univ.-Prof. Dr.-Ing Heinz Pitsch for his guidance. I express my sincere thanks to Prof. Dr. Yasuyuki Sakai for his valuable advice, motivation and efforts throughout my research and also for my extremely fruitful research stay in Japan. I would also like to thank Prof. Henry Curran and Dr. Chongwen Zhou for giving me an opportunity to perform research at NUIG, Ireland. My professors from India have important role in my research journey; sincere thanks to Prof. Julio Fernandes, Dr. Purnakala Samant, Mrs. Varsha Sail and Dr. Jyoti Sawant.

I am extremely thankful to my colleagues from PCFC namely Ajoy Ramalingam, Heiko Minwegen, Rene Büttgen, Sascha Jacobs, Philipp Morsch, Christian Hemken and Ultan Burke for a friendly working environment, helpful research discussions and for helping me with a German language whenever needed. Also thanks to Malte Döntgen, Wassja Kopp, Maximilliam Hombsch, Yasar Uygun, Changoyl Lee, Stijn Vranks for the help and support during my research. I would also like to acknowledge the cluster of excellence; TMFB at the RWTH Aachen University, Germany for supporting my research.

I am very much thankful to Ms. Valeen Almeida, Vritika, Vrishab and Rishaan for the everlasting care. Many thanks to my friends from India, Mira, Pranay, Dattaprasad, Sandesh, Daniel and many more for the motivation and support from India. My Indian friends in Germany; Rupali Tripathi, Smitha Manjunatha, Ajith Sathish, Tonima Muckerjee have been like a family away from home, thanks to everyone. I am very blessed to have very caring and loving sister Dr. Priteeja Parab and brother Devraj Parab, you both have filled my life with endless joy and happiness. Thanks a million to my very supportive and caring husband Dr. Gauresh Palav for the motivation, guidance, and many more; you are really the strength and pillar of my life. I would like to thank my in-laws Mr. Gajanan Palav and Mrs. Savita Palav and brother in law Dr. Shailesh Palav for their encouragement.

At the last but not the least countless thanks to my role models, my parents Mr. Rajaram Parab and Mrs. Rupali Parab. There are absolutely no words to explain how blessed and proud I feel being their daughter. It's only because of your love, care and long lasting and endless support I was able to travel miles of distance away from my home to fulfill the research dream. Thank you God!



I. Introduction

I.1 Energy and Environment

Currently, the major focus in combustion research area is moving towards alternative and promising fuel candidates. Principal reasons are the issues regarding energy security and environmental safety concerning Greenhouse Gas (GHG) emission. The major portion of the GHG emission in the environment arises from the combustion of the fossil fuels. The GHG such as carbon dioxide has an adverse effect on the environment [1-3]. In order to reduce GHG and pollutant emissions, sustainable fuel candidates that can be alternatives or blending components to conventional gasoline or diesel based fuels are in high demand. Also the dependence on the fossil fuels cannot be on a long term basis due to the depletion of the existing fossil fuels resources. In 2011, highly utilized fuels such as oil, coal and natural gas have accounted for ~87% of the global energy consumption [4]. In this context, biofuels are gaining popularity among the other classes of fuels due to advanced synthetic approaches and their compatibility with modern engine technologies [1-5]. Biofuels can also be used as additives to the already existing fossil fuels for the efficiency enhancement and pollution control. Since these fuels are novel, more details into their chemical reactivity during combustion is yet to be revealed especially emphasizing the key factors influencing pollutant emissions at engine relevant conditions.

This thesis provides theoretical insights on the combustion kinetics of biofuel candidates of interest at the Cluster of Excellence, Tailor Made Fuels from Biomass (TMFB) at the RWTH Aachen University, Germany. Detailed quantum mechanical studies have been carried out focusing on different functional group molecules such as alcohol, furanics and ketones. From the alcohol functional group; isopentanol, from furanics, 2-methyltetrahydrofuran (2-MTHF) and 3-methyltetrahydrofuran (3-MTHF) and from ketones, 2-butanone and acetone were investigated to understand their combustion behavior.

i. Biofuels

In 2012, transportation sector accounted for 25% of the global energy consumption [6] and produced 22% of the global anthropogenic CO₂ emissions [7]. Among the transportation sector, road transportation contributed largest emissions of 75% [8]. One way to reduce carbon emissions from the road transportation can be by using alternative fuels such as biofuels [8]. The use of biofuels in the transportation sector is increasing in recent years worldwide. In 2015, consumption of biofuel in the United States accounted for around 5% of primary transportation energy [9]. Biofuel has a tendency to reduce the GHG emission and

are also way of energy security over the existing fossil fuels. They are mainly classified into two major types: first and second generation biofuels. First generation biofuels are directly produced from the food crops such as corn, sugarcane and wheat, whereas the feedstock used in producing the second generation biofuels are generally non-food crops which do not compete with the food production. These second generation biofuels are also called as advanced biofuels

ii. Tailor Made Fuels from Biomass (TMFB) and Goals of this Thesis

The Cluster of Excellence, Tailor made fuel from Biomass (TMFB) at RWTH Aachen University, Germany, adopts novel approaches for the biofuel synthesis. The vision of TMFB is to establish innovative and sustainable processes for the conversion of whole plants into fuels that are tailor-made for novel low-temperature combustion engine processes with high efficiency and low pollutant emissions, paving the way to advanced biofuels. In this context, this thesis focuses on detailed theoretical understanding of the reaction kinetics of important reactions taking place during the combustion of biofuel candidates of interest at the TMFB. In addition to the reaction kinetics study, emphasis has also been put on computing thermodynamics properties of the intermediate species formed during fuel combustion. The kinetic and thermodynamic data obtained herein have major application in the combustion research area [10]. This information serves as a substantial input for the development of detailed chemical kinetic model as discussed in section I.2.

Among the various biofuels of interest at the TMFB, isopentanol was considered as one of the important alcoholic biofuel candidates. From the synthesis point of view, non-fermentive pathways have been reported for such higher branched chain alcohols [11]. Since branched chain C4 and C5 alcohols have higher octane number than the corresponding straight chain counterparts, it has been considered as a potential gasoline additive [12]. Herein, computational kinetics study was performed on the reaction kinetics of the H-atom abstraction reactions from isopentanol by H atom and HO2 radical. The conventional transition state theory has been implemented for computing high pressure limiting rate constant for these reactions. Details about these calculations are highlighted in section IV.1 Furthermore, the TMFB also showed research interests in furanic candidates due to reported biosynthetic approaches [13-15]. Considering tetrahydrofurans (THFs), methyl substituted tetrahydrofururans such as 2-Methyltetrahydrofuran (2-MTHF) and 3-Methyltetrahydrofuran (3-MTHF) are of prime interest. 3-MTHF and 2-MTHF can be synthesized using cellulosic

biomass from the biogenic platform chemicals, itaconic acid and levulinic acid respectively

[15, 16]. In order to understand more details about the reactions taking place during the low temperature combustion of 2-MTHF and 3-MTHF, a systematic computational study was carried out. The main focus here was to investigate reaction kinetics of one of the important low temperature reaction class i.e. alkylperoxy radical (ROÖ) to hydroperoxyalkyl radical (QOOH) reactions taking place during their combustion. Rate constants for this reaction class in the case of tetrahydrofuran (THF) are not available in the literature. Also, due to the presence of ring oxygen in THF, rate rule analogy cannot be used from cyclic alkanes such as methylcyclopentane (mcyc5). In this study, rate constants for the ROÖ to QOOH reactions were calculated for two THFs (2-MTHF and 3-MTHF) and then compared with similar reactions in mcyc5 to understand the effect of ring oxygen on reaction kinetics of these reactions. Furthermore, thermodynamic properties of all the ROÖ and QOOH species involved in 2-MTHF and 3-MTHF isomerization reactions are reported in section IV.2 and IV.3.

Another potential biofuel candidate of interest at the TMFB that has been considered here belongs to the ketone functional group; namely 2-butanone (2-BT). Due to the engine-relevant properties and sustainable production pathways, detailed investigation of 2-BT is of principal interest [16, 17]. In this regard, 2-BT is of highlight in understanding high pressure limiting rate constant for the H-atom abstraction reactions from the fuel by methylperoxy radical (CH₃OÖ). Details on this computation are presented in section IV.4.

Lastly, theoretical calculations were performed on the smallest member of the ketone family, i.e. Acetone. The main highlight here is towards understanding the reaction kinetics for the important reactions taking place during the oxidation of acetone. Rate constant were determined for the beta scission reaction taking place in the acetonyl radical. Also pressure dependent rate was computed for the addition of O_2 to the acetonyl radical to form acetonylperoxy radical by considering Quantum Rice-Ramsperger-Kassel (QRRK) theory. The isomerization of acetonylperoxy radical to the corresponding QOOH species were investigated together with thermochemistry of all the species involved in these reactions. The results are reported in section IV.5.

I.2 Combustion Chemistry

Combustion is a very complex phenomenon which can involve around hundreds of intermediate chemical species and about thousands of elementary reactions before giving final combustion products. Although combustion of fuels produces carbon dioxide and water

as major products, it also involves the formation of other side products such as carbon monoxide, oxides of nitrogen, soot, unburnt hydrocarbons etc. Due to the environmental hazards caused by these emitted pollutants, clean combustion is the main and prime requirement for any fuel candidate. In order to understand the combustion behavior of these fuels over a wide temperature and pressure regime, research has also been focused on the kinetics of elementary reactions. Figure 1 highlights kinetic scheme of the primary oxidation reactions in hydrocarbon (RH).

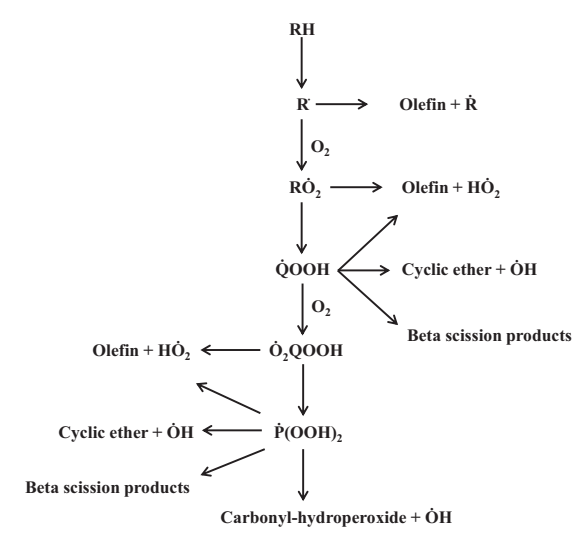


Figure 1. Schematic of overall reaction paths in hydrocarbon combustion [10, 18]

Due to a large number of elementary reactions involved in combustion mechanism, reactions are grouped into various classes and are called as "reaction classes". In general, the kinetic reaction mechanism for the hydrocarbon oxidation is divided into high temperature and low temperature reaction classes. At both high and low temperatures, combustion of fuel can be initiated by the H-atom abstraction from RH by radicals such as H, $H\dot{O}_2$, $\dot{O}H$, $\dot{C}H_3$ etc. At high temperatures, thermal decomposition of fuel radical (\dot{R}) into an olefin and smaller alkyl radical dominates. However at low temperatures, addition of molecular O_2 to alkyl radical primarily forms alkyl-peroxy radical ($R\dot{O}_2$) species. This $R\dot{O}_2$ can further undergo direct elimination of $H\dot{O}_2$ radicals and forming olefins. The $H\dot{O}_2$ radicals are relatively unreactive and its removal reactions involve formation of H_2O_2 . Since the H_2O_2 is stable up to ~ 1100 K, this channel leads to chain-termination at low temperatures [10]. The kinetics of $\dot{R}+O_2$ reaction channels has a major influence on the negative temperature coefficient regime.

Depending on the temperature and pressure various product channels can be formed which tends to have significant effect on the overall reactivity of fuel. The reaction of $\dot{R} + O_2$ can also proceed via vibrationally excited alkylperoxy complex (RO2*) leading to the formation of olefin and HO2 radical [19]. At high pressure and low temperature conditions, RO2* radicals undergo collisional stabilization. As the temperature increases, the equilibrium of R + O₂ to form \dot{R} O₂ tends to favor \dot{R} + O₂. In such cases the fuel radical are mostly consumed via decomposition. Understanding the competition between these various elementary reaction channels is helpful to investigate ignition in great detail. Another reaction of RO2 species involves isomerization to produce hydroperoxy-alkyl (OOOH) species. In the low temperature regime, QOOH can undergo reactions such as cyclic ether formation, beta scission reactions and direct elimination of HO₂. The formation of highly reactive OH radical via cyclic ether formation makes this reaction channel important for the chain-propagation. Further, QOOH can react with molecular O₂ to give hydroperoxyl-alkyl-peroxyl (O₂QOOH) radicals, Curran et al. [19, 20] provided details about such elementary reactions involved in n-heptane and iso-octane oxidation. However, a study by Miyoshi [21] and Bugler et al [19] presented some low temperature reaction classes that were not considered in previous mechanisms. It involves reactions of hydroperoxyl-alkyl-peroxyl (O₂OOOH) radicals similar to the alkyl-peroxy radical (RO2) species such as direct elimination of HO2, and formation of dihydroperoxyl-alkyl radicals P(OOH)2. These radicals react in a similar fashion as that of hydroperoxy-alkyl radicals (OOOH) as depicted in Figure 1. The dissociation of P(OOH) produces multiple radicals, ultimately leading to the chain branching at low temperature.

Considering a specific fuel, knowledge about aforementioned reaction classes is necessary for the development of detailed chemical kinetic model. For these models to be practical, accurate reaction kinetics of the elementary reactions along with thermodynamic properties (such as a standard enthalpy of formation, entropy and heat capacities) of involved chemical species is in high demand. In such cases computational chemistry plays a predominant role and provides essential parameters for kinetic modeling. Especially the information that is difficult to obtain via experiments is made available with the help of theoretical approach. For example, enthalpy of formation or entropy is relatively well determined experimentally for the stable molecules, but for the reactive intermediates such as free radicals the situation is more complex. Also the kinetics of complex reaction systems such as $\dot{R} + O_2$ is well understood by quantum chemistry methods. The advances in the quantum chemistry and reaction kinetics have also provided a synergy between theoretical

and experimental methods [10]. Another advantage of the theoretical methods is that they facilitate the extrapolation of kinetics data over the wide temperature and pressure regime.

A brief fundamental overview of the reaction kinetics and thermodynamic properties is given in the following sections.

I.3 Reaction Kinetics

Chemical reaction kinetics deals with detail understanding and study of reaction rates of chemical processes. The rate of a chemical reaction highlights the rate at which the reactant/reactants are converted into products. In another way round, it can also be stated as the rate at which the products are formed from the reactant/reactants. In chemical kinetics, a rate constant 'k' quantifies the rate of a chemical reaction. The unit of a rate constant depends on the order of reactions.

i. Reaction Rate Constant

Consider a simple irreversible reaction,

$$aA + bB \rightarrow cC$$
 (1)

In this reaction, A and B are the reactants with their stoichiometric coefficients 'a' and 'b' respectively while C represents a product with the corresponding stoichiometric coefficient 'c'. At any time 't', the rate of consumption of reactant A and B are given as -d[A]/adt and -d[B]/bdt respectively. In terms of product C, the rate of formation of product in above reaction is d[C]/cdt. The negative sign in case of reactants indicates a decrease in the molar concentration of reactants as a function of time. Whereas, product concentration increases as reaction proceed hence, a positive in latter. The rate at which reactant (either A and B) disappears is directly proportional to its molar concentration raised to the power of its stoichiometric coefficient. It can be written as follows:

$$-\frac{\mathrm{d}\left[\mathrm{A}\right]}{\mathrm{d}t} \propto \left[\mathrm{A}\right]^{a} \tag{2}$$

$$-\frac{\mathrm{d}\left[\mathrm{B}\right]}{\mathrm{d}t} \propto \left[\mathrm{B}\right]^{b} \tag{3}$$

Where [A] and [B] indicates molar concentrations of reactant A and B respectively which is the number of moles per volume. Accordingly, the rate of formation of product C is shown below:

$$\frac{\mathrm{d}\left[\mathrm{C}\right]}{\mathrm{d}t} \propto \left[\mathrm{C}\right]^{c} \tag{4}$$

Equations (2), (3) and (4) can be written in the following forms:

$$-\frac{\mathrm{d}\left[\mathbf{A}\right]}{\mathrm{d}t} = k[\mathbf{A}]^{a} \tag{5}$$

$$-\frac{\mathrm{d}\left[\mathrm{B}\right]}{\mathrm{d}t} = k[\mathrm{B}]^{b} \tag{6}$$

And for the formation of product C,

$$\frac{\mathrm{d}\left[\mathrm{C}\right]}{\mathrm{d}t} = k[\mathrm{C}]^{c} \tag{7}$$

The coefficient k in equations (5), (6) and (7) is called the rate constant of the reaction. The rate constant k is a very important parameter in understanding the reaction kinetics and plays a significant role in the development of detailed chemical kinetic models. Experimentally, one can determine k for the reaction of interest as a function of temperature or pressure. However, sometimes the complexity of the aforementioned reaction networks makes it difficult to investigate single elementary reactions experimentally at combustion conditions. In such cases, theoretical methods such as quantum mechanical methods can provide important information.

ii. Transition State Theory

In order to determine the reaction rate, various theories have been proposed and improved over a period of time for the accurate rate estimation. Among a collision theory, the transition state theory (TST) has taken a predominant part in the field of chemical kinetics. According to the TST, one of the important factors for a successful reaction is that the reactants must undergo an effective collision. The basic principles underlying the TST are highlighted below.

The effective collision of reactants in a chemical reaction leads to a formation of an activated complex, also known as transition state complex. The TST deals with understanding the rate constant of reactions based on the concepts of statistical thermodynamics. It is a widely used theory for calculating rates of bimolecular reactions in gas and also in condensed phases.

The TST was developed simultaneously by Henry Eyring [22] at the Princeton University and by Meredith Gwynne Evans and Michael Polanyi [23] at the University of Manchester in 1935. This theory is applicable to the canonical ensembles in which the Boltzmann distribution of a given temperature is attained among all the molecules in the ensemble. Consider a simple reaction below:

$$A + B \rightleftharpoons [AB]^{\#} \to P \tag{8}$$

One of the important features considered by Eyring, Evans and Polanyi is that the transition state complex, $[AB]^{\#}$ is in quasi-equilibrium with the reactants. Employing statistical mechanics, the concentration of transition state complex can be computed in term of concentration A and B. The equilibrium constant, $K^{\#}$ for the quasi-equilibrium can be written as:

$$K^{\#} = \frac{[AB]^{\#}}{[A][B]} \tag{9}$$

Hence, $[AB]^{\#} = K^{\#}[A][B]$

The rate equation for the formation of product P is,

$$\frac{d[P]}{dt} = k^{\#}[AB]^{\#} = k^{\#} \cdot K^{\#} \cdot [A][B] = k[A][B]$$
 (10)

Wherein, $k=k^{\#}K^{\#}$ and $k^{\#}=\lambda k_BT/h$, where λ is called as the transmission coefficient, k_B is the Boltzmann's constant and h is the Plank's constant.

Since $K^{\#}$ is the equilibrium constant between the reactants and the transition state, the thermodynamic formulation of the rate constant is written as,

$$k_{TST} = \frac{k_B T}{h} e \left(\frac{-\Delta G^{\#}}{RT} \right) \tag{11}$$

 $\Delta G^{\#}$ is the difference in the Gibbs free energy of the transition state and the reactants. Above equation (11) can be also written as:

$$k_{TST} = \frac{k_B T}{h} e\left(\frac{\Delta S^{\#}}{R}\right) e\left(\frac{-\Delta H^{\#}}{RT}\right)$$
 (12)

Further, k_{TST} can be also formulated in terms of the partition function of the transition state and the reactants according to the equation (13):

$$k_{TST} = \frac{k_B T}{h} \left(\frac{q^\#}{q_A q_B} \right) e \left(\frac{-\Delta H^\#}{RT} \right) \tag{13}$$

 $q^{\#}$, q_A and q_B indicate partition function of the transition state, reactant A and reactant B respectively. Since TST relies on the principles of the statistical thermodynamics, an overview of the statistical thermodynamic equations used in computing thermodynamic parameters are briefly discussed in the following sections.

I.4 Thermochemistry

Thermochemistry deals with the study of the energy transferred as heat when chemical reactions occur. It's a branch of thermodynamics since a reaction vessel and its contents act like a system and a chemical reaction leads to the exchange of energy between the system and

surrounding [24]. Thermochemistry finds a wide application in different fields. The thermodynamic parameters such as standard enthalpy of formation ($\Delta_t H^*$), entropy (dS) and heat capacity at constant pressure (C_p) plays a prime role in the development of detailed kinetic models. In kinetic modeling, the rates of the forward and backward reactions within reaction mechanisms are governed by the equilibrium constants that are obtained from thermodynamics. An overview of the computational tools implemented in determining these thermodynamic parameters are given in chapter III. These computations are based on the concepts of statistical thermodynamics which is a link between microscopic properties of matter and its bulk properties. The statistical thermodynamics is related to the Boltzmann distribution and ultimately to the molecular partition function. The Boltzmann distribution is given as:

$$p_i = \frac{e^{-\beta \epsilon_i}}{a} \tag{14}$$

Wherein p_i indicates the fraction of molecules in the state 'i' which is equal to n_i/N , ϵ_i is the energy of the ith level and 'q' is the molecular partition function which is given as:

$$q = \sum_{i} e^{-\beta \epsilon_i} \tag{15}$$

Where $\beta = 1/k_BT$, *T* is the thermodynamic temperature and k_B is the Boltzmann's constant. Equation (15) can be also written as follows:

$$q = \sum_{levels i} g_i e^{-\beta \epsilon_i} \tag{16}$$

In equation (16) g_i indicates the degeneracy of the state 'i' and the sum is over all the energy levels. The partition function 'q' depends on the temperature. When the T=0, the partition function is equal to the degeneracy of the ground state, g_0 i.e. only the ground level is accessible. At very high temperature, the term $\epsilon_{i}/k_BT \sim 0$ in equation (16) and hence the partition function tends to infinity. It indicates the very large value of 'q' and virtually all states are accessible. Eventually, the partition function gives an idea about the number of states that are thermally accessible to a molecule at the temperature of the system [24]. This molecular partition function consists of the all the information that is needed to compute the thermodynamic properties of a system of independent particles.

i. Standard Enthalpy of Formation

The standard enthalpy of formation $(\Delta_f H^\circ)$ of a substance is the standard reaction enthalpy for the formation of the compound from its elements in their reference states [24]. The reference state is the most stable state of an element at the specified temperature and at 1 atm.

Considering for example at 298.15 K, the reference state of oxygen is a gas of O₂ molecules while that of carbon is graphite. The standard enthalpies of formation for the elements in their reference states are always zero at all temperatures.

ii. Entropy

The thermodynamic definition of entropy focuses on the change in entropy (dS) that occur as a result of a process which can be either a physical or a chemical change [24].

The change in entropy is given by an equation (17),

$$dS = \frac{\partial q_{rev}}{T} \tag{17}$$

Wherein, q_{rev} is the reversible transfer of heat into the system and T is the temperature. The second law of thermodynamics states that the entropy of isolated system increases in the course of a spontaneous change: $\Delta S_{\text{tot}} > 0$.

iii. Heat Capacity at Constant Pressure

As mentioned before, the enthalpy of a substance depends on the temperature and increases as its temperature is raised. The change in enthalpy of a substance with temperature also depends on two other conditions i.e., either constant pressure or constant volume. The C_p is defined as the heat capacity at constant pressure at a given temperature and is an extensive property. It is given by an equation (18),

$$C_P = \left(\frac{\partial H}{\partial T}\right)_P \tag{18}$$

These thermodynamic properties (enthalpy, entropy and heat capacity) of atoms, molecules can be computed with the aid of quantum chemical calculations by considering the geometry and vibrational frequencies within the molecule. Also according to the statistical transition theory, rate of a chemical reaction can be computed from the thermodynamic properties of the transition states and reactants involved in a chemical reaction. To give an idea about the fundamentals underlying in computing these thermodynamic properties from the quantum mechanics and ultimately from the electronic structure calculations, a brief overview is given in the following section.

iv. Statistical Thermodynamics

The contributions to entropy, energy and heat capacity resulting from translational, rotational, vibrational and electronic motions within a molecule are calculated from the partition function, q(V, T). The partition function from any component can be used to compute the entropy contribution S from that particular component by using the following relation [25]

$$S = Nk_B + Nk_B \ln\left(\frac{q(V, T)}{N}\right) + Nk_B T \left(\frac{\partial \ln q}{\partial T}\right)_V$$
 (19)

In above equation (19), k_B is the Boltzmann constant.

The necessary equations implemented in available computational chemistry tools are as shown below. Herein, Gaussian software package [26] is used for all the electronic structure calculations (details provided in section III.1). In Gaussian, molar values are given hence dividing equation (19) by $n = N / N_A$; wherein 'n' indicates the number of moles, 'N' is the number of entities (atoms or molecules) and ' N_A ' is the Avogadro constant and on substituting $N_A k_B = R$ gives,

$$S = R + R \ln \left(\frac{q(V, T)}{N} \right) + RT \left(\frac{\partial \ln q}{\partial T} \right)_{V}$$
 (20)

With N=1 and moving the first term into the logarithm (as e),

$$S = R + R \ln(q(V, T)) + RT \left(\frac{\partial \ln q}{\partial T}\right)_{V}$$
 (21)

$$= R \ln(q(V,T)e) + RT \left(\frac{\partial \ln q}{\partial T}\right)_{V}$$
 (22)

$$= R \left[ln(q_t q_e q_r q_v e) + T \left(\frac{\partial ln q}{\partial T} \right)_V \right]$$
 (23)

In the above equation (23); q_t , q_e , q_r , q_v , indicates translational, electronic, rotational and vibrational partition functions respectively. Further, the internal thermal energy E is related to the partition function by the equation,

$$E = Nk_B T^2 \left(\frac{\partial \ln q}{\partial T}\right)_V \tag{24}$$

From the internal thermal energy E, heat capacity (at constant volume) can be obtained according to the following equation,

$$C_V = \left(\frac{\partial E}{\partial T}\right)_{NV} \tag{25}$$

Equations (23), (24) and (25) are used to derive the final expressions which are used to calculate the components of thermodynamic properties in Gaussian [26]. The individual contributions from the translation, electronic, rotational and vibrational motions within a molecule are discussed in detail below.

a) Contributions from the translation

The equation for the translational partition function as given by [27] is:

$$q_t = \left(\frac{2\pi m k_B T}{h^2}\right)^{3/2} V \tag{26}$$

In equation (26), h is the Plank constant. By taking a partial derivative of q_t with respect to T gives,

$$\left(\frac{\partial \ln q_t}{\partial T}\right)_V = \frac{3}{2T} \tag{27}$$

This equation is used to calculate the internal energy E_t and also the third term in equation (19). In the second term of equation (19), V is unknown. However, the value of V can be derived from the ideal gas equation, $PV = NRT = \left(\frac{n}{N_A}\right) N_A k_B T$

And $V = k_B T / P$ which gives the following equation

$$q_t = \left(\frac{2\pi m k_B T}{h^2}\right)^{3/2} \frac{k_B T}{P} \tag{28}$$

Equation (28) is used to calculate q_t in Gaussian. Further, this translational partition function is used to calculate translational entropy according to the following equation (29). The translational entropy includes the factor 'e' coming from Stirling's approximation [28].

$$S_t = R\left(\ln(q_t e) + T\left(\frac{3}{2T}\right)\right) = R\left(\ln q_t + 1 + 3/2\right)$$
 (29)

And the contribution to the internal energy from the translation is,

$$E_t = N_A k_B T^2 \left(\frac{\partial \ln q}{\partial T} \right)_V = R T^2 \left(\frac{3}{2T} \right) = \frac{3}{2} R T \tag{30}$$

The contribution to the heat capacity at the constant volume due to translation is given by:

$$C_t = \frac{\partial E_t}{\partial T} = \frac{3}{2} R \tag{31}$$

b) Contributions from the electronic motion

The equation for the electronic partition function as given by McQuarrie [27] is

$$q_e = \omega_0 e^{\frac{-\epsilon_0}{k_B T}} + \omega_1 e^{\frac{-\epsilon_1}{k_B T}} + \omega_2 e^{\frac{-\epsilon_2}{k_B T}} + \cdots$$
 (32)

In equation (32), ω is the degeneracy of the energy level whereas ϵ_n is the energy of the *n*-th level. The important assumption made in Gaussian [26] is that the first and higher electronic excitation energies are much greater than k_BT and hence these excited states are assumed to be not accessible at any temperatures. ϵ_0 , which is the energy of the ground state, is set equal to zero which leads to the simplification of equation (32) as follows.

$$q_e = \omega_0 \tag{33}$$

The contribution to the entropy from the electronic motion is:

$$S_e = R \left(\ln q_e + T \left(\frac{\partial \ln q_e}{\partial T} \right)_V \right) \tag{34}$$

$$S_e = R \left(\ln q_e + 0 \right) \tag{35}$$

Due to no temperature dependent terms in the electronic partition function given above, the electronic heat capacity and also the internal thermal energy due to the electronic motion are zero.

c) Contribution from the rotational motion

The rotational motion contribution is divided depending on different cases such as single atoms, linear polyatomic molecules and non-linear polyatomic molecules.

Considering the first case i.e. for a single atom, $q_r = 1$. As q_r is independent of temperature, the rotational contribution to the internal thermal energy, entropy and also heat capacity are zero. For a second case i.e. for a linear molecule, the contribution to the rotational partition function is

$$q_r = \frac{1}{\sigma_r} \left(\frac{T}{\theta_r} \right) \tag{36}$$

In above equation, $\theta_r = h^2/8 \pi^2 I k_B$, wherein *I* is the moment of inertia. σ_r is the rotational symmetry number. The contribution of rotational motion to the entropy is,

$$S_r = R \left(\ln q_r + T \left(\frac{\partial \ln q_r}{\partial T} \right)_V \right) = R \left(\ln q_r + 1 \right)$$
 (37)

The rotational contribution to the internal thermal energy is,

$$E_r = RT^2 \left(\frac{\partial \ln q_r}{\partial T}\right)_V = RT^2 \left(\frac{1}{T}\right)_V = RT \tag{38}$$

The contribution to the heat capacity due to the rotational motion is,

$$C_r = \left(\frac{\partial E_r}{\partial T}\right)_V = R \tag{39}$$

For the third case with a nonlinear polyatomic molecule, the contribution to the rotational partition function as given by McQuarrie [27] is:

$$q_r = \frac{\pi^{1/2}}{\sigma_r} \left(\frac{T^{3/2}}{\left(\theta_{r,x}\theta_{r,y}\theta_{r,z}\right)^{1/2}} \right)$$
 (40)

The contribution for the entropy is:

$$S_r = R \left(\ln q_r + T \left(\frac{\partial \ln q_r}{\partial T} \right)_{\nu} \right) \tag{41}$$

Substituting

$$\left(\frac{\partial \ln q}{\partial T}\right)_{V} = \frac{3}{2T} \tag{42}$$

Equation (41) becomes,

$$S_r = R\left(\ln q_r + \frac{3}{2}\right) \tag{43}$$

The internal thermal energy is,

$$E_r = RT^2 \left(\frac{\partial \ln q_r}{\partial T}\right)_V = RT^2 \left(\frac{3}{2T}\right) = \frac{3}{2}RT \tag{44}$$

And the heat capacity is,

$$C_r = \left(\frac{\partial E_r}{\partial T}\right)_V = \frac{3}{2}R\tag{45}$$

d) Contribution from the vibrational motion

The vibrational contribution to the partition function, entropy, internal energy and the heat capacity at the constant volume are composed of a sum (or product) of the contributions from each vibrational mode, *K*. Only the real modes are considered in calculating the contribution from the vibrational motion. The non-linear molecules consist of 3n-6 while for linear molecules 3n-5 vibrational modes wherein each of these modes has a characteristic vibrational temperature given as,

$$\theta_{v,K} = h v_K / k_B \tag{46}$$

 v_K indicate the frequency for the vibrational mode K. The partition function due to the vibrational motion can be computed in two ways depending on where one chooses the zero of energy i.e. either the bottom of the internuclear potential energy well or the first vibrational level.

Considering the first case, i.e. if the zero reference point is chosen to the bottom of the well (represented as BOT), then the contribution to the partition function from the given vibrational mode is given by the equation:

$$q_{V,K} = \frac{e^{-\theta_{V,K}/2T}}{1 - e^{-\theta_{V,K}/T}} \tag{47}$$

From the above equation (47), the overall vibrational partition function is:

$$q_{V} = \prod_{\nu} \frac{e^{-\theta_{V,K}/2T}}{1 - e^{-\theta_{V,K}/T}} \tag{48}$$

For the second case, where if the zero of energy is chosen as the first vibrational energy level (V=0), the partition function for each vibrational level is,

$$q_{V,K} = \frac{1}{1 - e^{-\theta_{V,K}/T}} \tag{49}$$

The overall partition function is given as:

$$q_V = \prod_{K} \frac{1}{1 - e^{-\theta_{V,K}/T}}$$
 (50)

In Gaussian, BOT is used as the zero of energy to determine thermodynamic quantities. The difference between the two references is by factor $\Theta_{V,K}/2$ in the equation for the internal energy E_v . However, in the expressions of heat capacity and entropy this term vanishes as one differentiates with respect to temperature (T).

The total entropy contribution from the vibrational partition function is given as,

$$S_V = R \left(\ln(q_V) + T \left(\frac{\partial \ln q}{\partial T} \right)_V \right) \tag{51}$$

$$S_V = R \left(\ln(q_V) + T \left(\sum_K \frac{\theta_{V,K}}{2T^2} + \sum_K \frac{(\theta_{V,K}/T^2)e^{-\theta_{V,K}/T}}{1 - e^{-\theta_{V,K}/T}} \right) \right)$$
(52)

$$= R \left(\sum_{K} \left(\frac{\theta_{V,K}}{2T} + \ln(1 - e^{-\theta_{V,K}/T}) \right) + T \left(\sum_{K} \frac{\theta_{V,K}}{2T^2} + \sum_{K} \frac{(\theta_{V,K}/T^2)e^{-\theta_{V,K}/T}}{1 - e^{-\theta_{V,K}/T}} \right) \right)$$
(53)

$$= R \left(\sum_{K} \ln(1 - e^{-\theta_{V,K}/T}) + \left(\sum_{K} \frac{(\theta_{V,K}/T)e^{-\theta_{V,K}/T}}{1 - e^{-\theta_{V,K}/T}} \right) \right)$$
(54)

Multiplying by $e^{\theta_{V,K}/T}/e^{\theta_{V,K}/T}$ for the above equation (54) gives,

$$S_V = R \sum_{K} \left(\frac{\theta_{V,K}/T}{e^{-\theta_{V,K}/T} - 1} - \ln(1 - e^{-\theta_{V,K}/T}) \right)$$
 (55)

The contribution from the molecular vibration to the internal energy is

$$E_V = R \sum_{V} \theta_{V,K} \left(\frac{1}{2} + \frac{1}{e^{-\theta_{V,K}/T} - 1} \right)$$
 (56)

And the contribution to constant volume heat capacity due to vibrational motion is,

$$C_V = R \sum_K e^{\theta_{V,K}} / T \left(\frac{\frac{\theta_{V,K}}{T}}{e^{-\frac{\theta_{V,K}}{T}} - 1} \right)^2$$
 (57)

In above computations, low frequency modes are included. Since some of these modes may be internal rotations, need to be treated separately depending on the temperature and torsional barriers. The details about this approach are provided in Chapter IV.

II. Computational Details and Quantum Chemistry

Computational chemistry is a branch of chemistry which deals with the computer simulations in order to solve the chemistry related problems. It employs various computer programs to get detailed information about the molecular structures and properties. Gaussian is one such computational chemistry program initially released in 1970 by John Pople and his research group at Carnegie-Mellon University as Gaussian 70 [29], since then it has been continuously updated. The name "Gaussian" originated from the use of Gaussian orbitals by Pople in order to speed up the calculations as compared to the Slater-type orbitals (details in section II.3). This thesis had employed Gaussian 09 [26] for all the electronic structure calculations. Recently, Gaussian 16 [30] has appeared which represents a further development of Gaussian 09 system. The electronic wave function of a polyatomic molecule depends on several parameters such as bond distances, bond angles, dihedral angles of rotation about single bonds. A theoretical treatment of a polyatomic molecule involves calculation of the electronic wave function for a range of these parameters. Finally, the equilibrium bond distances, bond angles and dihedral angles are found as those values for the molecule which lowers the electronic energy including the nuclear repulsion. The four different methods that are mostly used for computing the properties of molecules are the ab initio, the semi-empirical, the density-functional and the molecular mechanics methods, details of which are provided in the following section

II.1 Computational Chemistry Methods

i. Ab initio Methods

Ab initio methods are the computational chemistry methods based on the quantum chemistry. Ab initio is a Latin term meaning "from the beginning" and indicates calculations based on the fundamental principles. This term was first used by Robert Parr and coworkers, and its background is described by Parr [31]. The calculations performed by employing ab initio methods use the correct Hamiltonian (\hat{H}). Also, these methods do not use any experimentally determined data but use fundamental physical constants. The simplest ab initio electronic structure calculation method is the Hartree-Fock (HF) method. It is basically an extension of the molecular orbital theory however in HF method instantaneous electron-electron interactions are not considered whereas its average effect is included. In reality, the electrons motions are correlated with each other which are not considered in HF method. The HF

method is the basis for the use of atomic and molecular orbitals in many-electron systems. For the *n*-electron atom, the Hamiltonian operator is given as follows [32] [Levine chapter 11 pg 309]:

$$\hat{H} = -\frac{\hbar^2}{2m_e} \sum_{i=1}^n \nabla_i^2 - \sum_{i=1}^n \frac{Ze'^2}{r_i} + \sum_{i=1}^{n-1} \sum_{i=i+1}^n \frac{e'^2}{r_{ij}}$$
 (58)

In above equation (58), the first sum consists of the kinetic-energy operators for the n electrons. The second sum highlights the potential energy for the attractions between the electrons and the nucleus of charge Ze'. The last sum is the potential energy of the interelectronic repulsions. In this, j > i avoids counting each interelectronic repulsion twice. The Hamiltonian in equation (11.1) is incomplete because it omits spin-orbital and other interactions.

For the hydrogen, the exact wave function is known whereas for helium and lithium very accurate wave functions have been calculated. For atoms of higher atomic number, the good wave function is determined by first considering the HF wave function and further accounting various corrections as highlighted in the following sections. The major sources of error arising in *ab initio* molecular electronic calculations are due to 1) neglect or incomplete treatment of electron correlation, and 2) incompleteness of the basis set (description of basis set in section II.3). Hence, these effects are considered in the post-HF methods. The post-HF methods are basically the set of methods developed to improve the HF calculations. It adds instantaneous electron correlation to take into account repulsions between the electrons. Also the errors arising due to the incompleteness of the basis are tried to minimize in the post-HF methods. Some of the post-HF methods are briefly highlighted below.

a) Configuration Interaction (CI): CI is a popular approach in which correlation effects are incorporated into *ab initio* molecular orbital calculations. In this approach excited states are included in the description of an electronic state. For the molecular CI calculations, set of basis functions χ_i , (section II.3) are chosen in order to perform self-consistent field molecular orbital (SCF MO) calculations to find SCF occupied and virtual (occupied) MOs. These MOs are then used to form configuration (state) functions (CSFs), Φ_i . Further, the molecular wave function ψ is written as linear combinations of the CSFs. Consider the following example, the ground state of lithium has an electronic configuration, $1s^22s^1$. The excitation of outer valence electron gives states such as $1s^23s^1$. In such case the better description of the overall wave function is a linear combination of the ground and excited-state wave functions. More details about the CI approach can be found in [32].

b) Coupled-cluster (CC) method: The CC method for molecular electronic calculations were developed by Cizek, Paldus, Sinanoglu, and Nesbet in 1960s and by Pople and coworkers and Bartlett and co-workers in the 1970s [33]. The fundamental equation in CC theory is given as

$$\psi = e^{\hat{T}} \phi_0 \tag{59}$$

Wherein, Ψ is the exact non-relativistic ground-state molecular electronic wave function, Φ_0 is the normalized ground-state HF wave function. The $e^{\hat{T}}$ is the operator which is defined by the Taylor-series expansion.

$$e^{\hat{T}} = 1 + \hat{T} + \frac{\hat{T}^2}{2!} + \frac{\hat{T}^3}{3!} + \dots = \sum_{k=0}^{\infty} \frac{\hat{T}^k}{k!}$$
 (60)

The \hat{T} is called the cluster operator which is given as,

$$\hat{T} = \hat{T}_1 + \hat{T}_2 + \dots + \hat{T}_n \tag{61}$$

In equation (61), n is the number of electrons in the molecule. \hat{T}_1 and \hat{T}_2 are called the one-particle and two particle excitation operator respectively. In CC method, two approximations are made. Firstly instead of using complete and infinite set of basis functions (section II.3), finite basis set is used. Secondly, operator \hat{T} in equation (61) is approximated by including only some of the operators. In equation (60), if $\hat{T} = \hat{T}_1 + \hat{T}_2$, gives CC singles and doubles (CCSD) method. With $\hat{T} = \hat{T}_1 + \hat{T}_2 + \hat{T}_3$, one obtains CC singles, doubles, and triples (CCSDT) [34] method. CCSDT calculations are computationally demanding and are feasible for small molecules. One of the widely used method is CCSD(T), which is coupled cluster with inclusion of single and double excitations and perturbative inclusion of triple excitations. Pople and co-workers developed quadratic configuration interaction (QCI) method [35, 36] which is intermediate between CC and CI methods.

c) Moller-Plesset perturbation theory (MP2, MP3, MP4, etc): In 1934, Moller and Plesset proposed a perturbation treatment of atom and molecules to consider electron correlation effect. In their method, the unperturbed wave function is the Hartree-Fock function and developed theory is called as Moller-Plesset (MP) perturbation theory. The molecular application of MP perturbation theory began in 1975 with the work of Pople and co-workers and Bartlett and co-workers [37]. In MP, electron-correlation calculations are performed by choosing a basis set to carry out molecular orbital calculation to obtain Φ_0 , E_{HF} (HF energy) and virtual orbitals. To improve HF energy, corrections to the energy are accounted in MP theory. MP2, MP3 and MP4 indicate inclusion of energy corrections through second order, third and fourth order respectively. In MP4 calculations, the term that involves triply

substituted determinants is sometimes neglected which gives an approximation to MP4. In such cases it is denoted as MP4(SDQ), where SDQ indicates inclusion of single, double and quadruple excitations. The MP calculations are specified using the level of theory used (MP2, MP3, MP4) along with the basis set. For example, MP2/6-31G(d) indicates a second-order Moller-Plesset calculation with the 6-31G(d) basis set.

d) Quantum chemistry composite methods: The aim of the quantum chemistry composite methods is to achieve 1 kcal mol^{-1} or better accuracy with a computational time that allows calculations on molecules containing non-hydrogen atoms. Examples of composite methods are CBS-QB3 [38, 39], CBS-APNO [40], Gn (n=1, 2, 3, 4) [41-44], etc. These methods use series of *ab initio* computations along with empirical corrections. The details of these methods are provided in section II.3.ii.

ii. Density Functional Methods

The density functional theory methods (DFT) are sometimes also considered as *ab initio* methods to determine molecular structures, although most common functional use parameters that are obtained by empirical methods. A functional F[f] is a rule that associates a number with each function f. In 1964, Pierre Hohenberg and Walter Kohn proved that for molecules with a non-degenerate ground state, the ground-state molecular energy, wave function, and all molecular electronic properties are uniquely determined by the ground-state electron probability density, $\rho_0(x,y,z)$ [45]. The zero subscript in ρ indicates the ground state. Unlike *ab initio* methods, DFT methods do not calculate molecular wave function, but attempt to calculate ground-state electronic energy from the ground-state electron density (ρ_0). However, the Hohenberg-Kohn theorem does not tell how to calculate E_0 (ground-state molecular energy) from ρ_0 nor does it tell how to find ρ_0 without first finding wave function. Hence, in 1965 Kohn and Sham [46] devised a method for finding ρ_0 and then E_0 from ρ_0 . Fundamental details of this method are available in quantum chemistry textbook [32]. Overall, in DFT the energy of the system (E_{DFT}) is given as follows.

$$E_{\text{DFT}} = E_{\text{NN}} + E_{\text{T}} + E_{\text{v}} + E_{\text{coul}} + E_{\text{exch}} + E_{\text{corr}}$$
 (62)

Wherein, $E_{\rm NN}$ - nuclear-nuclear repulsion energy; $E_{\rm T}$ - kinetic energy of the electrons; $E_{\rm v}$ - nuclear-electron attraction energy; $E_{\rm coul}$ - classical electron-electron Coulomb repulsion energy; $E_{\rm exch}$ - non-classical electron-electron exchange energy; $E_{\rm corr}$ describes the energy due to the correlated movement of electrons of different spin.

iii. Semi-empirical Methods

The semi-empirical methods are simplified forms of HF theory using empirical corrections for performance improvement. These methods use a simpler Hamiltonian (\hat{H}) than the correct molecular Hamiltonian and are basically important for considering calculations involving large molecules. The semi-empirical methods are basically used for treating molecules for which the full HF method without approximations is very expensive.

iv. The molecular-mechanics methods

The molecular-mechanics (MM) methods do not belong to a quantum-mechanical method. In this method neither molecular Hamiltonian operator (\hat{H}) nor a wave function is used to calculate molecular energy. A molecule is considered as collections of atoms (balls) which are held together by bonds (spring between the balls) and hence the molecular energy is expressed in terms of the force constants. Using the parameters such as bond-stretching and bond-bending force constants, and also by allowing interactions between non-bonded atoms, the MM method constructs a potential-energy expression as a function of the atomic positions. It then predicts equilibrium geometries and relative energies by minimizing the potential-energy expression for various molecular conformers. MM methods find applications to organic, organometallic and transition-metal coordination compounds.

Further, in quantum chemistry the most important step in solving a chemical problem is based on the solution of Schrödinger equation. In order to solve the Schrödinger equation for one electron system, the Born-Oppenheimer approximation is used which is briefly discussed in the following section. However, Schrödinger equation cannot be solved exactly for many electron systems; hence various approximation methods are developed.

II.2 The Schrödinger Equation and the Born-Oppenheimer approximation

In 1926, Austrian physicist Erwin Schrödinger discovered the concept of the wave function and the equation governing its change as a function of time. The time-dependent Schrödinger equation is given as,

$$-\frac{i\hbar}{\partial t}\frac{\partial \Psi(x,t)}{\partial t} = -\frac{\hbar^2}{2m}\frac{\partial^2 \Psi(x,t)}{\partial x^2} + V(x,t)\Psi(x,t)$$
 (63)

In above equation, Ψ is called the state function or the wave function. For a one particle, one-dimensional system, $\Psi = \Psi(x,t)$. The constant $\hbar = (h/2\Pi)$, $i = \sqrt{-1}$, m is the mass of the

particle and V(x, t) is the potential energy function of the system. The wave function Ψ contains all possible information about a system.

The Schrödinger equation helps in getting the wave functions and energies of the system according to the equation (64),

$$\widehat{H}\Psi(q_i, q_\alpha) = E\Psi(q_i, q_\alpha) \tag{64}$$

 q_i and q_a indicate the electronic and nuclear coordinates respectively. \hat{H} is the Hamiltonian operator and E is the energy eigen value.

As mentioned before, one of the important approximations considered in quantum mechanics is the Born-Oppenheimer approximation which separates electronic and nuclear motions in the molecule. Born and Oppenheimer's mathematical treatment highlighted that the true molecular wave function is approximated as,

$$\Psi(q_i, q_\alpha) = \Psi_{el}(q_i; q_\alpha) \Psi_N(q_\alpha)$$
(65)

In above equation (65), Ψ_{el} and Ψ_{N} represent electronic and nuclear wave function respectively. The Born-Oppenheimer approximation is based on the fact that the nuclei are much heavier than the electrons and hence the electrons move much faster than the nuclei. Classically during the time of a cycle of the electronic motion, the change in nuclear configuration is negligible. Hence, considering the nuclei as fixed the nuclear kinetic energy terms are omitted from the molecular Hamiltonian to obtain the Schrödinger equation for the electronic motion [32].

II.3 Computational Models and Model Chemistries

The molecular quantum—mechanical methods mentioned in section II.1 such as CI, perturbation theory, coupled cluster, or density functional theory methods begin calculations with a set of basis functions ($\chi_{\rm r}$). The overview of basis functions is given in the following section. These basis functions are used to express the molecular orbitals, $\Phi_{\rm i}$. Gaussian consists of many model chemistries and theoretical models which are implemented to test different properties of molecules. These model chemistries are differentiated by the combination of theoretical methods and the basis sets.

i. Basis Set

A basis set is a set of mathematical functions (basis functions) used to define molecular orbitals within a system which is used to perform theoretical calculations. These basis functions are combined in linear combinations to create molecular orbitals. In the

computational models, calculations are usually performed by taking into account a finite set of basis functions. A general expression of the basis function is given as,

Basis Function
$$(\gamma) = N \cdot e^{(-\alpha r)}$$
 (66)

Wherein, N is a normalization constant, α is an orbital exponent and r is a radius in Angstrom.

Considering diatomic molecules, basis functions usually consists of atomic orbitals, some centered on one atom and the remaining centered on the second atom. This atomic orbital can be represented as a linear combination of one or more Slater-type orbitals (STOs). The STO's are expressed in the following form,

$$\chi_{n,l,m}^{STO} = NY_{l,m}(\theta, \phi) \exp^{(-\zeta r)}$$
(67)

In equation (67) n, l and m are the quantum numbers. ζ is the exponent and accounts for how diffuse (large) the orbital is. N is the normalization constant and $Y_{l,m}(\theta,\phi)$ are the spherical harmonics. In above equation, if n=1, the emerging STO is an exact hydrogen like 1s orbital. These STO's perform well with small basis set. However, major difficulties arose to evaluate general many-center molecular integrals with reasonable time and adequate accuracy. Hence, to overcome this problem, Gaussian-type orbitals (GTO's) were introduced and played an important role in the electronic structure calculations [47, 48]. The GTO's can be expressed in the following form,

$$\chi_{n,l,m}^{GTO} = NY_{l,m}(\theta,\phi) r^{2n-2-l} \exp^{(-\alpha r^2)}$$
 (68)

In equation (68) the orbital exponent α , is positive. It determines the radial extent (or spread) of a Gaussian function. GTO's are comparatively less accurate than STO's in the descriptions of electrons in regions close to and far away from the nucleus due to the exponential dependence on r^2 . For the hydrogen like wave functions, the correct cusp at the nucleus is well replicated by STO's whereas it is absent in the case of GTO's. Also GTO's were observed to fall off rapidly far from the nucleus. In order to improve the performance of the GTO's to get results with high accuracy; several authors [47-49] suggested an idea of representing the STO's atomic orbitals by linear combinations of GTO's. Pople et al. [50, 51] suggested using linear combinations up to K=6 GTO's which are obtained by least-squares methods as given below.

$$\chi_{\mu}^{STO} = \sum_{i}^{K} c_i \chi^{GTO}(\alpha_i) \tag{69}$$

The GTO's are called primitives and the resulting combination is known as contracted function. The notation used by Pople et al. [50, 51] for the minimum basis set is STO-KG. It was found that a good compromise between computation time and accuracy was achieved by

STO-3G. For Pople basis set, the "G" in the notation indicates that Gaussian primitives are used

Minimal basis set

A minimal basis set is the one that contains a minimum number of basis functions needed to define each atom. For better understanding, consider the following examples. For a hydrogen atom with 1s atomic orbital, minimum basis set contains only one basis function. However, for carbon atom with 1s, 2s, $2p_x$, $2p_y$ and $2p_z$ atomic orbitals, minimum basis set contains five basis functions in order to define a carbon atom. The basis sets STO-3G, STO-4G, etc. (STO-nG) are all minimal basis set in which n Gaussian functions are used to represent each orbital. However, extended basis set takes into account higher orbitals of the molecules which in turn account for the size and shape of the molecular charge distributions. These extended basis sets are classified into various types, details of which are explained below.

a. Double zeta basis set

The electronic energy of a molecule decreases and approaches closer to the exact value as the number of basis functions are increased. Hence, it is more important to consider more basis functions than a minimal basis set. The double zeta basis set (DZ) uses two basis functions of each type found in the separated atoms. Considering the example of a carbon atom, the double zeta basis includes two 1s, two 2s and two each of $2p_x$, $2p_y$ and $2p_z$ orbitals. The basis functions in this case is represented as 1s, 1s', 2s, 2s', 2p(3) and 2p'(3). 2p(3) represents the set of three 2p orbitals $(2p_x, 2p_y \text{ and } 2p_z)$. The two types of 1s, 2s and 2p orbitals considered in a basis set above are not identical, since they have a different orbital exponent.

b. Triple zeta basis set

The triple zeta (TZ) basis set employs three basis function of each type found in the separated atoms. A triple zeta basis set for the carbon atom includes three 1s, three 2s and three each of $2p_x$, $2p_y$ and $2p_z$ orbitals, hence it consists of total 15 basis functions. The three basis functions for each type considered above have different orbital exponents and are not identical. For the carbon atom, triple zeta basis set is denoted as 1s, 1s', 1s", 2s, 2s', 2s", 2p(3), 2p"(3) and 2p"(3). Further, there are also quadruple zeta and higher basis sets.

c. Split valence basis set

Split valence basis set consist of two or more basis functions that are used to define each valence orbital of an atom. Since the core electrons of an atom are less influenced by the chemical environment than the valence electrons, the former is treated with a minimal basis set while valence electrons are treated with a larger basis set. The notation used by Pople for the split-valence basis set is *X-YZg*. In this, *X* represents number of Gaussian primitive

containing each core atomic orbital basis functions. The Y and Z indicate that the valence orbitals are described by two basis functions each. The first one is composed of a linear combination of Y Gaussian primitive while second is composed of a linear combination of Z Gaussian primitive. Consider the following example of a split valence basis set. In 3-21G, the inner shells are described using a linear combination of 3 Gaussian primitives while the valence shell is described using the two sets of the basis functions; one is expanded in a set of 2 Gaussian primitives and the other in a set of 1 Gaussian primitive.

d. Polarized basis set

Polarized basis set adds orbitals with angular momentums for the proper description of the ground state of each atom. For example, for hydrogen/helium atoms in which the only occupied orbital is s-type, polarized basis set add p-type or d-type basis functions. For the carbon atom, d-type or f-type functions are known as the polarization functions. The polarized basis sets are included in order to improve the flexibility of the existing basis set. For example, the electron density of an isolated hydrogen atom is spherical in nature. When it is involved in the bond, the electron density is polarized and is no longer spherical. In such cases adding polarized basis functions can represent electron densities in molecule in a better way. The polarization is denoted by an asterisk (*) or as (d) when heavy atoms are corrected with the d-type functions or with two asterisks (**) or as ((d, p)) when correction is also applied for a hydrogen/helium atom with d and p-type function. Examples of the polarized basis sets are: 6-31G(d), 6-311G(d, p), 6-311G(df).

The 6-31G(d) basis set indicates that the d-type polarization has been added to each non-hydrogen atom in a molecule. In this case, no polarization function has been added to the hydrogen. In a second example, i.e. 6-311G(d, p) it indicates that one set of d-type polarization functions is added to the non-hydrogen atoms and one set of p-type polarization functions is added to hydrogen/helium atom. The notation 6-311(2df) mean that two sets of d-type polarization functions and one set of f-type polarization functions are added to all non-hydrogen atoms in a molecule.

e. Diffuse basis functions

Diffuse basis functions are the extra basis function usually s-type or p-type that are added to the basis set to represent broad electron distributions. These diffuse basis functions play important role in representing the electron density in case of anions and in intermolecular complexes. The use of the diffuse function is denoted by + or ++. In 6-31+G(d), + indicates that one set of sp-type diffuse basis functions is added to non-hydrogen atoms. In 6-31+G(d)

represents that one set of *sp*-type diffuse functions is added to each non-hydrogen atom and one *s*-type diffuse function is added to hydrogen atoms.

f. Correlation-consistent basis set

Dunning and co-workers [52] developed cc-pVnZ (wherein n goes from 2 to 6) basis sets which were designed for use in calculation methods that include electron correlation. These basis sets are denoted as cc-pVDZ (n = 2), cc-pVTZ (n = 3), cc-pVQZ (n = 4), cc-pv5Z (n = 5), and cc-pV6Z (n = 6). Here, cc-pVDZ stands for correlation-consistent, polarized valence double-zeta basis set. These sets are defined for the following elements. For H-Ar, Ca, and Ga-Kr, cc-pVDZ and cc-pVTZ. For H-Ar and Ca, cc-pVQZ and cc-pV5Z and for H and B-Ne, cc-pV6Z. Further, diffuse primitive non-polarization and polarization functions are added to the cc-pVnZ basis sets to give augmented basis sets. These augmented basis sets are represented as aug-cc-pVDZ, aug-cc-pVTZ, etc., and are suitable for calculations on anions and hydrogen-bonded species.

To perform a quantum-mechanical calculation, one has to specify the method along with the basis set to be used. For example, the notation HF/3-21G(d) indicate Hartree-Fock method with the 3-21G(d) basis set. In this thesis work, electronic structure calculations are performed employing various composite methods such as CBS-QB3 [38, 39], CBS-APNO [40], G3[43], G4 [44], and by also implementing coupled cluster method (Chapter IV). In the case of composite methods, all the distinct steps are performed automatically when the method is specified. A short overview of different steps involved in these composite methods is provided below. The commonly used keywords in the electronic structure calculations are discussed in chapter III (computational chemistry tools).

ii. Gaussian Composite Methods

The Gaussian composite methods are the computational methods which combine the results from several calculations with an aim to achieve better accuracy. It aims for the chemical accuracy which is defined as within 1 kcal mol⁻¹ of the experimentally determined value. These methods are commonly used for the computation of thermodynamic properties such as enthalpies of formation, atomization energies, bond dissociation enthalpies and also for studying the reaction kinetics. In these methods series of *ab initio* methods along with empirical corrections are used. The aim of these composite methods is to provide reasonable computational time which allows calculations on molecules containing several non-hydrogen atoms. Herein, CBS-QB3, CBS-APNO, G3 and G4 composite methods are implemented for computing thermodynamic and kinetics properties of interest. The detail

analyses of the results obtained by implementing these methods are provided in chapter IV however a brief overview of computational details is provided in the following section.

a. CBS-QB3, CBS-APNO methods

The CBS-QB3 [38, 39], CBS-APNO[40] methods are Complete Basis Set (CBS) methods developed by Petersson and coworkers. The CBS-OB3 composite method was devised to perform calculations on molecules containing the atoms H to Ar while CBS-APNO is available for first row atoms only. These methods use procedures designed to extrapolate computed energies to the complete-basis-set limit. In CBS-QB3 method, initial equilibrium structure is determined at the B3LYP level with the CBSB7 basis set. The B3LYP [53] is one of the DFT methods which stands for Becke, 3-parameter, Lee-Yang-Parr. The CBSB7 indicates 6-311G(2d,d,p) basis set. This notation specifies two additional d-type polarization functions on second row atoms, one d-type function on first row atoms and a p-type function on hydrogen atom. Further, the structure obtained at the B3LYP/CBSB7 is used to calculate harmonic frequencies. This is followed by single point energy computations at CCSD(T), MP4SDO, and MP2 levels. The final energy is computed by extrapolation to the completebasis-set limit. In CBS-APNO, the acronym APNO stands for atomic pair natural orbital. The CBS-APNO computation starts with (U)HF/6-311G(d,p) geometry optimization and frequency calculation wherein (U)HF represents unrestricted HF method [Levine]. It is followed by a second geometry optimization at the QCISD/6-311G(d,p) level. In next steps this geometry is used for series of single-point energy calculations at OCISD(T), MP2 (Full), HF, and MP2 levels, each with different basis sets. Similar to CBS-QB3, final energy is computed by extrapolation to the complete-basis-set limit.

b. Gaussian-3 (G3) and Gaussian-4 (G4) methods

The Gaussian-n (Gn; n = 1, 2, 3, 4) are the series of methods introduced by Curtiss, Pople, and co-workers [42-44, 51]. The G3 [43] is an improvement on its predecessors namely G1 and G2 methods whereas G4 [44] is an enhancement of G3 method. These Gn methods involve a sequence of well-defined *ab initio* molecular orbital calculations to obtain a total energy of a given molecular species. The details of the G3 methods are as follows. An initial equilibrium structure is determined at the Hartree-Fock level with the 6-31G(d) basis set. This structure is then used to calculate harmonic frequencies. Further, the equilibrium geometry of the molecule is refined at the MP2/6-31G(d) level. In next step, base energy E^{base} is computed from MP4/6-31G(d) calculation. Various corrections to the E^{base} are then found from the computed single point energies obtained at MP4/6-31+G(d), MP4/6-31G(2df,p), QCISD(T)/6-31G(d), and MP2/G3large methods. The G3 large indicates very large basis set

that includes more polarization functions for the second row and additional polarizations functions. Also an empirical higher-level correction is added to correct for the basis-set incompleteness. These corrections to the base energy allow for the effects of including diffuse, polarization basis functions and also higher level of electron correlation [32] The accuracy of G3 methods was tested against accurately known thermochemical data, the G3/05 test set. This test set consists of 270 enthalpies of formation, 105 ionization energies, 63 electron affinities, 10 proton affinities, and 6 dimerization energies of H-bonded dimers [54]. This G3/05 test set did not include any transition-metal compounds.

As mentioned before, G4 is an improvement on the G3 method. The major differences between these two methods are as follow. G4 method uses an extrapolation procedure to estimate the Hartree-Fock energy in the complete-basis-set limit using the following equation [32]

$$E_{SCF}(n) = E_{SCF}(\infty) + Ae^{-Bn}$$
(70)

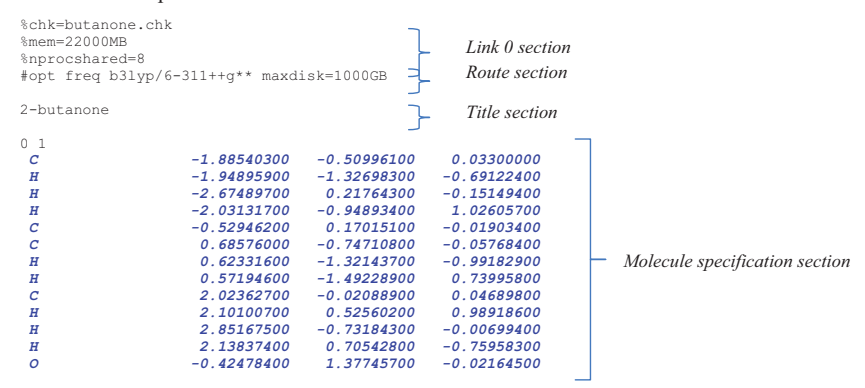
In above equation (70), $E_{SCF}(n)$ is the Hartree-Fock energy obtained with the cc-pVnZ basis set. $E_{SCF}(\infty)$ is the Complete Basis Set (CBS) limit predicted by cc-pVnZ in the limit $n \to \infty$. A and B are positive parameters whose values are determined by a least-squares fit of the calculated energies. The G4 method uses a larger basis set than G3 and replaces the QCISD(T) calculation of single point energy by CCSD(T). At G4, equilibrium geometry and zero-point energy are determined at B3LYP/6-31G(2df,p) and consist of two additional empirical parameters included in the higher-level correction. The details computations are presented in Curtiss et al [44]. For the G3/05 test set, mean absolute deviation for the G3 method is 1.13 kcal mol⁻¹ whereas for G4, 0.83 kcal mol⁻¹.

III. Computational Chemistry Tools

III.1 Gaussian Software package

As discussed in chapter II, Gaussian 09 [26] has been employed for performing all the electronic structure calculations. These computations were performed on the RWTH Compute Cluster, Aachen, Germany. This section will give a brief overview of Gaussian 09 considering some of the important keywords implemented herein. For the visualization of input and output files GaussView [55] and ChemCraft [56] tools were used.

In the electronic structure calculations, the first step involved is the optimization of geometry and then the computation of vibrational frequencies of a molecule of interest. This is performed by specifying the keyword 'opt' and 'freq' in the input file. The basic structure of the Gaussian input file is as shown below:



The *link 0 section* contains %chk keyword which defines a binary 'checkpoint' file in which all results are written. The next line shows %mem which indicates available memory for the calculation (in words). The following line starts with a %nprocessared which highlights the number of shared processors to be used for the computation.

The *route section* starts with '#' sign and consists of the keywords for the type of calculations, level of theory, basis set etc. In the above example, the route section highlights calculations to be performed for the geometry optimization and vibrational frequencies calculations at b3lyp/6-311++g** level of theory. The route section is terminated by a blank line and followed by the title section which consists of descriptive information about the calculation. The title section is also terminated by a blank line as shown in the example above. The next section highlights molecule specifications. The first line in this section

shows charge and spin multiplicity of the molecule. The spin multiplicity is given by 2S+1, wherein S is the total electron spin for a molecule. For example, paired electrons have a net zero spin. For one unpaired electron, the spin multiplicity is equal to 2 and the species is called doublet. Two unpaired electrons lead to the spin multiplicity equal to 3, i.e. triplet and so on. In the following lines, Cartesian coordinates of the molecule are given along with the atomic symbols. The molecule specification section is followed by a blank line.

This job will determine all the vibrational frequencies within a molecule based on the optimized geometry in the first step. The important output given by any composite method such as CBS-QB3, G3, G4 etc. looks like as shown below. The following lines show the output obtained by performing calculations at the CBS-QB3 method. For all methods used in Gaussian, the energy is given in atomic unit. The atomic unit of energy is called Hartree.

```
CBS-QB3 (0 K) = -232.045812 CBS-QB3 Energy = -232.039107 CBS-OB3 Enthalpy = -232.038163 CBS-OB3 Free Energy = -232.076764
```

In the output details shown above, "CBS-QB3 (0 K)" indicates total electronic energy including the scaled zero-point energy as defined in the model.

"CBS-QB3 Energy" is the total electronic energy plus the internal thermal energy. The internal thermal energy is taken from the thermochemistry output from the frequency part of the calculation and the scaled zero-point energy is included in this.

"CBS-QB3 Enthalpy" is the total electronic energy plus $H_{\rm corr}$ (thermal correction to Enthalpy), with the unscaled zero-point removed. This value is appropriate to calculate enthalpies of reaction.

"CBS-QB3 Free Energy" highlights total electronic energy plus G_{corr} (thermal correction to Gibbs free energy), with the unscaled zero-point energy removed. This value is suitable for computing Gibbs free energies of reaction.

For the calculations performed using composite methods such as CBS-QB3, G3, G4 etc. the keywords such as "opt" and "freq" from the route section can be omitted. For the TS, the route section for the optimization is a bit different than the one shown in the above example (reactants and products) and involves additional keywords as shown below.

```
#opt=(calcfc,ts,noeigentest) CBS-QB3 maxdisk=1000GB
```

The keyword "calcfc" specifies that the force constants be computed at the first point using the method given in the route section. The second term "ts" highlights the transition state. The next keyword, "noeigentest" suppresses testing the curvature in Berny optimizations [57]. This keyword is recommended for the calculations with large computing budgets to save computational time.

The optimized transition state can be analyzed by performing Intrinsic Reaction Coordinate (IRC) calculation [58] in order to visualize if the given transition state connects to reactants and products involved in a reaction. This calculation requires initial geometry of the transition state. The IRC calculations need initial force constants to proceed and hence in the route section keyword "irc=calcfe" is mentioned. "calcfe" computes the force constants at the beginning of the calculations. The IRC path of one such calculation as visualized by GaussView, from the output of the Gaussian file (.log) is highlighted below (Figure 2).

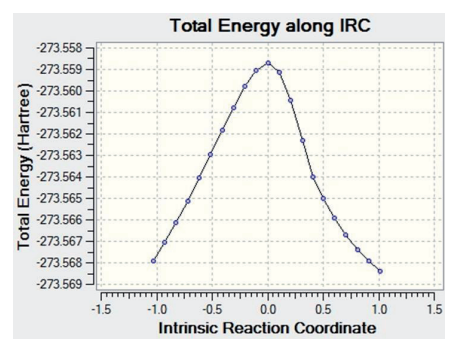


Figure 2. IRC path as visualized by GaussView

For performing relaxed potential energy surface scan, keyword "opt" along with "modredundant" is used in the route section. In the input file, after the molecule specification section, details of the scan to be performed should be mentioned as follows.

D N1 N2 N3 N4 S nsteps stepsize

In the above line, D is the dihedral angle; N1, N2, N3 and N4 are atom numbers. The action code "S" performs a relaxed potential energy scan. The scan is executed by *stepsize* increment in the coordinate a total of *nsteps* times with an optimization performed at each resulting starting geometry.



Figure 3. Optimized geometry with the atom numbers in isopentanol.

For example, to perform potential energy surface scan along the 2-11 bond in isopentanol (Figure 3), following syntax must be used.

D 7 2 11 14 S 36 10.0

In the above case scan is performed by scanning a dihedral angle from 0-360° with 10° increments. The lists of all the keywords implemented in Gaussian 09 are highlighted in Gaussian 09 user's reference [26].

The data obtained from the electronic structure calculations must be post-processed in order to obtain necessary results such as thermodynamic properties of species, rate constants for the reactions of interest etc. A post processing tool, Gaussian Post Processor abbreviated as GPOP [59] has been used for post processing Gaussian output files.

III.2 Gaussian Post Processor (GPOP)

GPOP is post processing software for the electronic structure calculations that are performed using Gaussian [26] and MOLPRO [60]. It has a collection of tools for pre-processing output files from the electronic structure calculations, for thermodynamic and rate constant calculations and also computational diagnostic and analysis. Some of the important tools from GPOP software that are implemented herein are briefly discussed in the following sections.

i. GPOP Pre-processing Tools

a. gpop1scf

This program preprocesses a Gaussian SCF/DFT-level job output which is required by the other programs in GPOP. It extracts all the essential data from the Gaussian output file needed for thermodynamic and rate constant calculations and saves them in a GPOP-format file named as "basename.gpo". The gpop1scf program generates two files namely "basename.gpo" and "basename.mod" files. The basename.gpo contains all the results of the quantum mechanical calculations. This is a text file and can be viewed or edited by text editors if required. File with basename.mod is a sample modification file essential for the "gpop3tst" program. More details about basename.mod file has been explained in gpop3tst section.

Computation details in gpop1scf

When gpop1scf pre-process the Gaussian output file, it looks for the quantum chemical method and the basis set employed in the calculation. If the method used matches with those registered in the gpop1scf, then it automatically sets preferred scaling factors to eliminate the systematic errors involved in such calculations [61]. The first one is the preferred scaling factor for (1<-> 0) vibrational transition (f_{VIB}), the second one is the scaling factor for the

zero-point energy ($f_{\rm ZPE}$), and the last one is the scaling factor for the zero-point energy as defined in the Gaussian theories, or Complete Basis Set Methods ($f_{\rm GT}$). In basename.gpo, the program gives three types of zero-point energies, a) unscaled, b) scaled by prefer scaling factor for the ZPE and c) scaled as in Gaussian theories (or CBS methods). The values of the energies are given in two units, wavenumber (cm⁻¹) and atomic unit (hartree). The methods and the scaling factors implemented within GPOP program are highlighted in Table 1.

The value of $f_{\rm GT}$ does not affect any calculations but only affects the zero-point energy (zpe_GT) given in "basename.gpo" file. The $f_{\rm ZPE}$ is taken into account when 'useSCFenergy+ZPE' keyword is mentioned in the "basename.mod" file and for the hindered rotor calculations. However, the $f_{\rm VIB}$ affects all the calculations that include vibrational partition function calculations such as computation of thermodynamic functions, rate constants and equilibrium constants.

Table 1. Methods and the scaling factors in GPOP program

method	index	$f_{ m VIB}$	$f_{ m ZPE}$	$f_{ m GT}$
HF/6-31G(D)	0	0.8929	0.9135	1 / 1.12
111/0 51G(D)	Ü	0.0727	0.7133	(~0.8929)
B3LYP/6-31G(D)	1	0.9613	0.9804	0.96
B3LYP/6-311G(D,P)	2	0.97	0.99	0.99
B3LYP/CBSB7	3	0.97	0.99	0.99
[CBSB7 = 6-311G(2D,D,P)]	3	0.97	0.99	0.55
B3LYP/6-311G(2D,D,P)	4	0.97	0.99	0.99
RS2/CC-PVTZ	4	0.97	0.99	0.99
RS2/CC-PVDZ	4	0.96	0.98	0.98
WB97XD/6-311G(D,P)	2	0.949	0.974	0.974
MP2/6-311G(D,P)	2	0.945	0.970	0.970

b. gpop3tst

Computation details in gpop3tst

The "basename.mod" file created by the gpop1scf as discussed before contains all the basic information needed to perform thermodynamic and rate constant calculations. Basename.mod file is the temporary modification file created by gpop1scf and hence "gpop3tst" program is used to do a modification to the created basename.mod file. This executable file performs modification according to the detailed information provided in the basename.mod file. This step is important before performing any thermodynamic and rate constant computations. The basename.mod file can take into account corrections to the electronic degeneracy, low energy electronic states, rotational symmetry number, the number of isomers, the energy for the rate constant calculation, intramolecular rotation and notification whether the geometry is

transition state or not. For example, if the Gaussian output file "ROO2c.log" is processed with gpop1scf, it creates "ROO2c.gpo" and "ROO2c.mod" files. The ROO2c.mod file looks like as shown below;

```
! gElec 2
! rotSymNbr 1
! numIsomers 2
! isTS false
! ## CBS-QB3 E(0K) is used as default. Change if necessary.
energyTST -420.828113
! useSCFenergy+ZPE
! setIntRotor idVib nSym moi1 moi2 Vθ comment
```

In the ROO2c.mod file as shown above, 'gElec' is the degeneracy of the electronic state including both the electronic spin degeneracy and electronic angular momentum degeneracy. 'rotSymNbr' indicates the rotational symmetry number. In GPOP, rotational symmetry number is determined from the point group identified by the Gaussian. 'numIsomers' is the number of isomers. In GPOP, a number of optical isomers is set as default value and is determined from the molecular symmetry. The next line shows 'isTS false' wherein 'false' highlights that the geometry is not a transition state while 'true' indicates a transition state geometry. The GPOP program set the default value as 'true' if at least one imaginary vibrational frequency is found in the Gaussian output file (.log). The next keyword is 'energyTST' which highlights the energy that is taken into account for the computation of the rate constant and it corresponds to the internal energy at 0 K. In the above example, internal energy at 0 K has been considered from the CBS-QB3 composite method. The next keyword is 'useSCFenergy+ZPE' which request the GPOP program to use SCF level energy corrected with ZPE for the calculation of the rate constant. The last line shows, 'setIntRotor idVib nSym moi1 moi2 V0 comment' The GPOP uses this keyword to define intramolecular rotor within a molecule. 'idvib' denotes the index of the vibrational mode that is treated as a hindered internal rotor. If the index is set to zero or the negative value then gpop3tst automatically detects the most similar vibrational mode. 'nSym' highlights the symmetry number of the internal rotation. 'moi1' and 'moi2' specifies the moieties for the intramolecular rotation. Each moiety is denoted by the list of atoms within a molecule. The first atom in both moieties must be the pivot atom for the intramolecular rotation. The numbering of the atoms must be exactly the same as in the Gaussian output file. Consider a following example of 2-butanone.

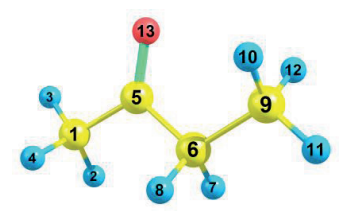


Figure 4. Optimized geometry with the atom numbers in 2-butanone.

In order to specify intramolecular rotation around C1-C5 bond in 2-butanone (Figure 4), moiety-1 must be denoted as 1-2-3-4 and moiety 2 as 5-6-7-8-9-10-11-12-13. The pivot carbon atom (1) must be the first atom in the moiety-1 and the counter pivot atom (5) must the first atom in the moiety-2. However the ordering of the other atoms in both the moieties can be given in an arbitrary manner. Since the moiety-2 contains all the other atoms which are not part of the moiety-1, the moiety-2 can be specified with the abbreviation '@'. For example, in the above case of 2-butanone moiety-1 and moiety-2 for the internal rotation along 1-5 bond can be specified as 1-2-3-4 and 5-@ respectively.

Lastly, the V θ in the ROO2c.mod file indicates the height of the hindrance potential. If V θ is zero then the given rotor is considered as a free rotor. If the positive V θ is found as an input, the value is used for the calculation. In the case of negative V θ , V_0 is computed from the following equations described below:

The setIntRotor keyword in the GPOP mod file treats the intramolecular rotor as sinusoidally hindered rotor with a potential energy curve given as,

$$V = \frac{V_0}{2} \left(1 - \cos n\theta \right) \tag{71}$$

In equation (71), V_0 is a barrier height, n is the symmetry number of rotation and θ is the angle of rotation. The potential barrier height, V_0 is determined from the harmonic frequency of the corresponding vibrational mode ν from the equation,

$$n^2 B V_0 = (h v)^2 (72)$$

In equation (72) h is the Plank's constant, B is the reduced moment of inertia and v is the vibrational frequency. Determination of barrier height by this method is fairly good for the symmetric rotors (methyl rotor). For asymmetric rotors more systematic approach is followed by using BEx1D program [62]. The detail of this code is provided in section III.3.

In the ROO2c.mod file shown above, '!' highlights the comment and the values shown are automatically taken from the Gaussian output file (.log) while pre-processing. If the values are correct then the lines are kept commented however if the values are different and incorrect then the comment '!' is taken out and the correct values are to be inserted.

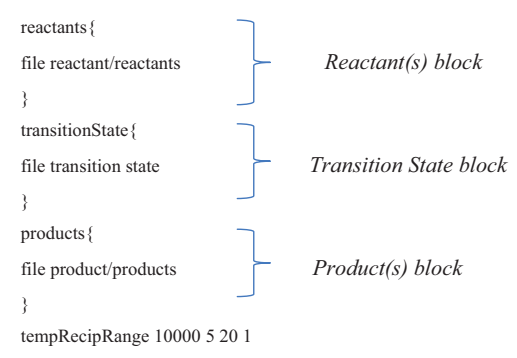
ii. Thermodynamic and Rate Constant Calculations

GPOP has an inbuilt program for the computation of thermodynamic and rate constant calculations for the reaction of interest. In order to get these data from the Gaussian output files, pre-processing is performed so that all the input information are in a format required by the GPOP tool. The pre-processing steps are performed using gopop1scf and gpop3tst executable files as discussed in an earlier section. The computations of thermodynamic properties of the species of interest are carried out using 'gpop4thf' tool within GPOP.

The gpop4thf program requires GPOP-format file i.e. "basename.mod" to calculate thermodynamic functions and the output results are given in the CSV file. Before running gpop4thf program, the GPOP-format file needs to be modified by running gpop3tst as explained before to take into account hindered internal rotors in a molecule.

For the determination of a rate constant, the program named 'tstrate' is employed. This program expects the following input files in the current directory. 1) GPOP-format files of reactants and transition state and 2) A reaction input file (*.rxn)

The reaction input file required for the rate constant calculation within GPOP looks as shown below:



The reaction input file as shown above contains three blocks; corresponding to reactants, transition state and products. Each block must contain at least one "file" key with the name of '*.gpo' file(s) to be read. If in the reaction input file only two blocks, i.e. reactant(s) and transition state are specified then the program computes only the rate constant for the reaction. However, if an additional block of the product(s) is specified as shown in the above example then the program calculates rate constant as well as the equilibrium constants for the reaction. The 'tstrate' tool computes the rate constant of a reaction by applying a tunneling

correction which is computed by considering an asymmetric Eckart potential [63]. This correction is taken into consideration when all three blocks are found in the reaction input file since in order to take tunneling correction into account it needs the energy of the products. Finally, these results are written to a csv-format file. The 'gpop6irt' is another important program within GPOP tool and is useful in calculating the reduced moment of inertia and the corresponding rotational constant of an internal rotor. These values are required by the BEx1D program [62]. This program reads the pre-processed GPOP-format file. The intramolecular rotation in a molecule is designated by specifying the two moieties on the command—line. The specifications of the moieties are done in a similar way as mentioned under the gpop3tst program.

As mentioned before, for the treatment of asymmetric internal rotations within molecule, more systematic approach is followed by using the BEx1D program. The brief overview of this program is highlighted below.

III.3 Basis-set Expansion solver for 1-Dimensional Schrödinger Equation (BEx1D)

BEx1D (an acronym for <u>Basis-set Expansion</u> solver for <u>1-Dimensional</u> Schrödinger equation) is a package of calculation tools for eigenstates and partition functions of intramolecular nuclear motions, for which harmonic oscillator approximation is inadequate, such as hindered rotations.

The two important tools used are 'bx1fitPlls' for the potential curve fitting and 'bx1HRsol' for an eigen problem solver. The bx1fitPlls tool derives a potential energy function by linear least square fitting either in a power or Fourier series, which is subsequently required for the bx1HRsol program. The bx1HRsol solves one-dimensional time-dependent Schrödinger equation with the periodic boundary condition suitable for the hindered internal rotations. For a potential energy curve given by a Fourier series (obtained from the bx1fitPlls program), the eigen states are computed. The eigen states are computed by expanding a wave function with a free-rotor basis function set. The important parameters that must be specified in the input file of the bx1HRsol are as follows. The 'maxAbsQN' keyword in the input file which is the abbreviation for the maximum absolute quantum number is used to set the size of basis-set by the maximum absolute quantum number. In bx1HRsol, the basis-functions used are the free-rotor basis functions as given in equation (3).

$$\Psi = \frac{e^{iJ\theta}}{(2\pi)^{1/2}} \qquad J = 0, \pm 1, \pm 2, \dots$$
 (73)

If the maxAbsQN value is specified as 50 then the program uses basis functions from J = -50 to +50, hence in total 101 basis functions. Another important input is the rotational constant which is specified by the keyword 'rotConst'. It is a coefficient (B) = $\hbar^2/2I$ in the one-dimensional Hamiltonian (equation 74).

$$H = -\left(\frac{\hbar^2}{2I}\right)\left(\frac{d^2}{dx^2}\right) + V(x) \tag{74}$$

As explained before under the GPOP section, 'gpop6irt' tool is used to calculate the rotational constant of an internal rotor. The rotational constant is given in the unit of cm⁻¹. The keyword 'output' is used to control the bx1HRsol output. The temperatures at which the partition functions to be calculated is specified by using 'tempRange T_start T_end T_step'. This sets equally spaced temperatures list from the T_start to T_end with the interval of T_step. For example, 'tempRange 400 1000 100' will set temperature list from 400 K to 1000 K with an interval of 100 K.

The potential function of the Fourier series is specified in the following format:

```
potPars{
    order-1 coefficient-1
    order-2 coefficient-2
    order-3 coefficient-3
    ...
}
```

This program can give four types of output files depending on the input specifications. The output of the eigen values and the partition functions are given by default. The eigen vector and the eigen functions output are generated if the keyword 'output all' is specified in the input file. The more details about this can be found on the BEx1D reference manual [62].

IV. Results and Discussion

IV. 1 Reaction Kinetics of the Hydrogen Atom Abstraction from Isopentanol by H atom and H \dot{O}_2 Radical

As highlighted in chapter I, isopentanol is among one of the biofuel candidates that can be synthesized from advanced biochemical synthetic routes and metabolic engineering approaches [11, 64-66]. Also, non-fermentive pathways have been reported for the synthesis of branched chain higher alcohols for example; isobutanol, 2-methyl-1-butanol, 3-methyl-1-butanol and 2-phenylethanol from glucose [11]. Since such branched chain C4 and C5 alcohols have higher octane number than the corresponding straight chain counterparts (due to methyl branching), they have been considered as potential gasoline additives [12]. In another study, a novel approach has been reported for the synthesis of isopentanol based on isoprenoid biosynthetic pathway [67].

From the combustion point of view, isopentanol behavior has been studied for Homogeneous Charge Compression Ignition (HCCI) engines [68]. This study revealed that isopentanol has a very high potential for HCCI applications and it also showed considerable ITHR (Intermediate Temperature Heat Release) similar to that of gasoline. The amount of ITHR is an important property of fuel and plays a major role in the combustion stability. Other than this, it has also grasped attention due to its advantages over a smaller chain alcohol, ethanol. It can be a better substitute over ethanol and can be used as a blend with gasoline due to its miscibility with hydrocarbon and higher energy density [69]. Less hygroscopic nature of isopentanol also makes it a better fuel for transportation and storage.

Another work on isopentanol highlights a jet stirred reactor study [70] in which concentration profiles of the stable species were measured for the range of equivalence ratios (0.35-4) and temperatures (530 - 1220 K) at 10 atm. This study indicated that the amount of acetaldehyde produced after combustion of isopentanol is a lot less as compared to that of ethanol. Ignition delay times of isopentanol are also reported [69] in high and low temperature regimes using the shock tube and rapid compression machine. Further, in their work an isopentanol model was presented which includes high and low temperature chemistry during combustion. Welz et al [71] experimentally investigated low temperature combustion pathways of autoignition of isopentanol using the technique of laser-induced Clinitiation and by analyzing the reacting mixture with time-resolved tunable synchrotron photoionization mass spectrometry at 8 Torr and at 550, 650 and 750 K. Sarathy et al [72] presented a detailed chemical kinetic model for the combustion of isopentanol. Their model is

based on the previously presented model for butanol isomer [73] and n-pentanol [74]. However, no theoretical study was found on the investigation of the H-abstraction reactions from isopentanol by H atom and $H\dot{O}_2$ radical.

Herein, detailed theoretical calculations were performed to compute high-pressure limiting rate constants for the H-abstraction from isopentanol by H atom and $H\dot{O}_2$ radical. Altogether, nine different H-abstraction sites in isopentanol were considered namely abstractions from hydroxyl group, alpha (two), beta (two), gamma (one) and delta (three) carbon sites. The optimized structure of isopentanol with labels is shown in Figure 5. All the electronic structure calculations involving geometry optimization, vibrational frequencies and single point energy calculation of reactants, transition states (TSs) and products were performed at the CBS-QB3 composite method [38, 39] implemented in Gaussian 09 package [26].

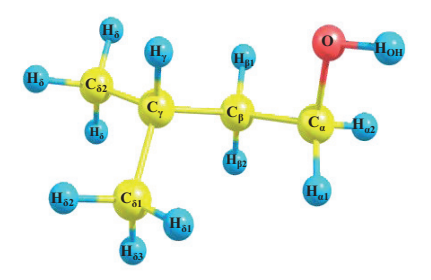


Figure 5. Labels of H-atom abstraction sites in isopentanol

In Figure 5, C_α is the carbon with hydroxyl (OH) functional group and hydrogens present on it are labeled as H_α . C_β is a secondary carbon with corresponding hydrogens denoted as H_β . C_γ is a tertiary carbon site (due to the presence of two methyl groups) with a hydrogen on it labeled as H_γ and C_δ are primary carbon sites with hydrogens on it denoted as H_δ . The hydrogen from the hydroxyl functional group is labeled as H_{OH} . The transition state (TS) involved during H-atom abstraction from isopentanol by H atom is denoted as TS-Hx; wherein x represents an abstracted hydrogen atom $(x: \alpha, \beta, \gamma, \delta \text{ or } OH)$ as labeled in Figure 5. The TS involving H-atom abstraction by $H\dot{O}_2$ radical is abbreviated as TS- $H\dot{O}_2$ _x $(x: \alpha, \beta, \gamma, \delta \text{ or } OH)$. Figure 6 and 7 highlights optimized structures of the TSs for H-atom abstraction from isopentanol by H atom and $H\dot{O}_2$ radical respectively. Herein, the vibrational frequencies obtained at the B3LYP/CBSB7 level within the CBS-QB3 method were scaled by 0.99 for zero point energy calculations and by 0.97 for the calculation of vibrational partition functions as recommended within CBS-QB3 method. The high pressure limit rate constants

for all H-atom abstraction channels in isopentanol by H atom and HÓ₂ radical were determined using GPOP [59] employing conventional transition state theory. Asymmetric Eckart tunneling corrections [63] were taken into account in the conventional transition state theory rate calculations within the GPOP program [Chapter III.2]. For the treatment of low frequency torsional modes in reactants and transition states, Pitzer-Gwinn like approximation [75, 76] was applied for computing torsional barrier heights and considered as hindered rotations. The potential energy surface (PES) scans are performed for the internal rotations in the reactants and TSs by scanning a dihedral angle from 0 to 360° with 10° increment.

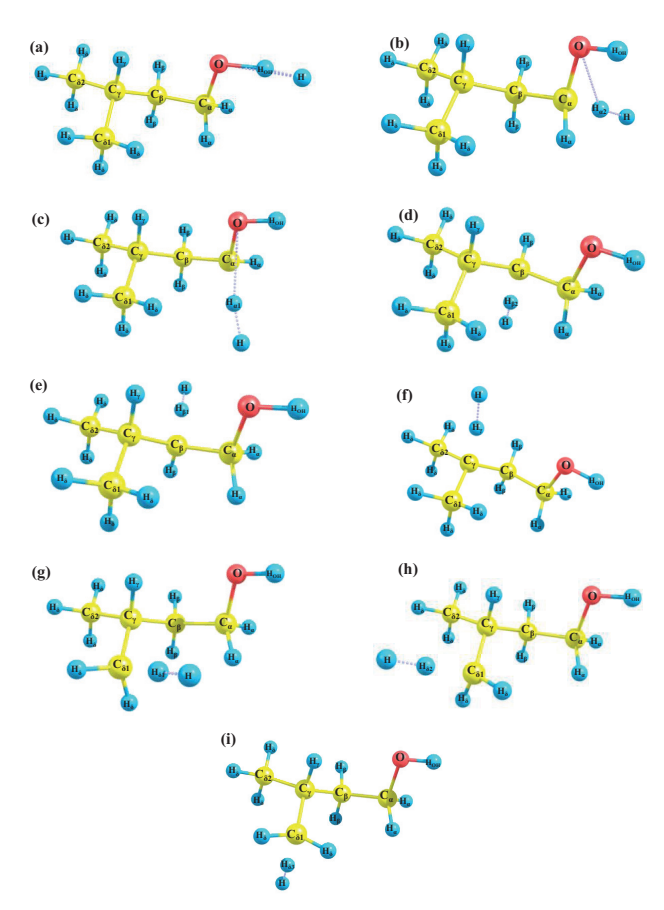


Figure 6. Optimized transition state structures for the H-atom abstraction reactions from isopentanol by H atom

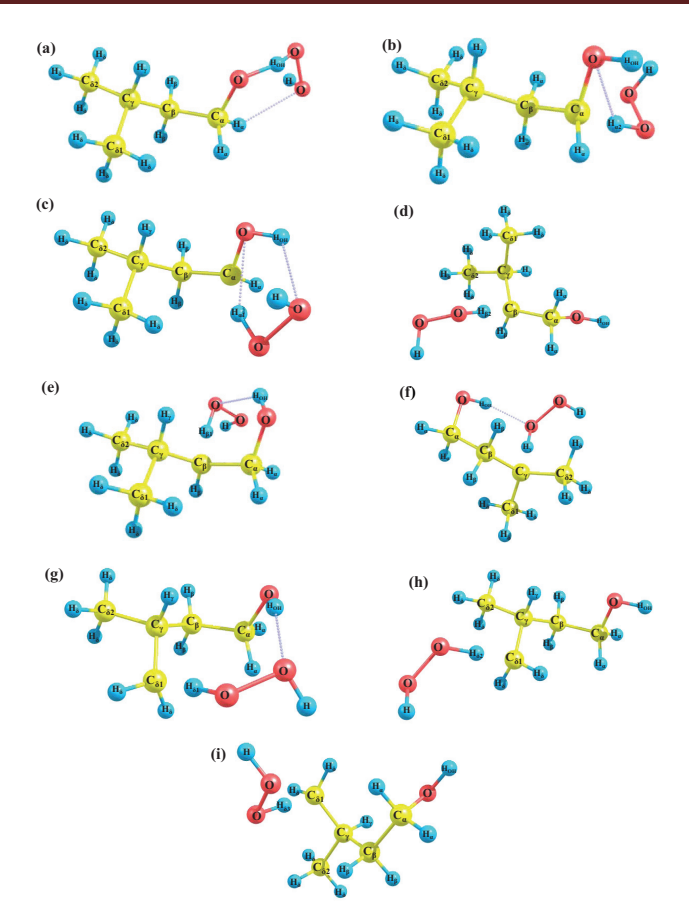


Figure 7. Optimized transition state structures for the H-atom abstraction reactions from isopentanol by $H\dot{O}_2$ radical

Figure 8 shows an example of the hindered rotor analysis for the OH rotor involved in the TS for the H-abstraction reaction from isopentanol by H atom. In Figure 8a, α is the torsional angle, which is defined as the dihedral angle between atoms C11–C14–O16–H18. The open circles in Figure 8b highlight potential energies calculated for the OH rotor in TS at the B3LYP/CBSB7 method and the solid curve represent Fourier-series interpolation. The BEx1D program [62] is used for the calculation of eigenstate energies of the hindered rotation.

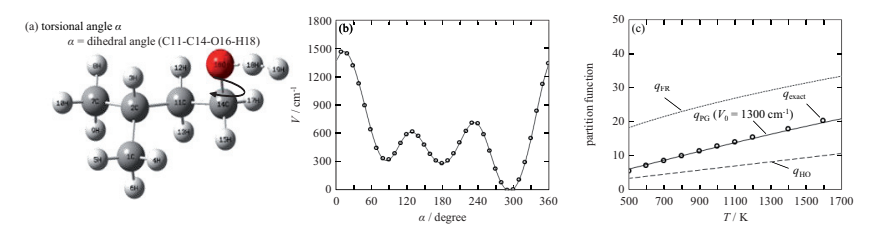


Figure 8. Hindered rotor analysis for the OH rotor in TS attached to the C_{α} atom in isopentanol; (a) definition of torsional angle α , for OH rotor, (b) potential energy calculated at B3LYP/CBSB7 method (open circle) and fitted curve (line), (c) Partition function calculated from eigenstate energies (q_{exact}) in comparison with harmonic oscillator (q_{HO}), free rotor (q_{FR}) and Pitzer–Gwinn (q_{PG}) approximations.

In Figure 8c, the partition functions derived from the eigenstate energies (q_{exact}) as a function of temperature are shown by the open circles. Whereas q_{HO} and q_{FR} represent the partition functions computed by assuming harmonic oscillator and free rotor approximations respectively. The partition function obtained by considering Pitzer-Gwinn approximation is denoted by q_{FG} . As seen from Figure 8c, Pitzer-Gwinn approximation with hindrance potential height of $V_0 = 1300 \text{ cm}^{-1}$ shows excellent agreement with the exact partition function (q_{exact}). Hence this internal rotation is treated as hindered with the hindrance potential height of 1300 cm^{-1} . Similarly, all the internal rotations in reactants and transition states were treated as hindered rotors with estimated hindered rotor parameters according to the Pitzer-Gwinn approximation (Figures A1-A38 in the Appendix). The calculated hindered rotor parameters for the Pitzer-Gwinn approximation involved in the H-atom abstractions from isopentanol by H atom are given in Table 2. In this table, V_0 is the height of the hindrance potential (cm⁻¹); σ is the symmetry number for the low frequency torsional modes in reactants and TSs. Some specific internal rotations involved in the transition states for the H-abstraction by H \dot{O}_2 radicals in isopentanol are provided in the Appendix (Table A1).

Table 2. Estimated Hindered Rotor Parameters in Pitzer-Gwinn Approximation for isopentanol and TSs for H-abstraction by H atom

bonding atom	type of rotor	V_0^{b} / cm^{-1}	σ^{c}
Ca in reactant	OH	500	1
C_{β} in reactant	CH ₂ OH	1400	1
C_{γ} in reactant	$\mathrm{CH_{2}CH_{2}OH}$	1900	1
	$C_{\delta 1}H_{_3}$	950	3
	$C_{\delta 2}H_{_3}$	1050	3
O in TS-H			
C_{α}	OH in TS	1300	1

C_{α} in TS-H $_{\alpha 1}$			
C_{α}	ОН	1300	1
C_{β}	$\mathrm{CH_2OH}$	1200	1
C _α in TS-H _{α2}			
C_{α}	ОН	1400	1
C_{β}	$\mathrm{CH_2OH}$	1750	1
C _β in TS-H			
C_{β}	$\mathrm{CH_2OH}$	1500	1
C _γ in TS-H			
C_{γ}	CH ₃	900	3
	CH ₂ CH ₂ OH	1100	1
C _δ in TS-H			
C_{β}	$\mathrm{CH_2OH}$	1500	1
C_{γ}	CH ₃ in TS	850	1
	CH ₂ CH ₂ OH	1600	1

^aabbreviations, $C\alpha$, C_{β} , $C\gamma$, and $C\delta$ are referred in Figure 5. ^bThe height of the hindrance potential. ^cThe symmetry number of the internal rotation for the H-abstraction reactions by H atom.

Further, reaction barriers (E_0) and energies (ΔE) were determined for the H-abstractions reactions in isopentanol to analyze the favorability of the specific reaction channel over others.

i. Reaction Barriers and Energies

Reaction barriers (E_0) and energies (ΔE) for H-abstraction reactions in isopentanol by H atom and $H\dot{O}_2$ radical are summarized in Table 3. E_0 was calculated from the difference in the computed CBS-QB3 energies between the TS and the reactants. Computed E_0 for H-atom abstraction by H and HO2 radical are within a range of 23-53 kJ mol-1 and 42-88 kJ mol-1 respectively indicating the favorability of abstraction by H atom over HO₂ radical. The CBS-OB3 energy difference between products and reactants gives the value of ΔE for a specific reaction channel, which helps in understanding the nature of the reaction as either exothermic or endothermic. As seen from Table 3, reactions involving abstraction by H atom are found to be exothermic in nature with negative ΔE whereas the ones involving abstraction by \dot{HO}_2 radical are endothermic in nature. As compared to all the abstraction reaction channels in isopentanol, abstraction of H_{α} by H atom showed highest exothermicity with $\Delta E = -46$ kJ mol⁻¹ whereas ΔE for the isopentanol + H \dot{O}_2 reaction from the same site (C_a) depicts lowest endothermicity with $\Delta E = 29 \text{ kJ mol}^{-1}$. For the H-atom abstraction by H, ΔE (Table 3) for C_{γ} , C_{β} , and C_{δ} sites are ~ 10 kJ mol⁻¹, 20 kJ mol⁻¹ and 30 kJ mol⁻¹ respectively higher than the abstraction from the C_{α} site indicating the favorability for H_{α} abstraction. Although C_{α} and C_{β} are both secondary carbon sites in isopentanol, a difference of $\sim 10 \text{ kJ mol}^{-1}$ in E_0 can be ascribed to the presence of alcoholic group neighboring Ca which weakens its C-H bond

strength. The H-atom abstraction from C_{γ} is also favorable due to weak C-H bond strength resulting from the tertiary carbon site [72]. The abstraction of alcoholic hydrogen by H atom and HO₂ radical are highly unfavorable as seen from high E_0 values (Table 3) for these reactions, reflected by the strong O-H bond. Sarathy et al [72] reported C-H and C-C bond dissociation energies (BDEs) in isopentanol at three different composite methods namely G3, G4 and CBS-QB3. This study reports strongest BDE value for the O-H bond among all the other C-H bonds in isopentanol. The reported BDE values for the O-H bond in isopentanol are 438.9, 441.8 and 430.1 kJ mol⁻¹ at CBS-QB3, G3 and G4 methods respectively [72]. Further, abstraction of delta hydrogens in isopentanol by H atom and HÓ₂ radical also showed high energy barriers which are ~42 kJ mol⁻¹ and 70-75 kJ mol⁻¹ respectively. This high E_0 can be attributed to the primary C-H bond in isopentanol which is also comparable to primary carbon site in alkane [72, 77].

Table 3. Reaction barriers and energies for the H-atom abstraction reactions in isopentanol by H atom and $H\dot{O}_2$ radical

Reactants a	H atom b	$E_0^{c}/\mathrm{kJ}\mathrm{mol}^{-1}$	$\Delta E^{d}/\text{kJ mol}^{-1}$
Isopentanol + H	\mathbf{H}_{OH}	53	-1
	Ηα1	26	-46
	Ηα2	23	-46
	Нβ1	34	-24
	Нβ2	36	-24
	$\boldsymbol{H}_{_{\boldsymbol{\gamma}}}$	26	-34
	Ηδ1	43	-17
	Ηδ2	42	-17
	Нδ3	42	-17
$\begin{array}{c} \text{Isopentanol} + \\ \text{H}\dot{\text{O}}_2 \end{array}$	$\boldsymbol{H}_{\mathrm{OH}}$	88	74
	Ηα1	45	29
	Ηα2	47	29
	Нβ1	67	51
	Нβ2	55	51
	$\boldsymbol{H}_{_{\boldsymbol{\gamma}}}$	42	41
	Ηδ1	69	58
	Ηδ2	71	58
	Нδ3	75	58

^aReactant abbreviations and their chemical structures are given in the Figure 5. ^bThe position of hydrogen atom being abstracted are given in the Figure 5. ^cReaction barrier. ^dReaction energies.

Overall, the abstraction of H_{α} and H_{γ} are favorable with energy barriers of 23-26 kJ mol⁻¹ for the H-atom abstraction by H. For the abstraction by H \dot{O}_2 , E_0 for H_{α} and H_{γ} are 42-47 kJ mol⁻¹. As discussed before, one of the factors that affect the E_0 and subsequently reaction kinetics

for the H-atom abstraction reaction is the bond strength of the abstracted hydrogen atom in a molecule. The stronger the bonding of H-atom in a molecule, the more difficult it makes for the H-atom abstraction which in turn reflects its BDE. The trend in computed C-H BDEs in isopentanol by Sarathy et al [72] at the CBS-QB3 method is $C_{\delta\text{-H}} > C_{\beta\text{-H}} > C_{\gamma\text{-H}} > C_{\alpha\text{-H}}$. Comparing these results with the computed reaction barriers, relatively good agreement is seen.

ii. High Pressure Limit Rate Constants

High pressure limit rate constants are obtained for the H-atom abstraction reactions from isopentanol by H atom and \dot{HO}_2 radical. The modified Arrhenius expression, $k = AT^n \exp(-Ea/(RT))$ is used to represent Arrhenius parameters for the titled reactions, which are obtained in the temperature range 500-2000 K. Table 4 summarizes Arrhenius parameters obtained for H-atom abstraction reactions from isopentanol by H atom and \dot{HO}_2 radical.

Table 4. High-Pressure Limit Rate Constants for H-atom abstraction reactions from isopentanol by H atom and $H\dot{O}_2$ radical

D 4 4 a	, b	Rate constant b		b
Reactants	H atom	A	n	E/R
Isopentanol + H	${\rm H}_{\rm OH}$	1.23E-19	2.594	4819
	Ηα1	2.19E-18	2.311	2057
	Ηα2	2.44E-18	2.268	1877
	Нβ1	2.19E-18	2.274	2876
	Нβ2	2.05E-18	2.277	3173
	Ηγ	3.16E-17	1.936	2241
	Ηδ1	2.69E-17	2.166	4016
	Ηδ2	1.72E-17	2.219	3888
	Ηδ3	1.00E-17	2.212	3826
Isopentanol +HO ₂	H_{OH}	8.26E-25	3.833	9399
	Hαl	2.92E-28	4.702	3390
	Ηα2	2.30E-28	4.812	3750
	Нβ1	2.36E-28	4.828	6390
	Нβ2	2.86E-27	4.514	5276
	Ηγ	1.82E-29	4.917	3148
	Ηδ1	4.76E-24	3.895	6989
	Ηδ2	2.18E-24	4.009	7642
	Ηδ3	4.86E-24	3.903	7086

^aReactants and products abbreviations and their chemical structures are given in Figure 5. ^bRate constants are given by the Arrhenius expression, k (cm³ molecule⁻¹ s⁻¹)= AT^n exp(-E/RT).

The Arrhenius plots showing rate constants for H-atom abstraction from isopentanol by H atom and $H\dot{O}_2$ radical are highlighted in Figure 9 and 10 respectively. In these figures, rate constant at the C_a is obtained by considering the contributions (by taking the sum) from both

 H_{α} hydrogens. Similarly, at C_{β} the contribution from both H_{β} hydrogens are taken into account. However, for the H-abstraction reactions from C_{δ} , rate constants computed from three abstraction sites are considered twice to take into account all six H_{δ} . As seen from the Figure 9, abstraction from C_{α} is dominant below 750 K. Above 750 K, H-abstraction from the primary carbon sites (C_{δ}) plays a major role which is faster than C_{α} by a factor of 2-4. This is on the one hand due to the presence of six delta abstraction sites leading to a higher pre-exponential factor. On the other hand, activation energy for the H-atom abstraction is higher on C_{δ} site leading to a stronger increase in the rate constant with increasing temperature. Comparing rate constant from C_{α} and C_{γ} , the former is by a factor of 2 faster over the entire temperature regime of the investigation. The abstraction of alcoholic H is slowest over the entire temperature range which is consistent with the computed energy barrier as shown in Table 3 due to the stronger O-H bond as compared to the C-H bonds in isopentanol. Below 650 K, the rate constant for the abstraction of H from C_{γ} is faster than C_{β} by a factor of 3-4 however it tends to approach the similar value of the rate constant (C_{β}) above 1000 K.

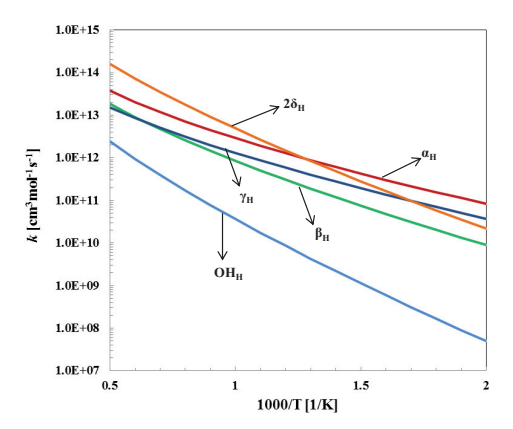


Figure 9. High-pressure limiting rate constants for the H-atom abstraction reactions from isopentanol by H atom

For the H-abstraction from isopentanol by $H\dot{O}_2$ radical (Figure 10), abstraction from the C_α is favored below 550 K. However, with the increase in temperature from 750 to 2000 K, overall contribution from the six H_δ are dominant for the same reason as already discussed before for the H-atom abstraction by H. Below 700 K, the rate constant at the C_γ is faster than C_β by a factor of 2-5. Moreover, above 1000 K, C_β becomes predominant. The abstraction of

alcoholic H remains least favorable reaction channel over an entire temperature regime of the investigation.

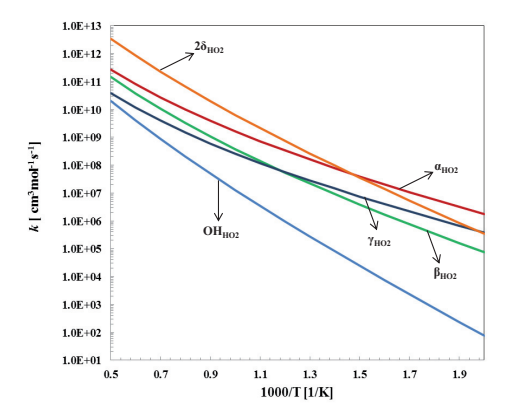


Figure 10. High-pressure limiting rate constants for the H-atom abstraction reactions from isopentanol by $H\dot{O}_2$ radical.

Figure 11a-e highlights computed rate constant as per hydrogen atom basis for the H-abstraction reaction from isopentanol by H atom and its comparison with the H-abstraction reactions from n-butanol by H atom [78]. In the study on n-butanol by Harper et al., also a CBS-QB3 method is used for computing high pressure limiting rate constants. However, the detailed computational approach followed in their work is slightly different than the one considered herein. The solid line in Figures 11a-e indicates the rate constants determined herein whereas dashed lines are the rate constant from the literature [78]. From these comparisons significant difference is seen in the abstraction of hydrogen from C_{γ} . At this site, the rate constant in the case of isopentanol is faster than n-butanol by a factor of 6 and 3 at 500 K and 1000 K respectively. This deviation arises due to the fact that in isopentanol, C_{γ} is a tertiary carbon site while secondary in n-butanol which ultimately results in weaker C-H bond strength in isopentanol. Apart from this, reaction rate constants are similar between the two alcoholic fuels and the observed deviations are resulting due to the differences in the detailed computational approach.

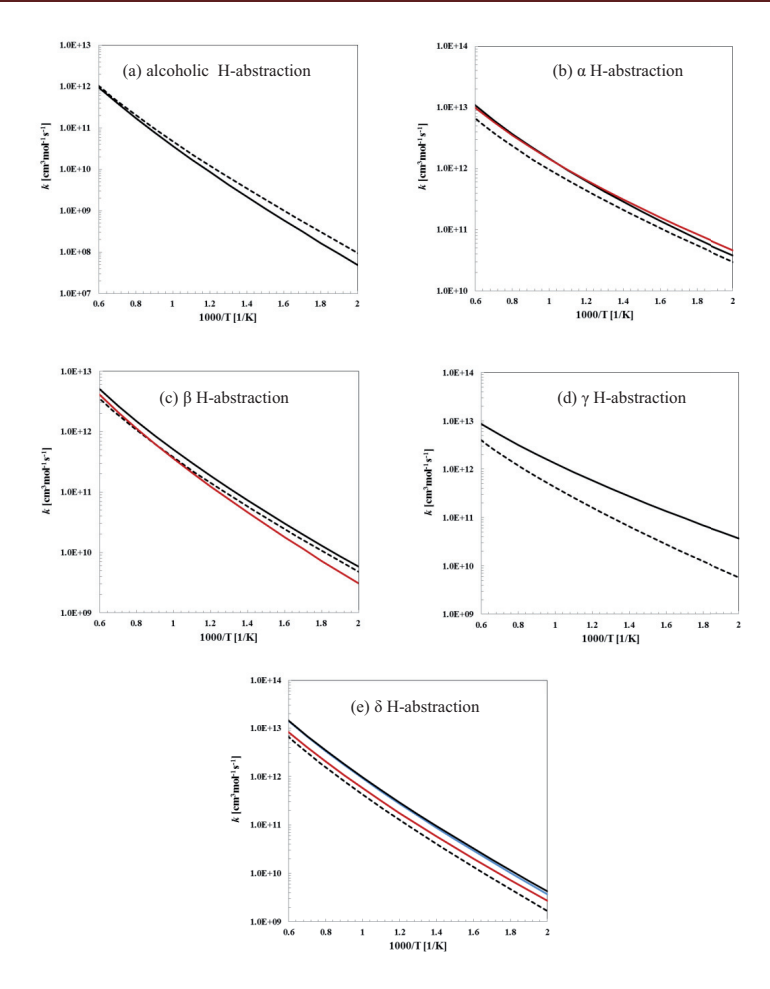


Figure 11. Comparison of H-abstraction rate constant by H atom determined in this work (solid line) and that provided by Harper et al. [78] (dashed line).

Figure 12a-e shows computed rate constant as per hydrogen atom basis for the H-abstraction reaction from isopentanol by HÖ₂ radical and its comparison with the H-abstraction reactions from n-butanol by HÖ₂ radical from Zhou et al. [79]. In their study, rate constants were determined based on the CCSD(T)/cc-pVTZ//MP2-6311G(d,p) potential energy surface by employing conventional transition state theory. The solid lines highlight rate constants for the

H-abstraction computed herein whereas dashed lines indicate computed rate constant for the H-abstraction reaction from n-butanol by Zhou et al. [79].

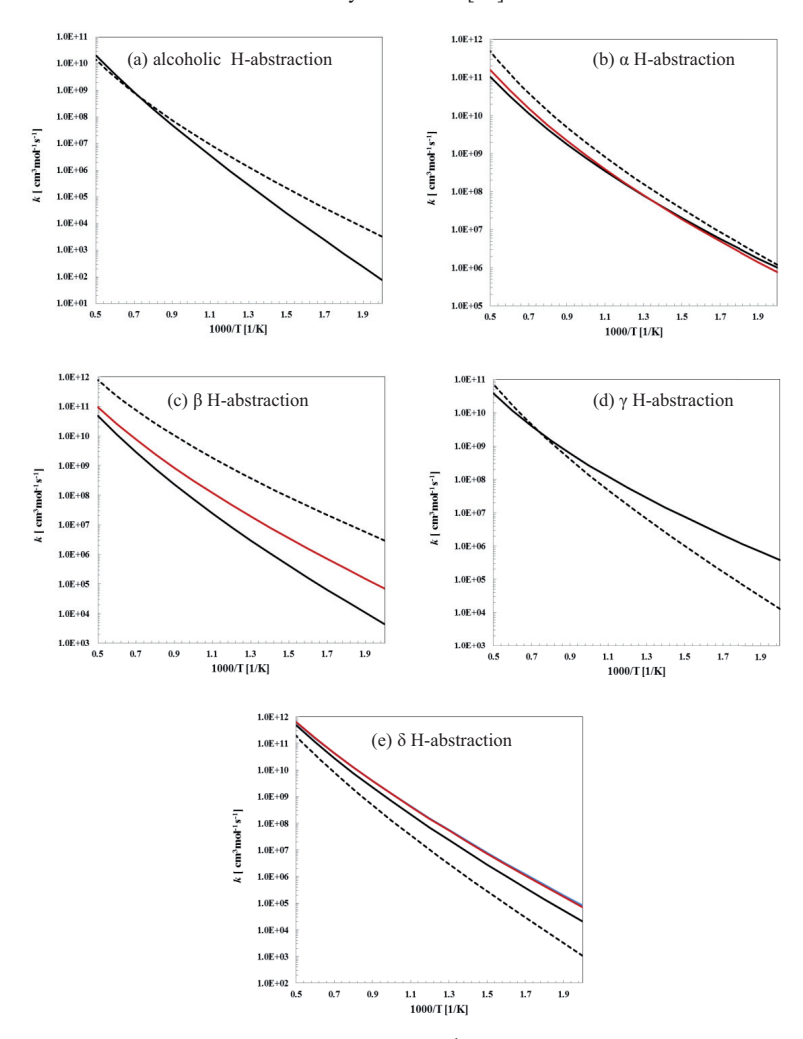


Figure 12. Comparison of H-abstraction rate constant by HO₂ radical determined in this work (solid line) and that provided by Zhou et al. [79] (dashed line).

Significant differences are noted between the computed rate constants in isopentanol at C_{β} and C_{δ} sites. It arises due to the formation of hydrogen bonding in the TSs. In Figures 12c

and 12e, the rate constants shown by the solid black lines involve the formation of hydrogen bonding in the TSs whereas the one with red lines does not involve any. The optimized TSs for the two H_B abstractions sites in isopentanol are shown in Figure 13.



Figure 13. Optimized transition states for the H_β abstractions from isopentanol by HO₂ radical

Figure 13a shows no H-bonding in the TSs whereas Figure 13b involves H-bonding between the oxygen and the hydrogen atom. This formation of hydrogen bonds in the TS can affect the rate constant of the abstraction in two ways [79]. It leads to the formation of ring structures, which can lower the energy barrier and thus an increase in the rate constant for the abstraction. Contrary, due to the formation of ring structures, entropy is lost which decreases the frequency factor for abstraction. Herein, for the abstraction of hydrogen from isopentanol by HO2 radical the second factor tends to dominate. Hence, due to a loss in entropy, rate constant decreases for the reactions involving the formation of hydrogen bond. Furthermore, comparing the rate constant for the abstraction of alcoholic hydrogen in isopentanol with that of n-butanol, former is a factor of 42 slower than n-butanol at 500 K. However at 1000 K, only variation by a factor of 2 is depicted which tends to approach the same value of the rate constant at a higher temperature. The rate constant for the abstraction of H_{β} in isopentanol is found to comparatively slower than n-butanol over the entire temperature regime of investigation. This might result due to the absence of H-bonding in TSs for the H_β abstraction in n-butanol as shown in a study by Zhou et al [79]. At 500 K, H_{γ} and H_{δ} abstraction in isopentanol are faster by a factor of ~ 29 and 67 respectively due to the weak C-H bond on the tertiary carbon site and the higher number of H-atoms on the primary site respectively, as already discussed for the H-atom abstraction by H. Hence it is seen that the commonly applied analogies in kinetic modeling are not valid here and computational chemistry provides helpful information.

IV. 2 Theoretical Investigation of Intramolecular Hydrogen Shift Reaction in 3-Methyltetrahydrofuran (3-MTHF) Oxidation

Understanding combustion phenomena of furans and their derivatives is of growing interest as can be seen from the ongoing research on experimental investigations [80-87], as well as studies dealing with the development of detailed chemical kinetic models [86-89]. These detailed chemical kinetics models assist researchers in delineating fuel combustion properties over the wide temperature and pressure regime. However, compared with the broad investigation on hydrocarbon fuels such as alkanes and alcohols, research on cyclic oxygenated compounds, especially furanics, is limited and nearly at its starting point [90], which necessitates further extensive study on their combustion behavior. In this aspect, a review by Zador et al. [10] specifically concentrates on the understanding of critical alkylperoxy and hydroperoxyalkyl reactions in relation to the modeling and prediction of low temperature combustion and autoignition. Low temperature combustion in alkanes (mentioned insection I.2) is initiated by hydrogen atom abstraction from the fuel molecule (RH) to produce alkyl radical (R). In the next step, alkyl radical undergoes O₂ addition to form alkylperoxy radical (ROO), which is followed by intramolecular hydrogen shift reactions to form hydroperoxy alkyl radicals commonly denoted as QOOH. Kinetics of ROO and QOOH radical species plays an eminent role especially for modeling ignition behavior of the fuel during low temperature combustion. Apart from the importance of this reaction in combustion chemistry. ROO species are also found to be of prime importance in atmospheric chemistry [91]. No theoretical kinetic study was found in the literature highlighting low temperature combustion reactions of methyltetrahydrofurans.

In the present work, computational calculations are performed to reveal kinetics of important low temperature reaction class in 3-MTHF, which involves internal hydrogen transfer from the peroxy radical (ROÖ) of the fuel to form the corresponding hydroperoxyalkyl radical (QOOH). Detailed calculations are performed to obtain high-pressure limit rate constants for the titled reactions in 3-MTHF, and corresponding Arrhenius parameters are presented. Further, effect of ring oxygen on the kinetics of the intramolecular H-shift reactions is analyzed by comparing its rate constant with ROÖ isomers of methylcyclopentane (mcyc5).

All electronic structure calculations involving geometry optimization, vibrational frequencies, and single point energy computation of reactants, transition states (TSs), and products are performed with the CBS-QB3 composite method [38, 39] implemented in

Gaussian 09 package [26]. Figure 14 represents the optimized three-dimensional structure of 3-MTHF with the labels used.



Figure 14. Labels of atoms in 3-Methyltetrahydrofuran.

In Figure 14, considering the oxygen position as 1, ring carbons are numbered from C2 to C5 while Cm represents the methyl side chain carbon. Due to the nonplanar five-membered ring in 3-MTHF, ring hydrogens are distinguished as cis (c) and trans (t) with respect to the methyl side chain, while Hm denotes methyl hydrogen. The high-pressure limit rate constants for the hydrogen shift reactions from ROO radicals of 3-MTHF to form the corresponding QOOH product radicals as a function of temperature are determined with the help of the GPOP program [59] employing conventional transition state theory (CTST) [92]. Asymmetric Eckart tunneling corrections [63] are taken into account in CTST rate calculations within the GPOP program. Low frequency torsional modes in reactants, transition states, and products involved in the titled reaction are treated as hindered rotations with the torsional barrier heights computed using Pitzer-Gwinn like approximation [75, 76].

The hindered rotor analysis approach followed herein is similar to the one discussed in Chapter IV.1. Figure 15 shows the plot of hindered rotor analysis for the methyl rotor attached to the C3 atom in 3-MTHF. As seen from Figure 15a, α is the torsional angle, which is defined as the dihedral angle between atoms C2–C3–Cm–Hm. Open circles in the Figure 15b indicate potential energies calculated for the CH₃ rotor in 3-MTHF at the CBS-QB3 level, whereas the solid curve represents Fourier-series interpolation. The BEx1D program [62] is used for the calculation of eigenstate energies of the hindered rotation. Partition functions directly derived from the eigenstate energies (q_{exact}) as a function of temperature are shown by the open circles in Figure 15c. Partition functions calculated by assuming harmonic oscillator approximation are represented by q_{HO} , those assuming free rotor approximations by q_{FR} , and those assuming Pitzer–Gwinn approximation by q_{PG} . Pitzer-Gwinn approximation (q_{PG}) with hindrance potential height of $V_0 = 1050$ cm⁻¹ shows excellent agreement with the exact partition function (q_{exact}) as seen from Figure 15c. Hence all the partition functions for the CH₃ internal rotor in ROO, TS, and QOOH are approximated by a Pitzer-Gwinn

approximation with hindrance potential height of 1050 cm^{-1} . In the case of TSs wherein hydrogen is abstracted from C3 and in the case of QOOH species involving a radical center on C3, the CH₃ rotor is treated with estimated barrier heights of 800 and 150 cm^{-1} respectively. Similarly all the internal rotors in reactants, transition states, and products are evaluated by the representative structure as provided in the Appendix (Figures A39–A54) of this thesis and treated with estimated barrier heights by considering Pitzer-Gwinn approximation, summarized in Table 5. V_0 in Table 5 represents the height of the hindrance potential (cm⁻¹); σ is the symmetry number for all the low frequency torsional modes in reactants, TSs, and products. All partition functions are computed with energy relative to the lowest energy isomer.

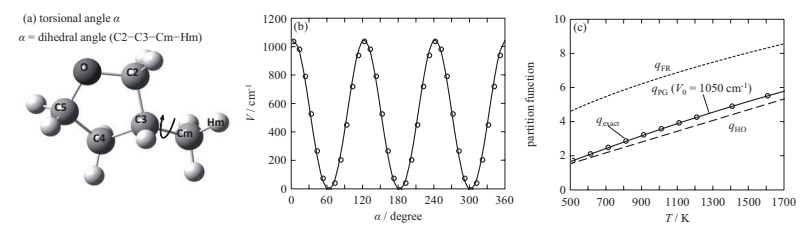


Figure 15. Hindered rotor analysis for the methyl rotor attached to the C3 atom in the tetrahydrofuran ring; (a) definition of torsional angle α , for methyl rotor (b) potential energy calculated by using a CBS-QB3 method (open circle) and fitted curve (line) (c) Partition function calculated from eigenstate energies (q_{exact}), in comparison with harmonic oscillator (q_{HO}), free rotor (q_{FR}) and Pitzer-Gwinn (q_{PG}) approximations.

Figure 16 shows another example of the hindered rotor analysis for a CH₂O \dot{O} rotor attached to the C3 atom in the tetrahydrofuran ring. In this case, hindered rotor analysis plots evince that the free rotor approximation (q_{FR}) is far off from the exact partition function (q_{exact}), whereas quantitative good agreement can be seen employing Pitzer-Gwinn approximation (q_{PG}) with that of exact partition function (q_{exact}). As seen in Figure 16b, the potential energy curve obtained for a CH₂O \dot{O} rotor is asymmetric in nature (unlike methyl rotor, Figure 15b) with hindrance potential height of 2000 cm⁻¹.

Table 5. Estimated Hindered Rotor Parameters in Pitzer-Gwinn Approximation

bonding atom	type of rotor	V_0^b / cm^{-1}	$\sigma^{^{c}}$
C3	CH ₃	1050	3
	•CH ₂	400	2
	СНО	700	1
	$\text{CH}_2\text{OO} \bullet$	2000	1

	CH ₂ OOH	1800	1
	00•	1000	1
	OOH	2000	1
hydrogen abstracting C3 in transition states	CH ₃	800	3
radical centered C3	CH_3	150	3
	$\mathrm{CH_2OOH}$	900	1
C2, C5	00•	1000	1
	OOH	6000	1
C4	00•	1000	1
	OOH	2000	1
Cm	00•	850	1
	OOH	1800	1
O in C2-OOH or C5-OOH	ОН	2200	1
O in C3-OOH or C4-OOH	ОН	1150	1
O in Cm-OOH	ОН	1000	1

^aabbreviations, C2, C3, C4, C5, and Cm are referred in Figure 14. ^bThe height of the hindrance potential. ^cThe symmetry number of the internal rotation.

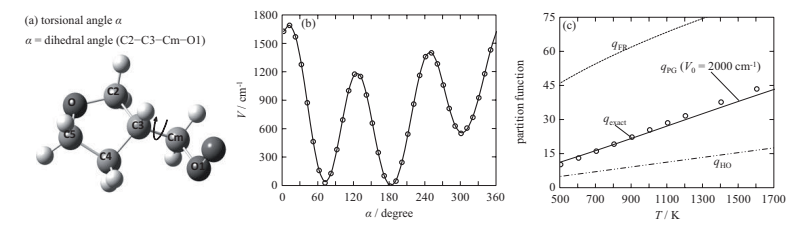


Figure 16. Hindered rotor analysis for CH₂OO rotor attached to the C3 atom in the tetrahydrofuran ring; (a) definition of torsional angle α , for CH₂OO rotor (b) potential energy calculated by using a CBS-QB3 method (open circle) and fitted curve (line) (c) partition function calculated from eigenstate energies (q_{exact}), in comparison with harmonic oscillator (q_{HO}), free rotor (q_{FR}) and Pitzer-Gwinn (q_{PO}) approximations.

The species abbreviation adopted for the reactants, TSs, and products are highlighted in Figure 17. In sum, eight ROO isomers of 3-MTHF have been considered, and their abbreviations used are as follows. ROOx indicates alkylperoxy radical with OO positioned on carbon x. As discussed before, cis and trans isomers in ROO, TSs, and QOOH species of 3-MTHF are distinguished by alphabet c and t, respectively. ROO2c in Figure 17 indicates alkylperoxy radical with OO group attached to the carbon bearing the second position on the tetrahydrofuran ring followed by letter c indicating a cis isomer. TSs are abbreviated as TSx-y, wherein x denotes the carbon with the OO group while the site from which the hydrogen atom is being abstracted is indicated by letter y. TSm-2c denotes a transition state with the OO group centered on the methyl carbon and hydrogen being abstracted from cis

carbon at position 2 on the ring. Product species QOOH*x-y* denotes hydroperoxyalkyl radical with OOH positioned on carbon *x* with radical center *y*. In the case of 1,3 H-shift reactions, product species RCHO*x* are formed with *x* being the carbon bearing doubly bonded oxygen. RCHO2 shown in Figure 17 is formed via 1,3 H-shift reaction in ROO2 isomer of 3-MTHF, which involves hydrogen shift from C2 to form QOOH with radical center C2. This QOOH species is unstable and readily decomposes to give RCHO2 and OH radical.

Figure 17. Species abbreviations used for 3-MTHF species. In ROOx, x is a carbon attaching OÓ group. In TSx-y, x is a carbon attaching OÓ group and y is a hydrogen atom abstracted carbon. In QOOHx-y, x is a carbon attaching OOH group and y is a radical centered carbon. In RCHOx, x is a carbon attached to double bonded oxygen.

The thermodynamic properties of ROO and QOOH species involved in the intramolecular H-shift reactions in 3-MTHF are not available in literature. Hence, standard enthalpies of formation ($\Delta_t H^0_{298}$), standard entropies (S^0_{298}), and heat capacities at constant pressures (C_p) for these species are computed and presented herein.

i. Thermochemistry

Limited experimental thermochemistry data can be found for tetrahydrofuran and its radical species. Pell and Pilcher [93] reported $\Delta_t H^0_{298}$ for tetrahydrofuran to be -184.2 ± 0.71 kJ mol⁻¹ from measurements of heat of combustion by flame calorimetry, whereas S^0_{298} as reported by Clegg et al. [94] is 301.7 ± 1.7 J mol⁻¹ K⁻¹. In another study, Feller et al. [95] theoretically calculated $\Delta_t H^0_{298}$ for tetrahydrofuran-2-yl and tetrahydrofuran-3-yl radical species. Table 6 lists computed thermodynamic properties of tetrahydrofuran, tetrahydrofuran-2-yl, and tetrahydrofuran-3-yl determined herein by the atomization method with the CBS-QB3 method and its comparison with the values from literature [93-95]. For tetrahydrofuran-2-yl and tetrahydrofuran-3-yl species, computed $\Delta_t H^0_{298}$ are -7.6 kJ mol⁻¹ and 11.1 kJ mol⁻¹, deviating by 5.5 kJ mol⁻¹ and 4.0 kJ mol⁻¹, respectively from the reported values [95]. $\Delta_t H^0_{298}$ and S^0_{298} values of tetrahydrofuran determined with the CBS-QB3

method differ by 4.2 kJ mol^{-1} and $2.4 \text{ J mol}^{-1} \text{ K}^{-1}$, respectively, from the experimental values [93, 94], which are within the uncertainty limit of the CBS-QB3 method [61]. The favorable comparison can be noticed between $\Delta_t H^0_{298}$ and S^0_{298} determined in this work and that reported in the literature. Hence, thermodynamic properties (standard enthalpies of formation, standard entropies, and heat capacities at constant pressures) for all the reactants and products involved in the isomerization reactions of 3-MTHF are computed employing the CBS-QB3 method and provided in Table A3 (Appendix).

Table 6. Thermodynamic properties

Species	Δ	$\Delta_{\rm f} H_{298}^{\circ} / { m kJ mol}^{-1}$		S	$S_{298}^{'}$ / J mol 1 K $^{-1}$	
	this work	ref.	diff. a	this work	ref.	diff. "
tetrahydrofuran	-180.0	$-184.2 \pm 0.71^{\ b}$	4.2	298.3	301.7 ± 1.7^d	-2.4
tetrahydrofuran-2-yl	-7.6	$-2.1\pm4.2^{\ ^{c}}$	-5.5	306.6		
tetrahydrofuran-3-yl	11.1	$15.1 \pm 4.2^{\circ}$	-4.0	310.9		

^a(this work) - (ref.), ^bPell et al. [93], ^cFeller et al. [95], ^dClegg et al. [94]

One of the factors that play an important role in the intramolecular H-shift reactions is the strength of a C-H bond that is involved in the H-shift reactions. This information can be obtained by computing C-H Bond Dissociation Energy (BDE). The following section highlights C-H BDEs in 3-MTHF.

ii. C-H Bond Dissociation Energies.

Bond dissociation energies at 0 K (BDEs) for all C–H bonds in 3-MTHF are computed at the CBS-QB3 level of theory and are listed in Table 7 From the computed values, it is observed that the C–H BDEs values for the secondary hydrogen atoms, α positions to the ring oxygen (H2t, H2c, H5t, and H5c in Figure 14) is 387 kJ mol⁻¹ corresponding to the weakest C–H bond in 3-MTHF. The lower BDE of these secondary C–H bonds compared with C4–H4 bonds (also a secondary C–H) is due to the presence of the oxygen heteroatom adjacent to C2 and C5. Since the oxygen atom is comparatively more electronegative than carbon, this results in the weakening of C–H bond strengths at positions adjacent to the ring oxygen. Another reason is due to the hyperconjugation effect as discussed by Agapito et al [96]. The lone pair of electrons on the O atom stabilizes the formed fuel radical at C2 and C5 sites, resulting in lower C-H BDE. The observed trend for C–H BDEs in 3-MTHF is C2, C5 (secondary) < C3 (tertiary) < C4 (secondary) < Cm (primary). As noticed, C2–H and C5–H bonds are weaker than C3–H3 (tertiary) by nearly 9 kJ mol⁻¹, whereas the

observed difference in BDEs between C2 and C5 and C4 (both secondary) is found to be around 19 kJ mol⁻¹. A primary C-H bond, as expected, is the strongest among all the C-H bonds in 3-MTHF, with C-H BDE value of 418 kJ mol⁻¹.

Table 7. C-H bond dissociation energies in 3-Methyltetrahydrofuran

bond	$D_0^b / \text{kJ mol}^{-1}$
C2-H2t or C2-H2c	387
C3-H3	396
C4-H4t or C4-H4c	406
C5-H5t or C5-H5c	387
Cm-Hm	418

^aAtom labels are given in Figure 14. ^bC-H bond dissociation energies calculated by using the CBS-QB3 method.

To analyze the favorability of isomerization reaction channels in all isomers of 3-MTHF, reaction barriers and energies are determined.

iii. Reaction Barriers and Energies

Reaction barriers involved for the intramolecular hydrogen shift reactions in ROO isomers of 3-MTHF are computed by considering the difference in energies (at CBS-QB3 method) between the TSs and reactants, represented by E_0 . The CBS-QB3 energy differences between products and reactants are used to compute reaction energies, ΔE , for the title reactions. Table 8 summarizes calculated E_0 and ΔE for the intramolecular hydrogen shift reactions in all ROO isomers of 3-MTHF considered herein. As seen from the values of reaction barriers, the lowest E_0 is obtained for the 1,5 H-shift reactions making it the most favorable reaction channel among others. Relative energy barriers for reactions involving six membered TSs (1,5 H-shift reactions) in all ROO isomers are found to lie within 64-96 kJ mol⁻¹, with the lowest energy barrier (64 kJ mol⁻¹) corresponding to ROOm isomer for the reaction involving H-shift from C2. Reactions involving H-shift from the same carbon site as that of the OO radical center proceed via a four membered TS giving RCHOx (x = 2, 4, 5, and m) and OH radical instead of hydroperoxyalkyl radical. Reaction energies for 1,3 H-shift reactions were noticed to be highly negative ranging from -109 kJ mol⁻¹ for ROOm reactant to -178 kJ mol⁻¹ for ROO2t isomer highlighting the highly exothermic nature of these reactions. In the ROO3 isomer, 1,3 H-shift products are not observed due to the unavailability of hydrogen at this site. However, significantly high relative barrier heights for 1,3 H-shift makes these reaction channels least dominant among others. ΔE for all other reaction paths excluding the reactions proceeding via four-membered TSs are endothermic in nature. One of the factors affecting the energy barriers of these reactions is found to be the cis/trans position

of the abstracted hydrogen to the OO radical center in 3-MTHF. For H5t hydrogen shift in ROO2t isomer, computed E_0 is 83 kJ mol⁻¹, which is 341 kJ mol⁻¹ lower than the H5c shift in the same isomer. In ROO4c, E_0 for H5c abstraction is 101 kJ mol⁻¹, which is about 90 kJ mol⁻¹ lower than the energy barrier involved for the abstraction of H5t. These results illustrate that cis H-shift to the peroxy group is accompanied by lower E_0 than trans. Proximity of the ring oxygen in 3-MTHF to the abstracted hydrogen also influences E_0 due to the higher electronegativity of the oxygen atom compared with the carbon, resulting in weakening of C-H bond strengths on adjacent carbon sites. This effect is discussed in detail under BDEs section. Of all 3-MTHF isomers under study, significantly, the lowest E_0 is noticed for H-shift reactions in the ROOm isomer (with OO radical on the methyl side chain). E_0 for H-shift in this isomer from C2 and C5 are 64 and 67 kJ mol⁻¹, respectively, which is about 15-20 kJ mol⁻¹ lower than C5 H-shift in ROO2t and ROO2c. The (S2) eigenvalues calculated at MP2/CBSB3 level within CBS-OB3 composite method are given in Table A2 in the Appendix. Among all the transition states, reaction of ROO2t isomer forming TS2t-5c to give QOOH2t-5 showed large (S2) eigenvalue. Considering the spin-contamination correction in the CBS-QB3 method, which is -5.2 kJ mol^{-1} for $\langle S2 \rangle = 0.96$, the possible errors in the potential energy barrier may be as large as the magnitude of the correction, -5.2 kJ mol⁻¹.

Table 8. Reaction Barriers and Energies for Hydrogen Shift Reactions in 3-MTHF

reactant ^a	H atom ^b	$E_0^c / \text{kJ mol}^{-1}$	$\Delta E^d / \text{kJ mol}^{-1}$	QOOH species	TS ring size ^e
ROO2c	H5c	88	28	QOOH2c-5	6
	Hm	97	55	QOOH2c-m	6
	H4c	110	43	QOOH2c-4	6
	H2t	165	-175	RCHO2 + OH	4
	Н3	207	29	QOOH2c-3	5
ROO2t	H5t	83	23	QOOH2t-5	6
	H4t	111	38	QOOH2t-4	6
	Н3	112	26	QOOH2t-3	5
	Hm	128	51	QOOH2t-m	6
	H2c	157	-178	RCHO2 + OH	4
	H5c	424	23	QOOH2t-5	6
ROO3	H5t	93	38	QOOH3-5	6
	H2t	107	27	QOOH3-2	5
	H4t	140	58	QOOH3-4	5
	Hm	149	71	QOOH3-m	5
	H2c	201	27	QOOH3-2	5
	H4c	209	58	QOOH3-4	5

ROO4c	H2c	90	35	QOOH4c-2	6
	Hm	96	63	QOOH4c-m	6
	H5c	101	24	QOOH4c-5	5
	H4t	172	-122	RCHO4 + OH	4
	H5t	192	24	QOOH4c-5	5
	Н3	195	39	QOOH4c-3	5
ROO4t	H2t	93	20	QOOH4t-2	6
	H5t	106	30	QOOH4t-5	5
	Hm	117	63	QOOH4-m	6
	Н3	127	40	QOOH4t-3	5
	H4c	171	-122	RCHO4 + OH	4
	H5c	190	30	QOOH4t-5	5
ROO5c	H2c	82	29	QOOH5c-2	6
	Hm	109	48	QOOH5t-m	7
	H4c	126	41	QOOH5c-4	5
	H5t	162	-176	RCHO5 + OH	4
	H4t	211	41	QOOH5c-4	5
ROO5t	H2t	87	29	QOOH5ttt-2	6
	Н3	104	32	QOOH5-3	6
	H4t	136	46	QOOH5t-4	5
	H5c	168	-172	RCHO5 + OH	4
	H4c	218	46	QOOH5-4	5
ROOm	H2c	64	28	QOOHm-2	6
	H5c	67	27	QOOHm-5	7
	H4c	83	49	QOOHm-4	6
	H2t	123	28	QOOHm-2	6
	Н3	126	41	QOOHm-3	5
	H4t	140	49	QOOHm-4	6
	Hm	169	-109	RCHOm + OH	4

^aReactant abbreviations and their chemical structures are given in Figure 17. ^bThe position of hydrogen atom being abstracted is given in Figure 14. ^cReaction barriers. ^dReaction energies, ^cRing size of the transition state.

Lastly, the high pressure limit rate constants are calculated for the intramolecular H-shift reactions in 3-MTHF and are presented in the following section.

iv. High Pressure Limit Rate Constants

Arrhenius plots for the high pressure limit rate constants of the intramolecular hydrogen shift reactions for eight ROÖ isomers of 3-MTHF are highlighted in Figure 18. Rate constants for all possible hydrogen shift reaction channels are determined by fitting the calculated rate to the modified Arrhenius expression given as $k = AT^n \exp(-E_d/(RT))$ in the temperature range of 500 to 2000 K. Arrhenius rate parameters for each isomerization

channel are listed in Table 9. Reactant and product abbreviations implemented in Table 9 are highlighted in Figure 17.

Table 9. High-pressure limit rate constants for the hydrogen shift reactions in 3-MTHF

		rate	constant b	nstant b	
reactant a	product a	A	N	E/R	
ROO2c	RCHO2 + OH	6.94E+06	1.774	18241	
	QOOH2c-3	6.70E+01	2.939	21369	
	QOOH2c-4	5.84E+04	2.040	11036	
	QOOH2c-5	7.04E+05	1.663	8723	
	QOOH2c-m	2.91E+05	1.902	9853	
ROO2t	RCHO2 + OH	2.85E+06	1.764	17371	
	QOOH2t-3	3.48E+04	2.154	11098	
	QOOH2t-4	1.51E+04	2.121	11139	
	QOOH2t-5	3.59E+05	1.709	8127	
	QOOH2t-m	8.04E+03	2.218	13023	
ROO3	QOOH3-2	7.38E+04	2.035	10586	
	QOOH3-4	1.26E+02	2.909	13503	
	QOOH3-5	2.14E+05	1.780	9252	
	QOOH3-m	1.33E+02	2.983	14555	
ROO4c	QOOH4c-2	2.67E+05	1.757	8898	
	QOOH4c-3	1.63E+01	3.044	19638	
	RCHO4 + OH	3.20E+05	2.136	18618	
	QOOH4c-5	2.21E+05	1.870	10005	
	QOOH4c-m	1.76E+05	1.848	9762	
ROO4t	QOOH4t-2	1.90E+05	1.877	9231	
	QOOH4t-3	1.54E+03	2.692	12166	
	RCHO4 + OH	9.00E+05	2.104	18675	
	QOOH4t-5	8.12E+04	2.095	10380	
	QOOH4t-m	6.41E+04	2.072	11936	
ROO5c	QOOH5c-2	5.62E+05	1.684	8066	
	QOOH5c-4	6.58E+03	2.428	12539	
	RCHO5 + OH	5.00E+06	1.775	17946	
	QOOH5c-m	1.93E+04	2.103	11034	
ROO5t	QOOH5t-2	8.62E+05	1.693	8577	
	QOOH5t-3	1.77E+05	1.927	10421	
	QOOH5t-4	2.18E+03	2.631	13418	
	RCHO5 + OH	8.36E+06	1.803	18680	
ROOm	QOOHm-2	9.20E+06	1.234	6256	
	QOOHm-3	1.00E+04	2.265	12426	
	QOOHm-4	3.24E+06	1.368	8532	
	QOOHm-5	1.21E+06	1.315	6389	
	RCHOm + OH	2.88E+06	1.883	18483	

^a Reactants and products abbreviations and their chemical structures are given in Figure 17. ^b Rate constants are given by the Arrhenius expression, $k(s^1) = AT^n \exp(-E/(RT))$.

H-Shift Reactions in ROOm

Figure 18a highlights high pressure limit rate constant comparison of all possible hydrogen shift reaction channels in the ROOm isomer. The higher rate is obtained for QOOHm–2 formation involving H-shift from the C2 site, which is at α position to the ring oxygen. The proximity of the ring oxygen to the abstracted hydrogens (H2c and H2t) results in lower C2–H2c and C2–H2t BDE values as seen in Table 7. C2–H2 and C5–H5 bonds in 3-MTHF exhibit BDE values of 387 kJ mol⁻¹; however, their rates differ by 4–6 times in the temperature range 500 to 1250 K as observed from the Arrhenius plot in Figure 18a. QOOHm–2 formation is observed to proceed via a six membered TS ring, while a conjugated/bicyclic TS involving five and eight membered ring formation is seen in the case of QOOHm–5 production. The BDE for the C4–H bond is found to be 406 kJ mol⁻¹, which is about 19 kJ mol⁻¹ higher than C2–H (387 kJ mol⁻¹) bonds in 3-MTHF, reflecting slower kinetics for QOOHm–4 formation compared with QOOHm–2 and QOOHm–5. 1,3 H-shift leading to RCHOm is a minor channel among all other H-shift reactions owing to its very high energy barrier of 169 kJ mol⁻¹. This channel proceeds via a four membered TS ring, which further readily forms RCHOm and OH radical.

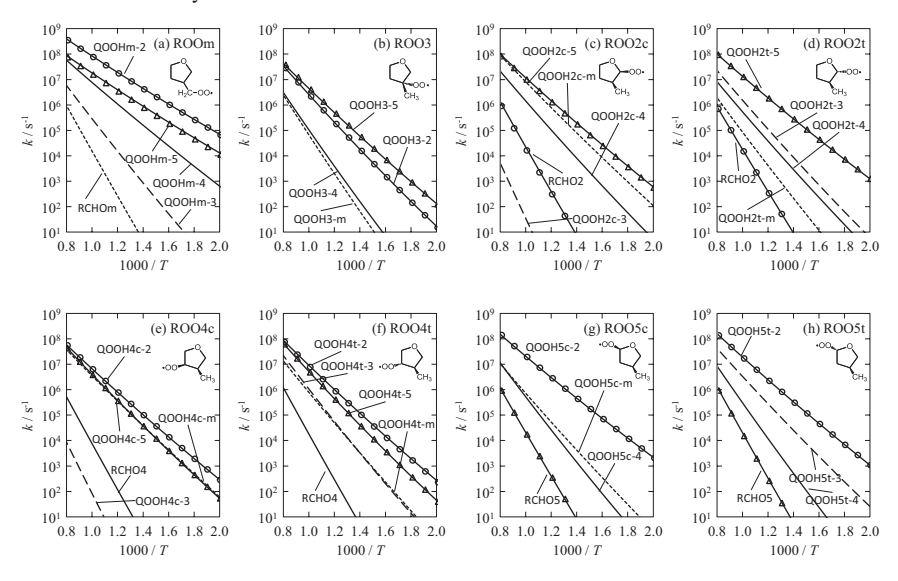


Figure 18. High pressure limit rate constants of the intramolecular hydrogen shift reactions in (a) ROOm, (b) ROO3, (c) ROO2c, (d) ROO2t, (e) ROO4c, (f) ROO4t, (g) ROO5c and (h) ROO5t isomers of 3-MTHF.

H-Shift Reactions in ROO3

QOOH3–5 and QOOH3–2 formation (Figure 18b) are the most favorable paths in the ROO3 isomer proceeding via six and five membered TS rings, respectively, rate constants of which tend to approach values of $4.4 \times 10^7 \ s^{-1}$ and $3.2 \times 10^7 \ s^{-1}$ at 1250 K, while a difference of about an order of magnitude can be seen in the low temperature regime around 500 K. Although both transition states involve hydrogen shift from the site α to the ring oxygen, variation in rate constant arises due to the difference in the ring size of the TSs as discussed in the case of the ROOm isomer. Kinetics of QOOH3–4 and QOOH3–m are much slower than QOOH3–5 and QOOH3–2. QOOH3–4 is produced via a five membered ring TS like QOOH3–2; however, a significant difference in rate constant between the two channels arises due to weaker C2–H bond strength assisting easy H-shift to produce QOOH3–2. H-shift from Cm, the primary carbon center in 3-MTHF, is least feasible accompanied with a high energy barrier of 149 kJ mol⁻¹ due to a strong Cm–Hm bond (418 kJ mol⁻¹ BDE). Due to the instability of the formed primary radical, the rate constant for this channel is lowest among others as expected.

H-Shift Reactions in ROO2c, ROO2t, ROO5c, and ROO5t (Neighboring Ring O)

C-H BDEs at C2 and C5 sites are observed to be lowest among all C-H bonds in 3-MTHF, making these sites most favorable for hydrogen abstraction and further O2 addition to form the corresponding alkylperoxy radical (ROO) during low temperature combustion. ROO2c, ROO2t, ROO5c, and ROO5t represents alkylperoxy radicals formed after the first O₂ addition on C2 and C5, neighboring the ring oxygen. The most favorable reaction channels in ROO2c and ROO2t involve H-shift from C5 to form QOOH2c-5 and QOOH2t-5, respectively, as shown in Figure 18c, d. A considerable difference can be seen in the kinetics of QOOH2c-3 and QOOH2t-3 toward lower temperature formation from ROO2c and ROO2t isomers, respectively, which is due to the formation of hydrogen bonding between the oxygen atom of the peroxy group and the ring hydrogen H2t in the TS of former isomer. Furthermore, in the ROO2c, the C3 hydrogen is trans to the peroxy radical, hindering transition state ring formation while it is cis in the latter isomer making H-shift in ROO2t facile. Comparing the rate constant for the H-shift from Cm in ROO2c and ROO2t (Figures 18c, d) shows that a difference of around 2 orders of magnitude is determined in the high temperature regime. In ROO5c and ROO5t isomers, the most dominant channel involves 1,5 H-shift from C2, whereas formation of RCHO5 via 1,3 H-shift is least favorable, as indicated by the slowest rates for this channel in Figure 18g,h.

H-Shift Reactions in ROO4c and ROO4t

Arrhenius plots 'e' and 'f' in Figure 18 summarizes H-shift reactions in ROO4c and ROO4t isomers, respectively. Reactions involving H-shift from C2 and C5 are most favorable, associated with lowest energy barriers in both isomers. In ROO4c, 1,5 and 1,4 H-shift reactions forming QOOH4c-m and QOOH4c-5 follow similar kinetics in the entire temperature regime as depicted in Figure 18e, although these channels proceed via different TS rings. In ROO4t, H-shift from C3 and Cm to form QOOH4t-3 and QOOH4t-m, respectively, demonstrate similar kinetics as shown in Figure 18f.

Further, branching ratio for the intramolecular hydrogen shift reactions in ROO isomers of 3-MTHF from all possible abstraction sites is computed to provide an overall idea about the favorability of a particular reaction channel over 500 to 1250 K.

v. Product Branching Ratio

For the hydrogen shift reactions in ROOm, branching ratio is depicted by Figure 19h, wherein at 500 K almost 99% contribution is seen from the C2 and C5 sites, which are α positions on the 3-MTHF ring, neighboring the ring oxygen atom. The percentage from these sites at 1250 K is around 88%, which is slightly lowered compared with 99% in the lower temperature regime. The remaining 11% at 1250 K arises from the C4 site to form QOOHm-4 radical. In the higher temperature regime, all isomers of 3-MTHF as summarized in Figure 19 show a higher percentage of product branching ratio from α sites (C2 and C5), which varies from 84% in ROO2c to almost 100% in ROO3 isomer. Higher contribution from these sites arises because C-H bonds neighboring the ring O atom are weakest as observed from the computed C-H BDEs values ensuring faster H shift. ROO2c and ROO2t isomers depict comparatively different percentages for H shift from the methyl side chain. The former isomer with OO substituent at the cis position to the methyl group contributes around 16% at low temperature, whereas around 43% is seen at high temperature as represented in Figure 19a, while almost no contribution is observed in latter isomer as summarized in Figure 19b. The major contribution of ROO2c for QOOH2c-m formation is due to the cis position of the peroxy radical to the abstracted H resulting in a highly favorable six membered ring transition state. However, in ROO2t, due to the trans position of the peroxy radical to the methyl hydrogen, this channel is not favored. The same reason holds for the absence of QOOH2c-3 species in the ROO2c isomer, while 17% is contributed for OOOH2t-3 due to cis H at the C3 site in ROO2t. Figure 19d, e displays branching ratios of ROO4c and ROO4t isomers, respectively. Analyzing percentages from C2 and C5 sites, major contribution is observed from C2 in both. Computed product branching percentages for

QOOH4c-m production from ROO4c are 15% and 26% at 500 and 1250 K, respectively. In ROO5c and ROO5t as highlighted in Figure 19f, g, considerable branching fraction arises from C2 sites on the ring approaching almost 100% at a lower temperature, whereas they are 89% and 77%, respectively at 1250 K. Figure 19c shows branching percentages of ROO3 depicting major contribution from C2 and C5 sites. Analyzing individual contribution from C2 and C5 sites, QOOH3-5 is observed in a higher fraction over the entire temperature range than QOOH3-2.

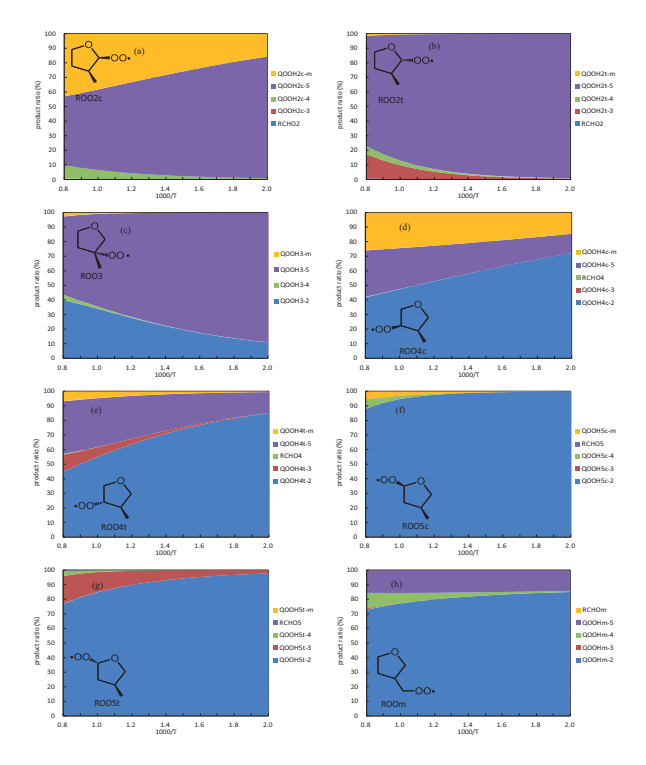


Figure 19. Product branching ratio of the intramolecular hydrogen shift reactions in (a) ROO2c, (b) ROO2t, (c) ROO3, (d) ROO4c, (e) ROO4t, (f) ROO5c, (g) ROO5t and (h) ROOm isomers of 3-MTHF.

As mentioned earlier, in order to understand the effect of ring oxygen on the kinetics of intramolecular hydrogen shift reactions in 3-MTHF, its comparison is carried out with similar reactions in methylcyclopentane (mcyc5), which is also a five membered ring compound with methyl substituent but without ring oxygen.

vi. 3-MTHF H-Shift Reaction Comparison with Methylcyclopentane

Figure 20 represents mcyc5 structure with atom labels. Altogether six ROO isomers of mcyc5 are considered. Structures of all six isomers with species abbreviation are represented in Figure 21. Like 3-MTHF, isomers of mcyc5 are distinguished as cis (c) and trans (t) with respect to methyl substituent on the five membered ring. Alkylperoxy radicals of mcyc5 are abbreviated as ROOx, with x being the position of the peroxy group. Table 10 summarizes computed reaction barriers and energies for hydrogen shift reactions in mcyc5.



Figure 20. Labels of atoms in methylcyclopentane.

BDEs of all the C-H bonds in mcyc5 (Figure 22b) are computed with the CBS-QB3 composite method and compared with 3-MTHF values as shown in Figure 22a. At C2 and C5 sites in 3-MTHF, BDEs are found to be around 10 kJ mol⁻¹ lower than those for the corresponding positions in mcyc5. The ring oxygen in 3-MTHF is found to have a significant effect on BDE values at carbon sites adjacent to the ring oxygen atom, and this effect is observed to become less pronounced at sites away from this heteroatom. The value of the BDE at the C3 position in 3-MTHF is around 6 kJ mol⁻¹ higher than that of the corresponding site in mcyc5, while no ring oxygen effect is observed on Cm-Hm bonds (Figure 22). As expected and discussed before, the lowest energy barriers in all ROO isomer of 3-MTHF are observed for the hydrogen transfer from C2 and C5 positions due to the weakest C-H BDE at these sites. For ROO2t isomers of both species, the energy barrier for H-shift from C5 (83 kJ mol⁻¹) is found to be 22 kJ mol⁻¹ lower than that in mcyc5 (105 kJ mol⁻¹). Similar to 3-MTHF, the lowest energy barrier in mcyc5 is observed for the ROOm isomer involving H-shift from the C2 site; however, the reaction barrier in 3-MTHF is around 14 kJ mol⁻¹ lower compared with that in mcyc5.

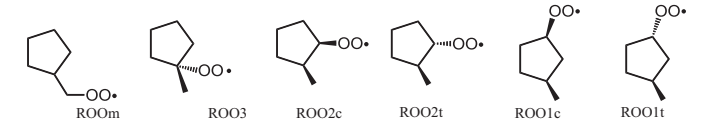


Figure 21. ROO isomers of methylcyclopentane.

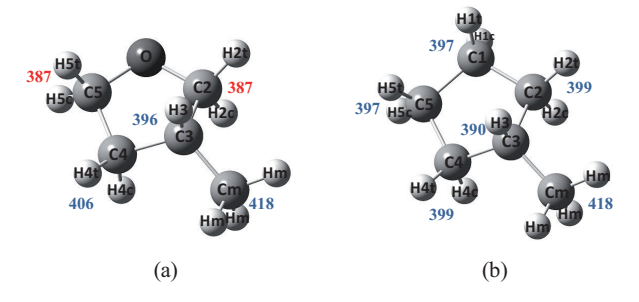


Figure 22. C-H BDE comparison of (a) 3-MTHF with (b) methlcyclopentane in kJ mol⁻¹ computed at CBS-QB3 method.

Table 10. Reaction Barriers and Energies for Hydrogen Shift Reactions in mcyc5

reactant a	H atom ^b	E_0^c / kJ mol ⁻¹	$\Delta E^{d}/\mathrm{kJ}\;\mathrm{mol}^{-1}$	product	TS ring size ^e
ROO1c	H4c	105	52	QOOH1c-4	6
	Hm	108	65	QOOH1c-m	7
	H2c	130	50	QOOH1c-2	5
	H5c	136	54	QOOH1c-5	5
	Hlt	173	-125	RCHO1 + OH	4
	H2t	187	50	QOOH1c-2	5
	H5t	188	54	QOOH1c-5	5
ROO1t	Н3	94	39	QOOH1t-3	6
	H4t	107	55	QOOH1t-4	6
	H5t	132	57	QOOH1t-5	5
	H2t	135	56	QOOH1t-2	5
	Hlc	170	-124	RCHO1 + OH	4
	H5c	189	57	QOOH1t-5	5
	H2c	192	56	QOOH1t-2	5
ROO2c	Hm	98	66	QOOH2c-m	6
	H4c	99	48	QOOH2c-4	6
	H5c	104	47	QOOH2c-5	6
	H1c	130	50	QOOH2c-1	5
	H2t	166	-127	RCHO2 + OH	4
	Н3	176	33	QOOH2c-3	5
	Hlt	187	50	QOOH2c-1	5
ROO2t	H5t	105	48	QOOH2t-5	6
	H4t	106	49	QOOH2t-4	6
	Hm	109	66	QOOH2t-m	6
	НЗ	118	35	QOOH2t-3	5
	H1c	136	51	QOOH2t-1	5
	H2c	164	-126	RCHO2 + OH	4

	Hlt	185	51	QOOH2t-1	5
ROO3	Hlt	103	49	QOOH3-1	6
	H2t	131	52	QOOH3-2	5
	Hm	146	73	QOOH3-m	5
	H2c	192	52	QOOH3-2	5
ROOm	H2c	78	45	QOOHm-2	6
	Hlc	81	44	QOOHm-1	7
	Н3	120	38	QOOHm-3	5
	H2t	129	45	QOOHm-2	6
	Hm	168	-107	RCHOm + OH	4

^aReactant abbreviations and their chemical structures in methylcyclopentane. ^bThe position of hydrogen atom being abstracted. ^cReaction barriers. ^dReaction energies. ^cRing size of the transition state.

Figure 23a–h compares total rate constant of 3-MTHF with mcyc5. Total rate constants for 3-MTHF and mcyc5 isomers are obtained by summing individual rate constants from all possible H-shift channels in a specific isomer. Solid and dashed lines in Figure 23a–h denote total rate constants computed for 3-MTHF and mcyc5, respectively. The ROOm isomer of 3-MTHF is found to have the highest rate constant over the entire temperature range as seen from Figure 23a, approaching a value $5.7 \times 108 \text{ s}^{-1}$ at 1250 K. Reaction kinetics of 3-MTHF isomers are observed to be faster than those of the corresponding isomers of mcyc5.

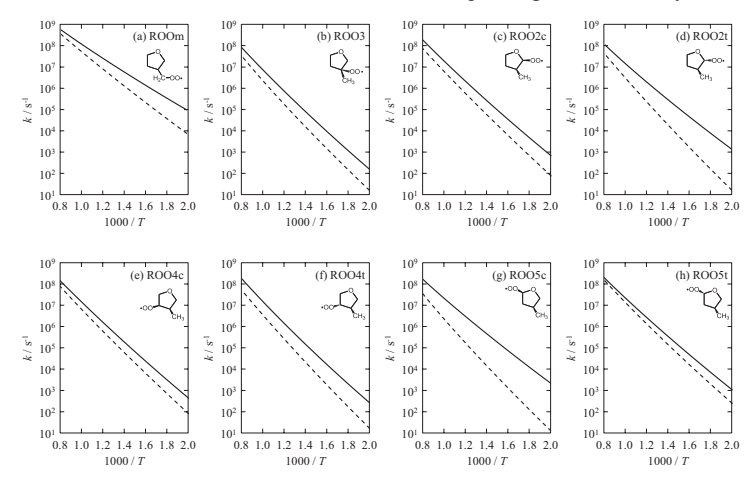


Figure 23. Comparison of total rate constants (a) ROOm, (b) ROO3, (c) ROO2c, (d) ROO2t, (e) ROO4c, (f) ROO4t, (g) ROO5c, (h) ROO5t of 3-MTHF with methlcyclopentane. Solid and dashed lines denote 3-methyltetrahydrofuran and methylcyclopentane respectively.

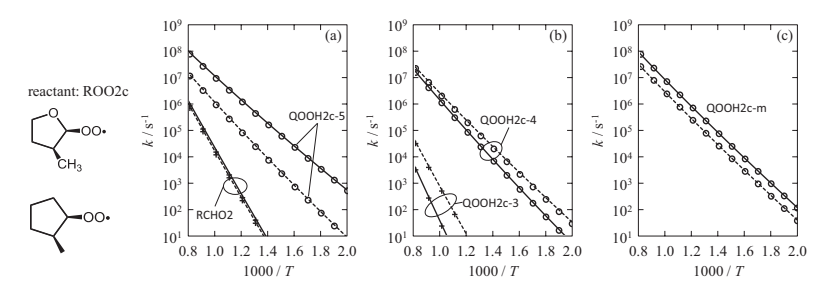


Figure 24. Comparison of rate constants ROO2c with methlcyclopentane, (a) hydrogen shift from C2 or C5, (b) hydrogen shift from C3 or C4, and (c) hydrogen shift from Cm. Solid and dashed lines denote 3-methyltetrahydrofuran and methylcyclopentane respectively.

Comparison of rate constants for individual sites in the ROO2c isomer of 3-MTHF with ROO2c isomer of mcyc5 is summarized in Figure 24. At lower temperature, a difference of about 2 orders of magnitude is seen between 3-MTHF and mcyc5 rate constants at the C5 site, which tends to differ by an order of magnitude at higher temperatures as shown in Figure 24a. Reaction kinetics for C5 and Cm hydrogen transfer in ROO2c of 3-MTHF (Figure 24a, c respectively) are faster than the corresponding isomer of mcyc5 over the temperature range 500 to 1250 K; however, observed kinetics for the hydrogen shift from C3 and C4 sites as shown in Figure 24b are faster in mcyc5 than in 3-MTHF. Comparison of rate constants for the titled reaction in the remaining seven ROO isomers of 3-MTHF with mcyc5 are summarized in Figures A55–A61 in the Appendix. From these comparisons, the effect of the ring oxygen can be clearly seen at C2 and C5 sites due to comparatively faster kinetics determined at these sites in 3-MTHF than in mcyc5. This is attributed to the lower BDEs at C2 and C5 sites in 3-MTHF due to the neighboring electronegative oxygen atom. These results indicate that the ring oxygen has a significant effect on the reaction kinetics of the intramolecular hydrogen shift reactions in all 3-MTHF isomers under investigation.

To summarize, a theoretical study is performed for computing high pressure limiting rate constants for the intramolecular H-shift reactions in alkylperoxy radicals (ROÖ) of 3-MTHF to form the corresponding hydroperoxyalkyl radicals (QOOH). All possible H-shift reaction channels from eight ROÖ isomers of 3-MTHF were studied, and the corresponding relative reaction barriers are reported. The most dominant H-shift channel is the one proceeding via a six membered transition state, whereas 1,3 H-shift are least favorable due to very high energy barriers for this channel. C-H bond dissociation energies at C2 and C5 sites in 3-MTHF are lowest (387 kJ mol⁻¹) as a result of the neighboring electronegative oxygen atom. Weaker C-H bonds strengths at these sites assist easier H-shift compared with the C3,

C4, and Cm. Effect of ring oxygen on the kinetics of the titled reaction is analyzed by comparing rate constant of 3-MTHF with ROO isomers of mcyc5. Total rate constant (obtained by summing individual rate constants) for 3-MTHF is found to be faster than that of mcyc5 in all isomers under study.

IV. 3 Theoretical Investigation of Intramolecular Hydrogen Shift Reactions in 2-Methyltetrahydrofuran (2-MTHF) Oxidation

In 1988, Rudolph and Thomas [97] reported the feasibility of using 2-MTHF as a fuel extender in spark ignition engine. With a molecular formula of $C_5H_{10}O$, it is observed to have a higher energy density (0.86 g mL⁻¹) than ethanol (0.789 g mL⁻¹). Also, it is found to be more suitable fuel than ethanol due to its higher heating value and hydrophobic nature. When compared to gasoline, 2-MTHF has a lower heating value. However, this is counterbalanced by the higher specific gravity, ultimately giving comparable fuel efficiency from 2-MTHF blends similar to that of gasoline [97, 98]. Furthermore, up to 70% of 2-MTHF can be used as a blend with gasoline without any engine modification [98].

This study highlights detailed computational study on the specific low temperature reaction class in combustion: ROO to QOOH, in 2-MTHF oxidation which is observed to occur via formation of cyclic transition states. High-pressure limit rate constants are presented for the titled reaction under study. Further, these results are compared with the reaction kinetics for the intramolecular H-shift reactions in mcyc5 and 3-MTHF [Section IV.21 to analyze how the position of the methyl substituent and the presence of ring oxygen atom affect reaction kinetics of the titled reactions. The detailed computational approach followed in this section is similar to the one implemented in the section IV.2. The CBS-OB3 composite method has been employed to perform geometry optimization, vibrational frequencies and single point energy computations of all the reactants, transitions states and products involved in this study [38, 39]. All the internal rotors in reactants, transition states and products are treated as hindered rotors with estimated barrier heights determined by considering Pitzer-Gwinn approximation as highlighted in Table 11 and provided in the Appendix (Figures A62-A71). In Table 11, some values for the height of the hindrance potential (V_0) are taken from the previous studies on the intramolecular H-shift reactions in 3-MTHF (section IV.2) due to the similar structure

The optimized three dimensional structure of 2-MTHF with the labels is represented in Figure 25. The species nomenclature followed for the reactants, transition states and products are also similar to those denoted in 3-MTHF studies. In Figure 25, ring carbons in 2-MTHF are numbered from C2 to C5 while Cm denotes the methyl side chain carbon. Hydrogens on the ring are distinguished as cis (c) and trans (t).



Figure 25. Optimized structure of 2-MTHF at CBS-QB3 method with the labels

Table 11. Estimated Hindered Rotor Parameters in Pitzer-Gwinn Approximation

bonding atom a	type of rotor	$V_0^{\ \ b} / \ {\rm cm}^{-1}$	σ^{c}
C2	CH ₃	1050	3
	•CH ₂	360	2
	СНО	1300	1
	$\mathrm{CH_2OO} \bullet$	1800	1
	$\mathrm{CH_2OOH}$	3500	1
	OO•	1000	1
	OOH	8000	1
hydrogen abstracting C2	CH_3	800	3
in transition states			
radical centered C2	CH_3	640	3
	$\mathrm{CH_2OOH}$	2000	1
C5	00•	1000	1
	ООН	6000 ^d	1
C3, C4	00•	1000	1
	ООН	2000	1
Cm	00•	850 ^d	1
	ООН	1800 ^d	1
O in C2-OOH or C5-OOH	ОН	2200^d	1
O in C3-OOH or C4-OOH	ОН	1150 ^d	1
O in Cm-OOH	ОН	1000 ^d	1

^aabbreviations, C2, C3, C4, C5, and Cm are referred in Figure 25. ^bThe height of the hindrance potential. ^cThe symmetry number of the internal rotation. ^dThe values were taken from the 3-methyltetrahydrofuran study.

In sum, eight ROO isomers of 2-MTHF are considered as reactants for the corresponding intramolecular H-shift reactions and are shown in Figure 26.

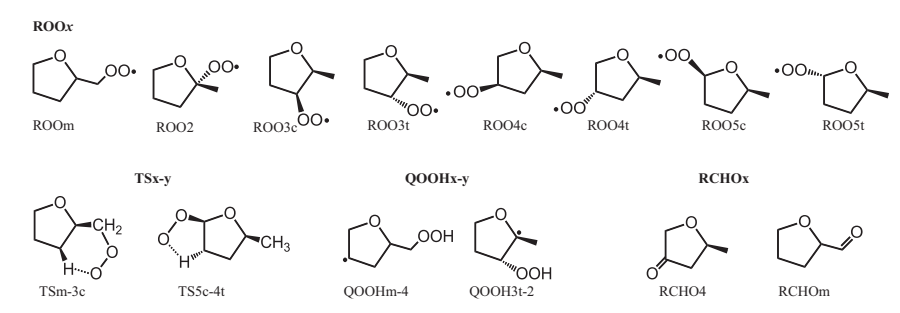


Figure 26. Species abbreviations used in this study. In ROOx, x is a carbon attaching OO group. In TSx-y, x is a carbon attaching OO group and y is a hydrogen atom abstracted carbon. In QOOHx-y, x is a carbon attaching OOH group and y is a radical centered carbon. In RCHOx, x is a carbon attaching CHO group.

For the 2-MTHF and its species (ROO and QOOH), experimental data on the thermodynamic properties are not available in the literature and hence are computed herein.

i. Thermochemistry

The CBS-QB3 composite method is used for the computation of thermodynamic properties (standard enthalpies of formation, standard entropies and heat capacities at constant pressure) by atomization method for all the reactants and products involved in the titled reaction and presented in Table A5 (Appendix). As specified in section IV.2, standard enthalpy of formation ($\Delta_t H^0_{298}$) and standard entropy (S^0_{298}) for terahydrofuran and its radical species are calculated at the CBS-QB3 level and compared with available experimental and theoretical data from literature [93, 94]. A difference of 4.2 kJ mol⁻¹ and 2.4 J mol⁻¹ K⁻¹ is observed for $\Delta_t H^0_{298}$ and S^0_{298} for tetrahydrofuran which are within the uncertainty limit of the CBS-QB3 method [38, 39]. In this study, [99] computed $\Delta_t H^0_{298}$ for tetrahydrofuran-2-yl and tetrahydrofuran-3-yl fuel radicals are -7.6 kJ mol⁻¹ and 11.1 kJ mol⁻¹ respectively. Due to a reasonable agreement observed between the theoretical and experimental results, the CBS-QB3 composite method is adopted for computing thermodynamic properties of all the species involved in the intramolecular H-shift reactions in 2-MTHF.

ii. C-H Bond Dissociation Energies

Calculated values of C-H BDEs in 2-MTHF are highlighted in Table 12. In the work of Simme [100] on kinetics and thermochemistry of 2,5-Dimethyltetrahydrofuran and related oxolanes, bond dissociation enthalpies (298.15 K) are reported for 2-MTHF. In their study, bond dissociation enthalpies (298.15 K) are computed from enthalpies of formation at 298.15 K of the involved species via isodesmic reactions by employing the model chemistries CBS-

QB3, G3 and CBS-APNO. These reported values from their study are compared with computed C-H bond dissociation enthalpies (298.15 K) and are summarized in Table 13. C-H bond dissociation enthalpies (298.15) in this study are calculated from the difference in the CBS-QB3 enthalpies at 298.15 K of the reactant and products formed due to the C-H bond cleavage in a 2-MTHF molecule. Excellent agreement is observed for all the computed values of C-H bond dissociation enthalpies (298.15 K) in this work at a CBS-QB3 method with the values from Simmie [100]. Further, C-H BDEs computed for 2-MTHF are also compared with the C-H BDE values of 3-MTHF (Table 12) in order to analyze how methyl group position on the tetrahydrofuran ring affects the C-H bond strength in 2-MTHF and 3-MTHF.

Table 12. C-H bond dissociation energies in 2-MTHF and 3-MTHF

$Bond^a$	D_0 / (kJ mol ⁻¹) 2-MTHF ^b	D_0 / (kJ mol ⁻¹) 3-MTHF ^c
C2-H2	382	387
C3-H3t or C3-H3c	409	396
C4-H4t or C4-H4c	404	406
C5-H5t or C5-H5c	386	387
Cm-Hm	424	418

^aAtom labels are given in Figure 25 and Figure 26. ^bC-H BDEs in 2-MTHF calculated at a CBS-QB3 level in this work, ^cC-H BDEs in 3-MTHF [99]

As compared to the C2-H2 bond strength in 3-MTHF, a difference of 5 kJ mol⁻¹ is observed featuring lower C-H bond strength in 2-MTHF. The observed difference in these bond strengths between two species (2-MTHF and 3-MTHF) arises due to the fact that C2 is a tertiary carbon site because of the presence of a methyl side group in 2-MTHF while secondary carbon site in 3-MTHF. This reason also applies for the stronger C3-H3 bond strength in 2-MTHF (~13 kJ mol⁻¹ higher) as compared to 3-MTHF. In 3-MTHF, C3 is a tertiary carbon center while secondary in 2-MTHF. C5-H5t and C5-H5c bonds with BDE values of 386 kJ mol⁻¹ respectively are observed to be the second weakest C-H bonds in 2-MTHF.

Table 13. C-H bond dissociation enthalpies (298.15 K) in 2-MTHF

Bond ^a	$D_{298.15}$ / (kJ mol ⁻¹) 2-MTHF ^b	$D_{298.15}$ / (kJ mol ⁻¹) 2-MTHF ^c
C2-H2	388.6	388.7 ± 0.4
C3-H3t or C3-H3c	415.5	415.7 ± 0.3
C4-H4t or C4-H4c	410.6	411.0 ± 0.5
C5-H5t or C5-H5c	392.0	391.9 ± 0.3
Cm-Hm	431.1	430.9 ± 1.5

^aAtom labels are given in Figure 25 ^bC-H bond dissociation enthalpies (298.15 K) in 2-MTHF calculated at a CBS-QB3 level in this work. ^cC-H bond dissociation enthalpies (298.15 K) in 2-MTHF from Simme [100].

Agapito et al. [96] in their theoretical study on C-H bond dissociation energies in ethers studied factors affecting the strength of C-H bonds in various molecules. Their study highlights hyperconjugation as one of the factors that affect the thermodynamic stabilization of the formed radical species. Considering this work, lower BDEs at C2 and C5 sites in 2-MTHF might result due to the stabilization of the formed radicals at these sites due to the hyperconjugation effect. The presence of a lone pair of electrons on the O atom stabilizes the formed fuel radical at C2 and C5 sites since it gets involved in the delocalization. It is observed that the BDE at C5 site is 23 and 18 kJ mol⁻¹ lower than at C3 and C4 sites respectively. In this case, higher C-H BDEs at C3 and C4 sites arises due to the lack of stabilization of the formed fuel radicals since the lone pair of electrons on O atom is now too far to take part in the delocalization. This strengthens C3-H3 and C4-H4 bonds in 2-MTHF relative to C2-H2 and C5-H5 bonds. The perceived trend in C-H BDEs in 2-MTHF computed is as follows: C2-H2 < C5-H5 < C4-H4 < C3-H3 < Cm-Hm. As expected, highest BDE value of 424 kJ mol⁻¹ is observed for the Cm-Hm bond which corresponds to the primary C-H bond in 2-MTHF which is found to be 6 kJ mol⁻¹ higher than the primary C-H bonds in 3-MTHF. Although, Cm-Hm bonds are primary bonds in both 2-MTHF and 3-MTHF, the difference in the bond strength arises due to the position of the methyl group on the tetrahydrofuran ring. In general if the formed radical after H-abstraction reaction is stable, then corresponding C-H BDE is small. This may be the reason for the highest Cm-Hm BDE in 2-MTHF as compared to that in 3-MTHF due to the higher stability of the formed fuel radical in the latter.

Based on the study on 3-MTHF (Section IV.2), it was observed that H-abstraction (a) from C2 and C5 sites (neighboring the ring oxygen atom) (b) same side of the plane, and (c) via six membered ring transition state are favored. These factors in the case of 2-MTHF isomerization reactions are discussed in detail in the following section.

iii. Reaction Barriers and Energies

The lowest reaction barriers in each isomer of 2-MTHF under this study are summarized as follows. In ROO2, H-abstraction from the C5 site via a six membered ring TS requires 84 kJ mol⁻¹. In ROO3c and ROO3t isomers, the H-abstraction from C5 proceeds with reaction barriers of 93 and 96 kJ mol⁻¹ respectively. In ROO4c, H-abstraction from C5 site occurs with an energy barrier of 110 kJ mol⁻¹. Considering ROO4t isomer, H-abstraction from C2 site is dominant with $E_0 = 88$ kJ mol⁻¹. In ROO5c, H-abstraction from a C3 site is most favorable with $E_0 = 116$ kJ mol⁻¹. In this isomer, abstraction of a hydrogen atom from the C2 site is infeasible since the OO group and H2 are both trans to each other. However in ROO5t, H-abstraction from a C2 site is predominant, accompanied with a reaction barrier of

75 kJ mol⁻¹. In ROOm isomer, H-abstraction from a C3 site is highly favored. The reaction barrier for this reaction channel is 78 kJ mol⁻¹. From Table 14 it is observed that, only in ROO4c, most favorable H-abstraction reaction proceeds via a five membered ring transition state. Whereas, in all other isomers, H-shifts via six membered ring transition state are dominant. In ROO4c, H-abstraction via formation of a six membered ring transition state is impossible due to a trans position of OO group and the hydrogen atom (H2).

Considering 1,3 H-shift reactions in 2-MTHF which involve abstraction of H from the same site as that of OO group, yield RCHOx (x = 3, 4, 5, and m) + OH which are observed to be highly exothermic in nature. For these reactions, ΔE largely depends on the H-abstraction site in 2-MTHF. Reaction energies for these 1,3 H-shift reactions range from -105 kJ mol⁻¹ for ROOm to -175 kJ mol⁻¹ for ROO5t as indicated in Table 14. For C3 and C4 sites, ΔH_{rxn} varies between -119 to -124 kJ mol⁻¹. Only in the case of ROO2, 1,3 H-shift reaction channel is infeasible due to the lack of hydrogen at the C2 site.

In order to get an idea of the potential well depths for the formation of alkylperoxy radicals ROOx, (x = 2, 3, 4 and m) which are formed by the addition of O_2 to the corresponding fuel radicals (formed by the H-atom abstraction from the fuel molecule), reaction energies ΔE are computed. These reaction energies are calculated from the difference in zero-point-corrected electronic energies of the parent radical (\dot{R}), O_2 and formed ROOx radical. These reactions are highly exothermic in nature with reaction energies between -145 to -161 kJ mol⁻¹. ΔH_{rxn} for the formation of ROO2, ROO3t, ROO5c and ROO5t are observed to be -161 kJ mol⁻¹, -150 kJ mol⁻¹, -156 kJ mol⁻¹ and -152 kJ mol⁻¹ respectively. For the formation of ROO3c, ROO4c, ROO4t and ROOm, the calculated ΔE is -145 kJ mol⁻¹. Due to the quite large well depths for the formation of alkylperoxy radicals (ROOx), the probability of the formed ROOx radicals to dissociate back into $\dot{R} + O_2$ might be less favored (also depends on temperature and pressure) as compared to the isomerization reactions to form corresponding QOOH radicals.

Table 14. Reaction barriers and energies for the hydrogen shift reactions in 2-MTHF

reactant ^a	H atom ^b	$E_0^c / \text{kJ mol}^{-1}$	$\Delta E^{d}/\text{kJ mol}^{-1}$	QOOH species	TS ring size ^e
ROO2	H5t	84	33	QOOH2-5	6
	H4t	113	47	QOOH2-4	6
	H3t	133	51	QOOH2-3	5
	Hm	149	70	QOOH2-m	5
	НЗс	222	51	QOOH2-3	5
ROO3c	H5c	93	33	QOOH3c-5	6
	Hm	97	68	QOOH3c-m	6

	H4c	136	53	QOOH3c-4	5
	H3t	170	-124	RCHO3+OH	4
	H2	185	14	QOOH3c-2	5
	H4t	202	53	QOOH3c-4	5
ROO3t	H5t	96	35	QOOH3t-5	6
	H2	100	19	QOOH3t-2	5
	Hm	127	68	QOOH3t-m	6
	H4t	144	56	QOOH3t-4	5
	Н3с	171	-119	RCHO3+OH	4
	H4c	204	56	QOOH3t-4	5
ROO4c	H5c	110	28	QOOH4c-5	5
	Hm	112	70	QOOH4c-m	7
	Н3с	136	56	QOOH4c-3	5
	H4t	175	-120	RCHO4+OH	4
	H5t	193	28	QOOH4c-5	5
	H3t	206	56	QOOH4c-3	5
ROO4t	H2	88	31	QOOH4t-2	6
	H5t	107	23	QOOH4t-5	5
	H3t	143	60	QOOH4-3	5
	H4c	173	-119	RCHO4+OH	4
	H5c	197	23	QOOH4t-5	5
	Н3с	209	60	QOOH4t-3	5
ROO5c	Н3с	116	44	QOOH5c-3	6
	Hm	124	60	QOOH5c-m	7
	H4c	138	48	QOOH5c-4	5
	H5t	169	-171	RCHO5 + OH	4
	H4t	218	48	QOOH5c-4	5
ROO5t	H2	75	24	QOOH5t-2	6
	H3t	114	40	QOOH5t-3	6
	H4t	131	41	QOOH5t-4	5
	H5c	163	-175	RCHO5 +OH	4
	H4c	213	41	QOOH5t-4	5
ROOm	Н3с	78	46	QOOHm-3	6
	H5c	82	28	QOOHm-5	7
	H4c	86	43	QOOHm-4	7
	H2	104	23	QOOHm-2	5
	H3t	146	46	QOOHm-3	6
	Hm	169	-105	RCHOm + OH	4

^aReactants abbreviations, ^bThe position of hydrogen atom being abstracted as given in Figure 25, ^cReaction barrier. ^dReaction energies. ^eRing size of the transition state.

Further, high pressure limit rate constants are determined for all the possible intramolecular H-shift reaction channels in eight ROO isomers of 2-MTHF and presented in detail in next sections.

iv. High Pressure Limit Rate Constants

Table 15 summarizes Arrhenius parameters obtained for the titled reaction in 2-MTHF. Reactant and product abbreviations of the 2-MTHF species are highlighted in Figure 26.

Table 15. High-pressure limit rate constants for the hydrogen shift reactions in 2-MTHF

			b	
reactant	product	ra	te constant	
	F	A	n	E/R
ROO2	QOOH2-3	4.45×10^3	2.511	13199
	QOOH2-4	3.93×10^4	2.065	11495
	QOOH2-5	7.28×10^{5}	1.664	8329
	QOOH2-m	2.39×10^{2}	2.889	14704
ROO3c	QOOH3c-2	9.55×10^2	2.525	19122
	RCHO3+OH	6.60×10^{5}	2.134	18437
	QOOH3c-4	1.07×10^{2}	2.928	12982
	QOOH3c-5	2.30 ×10 ⁵	1.749	9198
	QOOH3c-m	2.28×10^{5}	1.845	9874
ROO3t	QOOH3t-2	2.82×10^{5}	1.872	9980
	RCHO3+ОН	4.10×10^{5}	2.123	18593
	QOOH3t-4	7.45×10^2	2.744	14218
	QOOH3t-5	1.27×10^{5}	1.820	9524
	QOOH3t-m	1.80×10^4	2.137	13001
ROO4c	QOOH4c-3	2.98×10^2	2.819	13234
	RCHO4+OH	5.68×10^{5}	2.137	19164
	QOOH4c-5	5.15×10^4	2.080	10897
	QOOH4c-m	2.66×10^4	2.031	11495
ROO4t	QOOH4t-2	1.32×10^6	1.629	8753
	QOOH4t-3	1.99×10^3	2.688	14263
	RCHO4+OH	6.22×10^{5}	2.165	18853
	QOOH4t-5	6.35×10^{4}	2.116	10531
ROO5c	QOOH5c-3	3.13×10^4	2.076	11810
	QOOH5c-4	7.14×10^3	2.503	13923
	RCHO5+OH	8.53×10^6	1.778	18767
	QOOH5c-m	5.35×10^3	2.249	12650
ROO5t	QOOH5t-2	3.08×10^6	1.534	7361
	QOOH5t-3	4.16×10^4	2.080	11432
	QOOH5t-4	2.14×10^3	2.630	12882
	RCHO5+OH	5.88×10^6	1.778	18046
ROOm	QOOHm-2	4.69×10^{5}	1.765	10442
	QOOHm-3	3.33×10^6	1.387	7969
	QOOHm-4	3.71×10^{5}	1.562	8633
	QOOHm-5	7.79×10^{5}	1.453	8148
	RCHOm+OH	1.71×10^{6}	1.938	18466

^aReactants and products abbreviations and their chemical structures are given in Figure 26. ^bRate constants are given by the Arrhenius expression, $k(s^{-1}) = AT^n \exp(-E/RT)$.

H-Shift reactions in ROOm

The high pressure limit rate constants in ROOm isomer of 2-MTHF are summarized in Figure 27a. The higher rate is obtained for the H-abstraction reaction from a C3 site for the QOOHm-3 formation. This reaction proceeds via formation of a six membered ring transition state. The QOOHm-5, as shown in Figure 27a is formed by H-abstraction from C5 site in ROOm isomer. This reaction occurs via a seven membered ring transition state (Table 14). Rate constants for the production of QOOHm-3 and QOOHm-5 differs by a factor of 3-4 between 900-600 K and tends to approach 1.7×10^7 s⁻¹ and 5.2×10^6 s⁻¹ respectively at 1000 K. Hydrogen shift from the C2 site is not favorable due to the relatively higher barrier height (104 kJ mol⁻¹) which is around 22 kJ mol⁻¹ higher than H-shift from C5 site. The 1,3 H-shift from ROOm to yield RCHOm + OH is a minor reaction channel among all the isomerization reactions in this isomer; approaching $k = 1.1 \times 10^4$ s⁻¹ at 1000 K.

H shift reactions in ROO2

Figure 27b highlights comparison of high pressure limit rate constants comparison for the possible hydrogen shift reaction channels in ROO2 isomer of 2-MTHF. As seen from Figure 27b, a faster rate constant is observed for a QOOH2-5 formation which involves hydrogen abstraction from the C5 site; α position to the ring oxygen atom. This result is consistent with the computed C5-H5 BDE (386 kJ mol⁻¹) which is found to be lower than the C3-H3, C4-H4 and Cm-Hm BDEs values. At a lower temperature (500 K), k for the QOOH2-5 formation is 1.4×10^3 s⁻¹ which approaches 1.4×10^8 s⁻¹ at 1250 K. Although isomerization of ROO2 to form QOOH2-5 and QOOH2-4 proceeds via formation of six membered ring transition state, a significant difference in the rate constant is observed between these two reaction channels especially in the lower temperature regime. At a higher temperature (1250 K), rate constants between QOOH2-5 and QOOH2-4 differ by an order of magnitude whereas the difference of about three orders of magnitudes is seen at a lower temperature (500 K). A significant difference in the rate constant for these reaction channels is due to the weaker C5-H bond strength in 2-MTHF. The slowest rate constant in ROO2 is depicted for the H-shift from methyl side chain to form QOOH2-m. The main reason for this observed result is due to the stronger Cm-Hm bond strengths in 2-MTHF. Cm-Hm bond (discussed before in BDE section) is the primary C-H bond in 2-MTHF with BDE value of 424 kJ mol⁻¹. In this isomer, the C2 site is occupied by a methyl and OO group as shown in Figure 26, leading to the absence of 1,3 H-shift reaction channel. As discussed in section I.2, competition between these elementary reaction channels is important to understand ignition behavior of fuels.

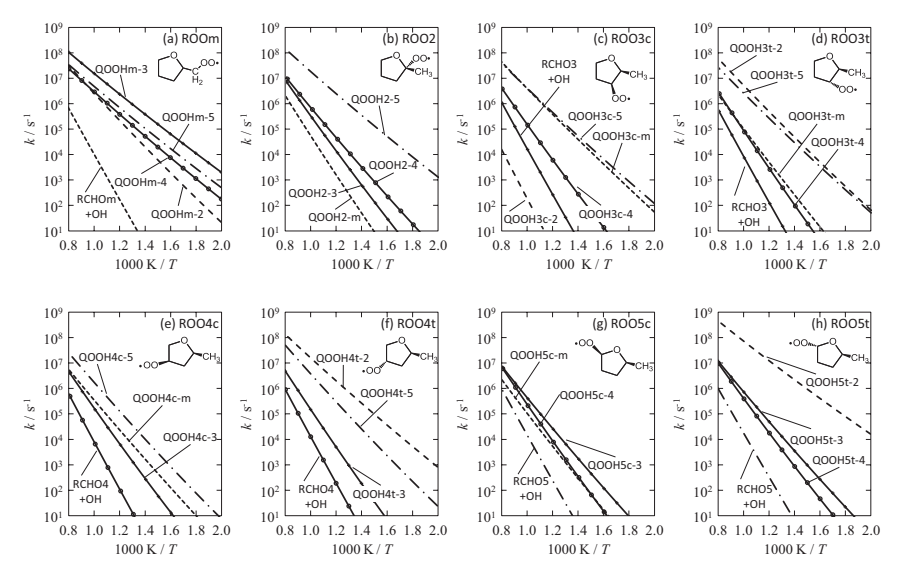


Figure 27. High pressure limit rate constants of the intramolecular hydrogen shift reactions in (a) ROOm, (b) ROO2, (c) ROO3c, (d) ROO3t, (e) ROO4c, (f) ROO4t, (g) ROO5c, and (h) ROO5t isomers of 2-MTHF.

H shift reactions in ROO3c and ROO3t

ROO3c and ROO3t isomers are formed by the addition of O_2 at the C3 radical site in 2-MTHF. In ROO3c, the OO group stands in cis-position to the methyl group while in trans in ROO3t leading to a difference in the rate constants for the QOOH3c-m and QOOH3t-m formation as highlighted in Figure 27c and 27d, respectively. The observed rate constants for the abstraction of methyl hydrogen in ROO3c at high (1250 K) and low (500 K) temperatures are faster than in ROO3t by one and three order of magnitudes respectively. Isomerization reaction involving H-shift from C5 site is a favorable reaction channel in both isomers (ROO3c and ROO3t) due to low C5-H5 BDE value (386 kJ mol⁻¹) in 2-MTHF. Although BDE of C2-H2 is lowest in 2-MTHF (382 kJ mol⁻¹), the rate constant for H2 shift in ROO3c is found to be slowest due to the trans position of the abstracted hydrogen with respect to the OO group. However, in ROO3t, the observed rate constant for the hydrogen shift from C2 is the fastest among all the reaction channels as highlighted in Figure 27d. High pressure limit rate constants for this reaction are $7.2 \times 10^1 \text{ s}^{-1}$ and $6.2 \times 10^7 \text{ s}^{-1}$ at 500 and 1250 K respectively. RCHO3 + OH product species are formed due to a 1, 3 H-shift reaction that involves the formation of the highly unstable QOOH species which then readily decomposes.

These reactions are observed to be highly exothermic in nature with computed $\Delta E = -124$ and -119 kJ mol⁻¹ in ROO3c and ROO3t isomers respectively.

H shift reactions in ROO4c and ROO4t

In ROO4c (Figure 27e), the most favorable H-shift reaction channel involves abstraction of hydrogen from C5 which occurs via formation of a five membered ring transition state to give QOOH4c-5. Whereas, in ROO4t (Figure 27f), H-shift from C2 is predominant among all other reaction channels. This reaction proceeds with a six membered ring transition state to produce QOOH4t-2. In ROO4c, abstraction of hydrogen from C2 is infeasible (trans H2 with respect to OO group). E_0 for H2 shift in ROO4t is 88 kJ mol⁻¹, which is the lowest among all the computed reaction barriers in ROO4t. In ROO4c, below 625 K, the rate constants for QOOH4c-m and QOOH4c-3 production differ by an order of magnitude whereas at 1250 K it approaches 5.3×10^6 s⁻¹ and 4.3×10^6 s⁻¹ respectively. In ROO4t, significant differences in the rate constants are depicted towards QOOH4t-5 and QOOH4t-3 productions at a temperature below 700 K. At 500 K, rate constant between these two products differs by around three orders of magnitude. Formation of RCHO4 + OH (in ROO4c and ROO4t) is the least favorable reaction channel with the slowest reaction kinetics in the entire temperature range of study. Estimated reaction barriers for these reaction channels are ~175 kJ mol⁻¹ in both ROO4c and ROO4t.

H shift reactions in ROO5c and ROO5t

Arrhenius plots in Figure 27g and 27h, summarize intramolecular H-shift reactions in ROO5c and ROO5t isomers in 2-MTHF respectively. As seen in the Arrhenius plot for ROO5C (Figure 27g), most dominant reaction channel is the one that involves the formation of QOO5c-3. For this isomer, abstraction of C5 hydrogen leads to the formation of RCHO5 + OH species, through a four membered ring transition state. This isomerization reaction requires a very high energy barrier (169 kJ mol⁻¹) and it is highly exothermic in nature with reaction energy = -171 kJ mol⁻¹. In ROO5t, the observed rate constant for the formation of RCHO5 + OH has similar kinetic behaviors as those in ROO5c due to comparable reaction barrier (E_0) and energy (ΔE). The most dominating reaction channel in ROO5t over the entire temperature range of investigation is the formation of QOOH5t-2. The reason for this observed result is due to low BDE for the C2-H2 bond in 2-MTHF. In ROO5c, kinetic behavior for the formation of QOOH5c-4 and QOOH5c-m are observed to follow the same trend in the low temperature regime (Figure 27g). However, in the high temperature regime, the rate constant of QOOH5c-4 dominates over QOOH5c-m and approaches to that of the QOOH5c-3 formation. In ROO5t, at a higher temperature (1250 K), rate constants for the

production of QOOH5t-3 and QOOH5t-4 approaches very close to each other, with the value of $1.3\times10^7~\text{s}^{-1}$ and $1.1\times10^7~\text{s}^{-1}$ respectively. However a difference of about an order of magnitude can be seen at 500 K.

v. Product Distribution

Product distributions are computed for all isomerization reactions in 2-MTHF to get an overall idea about the percentage fraction of the QOOH species that are formed in the temperature range of 500 - 1250 K. Figure 28a-h summarizes product distributions from ROO2, ROOm, ROO3c, ROO3t, ROO4c, ROO4t, ROO5c and ROO5t isomers of 2-MTHF towards the corresponding product formation. H-shift reactions in ROO2 isomer is represented in Figure 28a, wherein major contribution can be seen towards the QOOH2-5 formation. At 500 K, 100% product distribution arises from this reaction channel while at a higher temperature (1250 K) around 88% is observed. At this temperature, remaining contribution (12%) arises from the formation of QOOH2-3, QOOH2-4 and QOOH2-m product species as highlighted in Figure 28a. The major fraction arising from ROO2 to give QOOH2-5 is due to weak C5-H5 bonds in 2-MTHF which enables easy H-shift to yield QOOH2-5.

For ROOm, branching contribution summary is represented in Figure 28b. The paramount fraction in ROOm arises from the QOOHm-3 formation channel which involves intramolecular H-shift from the C3 site. This reaction channel proceeds via highly favorable six membered ring transition state. Contribution from this isomerization channel remains in between 54-74% in the temperature regime 500 -1250 K as shown in Figure 28b. Remaining 25% at lower temperature arises from the QOOHm-4 (~7%) and QOOHm-5 (~18%) reaction channels. Figure 28c, d highlights product distributions for the formation of all isomerization products from ROO3c and ROO3t isomers of 2-MTHF respectively. QOOH3c-5 formation decreases from 69% at 500 K to 44% at 1250 K whereas, for QOOH3c-m, product distribution increases from 31% at 500 K to almost 50% at 1250 K. In ROO3t, major contribution arises from the reaction involving H-abstraction from C2 site, which approaches from 56 % at 500 K to 65% at 1250 K. However for QOOH3t-5 formation channel, observed product distribution decrease from 44% at 500 K to 29 % at 1250 K. In ROO3c favorable contributions are seen from QOOH3c-m and QOOH3c-5 whereas QOOH3t-5 and QOOH3t-2 formation are predominant reaction channels in ROO3t.

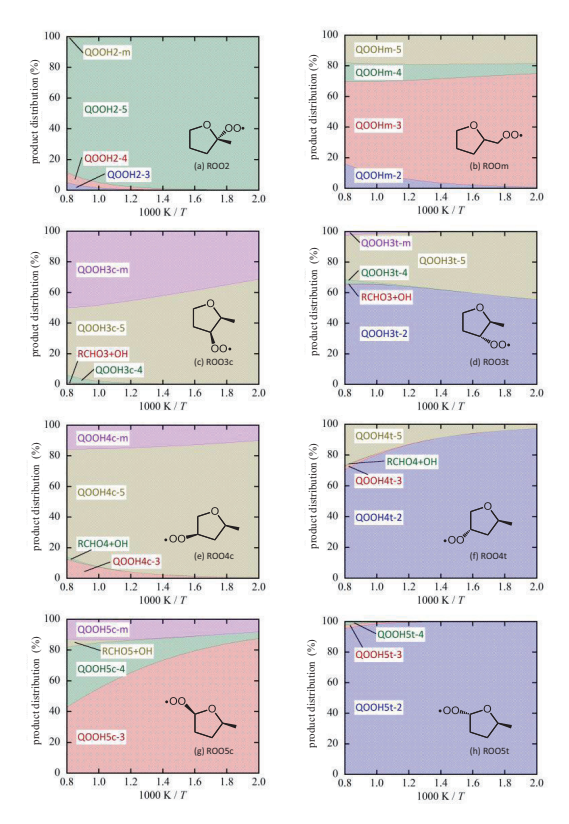


Figure 28. Product distributions of the intramolecular hydrogen shift reactions in 2-MTHF isomers. Chemical structures in the figures are reactants.

Figure 28e, f represents branching percentage in ROO4c and ROO4t isomers respectively. Major contribution in ROO4c for the QOO4c-5 formation arises from the fact that C5-H5 are weak bonds in 2-MTHF due to the presence of an electronegative oxygen atom at the neighboring sites and also due to the hyperconjugation effect. At lower temperature, almost 90% contribution can be observed from QOOH4c-5 while remaining 10% arises from QOOH4c-m. In ROO4t, due to the trans position of the OO to the methyl group, H-shift from Cm is infeasible, as a result, the contribution from this site is null. The QOOH4t-2 formation is a predominant pathway in ROO4t as seen from Figure 28f, which is due to the lowest C2-H2 bond strength (382 kJ mol⁻¹). As mentioned earlier, low C-H bond strengths assist in easy H-shift in the isomerization reactions. Comparing product distributions in ROO5c and ROO5t

in Figure 28g and 28h respectively, totally distinct contribution towards the product formation can be seen due to the differences in the structural components. QOOH5c-3 is observed in a higher fraction in ROO5c, which is formed due to the favorable six membered ring transition state. In this isomer, QOOH5c-2 is not produced due to the trans position of H2 to the OO group. This alignment in ROO5c makes H2 abstraction practically impossible. Another contribution in Figure 28g is seen from the intramolecular H-shift reaction from C4, taking place through a five membered ring transition state. Below 625 K, this reaction channel contributes less than 10% and its contributions tend to increase with the increase in temperature and reaches up to 39% at 1250 K. The computed product branching percentage in ROO5t shows 100% formation of QOOH5t-2 below 900 K whereas minor contributions (~2%) are seen from each of QOOH5t-3 and QOOH5t-4 at 1250 K. In all ROO isomers of 2-MTHF, almost 0-5% product branching contributions arise from the least favorable 1,3 H-shift reaction channels which form RCHOx + OH (x: 3, 4, 5, m) products as shown in Figure 28a-h. These insignificant contributions are due to very high E_0 for their isomerization channels as discussed before.

Further, these results are compared with the reaction kinetics for the intramolecular H-shift reactions in mcyc5 and 3-MTHF (Section IV.2) to analyze how the position of the methyl substituent and the presence of ring oxygen atom affect reaction kinetics of the titled reactions.

vi. 2-MTHF rate constant comparison with methylcyclopentane and 3-MTHF

Figure 29a-h highlights total rate constants comparison for the intramolecular H-shift reactions in 2-MTHF with that of methylcyclopentane (mcyc5). Total rate constants in each isomer of 2-MTHF are obtained by summing the individual rate constants for all possible hydrogen shift reaction channels in 2-MTHF and for the isomerization reactions in mcyc5 are considered from the results on 3-MTHF (Section IV.2). In all ROO isomers of 2-MTHF under investigation, ROO2 and ROO5t show significantly faster rate constants than mcyc5, especially in the lower temperature regime (below 700 K) as highlighted in Figure 29b and 29h respectively. This is as expected due to the fact that, in 2-MTHF, BDEs at C2 and C5 sites are 382 kJ mol⁻¹ and 386 kJ mol⁻¹ respectively which are ~17 and 11 kJ mol⁻¹ lower than C2 and C5 positions in mcyc5. These low BDEs in 2-MTHF tends to favor H-shift in 2-MTHF than in mcyc5. At 1250 K, the total rate constants in ROO2 and ROO5t isomers are a factor of 3 times faster in 2-MTHF than in mcyc5. In ROO5c at 500 K, total rate constants in ROO2 and ROO5t are 51 and 67 times faster in 2-MTHF than in mcyc5. In ROO5c at 500 K,

the total rate constant in 2-MTHF is by an order of magnitude slower than mcyc5 however at a higher temperature (1250 K) the rate constant between both differ by a factor of two. Considering Figures 29b-h, significant deviations in the total rate constants are observed between 2-MTHF and mcyc5 especially in the lower temperature regime. Out of all eight ROO isomers under investigation, isomerization reactions in ROO2 and ROO5t are of prime importance as clearly seen from Figure 29b and 8h respectively. However, this effect tends to become less significant with the increase in temperature.

Figure 30 summarizes individual rate constants for the intramolecular H-shift reactions from each site in ROO5c isomer of 2-MTHF and its comparison with similar isomer in mcyc5. Computed rate constants for RCHO5 + OH and QOOH5c-4 formation depict quite similar kinetic behavior in the temperature range 500 to 1250 K (Figure 30a, b) in 2-MTHF as well as in mcyc5. However, for QOO5c-3 and QOOH5c-m production, rate constants at 500 K are a factor of 11 and 29 times slower in 2-MTHF than in mcyc5. This might be due to the fact that in 2-MTHF, BDE at C3 is 409 kJ mol⁻¹ which is ~10 kJ mol⁻¹ higher than the corresponding site in mcyc5. Furthermore, slower kinetics for QOOH5c-m formation are observed due to stronger Cm-Hm bond in 2-MTHF (424 kJ mol⁻¹) than in mcyc5 (418 kJ mol⁻¹). This is consistent with the observed result in Figure 30g which highlights slower total rate constant of 2-MTHF than mcyc5.

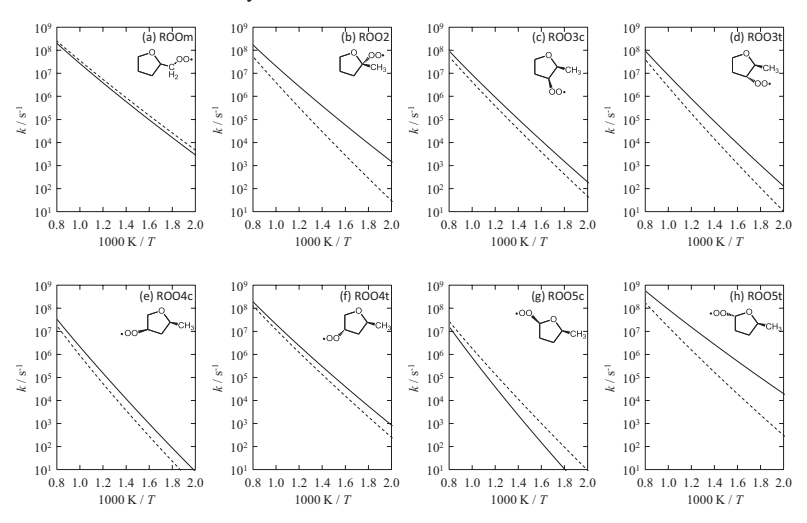


Figure 29. Comparison of total rate constants for (a) ROOm, (b) ROO2, (c) ROO3c, (d) ROO3t, (e) ROO4c, (f) ROO4t, (g) ROO5c, and (h) ROO5t isomers of 2-MTHF with methlcyclopentane. Solid and dashed lines denote 2-methyltetrahydrofuran and methylcyclopentane respectively.

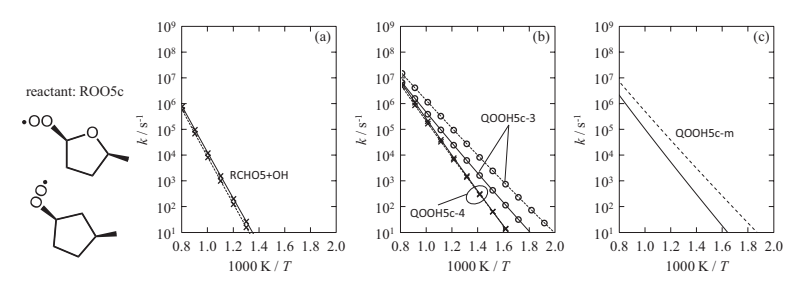


Figure 30. Comparison of rate constants in ROO5c in 2-MTHF with methlcyclopentane, (a) hydrogen shift from C5, (b) hydrogen shift from C3 or C4, and (c) hydrogen shift from Cm. Solid and dashed lines denote 2-methyltetrahydrofuran and methylcyclopentane respectively.

Figure 31a-c highlights comparison of individual rate constants in ROO2 isomer of 2-MTHF with the corresponding isomer in mcvc5. The ROO2 is another important ROO isomer of 2-MTHF due to its favorable production channel. In 2-MTHF and mcvc5, a significant difference in the rate constant is observed towards OOOH2-5 formation (Figure 31a) due to the presence of oxygen as a heteroatom at the alpha position to the C5 site in 2-MTHF which is not the case in mcyc5. This rate constant is also compared with the rate constant for the 1,5 H-shift reaction for the minimum representative molecule (alkane) in a study by Miyoshi [21]. Miyoshi performed a systematic computational study on the unimolecular reactions of alkylperoxy, hydroperoxyalkyl and hydroperoxyalkylperoxy radicals at the CBS-QB3 method. In the temperature range of 500-1000 K, the rate constant for the 1.5 H-shift reaction for the minimum energy structure (isopentane) is by a factor of 1.2-1.5 slower as compared to the ROO2 to QOOH2-5 isomerization reaction in our study. For the formation of QOOH2-3 and OOOH2-m as summarized in Figure 31b and c respectively, minor differences in the rate constant are seen between 2-MTHF and mcyc5 while for the production of QOOH2-4, the rate constant of 2-MTHF is slower than mcyc5 by about an order of magnitude. Comparison of individual rate constants in ROO3c, ROO3t, ROO4c, ROO4t, ROO5t and ROOm isomers of 2-MTHF with corresponding isomers in mcyc5 are summarized in Figures A72-A77 in the Appendix.

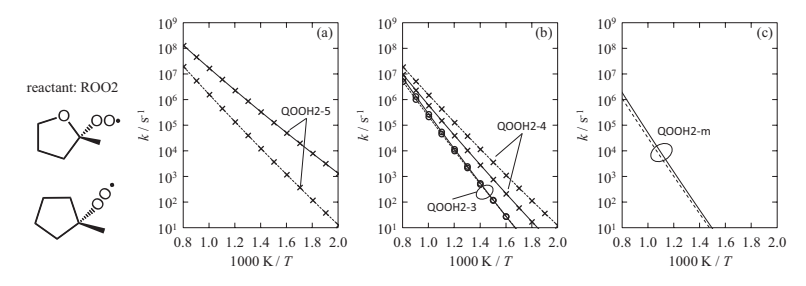


Figure 31. Comparison of rate constants in ROO2 in 2-MTHF with methlcyclopentane, (a) hydrogen shift from C5, (b) hydrogen shift from C3 or C4, and (c) hydrogen shift from Cm. Solid and dashed lines denote 2-methyltetrahydrofuran and methylcyclopentane respectively.

Figures 32a-c and 33a-c summarize rate constants for the hydrogen shift reactions from C2 and C5 sites in ROO2, ROO3t, ROO4c, ROO4t, ROO5t and ROOm isomers of 2-MTHF in comparison with the isomers of 3-MTHF. A significant difference in the rate constants in both reactants (2-MTHF and 3-MTHF) can be seen for the abstraction of hydrogen from the C2 site (Figure 33a-c). This result directly reflects the difference in the C2-H2 BDEs between 2-MTHF (382 kJ mol⁻¹) and 3-MTHF (387 kJ mol⁻¹) as shown in Table 12. Figure 32a highlights H-abstraction reactions from the C5 site in ROO2 isomers of 2-MTHF and 3-MTHF. At a temperature below 1000 K, rate constants between 2-MTHF and 3-MTHF for this reaction differ by a factor of two. Comparison between H-shift reactions from C2 and C5 sites in ROO3t and ROO4c isomers of 2-MTHF and 3-MTHF are highlighted in Figure 32b and c respectively. In ROO4c, at 500K, H-shift from C5 site in 3-MTHF is a factor of seven times faster than the corresponding site in 2-MTHF. In ROO4t (Figure 33a), a less significant difference is found for the H-shift from C5 whereas rate constants for H-shift from C2 between two reactant differ by a factor of 2-4 in the temperature range 1250-500 K respectively.

Figure 33a focuses the favorability of QOOH4t-2 formation over QOOH4t-5 in both 2-MTHF as well as in 3-MTHF. The main reason for this observed trend is directly reflected by the ring size of the transition state during H-shift reactions. QOOH4t-2 proceeds via formation of a six membered ring which is highly favored while for the reactions giving QOOH4t-5, five membered ring transition states are found. The computed E_0 for QOOH4t-2 are 88 and 93 kJ mol⁻¹ in 2-MTHF (Table 14) and 3-MTHF [99] respectively. However, for H-shift from C5 for QOOH4t-5 formation, reaction barriers are ~106 kJ mol⁻¹ in both reactants. Figure 33b focuses on QOOH5t-2 reaction kinetic which is favored in 2-MTHF as

compared to 3-MTHF. Below 625 K, rate constants between two reactants differ by an order of magnitude. Isomerization reactions in the ROOm isomer of 3-MTHF towards QOOHm-2 and QOOHm-5 production are more favorable than in 2-MTHF as highlighted in Figure 33c. The computed rate constant for H-shift from C2 differs by one and three orders of magnitude at 1250 K and 500 K respectively. The main reason for this observed result is that, in 3-MTHF H2 shift proceeds via a favorable six membered ring transition state with E_0 = 64 kJ mol⁻¹ while in 2-MTHF H-shift from the same site (C2) occurs via a five membered ring transition state with E_0 = 104 kJ mol⁻¹ (Table 14).

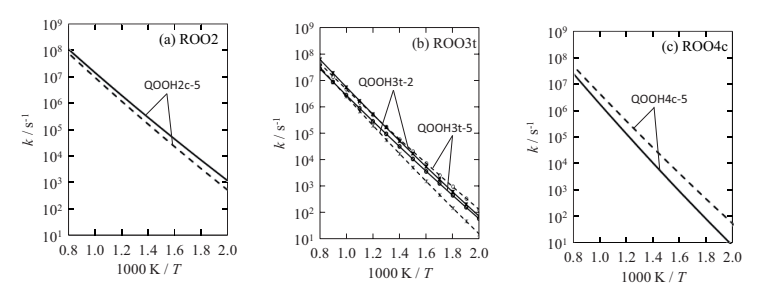


Figure 32. Comparison of 2-methyltetrahydrofuran rate constants with 3-methyltetrahydrofuran, (a) hydrogen shift from C5 in ROO3t (b) hydrogen shift from C2 and C5 in ROO3t (c) hydrogen shift from C5 in ROO4c. Solid and dashed lines denote 2-methyltetrahydrofuran and 3-methyltetrahydrofuran respectively.

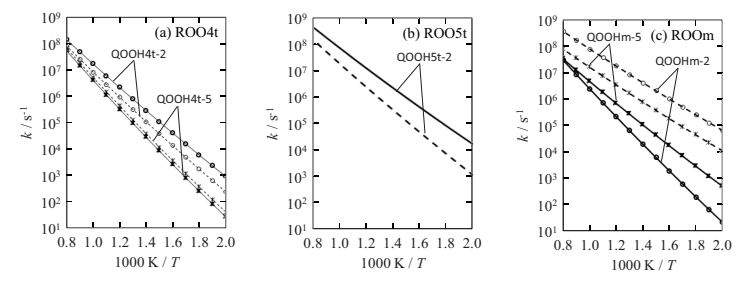


Figure 33. Comparison of 2-methyltetrahydrofuran rate constants with 3-methyltetrahydrofuran, (a) hydrogen shift from C2 and C5 in ROO4t (b) hydrogen shift from C2 in ROO5t (c) hydrogen shift from C2 and C5 in ROOm. Solid and dashed lines denote 2-methyltetrahydrofuran and 3-methytetrahydrofuran respectively.

For QOOHm-5 reaction, seven membered ring transition states are seen in both 2-MTHF and 3-MTHF, however, the reaction energy in 3-MTHF is 15 kJ mol⁻¹ lower than 2-MTHF indicating a higher rate constant as shown in Figure 33c. At 500 K, computed rate constants

in 3-MTHF and 2-MTHF for the isomerization reactions involving hydrogen from the C5 site are 1.2×10^4 s⁻¹ and 5.7×10^2 s⁻¹ differing by a factor of 22.

To summarize: the detailed theoretical study is performed on one of the important low temperature reaction class: ROO to QOOH in 2-MTHF oxidation. It has been noticed that the strength of the C-H bond (involved in the H-shift reaction) affects the kinetics of these isomerization reactions Lowest C-H BDEs were found at the C2 site (382 kJ mol⁻¹) while Cm-H (424 kJ mol⁻¹) depicts highest BDE among all the C-H bonds in 2-MTHF. Isomerization reactions proceeding via five and six membered transition state ring sizes are highly favorable and associated with the lowest reaction barriers. The comparison between the total rate constants computed for all ROO isomers of 2-MTHF with constants in mcyc5 highlights significantly faster total rate constants for the isomerization reactions in ROO2 and ROO5t isomers of 2-MTHF than ROO3c, ROO3t, ROO4c, ROO4t, ROO5c and ROOm isomers. The main reason is attributed to the weaker C2-H and C5-H5 bond strengths in 2-MTHF as compared to that in mcyc5. Further, comparison of individual rate constants for the isomerization reactions from C2 and C5 sites in ROO isomers of 2-MTHF with those of 3-MTHF indicates significant differences between two reactants which are due to lower C2-H2 BDE in 2-MTHF and also due to the ring sizes of the transition states involved in isomerization reactions.

IV. 4 Theoretical Study on 2-Butanone Combustion Reactions

The potential of 2-butanone (2-BT) as a fuel for the spark ignition engine has been investigated by Hoppe et al. [17]. Their work highlighted theoretical assessment and experimental investigation in both a rapid compression machine and in a single cylinder research engine. The Negative Temperature Coefficient (NTC) is not found for 2-BT which is an indication of its knock resistance behavior. Compared to ethanol, 2-BT showed better primary breakup and cold start ability, improved combustion stability and lower hydrocarbon emission and oil dilution in the catalyst-heating-load point. Overall, 2-BT serves as a prototype of tailor—made biofuels and showed superior performance than ethanol.

Several studies are performed to understand detailed reaction kinetics of the elementary reactions undergoing in 2-BT combustion. In a work of Zhou et al. [101], a theoretical study has been performed to investigate the reaction kinetics for the hydrogen abstraction reactions by OH radical from three ketones namely dimethyl, methylethyl and iso-propylmethyl ketone. The formations of pre- and post-reaction complexes were identified in some of these abstraction reaction channels. Tranter and Walker [102] experimentally presented the rate constants for H and OH attack on propanone, 2-butanone and pentan-3-one at 753 K, and further investigated the oxidation chemistry of the formed radicals. In another work, Badra et al. [103] performed a shock tube and laser absorption study of ignition delay time and OH reaction rates of two ketones, 2-BT and 3-buten-2-one. In their work, ignition delay measurements were conducted at two equivalence ratios (0.5 and 1.0) behind reflected shock waves. Also, the reaction rates of ketones with the OH radicals were measured at temperatures in the range 950-1530 K and pressures of 1.2-1.6 atm. In an experimental study of Lam et al. [104], high-temperature measurements of the reactions of OH with a series of ketones such as acetone, 2-BT, 3-pentanone and 2-pentanone were investigated behind the reflected shock waves over the temperature range of 870-1360 K and pressures of 1-2 atm. The values measured for the 2-BT + OH reaction in their work were found in close accord with the theoretical calculation from Zhou et al. [101]. In another work, Mendes et al. [105] performed ab-intio and chemical kinetic study of the reaction mechanisms of H-atom abstraction by the HO₂ radical on the series of ketones. High-pressure limit rate constants have been presented for these reactions using conventional transition state theory in the temperature range of 500-2000 K. In a more recent theoretical study, Kopp et al. [106] investigated reaction kinetics of the H-atom abstraction from 2-butanone by H and CH3 radicals and the subsequent unimolecular reactions.

However, till now no study can be found investigating reaction kinetics for the H-atom abstraction reactions from 2-BT by methylperoxy (CH₃OO) radical. H-atom abstraction by the CH₃OO radical from 2-BT is found to be important according to a recent chemical kinetic modelling on 2-BT by Burke et al. [107], which motivated to perform detailed theoretical investigation to compute rate constants for these reaction in 2-BT.

The electronic structure calculations involving geometry optimization, vibrational frequencies and single point energy computation of the reactants, transitions states (TSs) and products are performed at four different computational methods namely G3, G4, CBS-QB3 and at CCSD(T)/cc-pvtz//MP2/6-311G(d,p). Out of these four methods; G3, G4 and CBS-QB3 are composite methods while CCSD(T)/cc-pvtz//MP2/6-311G(d,p) involves geometry optimization and calculations of vibrational frequencies for a molecule at the MP2/6-311G(d,p) level and further a single point energy computation of the optimized geometry at the CCSD(T)/cc-pVTZ level. The computational steps involved in these methods are discussed in detail in Chapter II. The main highlight here is to analyze and compare rate constants obtained from these different methods for the H-atom abstraction reactions in 2-BT.

Mendes et al. [105] implemented CCSD(T)/cc-pVXZ method (X = D, T, Q) for analyzing reaction mechanism of dimethyl ketone + HO₂ radical and benchmarked this method against the computationally less expensive CCSD(T)/cc-pVTZ//MP2/6-311G(d,p) method. Considering their work and due to the similarity in the H-atom abstraction reactions involved herein, CCSD(T)/cc-pVTZ//MP2/6-311G(d,p) method is applied. Further, the results obtained from this method are compared with G3, G4 and CBS-QB3 composite methods to analyze which composite method shows a better agreement to the higher level method as stated above. Results such as reaction barriers, reaction energies as well as rate constant for the titled reaction are then compared at these methods. All the electronic structure calculations are performed with the help of Gaussian 09 package [26]. The optimized three-dimensional structures of reactants (2-BT and CH₃OO) with the labels are highlighted in Figure 34. The high-pressure limit rate constants for the H-atom abstraction reactions from the 2-BT by CH₃OO are determined with the help of GPOP program [59] employing conventional transition state theory [92]. Three abstraction sites from 2-BT are considered; abstraction of primary H bonded to the C1, secondary H bonded to the C3 and primary H attached to the C4. The detailed methodology and approach followed for computing rate constants is similar to the one implemented in section IV.2 and IV.3.

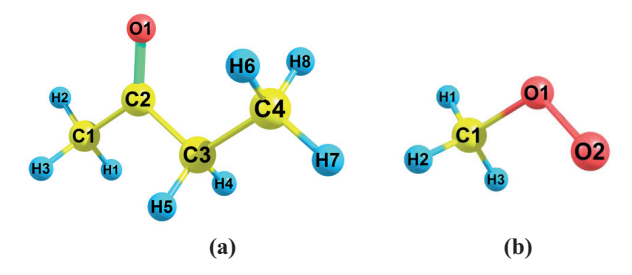


Figure 34. Optimized structure of (a) 2-butanone and (b) Methylperoxy radical with the labels used in this work.

For the hindered rotor analysis, the internal rotors in reactants, transition states and products are grouped according to the type of the rotation involved in each molecule. The torsional barriers V_0 are then obtained according to the Pitzer-Gwinn approximation [75, 76]. The potential energies for the internal rotations in reactants, TSs and products are obtained at the CBS-QB3 method. The estimated hindered rotor parameters for the internal rotors in reactants, TSs and products are summarized in Table 16. The hindered rotor analysis plots with the representative structures are provided in the Appendix (A78 –A96).

Table 16. Estimated Hindered Rotor Parameters in Pitzer-Gwinn Approximation for the H-atom abstraction reactions in 2-BT

bonding atom a	type of rotor	V_0^b / cm^{-1}	σ^{c}
H1 in the TS	CH ₃ OÒ	2400	1
H4 in the TS	$\mathrm{CH_3O}\dot{\mathrm{O}}$	1700	1
H6 in the TS	$\mathrm{CH_3O}\dot{\mathrm{O}}$	1000	1
radical centered C3	CH_3	150	3
C3 in product radical	${^\bullet\!\mathrm{CH}}_2$	2600	2
C2 in 2-BT	CH_3	1100	3
	$\mathrm{CH_{3}CH_{2}}$	140	1
C2 in product radical	CHCH_3	4500	2
C2 in the transition state	CH ₃ OOCH ₃	1700	1
C3 in 2-BT	CH_3	800	3
C3 in product radical	CH_3	150	3
	${^\bullet\!\mathrm{CH}}_2$	320	2
C3 in TS	$\mathrm{CH_{3}CO}$	4500	1
	CH_3	500	3

	CH ₃ OOCH ₃	2800	1
O in CH ₃ OO	CH ₃	320	3
O in CH ₃ OOH	CH ₃	1050	3
	ОН	1000	1
O in TS	CH ₃	1000	3
	OCH ₂	800	1

^aAbbreviations are referred in Figure 34(a). ^bThe height of the hindrance potential. ^cThe symmetry number of the internal rotation.

Furthermore, for the H-atom abstraction reaction, the strength of the C-H bond plays a vital role. For example, stronger the C-H bond in a molecule, difficult is its H-atom abstraction. Hence to get more insight, bond dissociation energies are determined for the C-H bonds in 2-BT.

i. C-H Bond Dissociation Energies

The Bond Dissociation Energies (BDEs) for the C-H bonds in 2-BT are computed at G3, G4, CBS-OB3 and CCSD(T)/cc-pvtz//MP2/6-311G(d,p) methods and are summarized in Table 17. Three different sites in 2-BT are chosen for BDEs computation; primary α -H (α to the carbonyl functional group), secondary α -H (α to the carbonyl functional group) and primary B-H (B to the carbonyl functional group). As seen in Table 17, lowest BDE is found for the C3-H4 bond, a secondary carbon site in 2-BT. The strength of the C-H bonds at alpha positions to the carbonyl functional group in 2-BT are significantly affected due to the hyperconjugation effect [96]. In 2-BT, product alkyl radicals formed after H-atom abstractions from C1 and C3 sites are stabilized due to electron delocalization while the C4 radical site is far away to take part in delocalization and hence is less stable, reflected by its C-H bond strength. For this reason, although both C1 and C4 are primary carbons sites in 2-BT, BDE for the C1-H1 bond (at G3, G4 and CBS-QB3 methods) is ~ 20-25 kJ mol⁻¹ lower than the C4-H6 bond. The strength of a C-H bond at this C4 site is observed to be similar to that of the primary site in alkanes [108]. The reported C-H BDE for the primary site in n-heptane is 425.88 kJ mol⁻¹[108], which is in close agreement with the G3 and CBS-QB3 computed values for the C4-H6 bond in 2-BT. However, at G4, computed BDE at the same site is ~ 10 kJ mol-1 lower than the above two methods whereas the value computed at CCSD(t)/ccpVTZ//MP2/6-311G(d,p) is deviating significantly and is ~ 30 kJ mol⁻¹ higher than in nheptane. This observation can be related to a recent study by Somers et. al [109] which highlighted G3 and CBS-OB3 methods over predict heat of formation while G4 under

predicts the same. Large variations in the computed BDEs values are observed at CCSD(t)/cc-pVTZ//MP2/6-311G(d,p) in comparison to the remaining three methods which arises due to the differences in the computed single point energy (SPE) at the corresponding method. The variations in computed SPE of the stationary points between the methods are discussed in the following sections.

Table 17. C-H Bond Dissociation Energies

Bond ^a			D ₀ / (kJ mol ⁻¹) 2-BT			
	G3	G4	CBS-QB3	CCSD(T)/cc-pVTZ//MP2/6-311G(d,p)		
C1-H1 (primary α)	399.36	394.27	399.28	436.14		
C3-H4 (secondary α)	378.31	372.96	371.51	416.12		
C4-H6 (primary β)	425.46	415.20	423.52	456.11		

^aAtom labels are given in Figure 34(a)

Further, in order to analyze the favorability of a specific H-atom abstraction reaction channel, reaction barriers and energies are determined and the obtained results are then compared to the four different computational methods stated before.

ii. Reaction Barriers and Energies

Reaction barriers (E_{θ}) and energies (ΔE) are computed for reactions (1), (2) and (3) in 2-BT at G3, G4, CBS-QB3 and CCSD(T)/cc-pvtz//MP2/6-311G(d,p) methods and are summarized in Table 18.

$$\mathsf{CH_3COCH_2CH_3} + \mathsf{CH_3O\dot{O}} \rightarrow \mathsf{CH_2COCH_2CH_3} + \mathsf{CH_3OOH} \qquad (1)$$

$$CH_3COCH_2CH_3 + CH_3O\dot{O} \rightarrow CH_3COCHCH_3 + CH_3OOH$$
 (2)

$$\mathsf{CH_3COCH_2CH_3} + \mathsf{CH_3O\dot{O}} \rightarrow \mathsf{CH_3COCH_2CH_2} + \mathsf{CH_3OOH} \tag{3}$$

At G3 and G4 composite methods, reaction barriers at the C3 (secondary) carbon site i.e. for reaction 2 are observed to be lowest with $E_0 = 58.48 \text{ kJ mol}^{-1}$ and 55.18 kJ mol⁻¹ respectively. Whereas CBS-QB3 method gave similar energy barriers for the H-atom abstraction reactions from C3 (51.66 kJ mol⁻¹) and C4 (51.77 kJ mol⁻¹) sites; reaction 2 and 3 respectively. The trend in E_0 observed at G3 method is C3-H4 < C4-H6 < C1-H1. Whereas G4 methods followed C3-H4 < C1-H1 < C4-H6 order. Comparing CBS-QB3 composite method, the variation is; C3-H4 ~ C4-H6 < C1-H1. Except for CCSD(T)/cc-pVTZ//MP2/6-311G(d,p) method, all the composite methods showed lowest energy barrier for the H-atom abstraction from the secondary carbon site (C3). At the CCSD(T)/cc-pVTZ//MP2/6-311G(d,p), E_0 are in

the order C4-H6 < C3-H4 < C1-H1. For the secondary H-atom abstraction from 2-BT, E_0 at this method is higher by ~15-23 kJ mol⁻¹ than the G3, G4 and CBS-QB3 calculated values.

Table 18. Reaction barriers and energies

Reactants	Products a	H atom ^b	Method	E_{θ} kJ mol ⁻¹	ΔE kJ mol ⁻¹
CH ₃ COCH ₂ CH ₃ + CH ₃ OȮ	CH ₂ COCH ₂ CH ₃ + CH ₃ OOH	H1	G3	86.83	46.63
			G4	66.17	42.43
			CBS-QB3	64.04	42.10
			CCSD(T)/cc-pVTZ//MP2/6-	85.14	56.00
			311G(d,p)		
CH ₃ COCH ₂ CH ₃ + CH ₃ OÓ	CH ₃ COCHCH ₃ + CH ₃ OOH	H4	G3	58.48	25.57
			G4	55.18	21.12
			CBS-QB3	51.66	20.33
			CCSD(T)/cc-pVTZ//MP2/6-	74.29	35.98
			311G(d,p)		
CH ₃ COCH ₂ CH ₃ + CH ₃ OO	CH ₃ COCH ₂ CH ₂ + CH ₃ OOH	Н6	G3	74.69	72.72
			G4	68.90	63.36
			CBS-QB3	51.77	66.34
			CCSD(T)/cc-pVTZ//MP2/6-	55.97	75.97
			311G(d,p)		

^aAtom labels are given in Figure 34(a)

From the above results and discussion, it is observed that depending on the computational method implemented for the geometry optimization and SPE calculation of the reactants and TSs, significant deviations are seen in the reaction barriers. The reason underlying these results may arise due to the differences in the optimized geometries at these four methods hence further analysis is carried out. On having a closer look at the optimized geometries of the reactants and TSs involved in the titled reactions, following observations are made. The breakings of C-H bonds (percentage of bond elongation) are analyzed at all the computational methods considered herein.

Table 19. Percentage of bond elongation in 2-BT

Bond^a		Perce	ntage of bond elongation 2-BT	on
	G3	G4	CBS-QB3	CCSD(T)/cc-pVTZ//MP2/6- 311G(d,p)
C1-H1 (primary α)	25.30	29.35	29.33	20.86
C3-H4 (secondary α)	23.78	24.37	24.19	17.29
C4-H6 (primary β)	24.78	30.17	29.76	17.20

^aAtom labels are given in Figure 34(a)

Table 19 highlights percentages of bond elongation during the H-atom abstraction reactions in 2-BT. The G4 and CBS-QB3 values showed good agreement with each other. This might result due to the use of the B3LYP functional for the geometry optimization in both the methods. The percentages of C-H bond elongation in TS at G4 and CBS-QB3 methods are 29%, 24% and 30% for H1, H4 and H6 abstraction respectively. However at the G3 method, percentages of C-H bond elongation are lowered by 4-6% for H1 and H6 in comparison to the aforementioned methods. At the MP2/6-311G(d,p) method, considerable differences are noted for the C-H bond elongation in the TSs. At this method, C-H bonds are elongated to a lesser extent than the above composite methods. The C1-H1 is elongated by 21% whereas C3-H4 and C4-H6 bonds are elongated by 17%. Further, on analyzing reaction energies (ΔE) for reactions (1), (2) and (3), well agreement is depicted between G4 and CBS-QB3 methods. ΔE for reactions (1) and (2) at the G3 method are observed to be ~ 4 kJ mol⁻¹ higher than G4 and CBS-QB3 methods, while for reaction (3) higher by ~ 10 kJ mol⁻¹. However, in the case of CCSD(T)/cc-pVTZ//MP2/6-311G(d,p) method, ΔE varies by ~ 12-17 kJ mol⁻¹ in comparison with the composite methods for all reactions of interest in 2-BT. On analyzing computed SPE for 2-BT at the CCSD(t)/cc-pVTZ//MP2/6-311G(d,p) and at the CBS-QB3 method; a difference of 82.58 kJ mol⁻¹ is observed while 45.74 kJ mol⁻¹ variation is seen for CH3OO radical. At the CCSD(t)/cc-pVTZ//MP2/6-311G(d,p) method, SPE of the optimized geometries is found to be lower than the CBS-QB3 method. These differences in the computed single point energies results in the variation of BDEs obtained employing former method. Also, T1 diagnostic [110] has been performed for the stationary points to judge the reliability of a coupled cluster calculations. If the value of T1 diagnostic is below 0.03 then a coupled cluster results are reliable. For the calculations involved herein, observed T1

diagnostic value is below 0.03 in all cases which is an indication of no multi-reference character.

Further, high pressure limit rate constant are computed for reactions (1), (2) and (3) at all four methods. Details of which are discussed in the following section.

iii. High Pressure Limit Rate Constants

High pressure rate constants for the H-atom abstraction reactions from 2-BT are computed at G3, G4, CBS-QB3 and CCSD(T)/cc-pVTZtz//MP2/6-311G(d,p) methods. The Arrhenius parameters for the H-atom abstraction reactions are determined by fitting the calculated rate to the modified Arrhenius expression which is given as; $k = AT^n \exp(-Ea/(RT))$, in the temperature range 500-2000 K. Computed Arrhenius rate parameters for these reactions are provided in Table 20. Figure 35 summarizes comparison of high pressure limit rate constants obtained by different computational methods.

In Figure 35, the primary α -H indicates H-atom abstraction from C1; the secondary α -H is from C3 while the primary β -H is from C4 sites in 2-BT (Figure 34a). At G3 method (Figure 35a), abstraction of secondary α -H is the most favorable over an entire temperature regime of investigation (500-2000 K), followed by primary β -H and primary α -H. Although the rate constants for the primary α -H and primary β -H are inconsistent with the computed BDEs at the G3 method, it is observed to follow exactly the same trend as depicted for its E_0 (Table 18).

Table 20. High-Pressure Limit Rate Constants for the H-atom abstraction reactions in 2-BT

Reactants	abstracted H-atom ^a	products	Method	rate constant		
reactants	aostracted 11-atom		Moniou	A	n	E/R
CH ₃ COCH ₂ CH ₃ + CH ₃ OO	H1	CH ₂ COCH ₂ CH ₃ + CH ₃ OOH	G3	2.58E-34	6.533	5735
			G4	3.71E-29	5.091	6252
			CBS-QB3	6.90E-29	5.056	6013
			CCSD(T)/cc-pVTZ//MP2/6- 311G(d,p)	1.31E-29	5.139	8046
CH ₃ COCH ₂ CH ₃ + CH ₃ OO	H4	CH ₃ COCHCH ₃ + CH ₃ OOH	G3	3.39E-31	5.525	3141
			G4	1.68E-28	4.760	4701
			CBS-QB3	2.08E-28	4.720	4309
			CCSD(T)/cc-pVTZ//MP2/6- 311G(d,p)	7.90E-29	4.778	6645

CH ₃ COCH ₂ CH ₃ + CH ₃ OÖ	Н6	CH ₃ COCH ₂ CH ₂ + CH ₃ OOH	G3	5.06E-25	4.193	8220
			G4	2.26E-25	4.309	7206
			CBS-QB3	8.96E-26	4.228	7462
			CCSD(T)/cc-pVTZ//MP2/6-	1.35E-25	4.350	8809
			311G(d,p)	1.55E-25	4.550	8809

^aAtom labels are given in Figure 34. ^bRate constants are given by the Arrhenius expression, k (cm³ molecule¹ s¹) = $AT^n \exp(-E/RT)$.

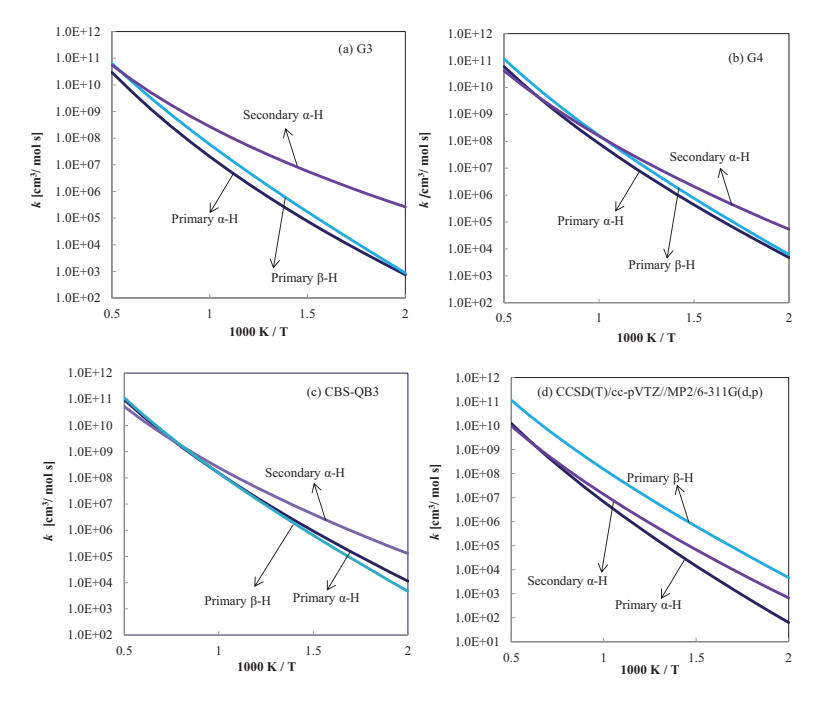


Figure 35. High pressure limit rate constants for the H-atom abstraction reactions from 2-BT computed at (a) G3, (b) G4, (c) CBS-QB3 and (d) CCSD(t)/CC-PVTZ/MP2/6-311G(d,p) methods.

The rate constant for the H-atom abstraction from the secondary carbon site is seen to be feasible at G3 (Figure 35a), G4 (Figure 35b) and also at CBS-QB3 (Figure 35c) methods. These results are also observed to be in close agreement with the computed reaction barriers (E_0) and with the C-H BDEs values determined at the respective methods. At the CBS-QB3 method, at higher temperatures (above 1250 K) H-abstraction from both the primary carbon sites in 2-BT is analogous to each other while below 700 K a factor of 2 discripancy is noticed. However, results obtained at the CCSD(T)/cc-pVTZ//MP2/6-311G(d,p) method are

contradicting with that computed using composite methods in some cases. As seen in Figure 35d, abstraction of H-atom from the primary carbon site (H6) which is at the beta position to the carbonyl functional group in 2-BT is highly favored. On comparing this H6 abstraction rate constant with that obtained at G4 and CBS-QB3, the good agreement is obtained between these methods as depicted in Figure 36c. However below 600 K, the rate constant determined by the G3 method is observed to be slower by a factor of 5 than that calculated at the CCSD(T)/cc-pVTZ//MP2/6-311G(d,p) method. Figure 36a, 36b and 36c indicate comparison of H1, H4 and H6 abstraction rate constants obtained from all four computational methods of interest herein. From this comparison, it can be seen that abstraction of H-atom further from the carbonyl functional group in 2-BT is less influenced by the level of theories implemented. However, deviations are observed for the H-atom abstraction at the alpha position to the carbonyl group. For the H1 abstraction, rate constant determined at the CBS-QB3 and G4 methods varies within a factor of 2.4 - 1.6 over 500 to 2000 K. Below 600 K, H1 abstraction rate constant calculated at G3 differs by an order of magnitude than the CBS-OB3 value. The large discrepancy is noticed between the CCSD(T)/cc-pVTZ//MP2/6-311G(d,p) and CBS-QB3 values. Below 600 K ~ 2 order of magnitude is perceived as shown in Figure 36a. Further, analyzing H4 abstraction reactions, it is noticed that at a temperature above 900 K; G3, G4 and CBS-QB3 methods showed good agreement with each other while a maximum of a factor of 5 deviations are seen between G3, G4 and CBS-QB3 in the lower temperature regime. Only the rate constant from CCSD(T)/cc-pVTZ//MP2/6-311G(d,p) method showed significant variation in comparison with the other composite methods. For the H4 abstraction, computed rate constant at CCSD(T)/cc-pVTZ//MP2/6-311G(d,p) is a factor of 4 slower at 2000 K which tends to differ by ~ a factor of 80 slower than that determined at G4 method. Overall, it is seen that for H-atom abstraction sites neighboring carbonyl group in 2-BT, rate constant is found to be slower than the composite methods. Although these trends in the rate constants for H1 and H6 abstraction are contradicting with the results obtained from the composite methods, the observed trend is found to be consistent with computed E_{θ} (Table 18) obtained at the CCSD(T)/cc-pVTZ/MP2/6-311G(d,p). The evaluated values of E_{θ} are further related to the calculated single point energies of the reactants and transition states at the respective method as discussed in the earlier section. These variations in the computed rate constant at different methods might result from the difference in the single point energies of the stationary points as highlighted in reaction barriers and energy section.

To analyze these observed deviations in more detail, the H4 abstraction site (neighboring carbonyl group) is considered for a case study. Furthermore, the rate constant for H4 abstraction is determined at the CCSD(T)/cc-pVTZ//B3LYP/CBSB7 method and compared with the rate constant obtained at the CCSD(T)/cc-pVTZ//MP2/6-311G(d,p) method. The former method involves geometry optimization and computation of vibrational frequencies at the B3LYP/CBSB7 level and SPE determination at the CCSD(T)/cc-pVTZ level. Whereas, the later method optimizes the geometry of the molecule and computes vibrational frequencies at the MP2/6-311G(d,p) level with SPE computation at the CCSD(T)/cc-pVTZ level. The only difference in these two methods underlies in the steps involved in the geometry optimization and vibrational frequency calculations.

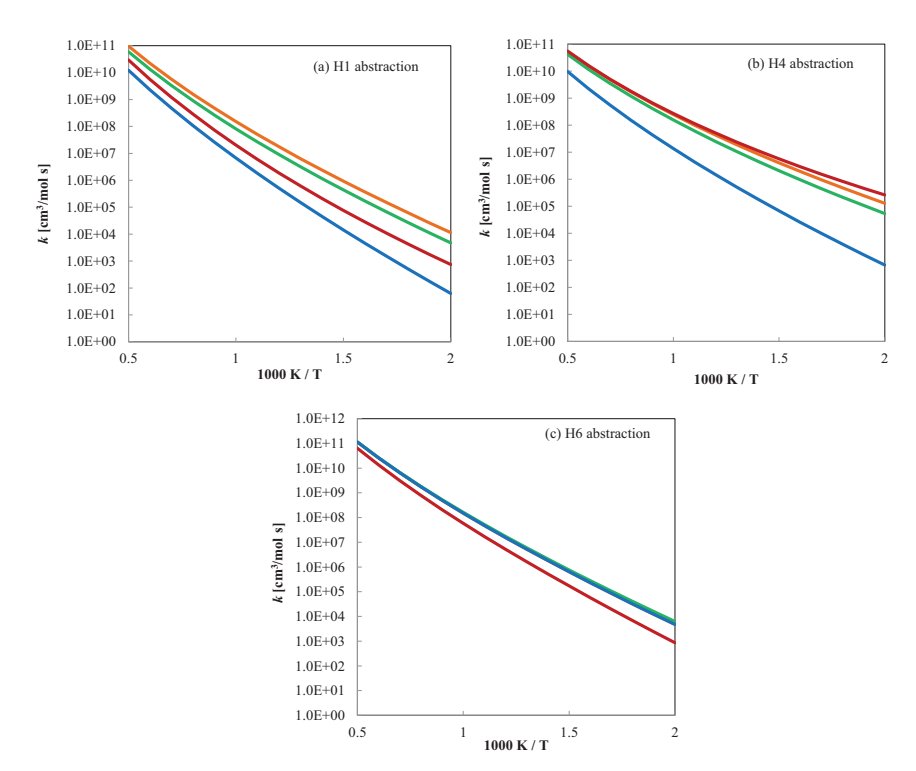


Figure 36. High pressure limit rate constants comparison for the H-atom abstraction reactions from 2-butanone at (—) G3, (—) G4, (—) CBS-QB3 and (—) CCSD(T)/CC-PVTZ//MP2/6-311G(d,p) methods for (a) H1 abstraction, (b) H4 abstraction, (c) H6 abstraction; atom labels are given in Figure 34.

Herein, B3LYP/CBSB7 level is chosen for comparison since it is a default method implemented in the CBS-QB3 composite method for the geometry optimization and the vibrational frequency calculations which will aid a better comparison between the CBS-OB3 method. It was noticed that the calculated rate constants between CCSD(T)/ccpVTZ//B3LYP/CBSB7 and CCSD(T)/cc-pVTZ//MP2/6-311G(d,p) differs by less than a factor of two over the entire temperature regime of the investigation. Further, for the H4 abstraction case, reaction barriers are determined at CCSD(T)/cc-pVTZ//B3LYP/CBSB7 and CCSD(T)/cc-pVTZ//MP2/6-311G(d,p) methods to see if the difference in the optimized geometries has any effect on the computed SPE. The value of E_0 at the former method is 73.68 kJ mol⁻¹ while later gave 74.29 kJ mol⁻¹, deviating by less than 1 kJ mol⁻¹. Hence it can be attributed that the method implemented for the geometry optimization has a minor effect on the computed SPE. Further on comparing this E_0 with that obtained from the composite CBS-QB3 method which is 51.66 kJ mol⁻¹, a difference of ~ 23 kJ mol⁻¹ is observed. The CBS-OB3 method computed lower SPE than CCSD(T)/cc-pVTZ//B3LYP/CBSB7 and CCSD(T)/cc-pVTZ//MP2/6-311G(d,p) methods. Hence at the CBS-OB3 method, this difference in E_{θ} might have resulted in a faster rate constant for the H4 abstraction than that determined at CCSD(T)/cc-pVTZ//MP2/6-311G(d,p) (Figure 36b). From this analysis, it appears that the deviations in the computed rate constants especially at sites neighboring to the carbonyl group arise mainly due to a difference in SPEs obtained within composite methods. Further, the effect of basis set on the computed SPEs for the H4 abstraction sites in 2-BT is analyzed. For this analysis, CCSD(T)/cc-pVDZ//MP2/6-311G(d,p) and CCSD(T)/aug-cc-pVDZ//MP2/6-311G(d,p) methods are considered. In the aforementioned methods, the basis set used for the computation of SPE differs i.e. cc-pVDZ in former while aug-cc-pVDZ in latter. On comparing computed E_0 from these methods, a difference of ~ 12 kJ mol⁻¹ is observed. E_0 obtained at CCSD(T)/cc-pVDZ//MP2/6-311G(d,p) and CCSD(T)/aug-cc-pVDZ//MP2/6-311G(d,p) methods are 77.78 kJ mol⁻¹ and 65.48 kJ mol⁻¹ respectively. From this results it appears that the coupled cluster method with the basis set implemented herein i.e. CCSD(T)/cc-pVTZ/MP2/6-311G(d,p) performs poorly for this reaction system. Instead the results obtained from the G4 method are reliable as it is the most recent composite method of Gn series and will be helpful in the development of detailed chemical kinetic models. Moreover, further computations can be performed to analyze the effects of basis set in more detail but currently limited herein.

Overall, the detailed theoretical analysis is performed for computing high pressure limit rate constants for the H-atom abstraction reactions from 2-Butanone (2-BT) by methylperoxy

radical (CH3OÓ). These reactions are studied at three different abstractions sites in 2-BT by employing four different computational methods namely G3, G4, CBS-QB3 and CCSD(t)/cc-pVTZ//MP2/6-311G(d,p) methods. Among this, the latter method gave significantly different results for the BDEs, reaction barriers (E_0), reaction energies (ΔE) and also high pressure limit rate constants especially at sites neighboring carbonyl functional group. The main reason seen for this observation arises due to the difference in the computed SPE at the methods considered herein. Further, this difference is seen to appear in E_0 , ultimately affecting the high pressure limit rate constants at the respective sites. The effect is observed to be pronounced for the reactions involving H-atom abstraction from the site neighboring carbonyl functional group in 2-BT. It has been observed that, at G3, G4 and CBS-QB3 composite methods, abstraction of H-atom from the secondary carbon site (neighboring carbonyl functional group) is favored.

IV.5 Reaction Kinetics and Thermochemistry of the Smallest Ketone: Acetone

The smallest member of the ketone family is the acetone, also known as dimethylketone. Acetone is not a biofuel candidate however of highlight herein since the detailed study of its combustion kinetics will assist in getting insight into the oxidation behavior of higher ketone molecules. Furthermore, acetone has been widely used as a fuel tracer in Laser Induced Fluorescence (LIF) imaging [111]. This technique finds its application in combustion research area for monitoring fuel behavior in terms of its distribution, concentration and temperature. However, not much is known about acetone's chemical behavior in the hot oxidizing environment and hence its effective lifetime as a tracer in combustion conditions [111]. Acetone and higher ketones are also important in atmospheric chemistry [112, 113] since they are formed by the atmospheric oxidation of hydrocarbons [114]. It has also been found as the most abundant oxygenated organic species in the upper troposphere [115].

Focusing on acetone combustion, its favorable reactions includes H-atom abstraction reaction from the fuel by species such as OH, H, HO2, O2 etc. which gives rise to acetonyl (CH₃COCH₂) radical. Most of these H-atom abstraction reactions have been investigated both experimentally as well as theoretically [101, 102, 116-120] and are not in the focus of this study. However, fundamental quantum mechanical studies on subsequent reactions in acetone are scarce. Figure 37 highlights overview of acetone reactions analyzed herein. As seen in Figure 37, the acetonyl radical formed after the H-atom abstraction from acetone can undergo beta-scission to give methyl radical and ketene (CH₂CO). It can also react with O₂ to form acetonylperoxy radicals (CH₃COCH₂OO). Further, isomerization reactions of CH₃COCH₂OO radical form corresponding hydroperoxyalkyl radical (QOOH) species. These isomerization reactions can occur via 1,3 or 1,5 H-shifts as depicted in Figure 37. El-Nahas et. al. [121, 122] determined thermochemical and kinetic parameters of the isomerization and decomposition reactions of the acetonylperoxy radical at the CBS-QB3 level. Their findings revealed formation of the primary acetonylhydroperoxy radical as a main reaction channel in isomerization reactions. In their study CBS-QB3 composite method is considered whereas herein higher levels of theories are implemented for better results. The details about the computational methods are given in the following sections.

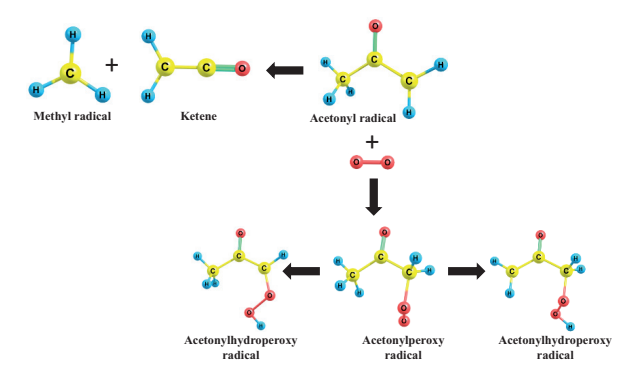


Figure 37. Acetone reaction scheme

This study is focused on the acetone combustion phenomena especially highlighting the reactions taking place in the lower temperature regime. The detailed computational calculations have been performed to determine thermodynamic properties of species (shown in Figure 38) formed during acetone combustion. Further, high pressure limit rate constant is presented for the addition of methyl radical to ketene which leads to the formation of acetonyl radical. For the reaction of O₂ with acetonyl radical, pressure dependent rates are computed by applying ORRK theory as implemented in ChemDis code [123, 124]. Furthermore, the rate constants are computed for the 1,3 and 1,5 H-shifts reactions in acetonylperoxy radical. The M062X computational method [125] with the 6-311++G(d,p) basis set is considered for the geometry optimization and frequency calculations of the species by using Gaussian 09 package [26]. The potential energy surface scans are performed for the internal rotations in the reactants and the transition states at the aforementioned method (Figures A98-A101 in Appendix). Next, single point energy is calculated at the CCSD(T)/cc-pVXZ level of theory (where X = T and Q) which are then extrapolated to the complete basis set (CBS) limit [126, 127]. The T1 diagnostic (as mentioned in Chapter IV.4) at CCSD(T) method for the saddle point in reactant and transition states are found to be less than 0.02 critical value, indicating that the single-reference method is good enough for the appropriate description of the wave function [110].

i. Thermochemistry

For computing thermodynamic properties such as standard enthalpy of formation ($\Delta_t H_{298}$), standard entropy (S_{298}) and heat capacities at constant pressure (C_p), four compound methods have been chosen. It includes calculations at CBS-QB3, CBS-APNO, G3 and G4 composite

methods. The reason behind choosing different composite methods is to provide better accuracy by combinations of the above mentioned methods as recommended by Sommers et al. [128]. Their work benchmarked various composite methods for computing the formation enthalpies of the radicals against the active thermochemical tables. The accuracy of each method has been interpreted in terms of mean-unsigned error (absolute) and mean-signed (average) errors and also provided practical recommendations for computing formation enthalpies of the closed shell and radical species. The optimized three dimensional structures of the acetone species for computing thermodynamic properties are highlighted in Figure 38.

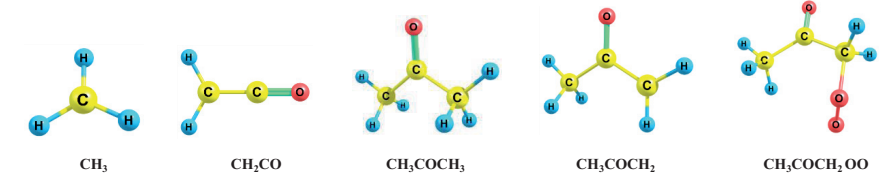


Figure 38. Optimized structures of species of interest for computing thermodynamic properties

The thermodynamic properties of species (Figure 38) are obtained from the Thermo module of MultiWell program [129]. The standard enthalpy of formation ($\Delta_f H^2_{298}$) is determined by the atomization method. Table containing computed $\Delta_f H_{298}$, S^2_{298} and C_p for temperatures between 300 and 2500 K at CBS-QB3, G3, G4 and CBS-APNO methods is provided in the Appendix (Table A6).

Table 21. Standard enthalpies of formation ($\Delta_f H^2_{298}$)

Species				$\Delta_{ m l} \mathring{H}^{^{\circ}}_{298}$ /	kJ mol ⁻¹		
Species	CBS-QB3	G3	G4	CBS-APNO	CBS-APNO/G4/G3 ^a	G4/G3 ^a	Experimental
ĊH ₃	151.05	144.72	147.04	146.61	146.12	145.88	145.69 ^b
CH ₂ CO	-50.42	-52.35	-50.34	-52.44	-51.71	-51.34	$\text{-}48 \pm 2^c$
CH ₃ COCH ₃	-214.14	-215.12	-213.53	-221.55	-216.73	-214.32	$\text{-}218 \pm 0.59^{d}$
$CH_3CO\dot{C}H_2$	-31.94	-32.57	-34.70	-37.96	-35.08	-33.64	34.6 ± 8.4^e
CH3COCH2OO	-137.73	-132.61	-135.80	-139.67	-136.03	-134.21	-

^aAverage formation enthalpies ($\Delta_f H_{298}$) of species from CBS-APNO/G4/G3 and G4/G3 composite methods as recommended by Sommers et al [128], ^b[130], ^c[131], ^d[132], ^e[133].

Table 21 provides computed formation enthalpies at the composite methods and computed average formation enthalpies as recommended by Somers et al [128]. Comparing G4 method

with a commonly used CBS-QB3 method, the latter over predicts $\Delta_f H_{298}$ by $\sim 2-4$ kJ mol⁻¹ for the $\dot{C}H_3$, $CH_3CO\dot{C}H_2$ while under predicts for $CH_3COCH_2O\dot{O}$ by ~ 2 kJ mol⁻¹ as seen in Table 21. However these deviations are within the uncertainty limit predicted by the CBS-QB3 method [38, 39]. For the S_{298}° and C_{p} values, well agreement was depicted between both methods (Table A6 in Appendix). On comparing formation enthalpies obtained at the G4 with the G3 method, the latter under predicts by ~ 2 kJ mol⁻¹ for CH₃, CH₂CO and CH₃COCH₃ while over predicts for CH₃COCH₂ and CH₃COCH₂OO by ~ 2-3 kJ mol⁻¹. Overall these values are also within the chemical accuracy. Further, average formation enthalpies of species are determined by considering the average from three composite methods namely CBS-APNO, G4 and G3. Sommers et al. [128] recommended these combinations if three methods are used while G4 and G3 are suggested if average from two methods are to be considered. The computed average formation enthalpies of the species at CBS-APNO/G4/G3 (Table 21) are in good agreement with values obtained from the NIST database. The experimentally determined $\Delta_f H^2_{298}$ for $\dot{C}H_3$, CH_2CO and CH_3COCH_3 are 145.69 kJ mol⁻¹ [130], -48 \pm 2 kJ mol⁻¹ [131] and -218.5 \pm 0.59 kJ mol⁻¹ [132] respectively which are in well agreement with the average formation enthalpies determined herein. Only for the CH₃COCH₃ the difference of ~ 4 kJ mol⁻¹ (within a chemical accuracy) is noticed between the literature and the average G4/G3 value. For the CH3COCH2, the experimental $\Delta_f H_{298}$ is 34.6 ± 8.4 kJ mol⁻¹ [133]. In their study, $\Delta_f H_{298}$ is obtained from the gas-phase basicities and proton affinities of radicals which are determined by mass spectrometry. This value for CH₃COCH₂, also shows a good agreement with the average formation enthalpies given in Table 21.

Further to give an idea about the strengths of the C-C and C-H bonds in acetone, bond dissociation enthalpies are determined.

ii. Bond Dissociation Enthalpies

The C-C bond cleavage in acetone results in the formation of a methyl and CH₃CO radicals. The computed value for the C-C bond dissociation enthalpy (BDE) in acetone at G4 method is 349 kJ mol⁻¹. The values computed for the same bond cleavage at the G3, CBS-QB3 and CBS-APNO methods are 350 kJ mol⁻¹, 356 kJ mol⁻¹ and 354 kJ mol⁻¹ respectively as shown in Table 22.

Table 22. Bond dissociation enthalpies

	D_0^a/kJ	mol ⁻¹
Method	С-С	С-Н
CBS-QB3	356	404
G3	350	404
G4	349	401
CBS-APNO	354	405

^aBond dissociation enthalpies (298.15 K) for the C-C and C-H bonds in acetone.

Further, calculated C-H BDE at G4 method is 401 kJ mol⁻¹. The values for the C-H bonds are also determined at the G3, CBS-QB3 and at the CBS-APNO methods (Table 22). G3 and CBS-QB3 methods gave 404 kJ mol⁻¹ while CBS-APNO showed 405 kJ mol⁻¹. Hence, in general the values obtained by G3, CBS-OB3 and CBS-APNO composite methods are ~ 4-5 kJ mol⁻¹ higher than that determined by the G4 method (within the chemical accuracy of the methods). This C-H bond strength in acetone is compared with the C-H BDE at the primary carbon site, adjacent to the carbonyl functional group in higher ketones. The reported value [134] for a similar site in 2-butanone and 2-pentanone is 400 kJ mol⁻¹, agrees well with the acetone. Further, on comparing this value with primary C-H bond strengths in ethane, npropane and n-butane [77, 135, 136] which are in the range of 420-423 kJ mol⁻¹, the C-H BDE in ketones at the carbon site neighboring the carbonyl group are lowered. This is due to resonance with the carbonyl functional group present in ketones. In general, the strength of C-H bond in species can be correlated to the stability of the product radical that is formed after the C-H bond cleavage. In the case of the primary C-H bond (adjacent to the carbonyl group) in ketones, the product radical formed after the H-atom abstraction is more stable due to its resonance with the carbonyl group and hence low C-H BDE.

Additionally, reaction barriers and reaction energies are computed for the reactions of interest in the acetone combustion, details of which are given in the following section.

iii. Reaction barriers and Energies

As stated earlier, M062X computational method with the 6-311++G(d,p) basis set is implemented for the geometry optimization and frequency calculations of the species. To achieve more reliable energies, single point energy of the species involved in the beta scission, O_2 addition and isomerization reactions are calculated at the CCSD(T)/cc-pVXZ level of theory (where X = T and Q) which are then extrapolated to the complete basis set

(CBS) limit. The CBS extrapolation equation by the CCSD(T) method and cc-pVXZ basis sets as provided by Peterson et al. [137] is considered here. As mentioned before, the beta scission reaction has been studied as a reverse of addition reaction to calculate high pressure limit rate constant. Computed reaction barrier and reaction energy for the addition of methyl radical to ketene are found to be 47 kJ mol⁻¹ and -121 kJ mol⁻¹ respectively.

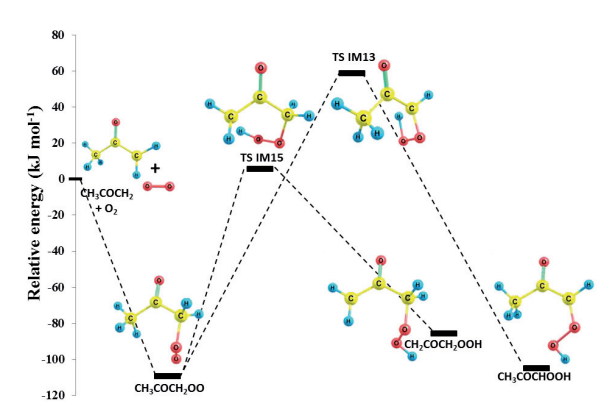


Figure 39. Potential energy diagram for the O₂ addition and isomerization reactions in acetone.

Furthermore, O2 molecule can undergo addition to the acetonyl radical to form acetonylperoxy radical. The addition of O₂ to the acetonyl radical is a barrier-less reaction and exothermic in nature with the well depth calculated at the CCSD(T)/CBS// M062X/6-311++G(d,p) method is -109.45 kJ mol⁻¹ as depicted in Figure 39. Considering alkanes, the reported well depth [138] for the n-propylperoxy species formed via a reaction of n-propyl + O₂ is -139.33 kJ mol⁻¹. Comparing these two well depths indicates higher stability of npropylperoxy radical than the acetonylperoxy radical. For the isomerization reactions of acetonylperoxy radical, to form corresponding hydroperoxyalkyl species the reaction barriers and reaction energies are as follows. The acetonylperoxy species can isomerize via 1,5-H shift or 1,3-H shift reaction channels. The former reaction proceeds via a six membered ring transition state whereas later through less favorable four membered ring transition state. The TS structures for these isomerization reactions are shown in Figure 40. The reaction barriers at the CCSDT/CBS// M062X/6-311++G(d,p) method for 1,5 isomerization is found to be 115.9 kJ mol⁻¹ while 168.2 kJ mol⁻¹ for the 1,3 isomerization channel. Computed reaction energies are 37.5 kJ mol⁻¹ and 19.7 kJ mol⁻¹ respectively for the 1,5 and 1,3 isomerization channels respectively. On comparing 1,5 isomerization reactions in n-propylperoxy species with that in acetonylperoxy, barrier height for the former species is 12 kJ mol⁻¹ higher.

Further, 1,3 isomerization channel in acetonylperoxy species is 30 kJ mol⁻¹ higher than in n-propylperoxy radical [138].

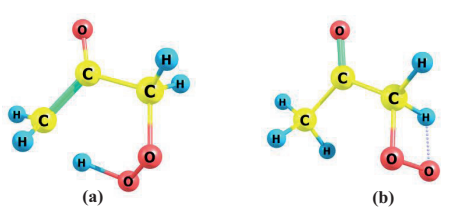


Figure 40. Optimized structures of the TS involved in the isomerization reactions (a) 1,5 isomerization TS (b) 1,3 isomerization TS.

iv. Rate Constants

The high pressure limit rate constant is determined for the addition of methyl radical to the ketene and also for the isomerization reactions of the acetonylperoxy radical to the corresponding QOOH species. The corresponding Arrhenius parameters for these reactions are summarized in Table 23. The three dimensional optimized structure of ketene (CH₂CO) is shown in Figure 37. As stated earlier, the addition reaction between methyl radical and ketene is a reverse of the beta scission reaction of the acetonyl radical. Having a look on the isomerization reactions of the acetonylperoxy radical, two reaction channels are considered for determining high pressure limit rate constants (Figure 37). The optimized four and six membered ring TSs involved in the isomerization reactions are shown in Figure 40. For computing high-pressure limit rate constants, conventional transition state theory [139] with asymmetric Eckart tunneling correction [63] has been used. The low-frequency torsional modes in reactants and transition states are considered as hindered rotors using a Pitzer-Gwinn-like approximation [75, 76]. Relaxed potential energy surface scans have been performed by scanning dihedral angle within a molecule from $0-360^{\circ}$ in steps of 10° (Figure A98 - A101 in Appendix). The calculated high pressure limit rate constant for the methyl radical + ketene reaction at the CCSD(T)/CBS//MO62X/6-311++G(d,p) is, k (cm³mol⁻¹s⁻¹) = $7.26 \times 10^3 T^{2.43} e^{-37.49/RT}$. The high pressure limit rate constant for the beta scission reaction, k $(s^{-1}) = 1.00 \times 10^{13} T^0 e^{-117/RT}$ is then obtained by considering the reverse of reaction $\dot{C}H_3$ + CH₂CO. For the isomerization reaction occurring via six and four membered ring TS, computed rate constants are k (s⁻¹) = 2.79 × 10¹³ $T^{0.75}$ e^{-225.52/RT} and 7.61 × 10¹³ $T^{0.59}$ e^{-277.82/RT} respectively. The rate constant for the 1,5 isomerization reaction is dominant compared to the 1,3 isomerization due to highly favorable six membered ring formation.

Table 23. High Preesure Limit Rate Constants

Reactions ^a	A^b	n^b	E^{b}
$\dot{\mathrm{CH}}_{3} + \mathrm{CH}_{2}\mathrm{CO} \rightarrow \mathrm{CH}_{3}\mathrm{COCH}_{2}$	7.26×10^{3}	2.43	37.49
1,5 isomerization	2.79×10^{13}	-0.75	225.52
1,3 isomerization	7.61×10^{13}	-0.59	277.82

^aReaction are highlighted in Figure 37. ^bModified Arrhenius expression, $k = AT^n$ exp (-E/(RT)) is used to represent Arrhenius parameters.

The pressure dependent rate constants for the reaction of O_2 with the acetonyl radical (CH₃COCH₂) are investigated by employing Quantum Rice-Ramsperger-Kassel (QRRK) theory with the help of ChemDis [140, 141]. ChemDis is a Fortran based code with a Modified Strong Collision (MSC) approach for the Collisional Energy Transfer (CET) for the reaction systems with arbitrary numbers of wells and product channels. Figure 41 highlights pressure dependent rate constant for the addition of O_2 to the acetonyl radical (CH₃COCH₂). For computing pressure dependent rate constants by the QRRK theory, following reaction have been considered.

1.
$$CH_3CO\dot{C}H_2 + O_2 \leftrightarrow CH_3COCH_2O\dot{O}$$
. (R+O₂ \leftrightarrow RO2).

This reaction involves the addition of O_2 to the acetonyl radical leading to the formation of acetonylperoxy radical.

2.
$$CH_3CO\dot{C}H_2 + O_2 \rightarrow CH_2CO\dot{C}H_2OOH. (R+O_2 \rightarrow IM15)$$

The energetically excited adduct, RO2 formed in the above reaction can directly isomerize to $\dot{C}H_2COCH_2OOH$. This reaction occurs via formation of a six membered cyclic ring TS.

3.
$$CH_3CO\dot{C}H_2 + O_2 \rightarrow CH_3CO\dot{C}HOOH. (R+O_2 \rightarrow IM13)$$

This reaction is similar to the reaction 2 mentioned above, however in this case isomerization reaction occurs via formation of a four membered cyclic ring TS.

4.
$$CH_3COCH_2O\dot{O} \rightarrow \dot{C}H_2COCH_2OOH. (RO_2 \rightarrow IM15)$$

The stabilized adduct, RO2 formed in reaction 1 can undergo isomerization to form ĊH₂COCH₂OOH via a six membered cyclic ring TS.

5.
$$CH_3COCH_2O\dot{O} \rightarrow CH_3CO\dot{C}HOOH. (RO_2 \rightarrow IM13)$$

This isomerization reaction is similar to the one mentioned in reaction 4, however in this reaction isomerization occurs via a four membered cyclic ring TS.

The results of the QRRK calculations for the $O_2 + CH_3CO\dot{C}H_2$ are summarized in Figure 41. For simplicity the discussions are limited to the results determined at 1 atm (Figure 41). The

plots of rate constant at other pressures (0.01 and 10 atm) are provided in the Appendix (Figure A97).

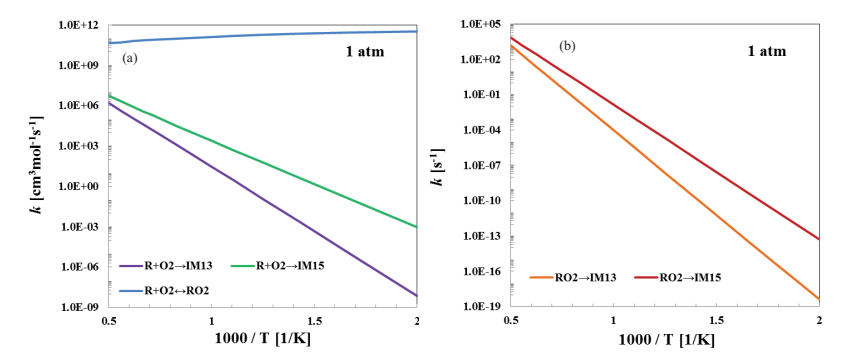


Figure 41. QRRK results for the CH₃COCH₂+O₂ at 1 atm, IM13 and IM15 indicates QOOH formation via for and six membered cyclic ring transition states respectively. $k = [cm^3mol^{-1}s^{-1}]$ for the bimolecular reaction and $[s^{-1}]$ for the unimolecular reaction.

As seen in Figure 41, the favorable product channel is the formation of RO_2 ie. $CH_3COCH_2O\dot{O}$. At 800 K, the rate constant for the $R+O_2\to IM15$ and $R+O_2\to IM13$ are 9 and 12 orders of magnitude smaller than the RO_2 production channel. Increase in temperature from 500 to 2000 K decreases the stabilization of $CH_3COCH_2O\dot{O}$ as seen in Figure 41a. Hence at higher temperature, it leads to increase in the rate constant for the chemically activated pathways; $R+O_2\to IM15$ and $R+O_2\to IM13$ i.e. isomerization products via six and four membered TSs respectively. At higher temperature ~ 1000 K, 7 and 9 orders of magnitude difference is depicted between the stabilization channel and $R+O_2\to IM15$ and $R+O_2\to IM13$ channels respectively. The favorability of the isomerization product formed (Figure 41b) via six membered ring transition state is due to the lesser ring strain involved in the transition state as compared to the one with four membered ring transition state. Comparing these two isomerization channels, at 500 K \sim 5 orders of magnitude difference is depicted which becomes around an order of magnitude with the increase in temperature (< 1200 K).

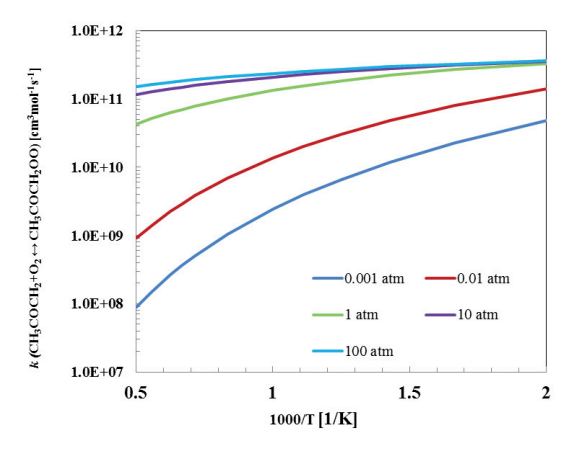


Figure 42. QRRK results for the CH₃COĊH₂+O₂ ↔ CH₃COĊH₂OO reactions at 0.001, 0.01, 1, 10 and 100 atm.

Figure 42 depicts the effect of pressure on the computed rate constant of $CH_3CO\dot{C}H_2 + O_2 \leftrightarrow CH_3COCH_2O\dot{O}$ reaction. As the pressure is increased from 0.001 at 100 atm, the rate constant for the collisional stabilization also increases. This indicates that at higher pressure more amount of $CH_3COCH_2O\dot{O}$ will be formed which further can lead to low temperature pathways. At lower pressure ~ 0.001 atm, an energetically excited RO_2 adduct may undergo isomerization or decomposition pathways instead of collisional stabilization to RO_2 .

The complete set of the rate coefficients for the $O_2 + CH_3CO\dot{C}H_2$ reactions are provided in the Appendix (Table A7) in a CHEMKIN-compatible PLOG format, with the modified Arrhenius parameters at 0.001, 0.01, 1, 10, and 100 atm.

V. Summary

This thesis put highlight on the fundamental understanding of elementary combustion reactions with the aid of theoretical approaches. Ab-initio quantum mechanical calculations were performed to reveal kinetics and thermodynamic properties of reactions with the help of electronic structure methods and by employing statistical rate theories. The fuel candidates considered herein are the ones which were of interest for the cluster of excellence "Tailor Made Fuels from Biomass (TMFB)" at the RWTH Aachen University. Since these proposed molecules are scarcely investigated for their combustion behavior, put a spotlight in investigating the fundamental details both from the chemistry and engine perspective. From an alcohol functional group, isopentanol was considered to investigate kinetics of the Habstraction reactions by H atom and HO₂ radical. One of the important factors affecting the kinetics of these reactions was found to be the strength of the C-H bond in a molecule. To support this analysis, C-H bond dissociation energies were determined by performing quantum calculations. Another important factor that also plays a chief role was the formation of H-bond in a molecule. This mainly occurs due to the presence of electronegative atom (such as oxygen) in molecules which ultimately affects reaction barrier and also entropy of a reaction.

Furthermore, focus was put on the cyclic oxygenated species such as tetrahydrofurans which can be produced via biosynthetic approaches. Two important candidates in this category are 2- and 3-methyltetrahydrofuran. The difference between these two molecules lies in the position of the methyl substituent on a ring. This structural difference has an effect on their elementary reactions in combustion. The reactions of interest considered herein are the isomerization reactions (ROO to QOOH) that occur after the first O_2 addition to the fuel radical. Detail analysis showed that the strength of the C-H bond, the position of the abstracted hydrogen (cis or trans), and also the ring size of the transition state were the main factors affecting the isomerization reaction kinetics.

Another candidate of interest is from ketone functional group, namely 2-butanone. Herein, detail quantum calculations were performed to investigate reaction kinetics of the H-abstraction reaction from 2-butanone by methylperoxy radical (CH₃OO). This study was performed at different computational methods and the results obtained were analyzed in detail. Significant differences in the results were noted between the composite methods and that obtained from the coupled cluster method. On further analysis it was observed that these deviations were mainly arising from the differences in the computed single point energies

within the methods. This study can be further extended for better understanding and in-depth analysis of the computational methods but at present limited herein.

Lastly, due to high interest in ketonic fuels, the smallest member of the ketone family; acetone was chosen to get insight into its elementary reactions occurring during combustion. Detail theoretical study was carried out on the beta-scission, O_2 addition and the isomerization reactions and also on the thermochemistry of the involved species. These will ultimately support in understanding the combustion mechanism of higher ketones.

To sum up, the computations performed in *this thesis* such as bond dissociation energies, rate constants, thermochemistry etc. are highly beneficial for the fundamental understandings as well as for the development of detailed kinetic models for alcohols, furans and ketonic species.

Bibliography

- [1] G.W. Huber, S. Iborra, A. Corma, Synthesis of transportation fuels from biomass: chemistry, catalysts, and engineering, Chemical reviews, 106 (2006) 4044-4098.
- [2] P.P. Upare, J.M. Lee, Y.K. Hwang, D.W. Hwang, J.H. Lee, S.B. Halligudi, J.S. Hwang, J.S. Chang, Direct hydrocyclization of biomass-derived levulinic acid to 2-methyltetrahydrofuran over nanocomposite copper/silica catalysts, ChemSusChem, 4 (2011) 1749-1752.
- [3] L.R. Lynd, J.H. Cushman, R.J. Nichols, C.E. Wyman, Fuel ethanol from cellulosic biomass, Science(Washington), 251 (1991) 1318-1323.
- [4] K. Yan, C. Jarvis, J. Gu, Y. Yan, Production and catalytic transformation of levulinic acid: A platform for speciality chemicals and fuels, Renewable and Sustainable Energy Reviews, 51 (2015) 986-997.
- [5] A.J. Janssen, F.W. Kremer, J.H. Baron, M. Muether, S. Pischinger, J. Klankermayer, Tailor-Made Fuels from Biomass for Homogeneous Low-Temperature Diesel Combustion, Energy & Fuels, 25 (2011) 4734-4744.
- [6] International Energy outlook, 2013, U. S. Energy Information Administration, DOE/EIA-0484, availabe at http://www.eia.gov/outlooks/ieo/pdf/0484(2013).pdf.
- [7]International Energy Agency, 2012, Annual report, available at https://www.iea.org/publications/freepublications/publication/IEA Annual Report publicversion.pdf
- [8] L.E. Hombach, C. Cambero, T. Sowlati, G. Walther, Optimal design of supply chains for second generation biofuels incorporating European biofuel regulations, Journal of Cleaner Production, 133 (2016) 565-575.
- [9] International Energy Outlook ,2016, DOE/EIA-0484(2016), availabe at https://www.eia.gov/outlooks/ieo/.
- [10] J. Zádor, C.A. Taatjes, R.X. Fernandes, Kinetics of elementary reactions in low-temperature autoignition chemistry, Progress in energy and combustion science, 37 (2011) 371-421.
- [11] S. Atsumi, T. Hanai, J.C. Liao, Non-fermentative pathways for synthesis of branched-chain higher alcohols as biofuels, Nature, 451 (2008) 86-89.
- [12] S.K. Lee, H. Chou, T.S. Ham, T.S. Lee, J.D. Keasling, Metabolic engineering of microorganisms for biofuels production: from bugs to synthetic biology to fuels, Current opinion in biotechnology, 19 (2008) 556-563.
- [13] E. Baker, J.M. Keisler, Cellulosic biofuels: Expert views on prospects for advancement, Energy, 36 (2011) 595-605.
- [14] Y. Su, H.M. Brown, X. Huang, X.-d. Zhou, J.E. Amonette, Z.C. Zhang, Single-step conversion of cellulose to 5-hydroxymethylfurfural (HMF), a versatile platform chemical, Applied Catalysis A: General, 361 (2009) 117-122.
- [15] F.M. Geilen, B. Engendahl, A. Harwardt, W. Marquardt, J. Klankermayer, W. Leitner, Selective and flexible transformation of biomass-derived platform chemicals by a multifunctional catalytic system, Angewandte Chemie, 49 (2010) 5510-5514.
- [16] M. Hechinger, A. Voll, W. Marquardt, Towards an integrated design of biofuels and their production pathways, Computers & Chemical Engineering, 34 (2010) 1909-1918.
- [17] F. Hoppe, U. Burke, M. Thewes, A. Heufer, F. Kremer, S. Pischinger, Tailor-Made Fuels from Biomass: Potentials of 2-butanone and 2-methylfuran in direct injection spark ignition engines, Fuel, 167 (2016) 106-117.
- [18] J. Bugler, K.P. Somers, E.J. Silke, H.J. Curran, Revisiting the Kinetics and Thermodynamics of the Low-Temperature Oxidation Pathways of Alkanes: A Case Study of the Three Pentane Isomers, The journal of physical chemistry. A, 119 (2015) 7510-7527.
- [19] H.J. Curran, P. Gaffuri, W.J. Pitz, C.K. Westbrook, A comprehensive modeling study of n-heptane oxidation, Combustion and flame, 114 (1998) 149-177.
- [20] H.J. Curran, P. Gaffuri, W. Pitz, C.K. Westbrook, A comprehensive modeling study of iso-octane oxidation, Combustion and flame, 129 (2002) 253-280.
- [21] A. Miyoshi, Systematic computational study on the unimolecular reactions of alkylperoxy (RO2), hydroperoxyalkyl (QOOH), and hydroperoxyalkylperoxy (O2QOOH) radicals, The journal of physical chemistry. A, 115 (2011) 3301-3325.
- [22] H. Eyring, The activated complex in chemical reactions, The Journal of Chemical Physics, 3 (1935) 107-115.
- [23] M.G. Evans, M. Polanyi, Some applications of the transition state method to the calculation of reaction velocities, especially in solution, Transactions of the Faraday Society, 31 (1935) 875-894.
- [24] P. Atkins, J. De Paula, Elements of physical chemistry, Oxford University Press, USA, 2013.
- [25] J.W. Ochterski, Thermochemistry in gaussian, Gaussian Inc, (2000) 1-19.
- [26] M.J. Frisch, G.W. Trucks, H.B. Schlegel, G.E. Scuseria, et al Gaussian 09, revision D.01; Gaussian, Inc.: Wallingford, CT., (2009).
- [27] D.A. McQuarrie, J.D. Simon, Molecular thermodynamics, University Science Books Sausalito, CA, 1999.
- [28] C. Leubner, Generalised Stirling approximations to N!, European Journal of Physics, 6.4 (1985) 299-301.

- [29]W. Hehre, W. Lathan, R. Ditchfield, M. Newton, J. Pople, Gaussian 70, Quantum Chemistry Program Exchange No. 236, Indiana University, Bloomington, Indiana.
- [30] M.J. Frisch, G.W. Trucks, H.B. Schlegel, G.E. Scuseria, et al. Gaussian 16, in, Wallingford, CT, 2016.
- [31] R.G. Parr, On the genesis of a theory, International Journal of Quantum Chemistry, 37 (1990) 327-347.
- [32] N.L. Ira, Quantum Chemistry, Pearson Prentice Hall, 2009.
- [33] R.J. Bartlett, Coupled-cluster approach to molecular structure and spectra: a step toward predictive quantum chemistry, The Journal of Physical Chemistry, 93 (1989) 1697-1708.
- [34] J. Noga, R.J. Bartlett, The full CCSDT model for molecular electronic structure, The Journal of Chemical Physics, 86 (1987) 7041-7050.
- [35] J.A. Pople, M. Head-Gordon, K. Raghavachari, Quadratic configuration interaction. A general technique for determining electron correlation energies, The Journal of Chemical Physics, 87 (1987) 5968-5975.
- [36] J.A. Pople, M. Head-Gordon, K. Raghavachari, Quadratic configuration interaction: Reply to comment by Paldus, Cizek, and Jeziorski, The Journal of Chemical Physics, 90 (1989) 4635-4636.
- [37] R.J. Bartlett, Many-body perturbation theory and coupled cluster theory for electron correlation in molecules, Annual review of physical chemistry, 32 (1981) 359-401.
- [38] J.A. Montgomery, M.J. Frisch, J.W. Ochterski, G.A. Petersson, A complete basis set model chemistry. VI. Use of density functional geometries and frequencies, The Journal of Chemical Physics, 110 (1999) 2822-2827.
- [39] J.A. Montgomery Jr, M.J. Frisch, J.W. Ochterski, G.A. Petersson, A complete basis set model chemistry. VII. Use of the minimum population localization method, The Journal of Chemical Physics, 112 (2000) 6532-
- vii. Ose of the minimum population localization method, The Journal of Chemical Physics, 112 (2000) 032-0542.
- [40] J.W. Ochterski, G.A. Petersson, J.A. Montgomery, A complete basis set model chemistry. V. Extensions to six or more heavy atoms, The Journal of Chemical Physics, 104 (1996) 2598-2619.
- [41] L.A. Curtiss, C. Jones, G.W. Trucks, K. Raghavachari, J.A. Pople, Gaussian-1 theory of molecular energies for second-row compounds, The Journal of Chemical Physics, 93 (1990) 2537-2545.
- [42] L.A. Curtiss, K. Raghavachari, G.W. Trucks, J.A. Pople, Gaussian-2 theory for molecular energies of first-and second-row compounds, The Journal of Chemical Physics, 94 (1991) 7221-7230.
- [43] L.A. Curtiss, K. Raghavachari, P.C. Redfern, V. Rassolov, J.A. Pople, Gaussian-3 (G3) theory for molecules containing first and second-row atoms, The Journal of Chemical Physics, 109 (1998) 7764-7776.
- [44] L.A. Curtiss, P.C. Redfern, K. Raghavachari, Gaussian-4 theory, J Chem Phys, 126 (2007) 084108.
- [45] P. Hohenberg, W. Kohn, Inhomogeneous electron gas, Physical review, 136 (1964) B864.
- [46] W. Kohn, L.J. Sham, Self-consistent equations including exchange and correlation effects, Physical review, 140 (1965) A1133.
- [47] J. Foster, S. Boys, A quantum variational calculation for HCHO, Reviews of Modern Physics, 32 (1960) 303.
- [48] C.M. Reeves, R. Fletcher, Use of Gaussian Functions in the Calculation of Wavefunctions for Small Molecules. III. The Orbital Basis and Its Effect on Valence, The Journal of Chemical Physics, 42 (1965) 4073-4081.
- [49] S.F. Boys, Electronic wave functions. I. A general method of calculation for the stationary states of any molecular system, in: Proceedings of the Royal Society of London A: Mathematical, Physical and Engineering Sciences, The Royal Society, 1950, pp. 542-554.
- [50] W.J. Hehre, R.F. Stewart, J.A. Pople, Self-Consistent Molecular-Orbital Methods. I. Use of Gaussian Expansions of Slater-Type Atomic Orbitals, The Journal of Chemical Physics, 51 (1969) 2657-2664.
- [51] J.A. Pople, M. Head-Gordon, D.J. Fox, K. Raghavachari, L.A. Curtiss, Gaussian-1 theory: A general procedure for prediction of molecular energies, The Journal of Chemical Physics, 90 (1989) 5622-5629.
- [52] T.H. Dunning, Gaussian basis sets for use in correlated molecular calculations. I. The atoms boron through neon and hydrogen, The Journal of Chemical Physics, 90 (1989) 1007-1023.
- [53] A.D. Becke, Density-functional thermochemistry. III. The role of exact exchange, The Journal of Chemical Physics, 98 (1993) 5648-5652.
- [54] L.A. Curtiss, P.C. Redfern, K. Raghavachari, Assessment of Gaussian-3 and density-functional theories on the G3/05 test set of experimental energies, The Journal of Chemical Physics, 123 (2005) 124107.
- [55] R. Dennington, T. Keith, J. Millam, GaussView, version 5, Semichem Inc., Shawnee Mission, KS, (2009).
- [56] G. Zhurko, D. Zhurko, Chemcraft, Version 1.7 (build 365), in, 2013.
- [57] X. Li, M.J. Frisch, Energy-represented direct inversion in the iterative subspace within a hybrid geometry optimization method, Journal of chemical theory and computation, 2 (2006) 835-839.
- [58] K. Fukui, The path of chemical reactions-the IRC approach, Accounts of chemical research, 14 (1981) 363-368.
- [59] A. Miyoshi, GPOP program suite, Revision 2010.02.14m3, available at http://akrmys.com/gpop/.
- [60] H. Werner, P. Knowles, G. Knizia, F. Manby, M. Schütz, P. Celani, T. Korona, R. Lindh, A. Mitrushenkov, G. Rauhut, Molpro, A package of ab initio programs, (2010).

- [61] K.K. Irikura, R.D. Johnson, R.N. Kacker, Uncertainties in scaling factors for ab initio vibrational frequencies, The Journal of Physical Chemistry A, 109 (2005) 8430-8437.
- [62] A. Miyoshi, BEx1D software, rev. 2012.03.12, available at http://akrmys.com/bex1d.
- [63] H.S. Johnston, J. Heicklen, Tunneling Corrections for Unsymmetrical Eckart Potential Energy Barriers, J. Phys. Chem. A, 66 (1962) 532–533.
- [64] P.P. Peralta-Yahya, J.D. Keasling, Advanced biofuel production in microbes, Biotechnology journal, 5 (2010) 147-162.
- [65] C.K. Westbrook, Biofuels combustion, Annual review of physical chemistry, 64 (2013) 201-219.
- [66] C. Dellomonaco, F. Fava, R. Gonzalez, The path to next generation biofuels: successes and challenges in the era of synthetic biology. Microbial Cell Factories, 9 (2010) 3.
- [67] S.T. Withers, S.S. Gottlieb, B. Lieu, J.D. Newman, J.D. Keasling, Identification of isopentenol biosynthetic genes from Bacillus subtilis by a screening method based on isoprenoid precursor toxicity, Applied and environmental microbiology, 73 (2007) 6277-6283.
- [68] Y. Yang, J.E. Dec, N. Dronniou, B. Simmons, Characteristics of isopentanol as a fuel for HCCI engines, SAE International Journal of Fuels and Lubricants, 3 (2010) 725-741.
- [69] T. Tsujimura, W.J. Pitz, F. Gillespie, H.J. Curran, B.W. Weber, Y. Zhang, C.-J. Sung, Development of Isopentanol Reaction Mechanism Reproducing Autoignition Character at High and Low Temperatures, Energy & Fuels, 26 (2012) 4871-4886.
- [70] G. Dayma, C. Togbé, P. Dagaut, Experimental and Detailed Kinetic Modeling Study of Isoamyl Alcohol (Isopentanol) Oxidation in a Jet-Stirred Reactor at Elevated Pressure, Energy & Fuels, 25 (2011) 4986-4998.
- [71] O. Welz, J. Zador, J.D. Savee, M.Y. Ng, G. Meloni, R.X. Fernandes, L. Sheps, B.A. Simmons, T.S. Lee, D.L. Osborn, C.A. Taatjes, Low-temperature combustion chemistry of biofuels: pathways in the initial low-temperature (550 K-750 K) oxidation chemistry of isopentanol, Physical chemistry chemical physics: PCCP, 14 (2012) 3112-3127.
- [72] S. Mani Sarathy, S. Park, B.W. Weber, W. Wang, P.S. Veloo, A.C. Davis, C. Togbe, C.K. Westbrook, O. Park, G. Dayma, Z. Luo, M.A. Oehlschlaeger, F.N. Egolfopoulos, T. Lu, W.J. Pitz, C.-J. Sung, P. Dagaut, A comprehensive experimental and modeling study of iso-pentanol combustion, Combustion and Flame, 160 (2013) 2712-2728.
- [73] S.M. Sarathy, S. Vranckx, K. Yasunaga, M. Mehl, P. Oßwald, W.K. Metcalfe, C.K. Westbrook, W.J. Pitz, K. Kohse-Höinghaus, R.X. Fernandes, H.J. Curran, A comprehensive chemical kinetic combustion model for the four butanol isomers, Combustion and Flame, 159 (2012) 2028-2055.
- [74] K.A. Heufer, S.M. Sarathy, H.J. Curran, A.C. Davis, C.K. Westbrook, W.J. Pitz, Detailed Kinetic Modeling Study ofn-Pentanol Oxidation, Energy & Fuels, 26 (2012) 6678-6685.
- [75] K.S. Pitzer, W.D. Gwinn, Energy Levels and Thermodynamic Functions for Molecules with Internal Rotation I. Rigid Frame with Attached Tops, The Journal of Chemical Physics, 10 (1942) 428-440.
- [76] K.S. Pitzer, Energy Levels and Thermodynamic Functions for Molecules with Internal Rotation: II. Unsymmetrical Tops Attached to a Rigid Frame, The Journal of Chemical Physics, 14 (1946) 239-243.
- [77] S.J. Blanksby, G.B. Ellison, Bond dissociation energies of organic molecules, Accounts of chemical research, 36 (2003) 255-263.
- [78] M.R. Harper, K.M. Van Geem, S.P. Pyl, G.B. Marin, W.H. Green, Comprehensive reaction mechanism for n-butanol pyrolysis and combustion, Combustion and Flame, 158 (2011) 16-41.
- [79] C.-W. Zhou, J.M. Simmie, H.J. Curran, Rate constants for hydrogen abstraction by HO2 from n-butanol, International Journal of Chemical Kinetics, 44 (2012) 155-164.
- [80] Z. Tian, T. Yuan, R. Fournet, P.A. Glaude, B. Sirjean, F. Battin-Leclerc, K. Zhang, F. Qi, An experimental and kinetic investigation of premixed furan/oxygen/argon flames, Combust Flame, 158 (2011) 756-773.
- [81] Y. Uygun, S. Ishihara, H. Olivier, A high pressure ignition delay time study of 2-methylfuran and tetrahydrofuran in shock tubes, Combustion and Flame, 161 (2014) 2519-2530.
- [82] D. Liu, C. Togbe, L.S. Tran, D. Felsmann, P. Osswald, P. Nau, J. Koppmann, A. Lackner, P.A. Glaude, B. Sirjean, R. Fournet, F. Battin-Leclerc, K. Kohse-Hoinghaus, Combustion chemistry and flame structure of furan group biofuels using molecular-beam mass spectrometry and gas chromatography Part I: Furan, Combust Flame, 161 (2014) 748-765.
- [83] L.S. Tran, C. Togbe, D. Liu, D. Felsmann, P. Osswald, P.A. Glaude, R. Fournet, B. Sirjean, F. Battin-Leclerc, K. Kohse-Hoinghaus, Combustion chemistry and flame structure of furan group biofuels using molecular-beam mass spectrometry and gas chromatography Part II: 2-Methylfuran, Combust Flame, 161 (2014) 766-779.
- [84] C. Togbe, L.S. Tran, D. Liu, D. Felsmann, P. Osswald, P.A. Glaude, B. Sirjean, R. Fournet, F. Battin-Leclerc, K. Kohse-Hoinghaus, Combustion chemistry and flame structure of furan group biofuels using molecular-beam mass spectrometry and gas chromatography Part III: 2,5-Dimethylfuran, Combust Flame, 161 (2014) 780-797.

- [85] G. Vanhove, Y. Yu, M.A. Boumehdi, O. Frottier, O. Herbinet, P.-A. Glaude, F. Battin-Leclerc, Experimental Study of Tetrahydrofuran Oxidation and Ignition in Low-Temperature Conditions, Energy & Fuels, 29 (2015) 6118-6125.
- [86] L.-S. Tran, M. Verdicchio, F. Monge, R.C. Martin, R. Bounaceeur, B. Sirjean, P.-A. Glaude, M.U. Alzueta, F. Battin-Leclerc, An experimental and modeling study of the combustion of tetrahydrofuran, Combustion and Flame, 162 (2015) 1899-1918.
- [87] P. Dagaut, M. McGuinness, J.M. Simmie, M. Cathonnet, The Ignition and Oxidation of Tetrahydrofuran: Experiments and Kinetic Modeling, Combustion Science and Technology, 135 (1998) 3-29.
- [88] K.P. Somers, J.M. Simmie, F. Gillespie, C. Conroy, G. Black, W.K. Metcalfe, F. Battin-Leclerc, P. Dirrenberger, O. Herbinet, P.-A. Glaude, P. Dagaut, C. Togbé, K. Yasunaga, R.X. Fernandes, C. Lee, R. Tripathi, H.J. Curran, A comprehensive experimental and detailed chemical kinetic modelling study of 2,5-dimethylfuran pyrolysis and oxidation, Combustion and Flame, 160 (2013) 2291-2318.
- [89] K. Moshammer, S. Vranckx, H.K. Chakravarty, P. Parab, R.X. Fernandes, K. Kohse-Höinghaus, An experimental and kinetic modeling study of 2-methyltetrahydrofuran flames, Combustion and Flame, 160 (2013) 2729-2743.
- [90] L. Sy Tran, B. Sirjean, P.A. Glaude, R. Fournet, F. Battin-Leclerc, Progress in Detailed Kinetic Modeling of the Combustion of Oxygenated Components of Biofuels, Energy (Oxf), 43 (2012) 4-18.
- [91] J.D. Savee, E. Papajak, B. Rotavera, H. Huang, A.J. Eskola, O. Welz, L. Sheps, C.A. Taatjes, J. Zádor, D.L. Osborn, Direct observation and kinetics of a hydroperoxyalkyl radical (QOOH), Science, 347 (2015) 643-646.
- [92] D.G. Truhlar, B.C. Garrett, S.J. Klippenstein, Current status of transition-state theory, The Journal of physical chemistry, 100 (1996) 12771-12800.
- [93] A. Pell, G. Pilcher, Measurements of heats of combustion by flame calorimetry. Part 3.—Ethylene oxide, trimethylene oxide, tetrahydrofuran and tetrahydropy, Transactions of the Faraday Society, 61 (1965) 71-77.
- [94] G. Clegg, D. Gee, T. Melia, A. Tyson, Thermodynamics of polymerization of heterocyclic compounds II—The heat capacity, entropy, enthalpy and free energy of polytetrahydrofuran, Polymer, 9 (1968) 501-511.
- [95] D. Feller, J.A. Franz, A Theoretical Determination of the Heats of Formation of Furan, Tetrahydrofuran, THF-2-yl, and THF-3-yl, The Journal of Physical Chemistry A, 104 (2000) 9017-9025.
- [96] F. Agapito, B.J.C. Cabral, J.A.M. Simões, Carbon-hydrogen bond dissociation enthalpies in ethers: a theoretical study, Journal of Molecular Structure: THEOCHEM, 719 (2005) 109-114.
- [97] T. Rudolph, J. Thomas, NOx, NMHC and CO emissions from biomass derived gasoline extenders, Biomass, 16 (1988) 33-49.
- [98] D.M. Alonso, J.Q. Bond, J.A. Dumesic, Catalytic conversion of biomass to biofuels, Green Chemistry, 12 (2010) 1493.
- [99] P.R. Parab, N. Sakade, Y. Sakai, R. Fernandes, K.A. Heufer, Theoretical Investigation of Intramolecular Hydrogen Shift Reactions in 3-Methyltetrahydrofuran (3-MTHF) Oxidation, The journal of physical chemistry. A, 119 (2015) 10917-10928.
- [100] J.M. Simmie, Kinetics and thermochemistry of 2,5-dimethyltetrahydrofuran and related oxolanes: next next-generation biofuels, The journal of physical chemistry. A, 116 (2012) 4528-4538.
- [101] C.W. Zhou, J.M. Simmie, H.J. Curran, Ab initio and kinetic study of the reaction of ketones with OH for T=500-2000 K. Part I: hydrogen-abstraction from H3CC(O)CH(3-x)(CH3)x, x=0 to 2, Physical chemistry chemical physics: PCCP, 13 (2011) 11175-11192.
- [102] R.S. Tranter, R.W. Walker, Rate constants for H and OH attack on propanone, butanone and pentan-3-one at 753 K, and the oxidation chemistry of the radicals formed, Physical Chemistry Chemical Physics, 3 (2001) 1262-1270.
- [103] J. Badra, A.E. Elwardany, F. Khaled, S.S. Vasu, A. Farooq, A shock tube and laser absorption study of ignition delay times and OH reaction rates of ketones: 2-Butanone and 3-buten-2-one, Combustion and Flame, 161 (2014) 725-734.
- [104] K.Y. Lam, D.F. Davidson, R.K. Hanson, High-temperature measurements of the reactions of OH with a series of ketones: acetone, 2-butanone, 3-pentanone, and 2-pentanone, The journal of physical chemistry. A, 116 (2012) 5549-5559.
- [105] J. Mendes, C.W. Zhou, H.J. Curran, Theoretical and kinetic study of the reactions of ketones with HO2 radicals. Part I: abstraction reaction channels, The journal of physical chemistry. A, 117 (2013) 4515-4525.
- [106] W.A. Kopp, U. Burke, M. Döntgen, L.C. Kröger, H. Minwegen, K.A. Heufer, K. Leonhard, Ab initio kinetics predictions for H-atom abstraction from 2-butanone by and and the subsequent unimolecular reactions, Proceedings of the Combustion Institute, 36 (2017) 203-210.
- [107] U. Burke, J. Beeckmann, W.A. Kopp, Y. Uygun, H. Olivier, K. Leonhard, H. Pitsch, K.A. Heufer, A comprehensive experimental and kinetic modeling study of butanone, Combustion and Flame, 168 (2016) 296-309.

- [108] J.M. Hudzik, J.W. Bozzelli, J.M. Simmie, Thermochemistry of C7H16 to C10H22 alkane isomers: primary, secondary, and tertiary C-H bond dissociation energies and effects of branching, The journal of physical chemistry. A, 118 (2014) 9364-9379.
- [109] K.P. Somers, J.M. Simmie, Benchmarking Compound Methods (CBS-QB3, CBS-APNO, G3, G4, W1BD) against the Active Thermochemical Tables: Formation Enthalpies of Radicals, The journal of physical chemistry. A, 119 (2015) 8922-8933.
- [110] T.J. Lee, A.P. Rendell, P.R. Taylor, Comparison of the quadratic configuration interaction and coupledcluster approaches to electron correlation including the effect of triple excitations, Journal of Physical Chemistry, 94 (1990) 5463-5468.
- [111] S. Pichon, G. Black, N. Chaumeix, M. Yahyaoui, J. Simmie, H. Curran, R. Donohue, The combustion chemistry of a fuel tracer: Measured flame speeds and ignition delays and a detailed chemical kinetic model for the oxidation of acetone, Combustion and Flame, 156 (2009) 494-504.
- [112] Y. Wang, D.J. Jacob, J.A. Logan, Global simulation of tropospheric O3-NOx-hydrocarbon chemistry: 1. Model formulation, Journal of Geophysical Research: Atmospheres, 103 (1998) 10713-10725.
- [113] D.J. Jacob, B.D. Field, E.M. Jin, I. Bey, Q. Li, J.A. Logan, R.M. Yantosca, H.B. Singh, Atmospheric budget of acetone, Journal of Geophysical Research: Atmospheres, 107 (2002) ACH 5-1-ACH 5-17.
- [114] H.B. Singh, D. O'hara, D. Herlth, W. Sachse, D. Blake, J. Bradshaw, M. Kanakidou, P. Crutzen, Acetone in the atmosphere: Distribution, sources, and sinks, Journal of Geophysical Research: Atmospheres, 99 (1994) 1805-1819.
- [115] H. Singh, Y. Chen, A. Staudt, D. Jacob, Evidence from the Pacific troposphere for large global sources of oxygenated organic compounds, Nature, 410 (2001) 1078.
- [116] P.F. Ambidge, J.N. Bradley, D.A. Whytock, Kinetic study of the reactions of hydrogen and oxygen atoms with acetone, Journal of the Chemical Society, Faraday Transactions 1: Physical Chemistry in Condensed Phases, 72 (1976) 1870-1876.
- [117] J.R. Álvarez-Idaboy, A. Cruz-Torres, A. Galano, M.E. Ruiz-Santoyo, Structure—Reactivity Relationship in Ketones+ OH Reactions: A Quantum Mechanical and TST Approach, The Journal of Physical Chemistry A, 108 (2004) 2740-2749.
- [118] E. Henon, S. Canneaux, F. Bohr, S. Dóbé, Features of the potential energy surface for the reaction of OH radical with acetone, Phys. Chem. Chem. Phys., 5 (2003) 333-341.
- [119] T. Cours, S. Canneaux, F. Bohr, Features of the potential energy surface for the reaction of HO2 radical with acetone, International Journal of Quantum Chemistry, 107 (2007) 1344-1354.
- [120] K. Sato, Y. Hidaka, Shock-tube and modeling study of acetone pyrolysis and oxidation, Combustion and flame, 122 (2000) 291-311.
- [121] A.M. El-Nahas, J.M. Simmie, M.V. Navarro, J.W. Bozzelli, G. Black, H.J. Curran, Thermochemistry and kinetics of acetonylperoxy radical isomerisation and decomposition: a quantum chemistry and CVT/SCT approach, Physical chemistry chemical physics: PCCP, 10 (2008) 7139-7149.
- [122] A.M. El-Nahas, J.W. Bozzelli, J.M. Simmie, M.V. Navarro, G. Black, H.J. Curran, Thermochemistry of acetonyl and related radicals, The Journal of Physical Chemistry A, 110 (2006) 13618-13623.
- [123] A. Dean, Predictions of pressure and temperature effects upon radical addition and recombination reactions, The Journal of Physical Chemistry, 89 (1985) 4600-4608.
- [124] A. Chang, J. Bozzelli, A. Dean, Kinetic analysis of complex chemical activation and unimolecular dissociation reactions using QRRK theory and the modified strong collision approximation, Zeitschrift für Physikalische Chemie, 214 (2000) 1533.
- [125] Y. Zhao, D.G. Truhlar, The M06 suite of density functionals for main group thermochemistry, thermochemical kinetics, noncovalent interactions, excited states, and transition elements: two new functionals and systematic testing of four M06-class functionals and 12 other functionals, Theoretical Chemistry Accounts, 120 (2008) 215-241.
- [126] J.M.L. Martin, Ab initio total atomization energies of small molecules towards the basis set limit, Chem. Phys. Lett., 259 (1996) 669-678.
- [127] D. Feller, D.A. Dixon, Extended benchmark studies of coupled cluster theory through triple excitations, The Journal of Chemical Physics, 115 (2001) 3484-3496.
- [128] J.M. Simmie, K.P. Somers, Benchmarking Compound Methods (CBS-QB3, CBS-APNO, G3, G4, W1BD) against the Active Thermochemical Tables: A Litmus Test for Cost-Effective Molecular Formation Enthalpies, The journal of physical chemistry. A, 119 (2015) 7235-7246.
- [129] J. Barker, T. Nguyen, J. Stanton, C. Aieta, M. Ceotto, F. Gabas, T. Kumar, C. Li, L. Lohr, A. Maranzana, MultiWell-2016 Software Suite, JR Barker, University of Michigan, Ann Arbor, Michigan, USA, (2016).
- [130] M.W.J. Chase, NIST-JANAF Thermochemical Tables, in: Fourth Edition, J. Phys Chem Ref Data, 1998, pp. 1-1951.
- [131] R. Nuttall, A. Laufer, M. Kilday, The enthalpy of formation of ketene, The Journal of Chemical Thermodynamics, 3 (1971) 167-174.

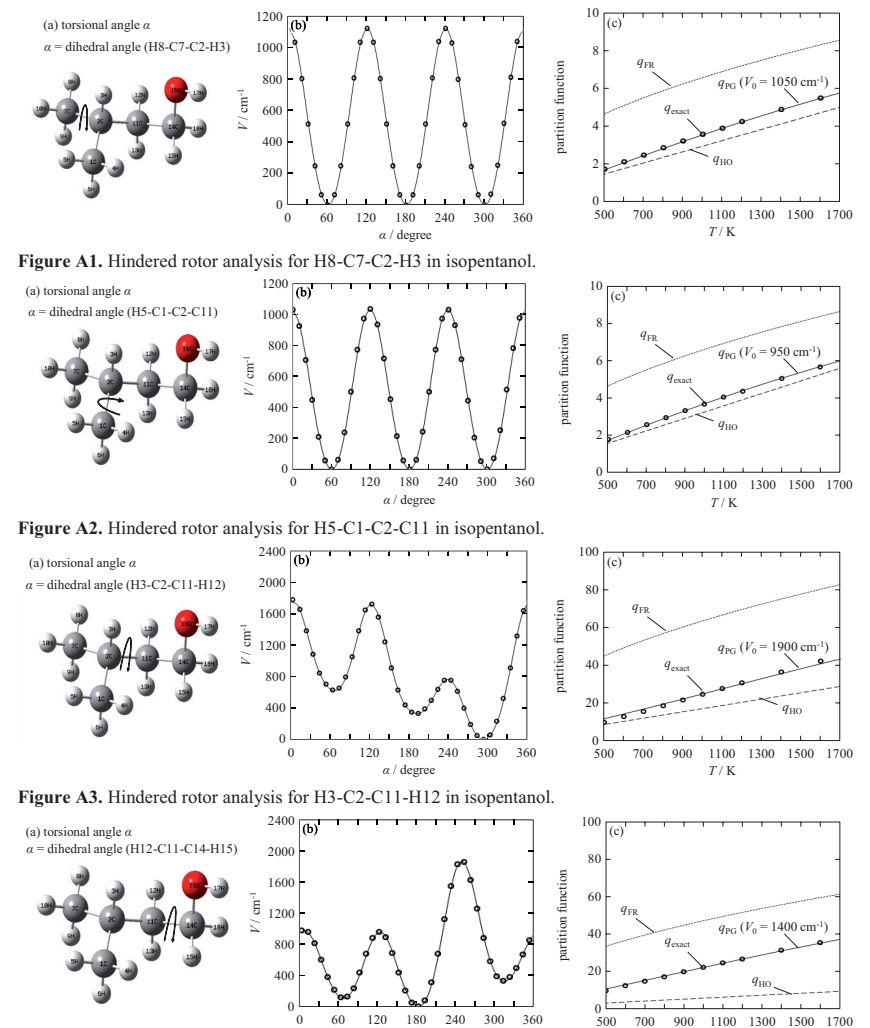
- [132] K.B. Wiberg, L.S. Crocker, K.M. Morgan, Thermochemical studies of carbonyl compounds. 5. Enthalpies of reduction of carbonyl groups, Journal of the American Chemical Society, 113 (1991) 3447-3450.
- [133] G. Bouchoux, J. Chamot-Rooke, D. Leblanc, P. Mourgues, M. Sablier, Proton Affinity and Heat of Formation of Vinyloxy [CH2CHO]. and Acetonyl [CH2COCH3]. Radicals, ChemPhysChem, 2 (2001) 235-241.
- [134] J.M. Hudzik, J.W. Bozzelli, Thermochemistry and bond dissociation energies of ketones, The journal of physical chemistry. A, 116 (2012) 5707-5722.
- [135] Y.R. Luo, Comprehensive Handbook of Chemical Bond Energies; CRC Press: Boca Raton, FL, (2007).
 [136] C.W. Bauschlicher, The bond dissociation energies of 1-butene, Chemical physics letters, 239 (1995) 252-
- [137] K.A. Peterson, D.E. Woon, T.H. Dunning, Benchmark calculations with correlated molecular wave functions. IV. The classical barrier height of the H+H2→H2+H reaction, The Journal of Chemical Physics, 100 (1994) 7410-7415.
- [138] C.F. Goldsmith, W.H. Green, S.J. Klippenstein, Role of O2 + QOOH in low-temperature ignition of propane. 1. Temperature and pressure dependent rate coefficients, The journal of physical chemistry. A, 116 (2012) 3325-3346.
- [139] S. Glasstone, H. Eyring, K.J. Laidler, The theory of rate processes, McGraw-Hill, 1941.
- [140] A.M. Dean, Predictions of Pressure and Temperature Effects upon Radical Addition and Recombination Reactions J Phys Chem, 89 (1985) 4600-4608.
- [141] A.Y. Chang, J.W. Bozzelli, A.M. Dean, Kinetic Analysis of Complex Chemical Activation and Unimolecular Dissociation Reactions using QRRK Theory and the Modified Strong Collision Approximation, Zeitschrift für Physikalische Chemie, 214 (2000) 1533-1568.

I	List of Figures	
1.	Schematic of overall reaction paths in hydrocarbon combustion	4
2.	IRC path as visualized by GaussView	30
3.	Optimized geometry with the atom numbers in isopentanol	30
4.	Optimized geometry with the atom numbers in 2-butanone	34
5.	Labels of H-atom abstraction sites in isopentanol	39
6.	Optimized transition state structures for the H-atom abstraction reactions from	40
7.	isopentanol by H atom	41
8.	Hindered rotor analysis for the OH rotor in TS attached to the $C\alpha$ atom in isopentanol	42
0	High pressure limiting rate constants for the H-atom abstraction reactions from	46
9.	isopentanol by H atom	40
10.	High pressure limiting rate constants for the H-atom abstraction reactions from isopentanol by $H\dot{O}_2$ radical	47
11.	Comparison of H-abstraction rate constant by H atom determined in this work with Harper et al. rate constants.	48
	Comparison of H-abstraction rate constant by HO ₂ radical determined in this work	
12.	with Zhou et al rate constants	49
13.		50
14.	Optimized transition states for the H_{β} abstractions from isopentanol by HO_2 radical Labels of atoms in 3-Methyltetrahydrofuran	52
15.	Hindered rotor analysis for the methyl rotor attached to the C3 atom in the	53
	tetrahydrofuran ring (3-MTHF)	
16.	Hindered rotor analysis for the CH ₂ OO rotor attached to the C3 atom in the tetrahydrofuran ring (3-MTHF)	54
17.	Species abbreviations used for 3-MTHF species.	55
18.	High pressure limit rate constant of the intramolecular hydrogen shift reactions in (a) ROOm, (b) ROO3, (c) ROO2c, (d) ROO2t, (e) ROO4c, (f) ROO4t, (g) ROO5c and (h) ROO5t isomers of 3-MTHF	61
19.	Product branching ratio of the intramolecular hydrogen shift reactions in (a) ROO2c, (b) ROO2t, (c) ROO3, (d) ROO4c, (e) ROO4t, (f) ROO5c, (g) ROO5t and (h) ROOm isomers of 3-MTHF.	64
20.	Labels of atoms in methylcyclopentane	65
21.	ROO isomers of methylcyclopentane	65
22.	C-H BDE comparison of (a) 3-MTHF with (b) methlcyclopentane in kJ mol ⁻¹	66
22.	computed at CBS-QB3 method.	00
	Comparison of total rate constants (a) ROOm, (b) ROO3, (c) ROO2c, (d) ROO2t, (e)	
23.	ROO4c, (f) ROO4t, (g) ROO5c, (h) ROO5t isomers of 3-MTHF with	67
	methlcyclopentane	

24.	Comparison of rate constants ROO2c in 3-MTHF with methlcyclopentane (a) hydrogen shift from C2 or C5, (b) hydrogen shift from C3 or C4, and (c) hydrogen shift from Cm	68
25.	Optimized structure of 2-MTHF at CBS-QB3 method with the labels	71
26.	Species abbreviations in 2-MTHF	72
27.	High pressure limit rate constants of the intramolecular hydrogen shift reactions in (a) ROOm, (b) ROO2, (c) ROO3c, (d) ROO3t, (e) ROO4c, (f) ROO4t, (g) ROO5c, and (h) ROO5t isomers of 2-MTHF	79
28.	Product distributions of the intramolecular hydrogen shift reactions in 2-MTHF	82
	Comparison of total rate constants for (a) ROOm, (b) ROO2, (c) ROO3c, (d)	
29.	ROO3t, (e) ROO4c, (f) ROO4t, (g) ROO5c, and (h) ROO5t isomers of 2-MTHF with	84
	methlcyclopentane	
	Comparison of rate constants in ROO5c in 2-MTHF with methlcyclopentane, (a)	
30.	hydrogen shift from C5, (b) hydrogen shift from C3 or C4, and (c) hydrogen shift	85
	from Cm.	
31.	Comparison of rate constants in ROO2 in 2-MTHF with methlcyclopentane, (a) hydrogen shift from C5, (b) hydrogen shift from C3 or C4, and (c) hydrogen shift from Cm.	86
	Comparison of 2-methyltetrahydrofuran rate constants with 3-methyltetrahydrofuran,	
32.	(a) hydrogen shift from C5 in ROO2 (b) hydrogen shift from C2 and C5 in ROO3t	87
	(c) hydrogen shift from C5 in ROO4c	
	Comparison of 2-methyltetrahydrofuran rate constants with 3-methyltetrahydrofuran,	
33.	(a) hydrogen shift from C2 and C5 in ROO4t (b) hydrogen shift from C2 in ROO5t	87
	(c) hydrogen shift from C2 and C5 in ROOm	
34.	Optimized structure of (a) 2-butanone and (b) Methylperoxy radical with the labels used in this work	91
35.	High pressure limit rate constants for the H-atom abstraction reactions from 2-BT computed at (a) G3, (b) G4, (c) CBS-QB3 and (d) CCSD(t)/cc-pVTZ//MP2/6-	97
36.	311G(d,p) methods	99
37.	Acetone reaction scheme	103
38.	Optimized structures of species of interest for computing thermodynamic properties	104
39.	in acetone	107
	Optimized structures of the TS involved in the isomerization reactions in	
40.	acetonylperoxy (a) 1,5 isomerization TS (b) 1,3 isomerization TS	108
41.	QRRK results for the CH ₃ COCH ₂ +O ₂ at 1 atm	110
	QRRK results for the CH ₃ COCH ₂ +O ₂ \leftrightarrow CH ₃ COCH ₂ OO reactions at 0.001, 0.01, 1,	
42.	10 and 100 atm	111

II	List of Tables	
1.	Methods and the scaling factors in GPOP program	32
2.	Estimated Hindered rotor parameters in isopentanol by Pitzer-Gwinn approximation	42
3.	Reaction barriers and energies for the H-atom abstractions in isopentanol	44
4.	High-pressure limit rate constant for H-atom abstraction reactions in isopentanol by	15
	H atom and HÖ ₂ radical	45
_	Estimated hindered rotor parameters in Pitzer-Gwinn approximation for	52
5.	intramolecular H-shift reactions in 3-MTHF	53
6.	Thermodynamic properties of tetrahydrofuran, tetrahydrofuran-2-yl and tetrahydrofuran-3-yl	56
7.	C-H bond dissociation energies in 3-Methyltetrahydrofuran	57
8.	Reaction barriers and energies for H-shift reactions in 3-MTHF	58
9.	High pressure limit rate constant for the H-shift reactions in 3-MTHF	60
10.	Reaction barriers and energies for the H-shift reactions in mcyc5	66
11.	Estimated hindered rotor parameters in Pitzer-Gwinn approximation for	71
11.	intramolecular H-shift reactions in 2-MTHF	/ 1
12.	C-H bond dissociation energies comparison in 2- and 3-MTHF	73
13.	C-H bond dissociation enthalpies (298.15 K) in 2-MTHF	73
14.	Reaction barriers and energies for H-shift reactions in 2-MTHF	75
15.	High pressure limit rate constant for the H-shift reactions in 2-MTHF	77
16.	Estimated hindered rotor parameters in Pitzer-Gwinn approximation for H-atom abstraction reactions in 2-Butanone.	91
17.	C-H bond dissociation energies comparison in 2-Butanone	93
18.	Reaction barriers and energies for H-atom abstraction reactions in 2-Butanone	94
19.	Percentage bond elongation in 2-BT	95
20.	High pressure limit rate constants comparison for the H-atom abstraction reactions from 2-BT.	96
21.	Standard enthalpies of formation for the species involved in acetone combustion	104
22.	C-H and C-C bond dissociation enthalpies in acetone.	106
23.	High pressure limit rate constants in acetone.	109

Hindered rotor analysis performed by scanning dihedral angle at b3lyp/cbsb7 for the internal rotations involved in the H-atom abstraction from isopentanol by H atom and \dot{HO}_2 radical.



α / degree

Figure A4. Hindered rotor analysis for H12-C11-C14-H15 in isopentanol.

T/K

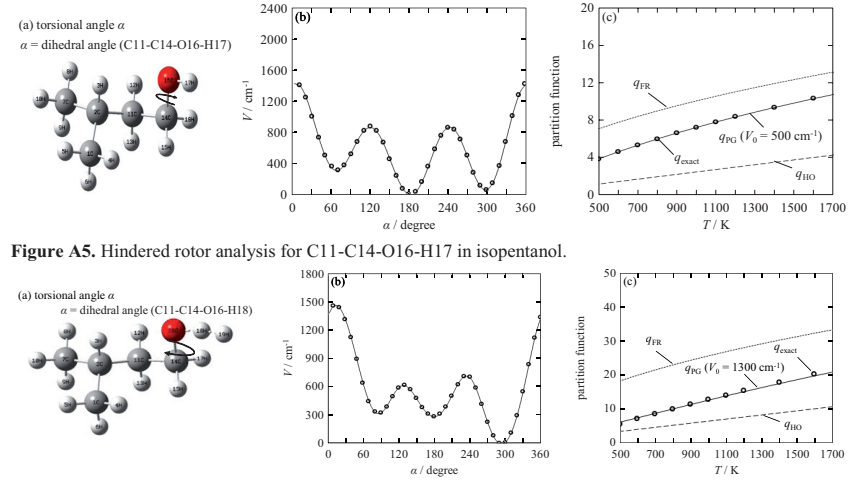


Figure A6. Hindered rotor analysis for C11-C14-O16-H18 in the TS for H-abstraction from isopentanol by H atom

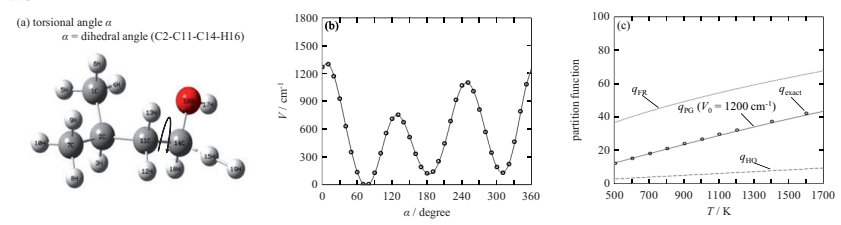


Figure A7. Hindered rotor analysis for C2-C11-C14-H16 in the TS for H-abstraction from isopentanol by H atom

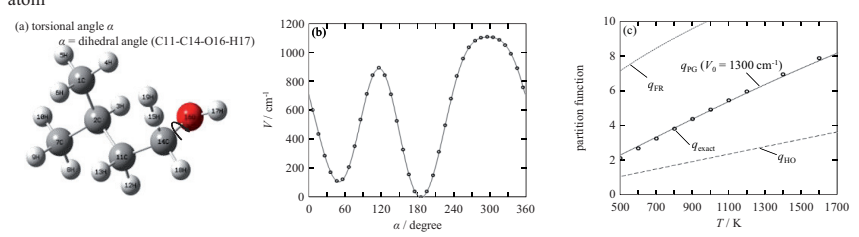


Figure A8. Hindered rotor analysis for C11-C14-O16-H17 in the TS for H-abstraction from isopentanol by H atom

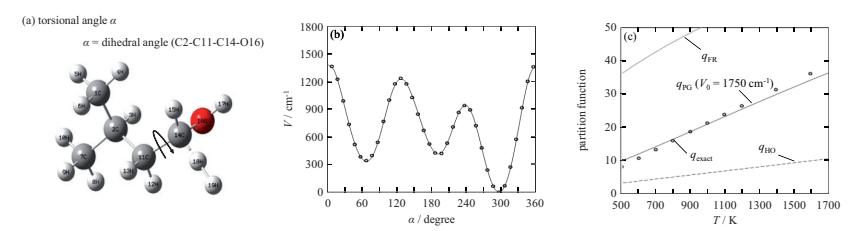


Figure A9. Hindered rotor analysis for C2-C11-C14-O16 in the TS for H-abstraction from isopentanol by H atom

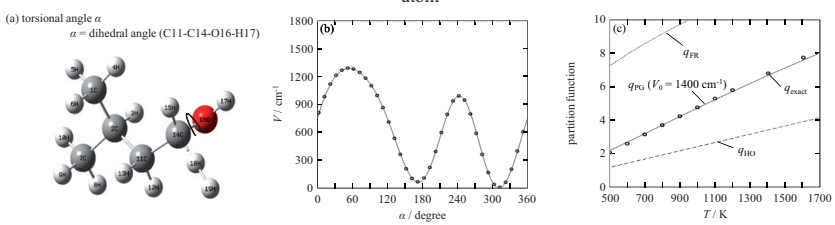


Figure A10. Hindered rotor analysis for C11-C14-O16-H17 in the TS for H-abstraction from isopentanol by H atom

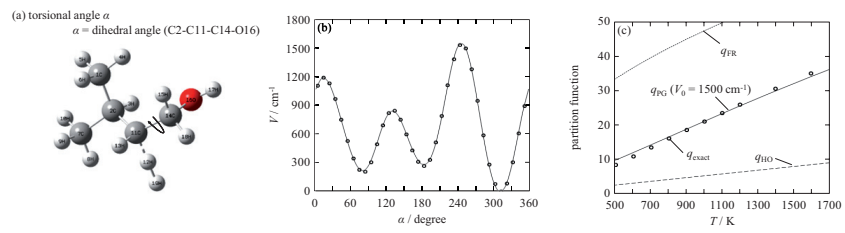


Figure A11. Hindered rotor analysis for C2-C11-C14-O16 in the TS for H-abstraction from isopentanol by H atom

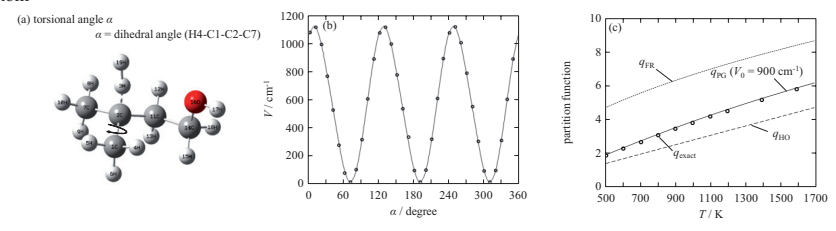


Figure A12. Hindered rotor analysis for H4-C1-C2-C7 in the TS for H-abstraction from isopentanol by H atom

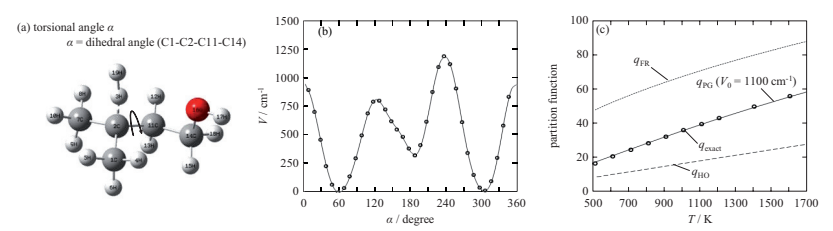


Figure A13. Hindered rotor analysis for C1-C2-C11-C14 in the TS for H-abstraction from isopentanol by H atom

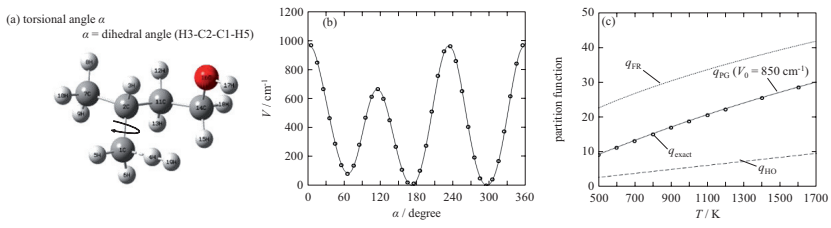


Figure A14. Hindered rotor analysis for H3-C2-C1-H5 in the TS for H-abstraction from isopentanol by H atom

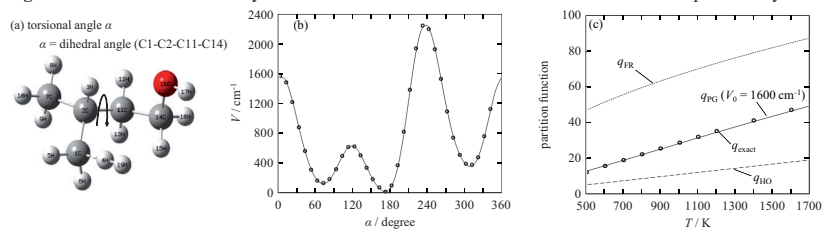


Figure A15. Hindered rotor analysis for C1-C2-C11-C14 in the TS for H-abstraction from isopentanol by H atom

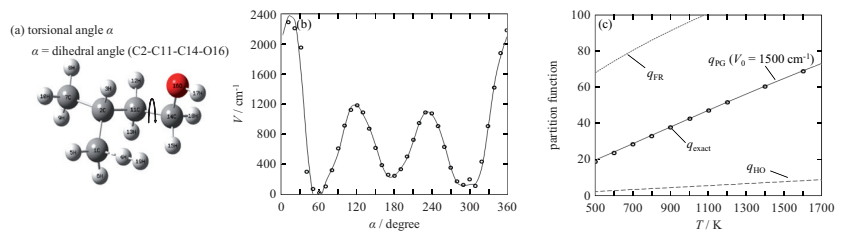


Figure A16. Hindered rotor analysis for C2-C11-C14-O16 in the TS for H-abstraction from isopentanol by H atom

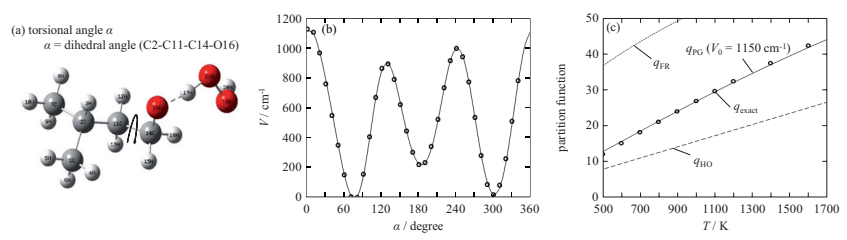


Figure A17. Hindered rotor analysis for C2-C11-C14-O16 in the TS for H-abstraction from isopentanol by HO₂ radical

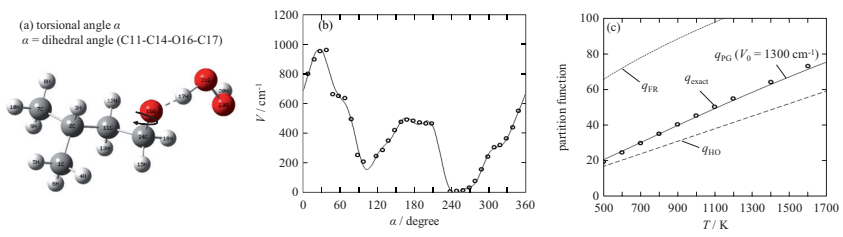


Figure A18. Hindered rotor analysis for C11-C14-O16-C17 in the TS for H-abstraction from isopentanol by $H\dot{O}_2$ radical

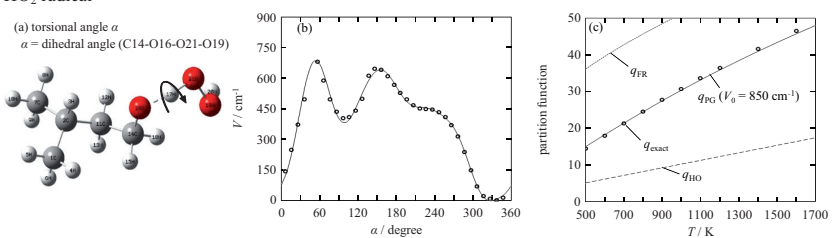


Figure A19. Hindered rotor analysis for C14-O16-O21-O19 in the TS for H-abstraction from isopentanol by $H\ddot{O}_2$ radical

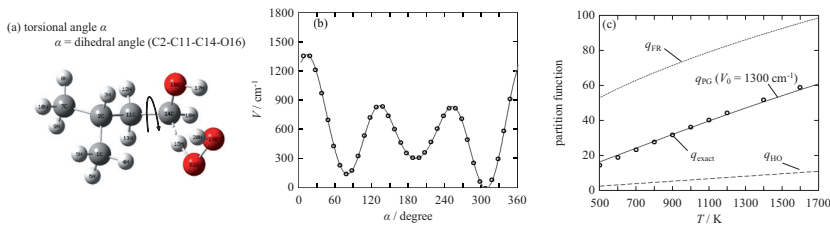


Figure A20. Hindered rotor analysis for C2-C11-C14-O16 in the TS for H-abstraction from isopentanol by \dot{HO}_2 radical

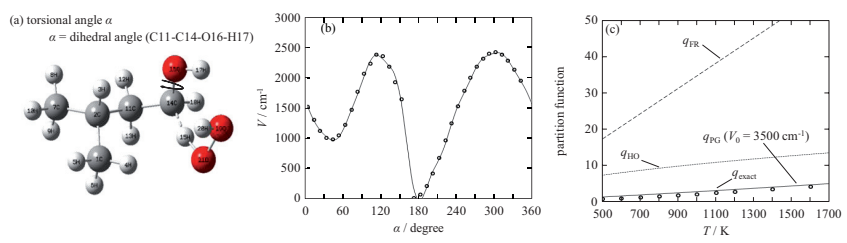


Figure A21. Hindered rotor analysis for C11-C14-O16-H17 in the TS for H-abstraction from isopentanol by $H\dot{O}_2$ radical

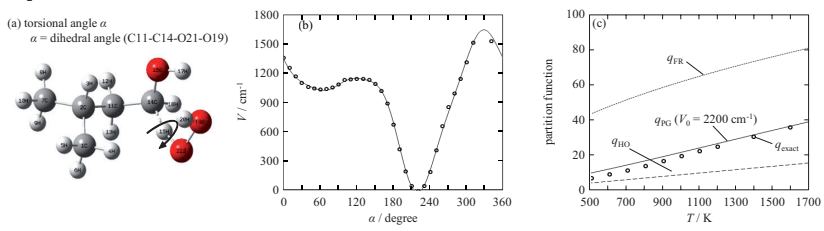


Figure A22. Hindered rotor analysis for C11-C14-O21-O19 in the TS for H-abstraction from isopentanol by HO₂ radical

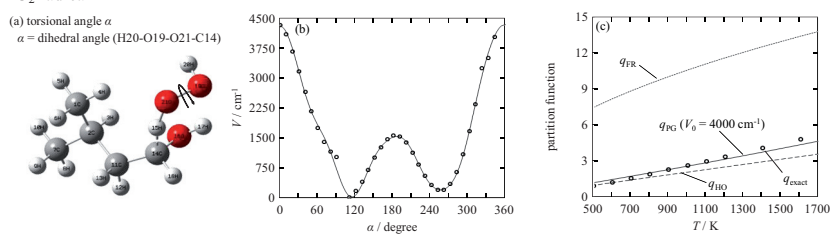


Figure A23. Hindered rotor analysis for H20-O19-O21-C14 in the TS for H-abstraction from isopentanol by $H\dot{O}_2$ radical

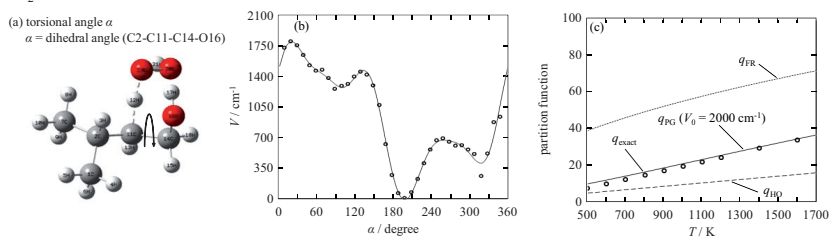


Figure A24. Hindered rotor analysis for C2-C11-C14-O16 in the TS for H-abstraction from isopentanol by \dot{HO}_2 radical

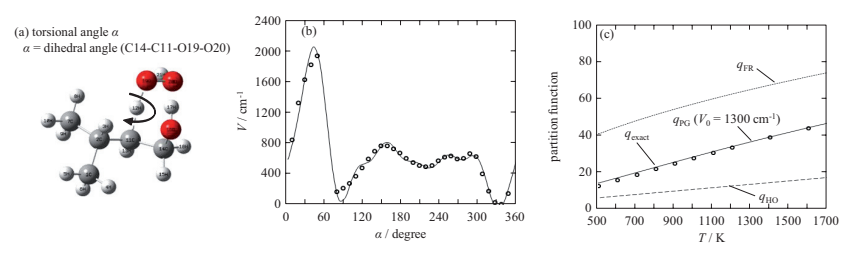


Figure A25. Hindered rotor analysis for C14-C11-O19-O20 in the TS for H-abstraction from isopentanol by $H\dot{O}_2$ radical

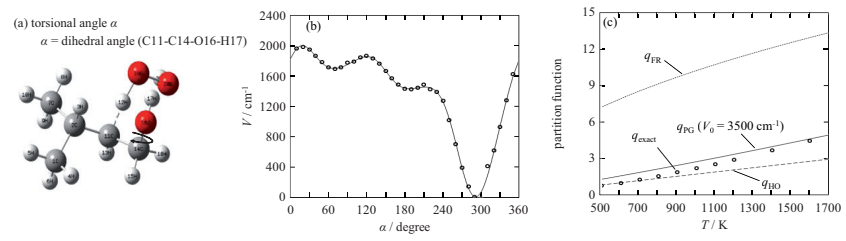


Figure A26. Hindered rotor analysis for C11-C14-O16-H17 in the TS for H-abstraction from isopentanol by HO₂ radical

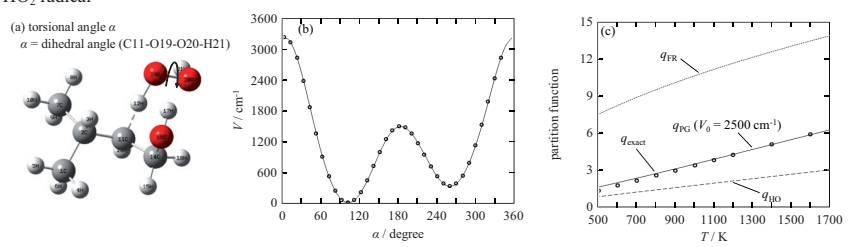


Figure A27. Hindered rotor analysis for C11-O19-O20-H21 in the TS for H-abstraction from isopentanol by $H\dot{O}_2$ radical

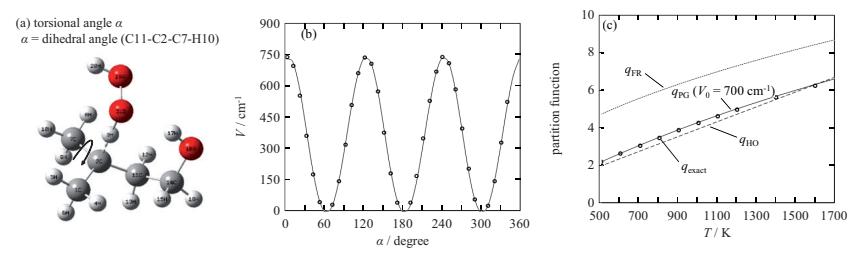


Figure A28. Hindered rotor analysis for C11-C2-C7-H10 in the TS for H-abstraction from isopentanol by HO₂ radical

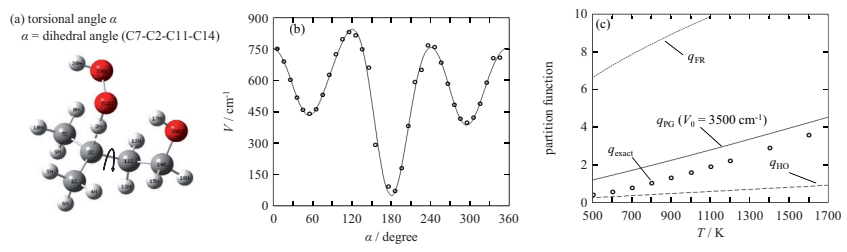


Figure A29. Hindered rotor analysis for C7-C2-C11-C14 in the TS for H-abstraction from isopentanol by HO₂ radical

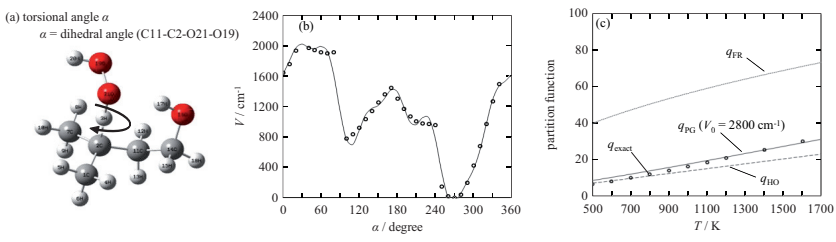


Figure A30. Hindered rotor analysis for C11-C2-O21-O19 in the TS for H-abstraction from isopentanol by \dot{HO}_2 radical

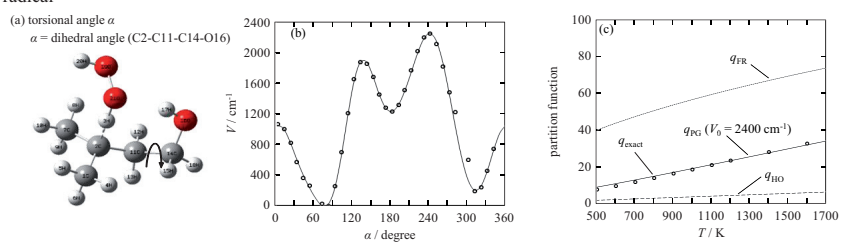


Figure A31. Hindered rotor analysis for C2-C11-O14-O16 in the TS for H-abstraction from isopentanol by \dot{HO}_2 radical

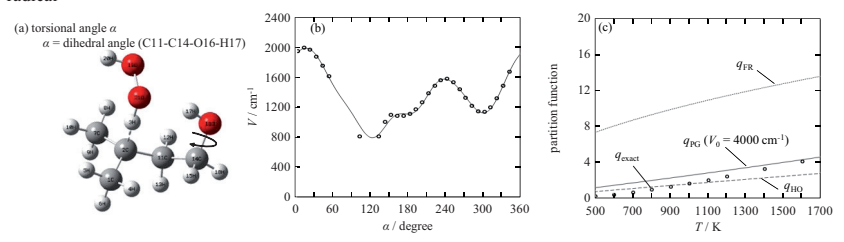


Figure A 32. Hindered rotor analysis for C11-C14-O16-H17 in the TS for H-abstraction from isopentanol by $H\ddot{O}_2$ radical

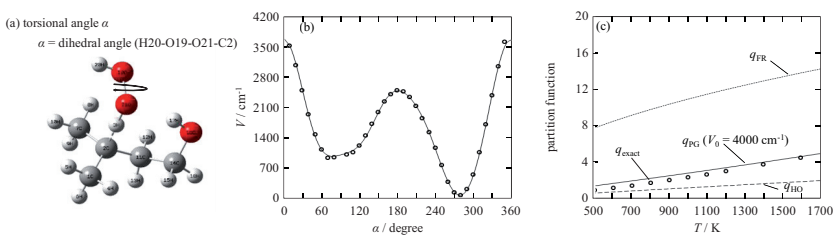


Figure A33. Hindered rotor analysis for H20-O19-O21-C2 in the TS for H-abstraction from isopentanol by \dot{HO}_2 radical

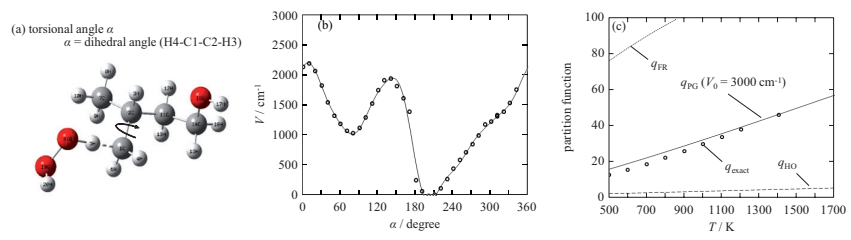


Figure A 34. Hindered rotor analysis for H4-C1-C2-H3 in the TS for H-abstraction from isopentanol by \dot{HO}_2 radical

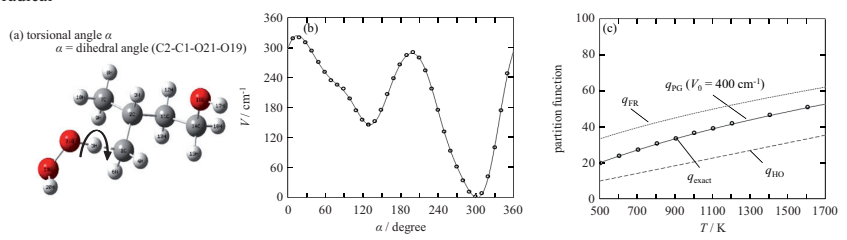


Figure A35. Hindered rotor analysis for C2-C1-O21-O19 in the TS for H-abstraction from isopentanol by \dot{HO}_2 radical

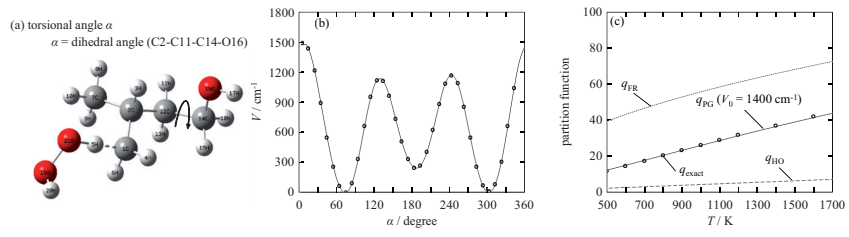


Figure A36. Hindered rotor analysis for C2-C11-C14-O16 in the TS for H-abstraction from isopentanol by \dot{HO}_2 radical

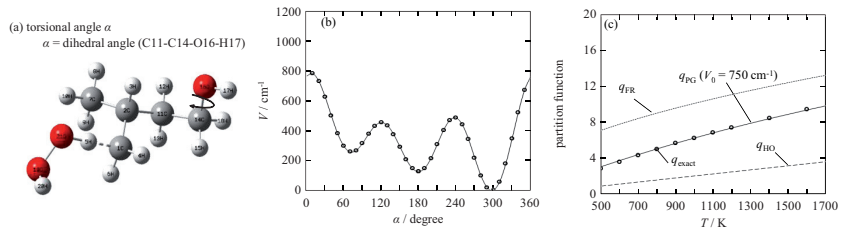


Figure A37. Hindered rotor analysis for C11-C14-O16-H17 in the TS for H-abstraction from isopentanol by $H\dot{O}_2$ radical

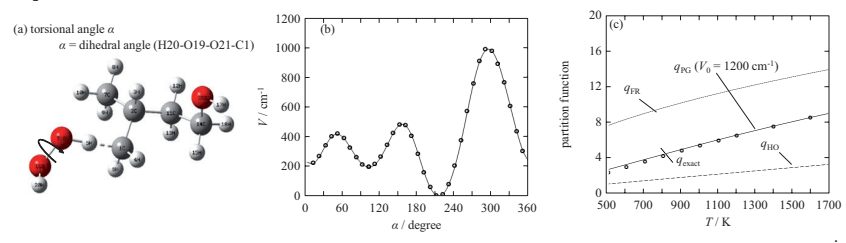


Figure A38. Hindered rotor analysis for H20-O19-O21-C1 in the TS for H-abstraction from isopentanol by \dot{HO}_2 radical

Table A1. Estimated Hindered Rotor Parameters in Pitzer-Gwinn Approximation for the H-atom abstraction reaction from isopentanol by $H\dot{O}_2$ radical

bonding atom	type of rotor	V ₀ ^b /cm ⁻¹	σ^{c}
O in TS-HÓ ₂			
C_{α}	OHO_2H	1300	1
C_{β}	$\mathrm{CH_{2}OHO_{2}H}$	1150	1
0	OH	850	1
$C_{\alpha 1}$ in TS-HÓ ₂			
C_{α}	ОН	3500	1
	ООН	2200	1
C_{β}	CH ₂ OH in TS	1300	1
O	ОН	4000	1
$C_{\beta 1}$ in TS-HÓ $_2$			
C_{α}	ОН	3500	1
C_{β}	$\mathrm{CH_2OH}$	2000	1
	ООН	1300	1
O	ОН	2500	1
C_{γ} in TS-HO $_2$			
C_{α}	ОН	4000	1
C_{β}	$\mathrm{CH_2OH}$	2400	1
C_{γ}	$C_{82}H_3$	700	3
	$\mathrm{CH_2CH_2OH}$	3500	1
	ООН	2800	1
0	ОН	4000	1

C ₆₂ in TS-HO 2										
C_{α}	ОН	750	1							
C_{β}	$\mathrm{CH_2OH}$	1400	1							
\mathbf{C}_{γ}	CH3 in TS	3000	1							
	$\mathrm{CH_{2}CH_{2}OH}$	1600	1							
$C_{\delta 1}$	ООН	400	1							
0	OH	1200	1							

^aabbreviations, C_{ω} C_{β} C_{γ} and C_{δ} are referred in Figure 5 in Chapter IV.1. ^bThe height of the hindrance potential. ^cThe symmetry number of the internal rotation for the H-abstraction reactions by $H\dot{O}_{2}$ radical.

Table A2. Spin contaminations for the transition state calculations in 3-MTHF.

species "	$\langle S^2 \rangle^b$	$\Delta E_{\rm spin}^{c}$	species "	$\langle S^2 \rangle^b$	$\Delta E_{\rm spin}^{}$
TS2c-2t	0.9395	-4.7	TS4t-2t	0.8091	-1.5
TS2c-3	0.8285	-2.0	TS4t-3	0.8135	-1.6
TS2c-4c	0.8042	-1.4	TS4t-4c	0.9519	-5.1
TS2c-5c	0.8049	-1.4	TS4t-5c	0.8328	-2.1
TS2c-m	0.7938	-1.1	TS4t-5t	0.8170	-1.7
TS2t-2c	0.9463	-4.9	TS4t-m	0.7999	-1.2
TS2t-3	0.8181	-1.7	TS5c-2c	0.8043	-1.4
TS2t-4t	0.8047	-1.4	TS5c-4c	0.8173	-1.7
TS2t-5c	0.9565	-5.2	TS5c-4t	0.8079	-1.5
TS2t-5t	0.8045	-1.4	TS5c-5t	0.9481	-5.0
TS2t-m	0.8000	-1.3	TS5c-m	0.7911	-1.0
TS3-2c	0.8319	-2.1	TS5t-2t	0.8045	-1.4
TS3-2t	0.8174	-1.7	TS5t-3	0.8065	-1.4
TS3-4c	0.8254	-1.9	TS5t-4c	0.8266	-1.9
TS3-4t	0.8116	-1.5	TS5t-4t	0.8175	-1.7
TS3-5t	0.8077	-1.4	TS5t-5c	0.9488	-5.0
TS3-m	0.8104	-1.5	TSm-2c	0.8035	-1.3
TS4c-2c	0.8090	-1.5	TSm-2t	0.8129	-1.6
TS4c-3	0.8281	-2.0	TSm-3	0.8166	-1.7
TS4c-4t	0.9501	-5.0	TSm-4c	0.7969	-1.2
TS4c-5c	0.8176	-1.7	TSm-4t	0.8043	-1.4
TS4c-5t	0.8330	-2.1	TSm-5c	0.8037	-1.3
TS4c-m	0.7934	-1.1	TSm-m	0.9422	-4.8

[&]quot;Species abbreviations in 3-MTHF. ^bEigenvalues calculated in the MP2/CBSB3 step of the CBS-QB3 composite method. Energy for spin contamination correction in the CBS-QB3 composite method.

Hindered rotor analysis performed at the CBS-QB3 method for the internal rotations involved in the isomerization reactions in 3-MTHF

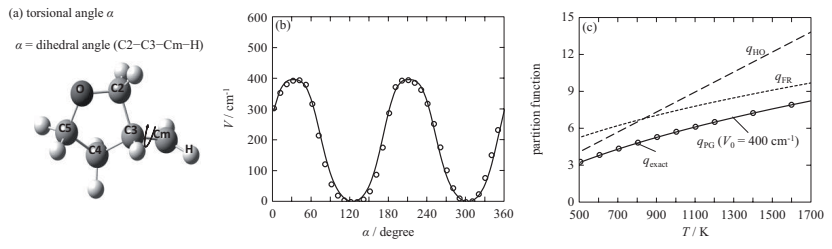


Figure A39. Hindered rotor analysis for •CH₂ rotor attached to the C3 atom in the tetrahydrofuran ring

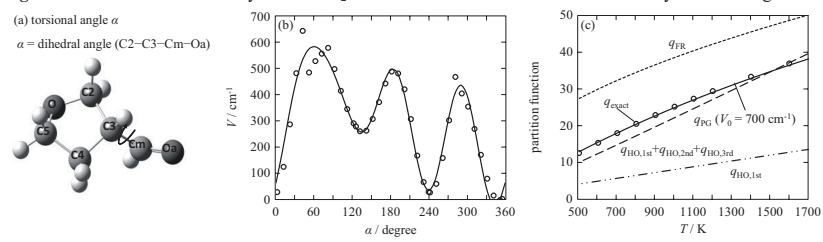


Figure A40. Hindered rotor analysis for CHO rotor attached to the C3 atom in the tetrahydrofuran ring

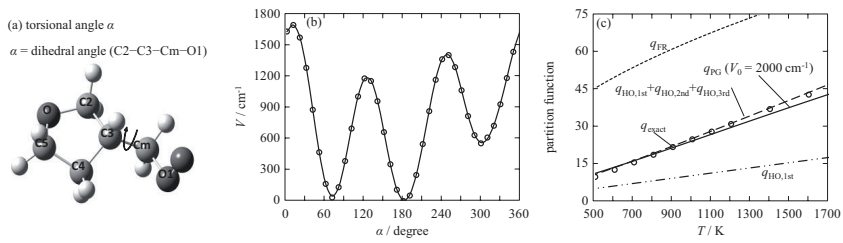


Figure A41. Hindered rotor analysis for CH₂OO• rotor attached to the C3 atom in the tetrahydrofuran ring

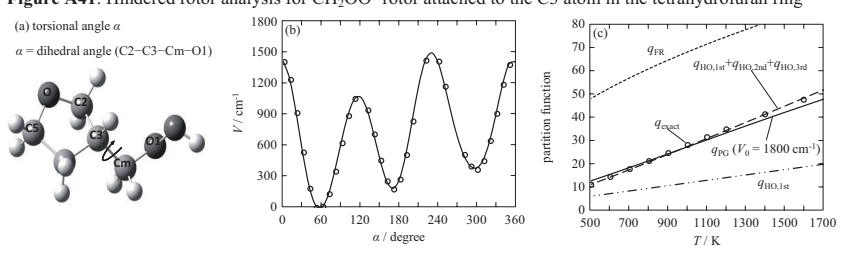


Figure A42. Hindered rotor analysis for CH₂OOH rotor attached to the C3 atom in the tetrahydrofuran ring

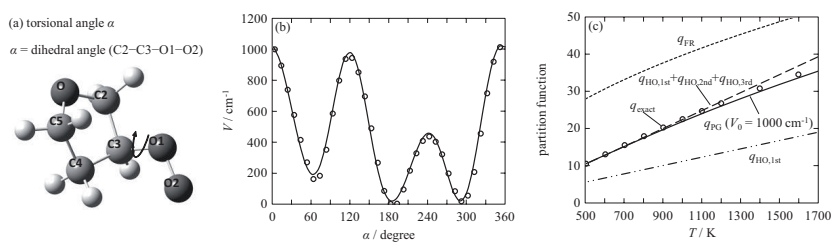


Figure A43. Hindered rotor analysis for OO• rotor attached to the C3 atom in the tetrahydrofuran ring

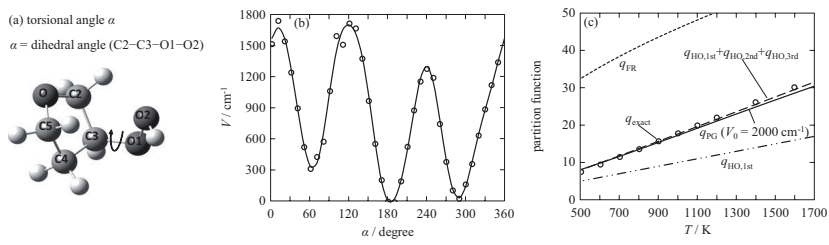


Figure A44. Hindered rotor analysis for OOH rotor attached to the C3 atom in the tetrahydrofuran ring

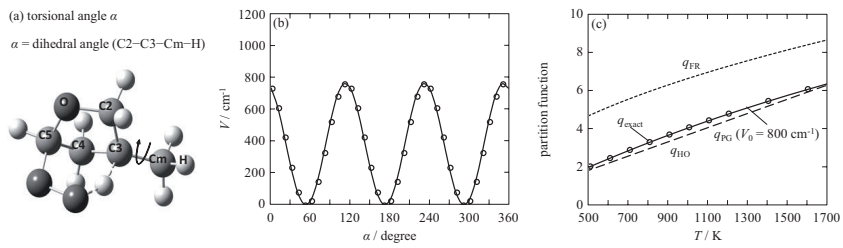


Figure A45. Hindered rotor analysis for methyl rotor attached to the hydrogen abstracting C3 atom in transition state

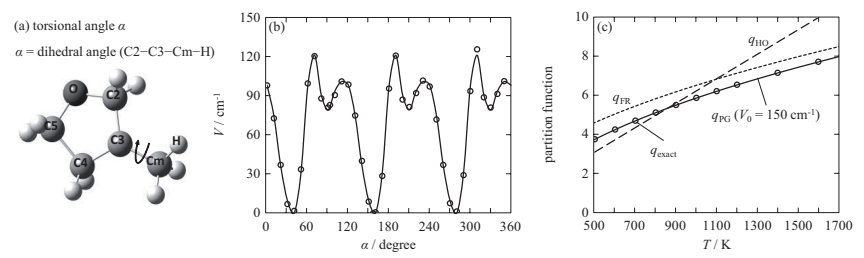


Figure A46. Hindered rotor analysis for methyl rotor attached to the radical centered C3 atom in the tetrahydrofuran ring

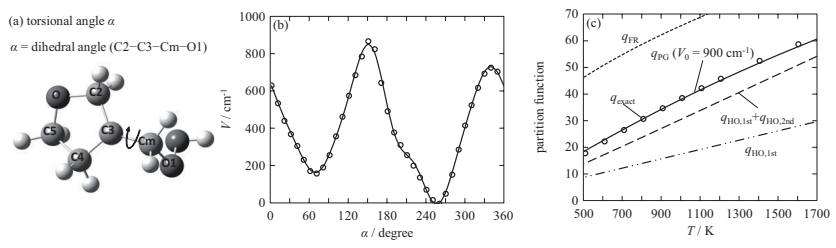


Figure A47. Hindered rotor analysis for CH₂OOH rotor attached to the radical centered C3 atom in the tetrahydrofuran ring

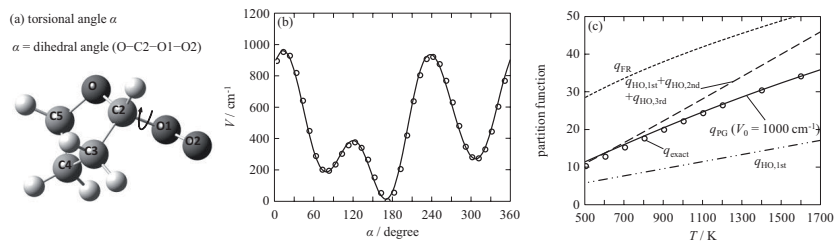


Figure A48. Hindered rotor analysis for OO• rotor attached to the C2 atom in the tetrahydrofuran ring

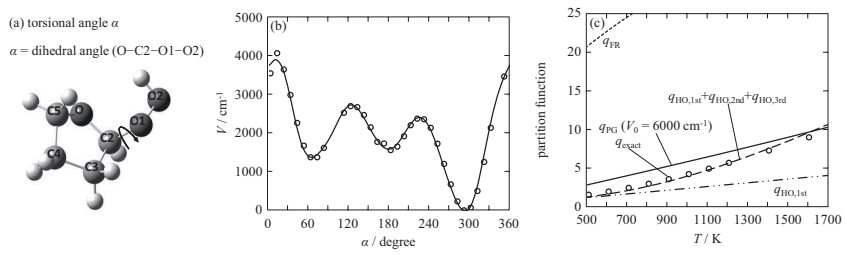


Figure A49. Hindered rotor analysis for OOH rotor attached to the C2 atom in the tetrahydrofuran ring

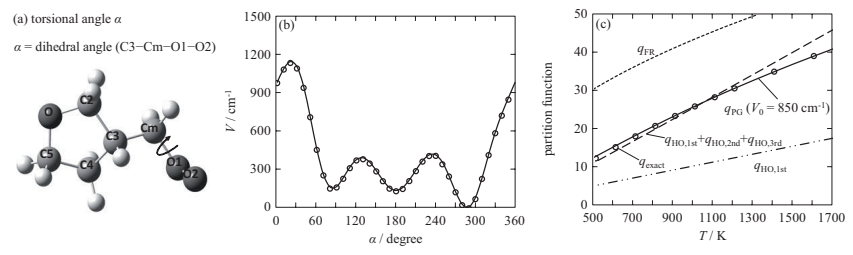


Figure A50. Hindered rotor analysis for the OO orotor attached to the Cm atom in the side chain

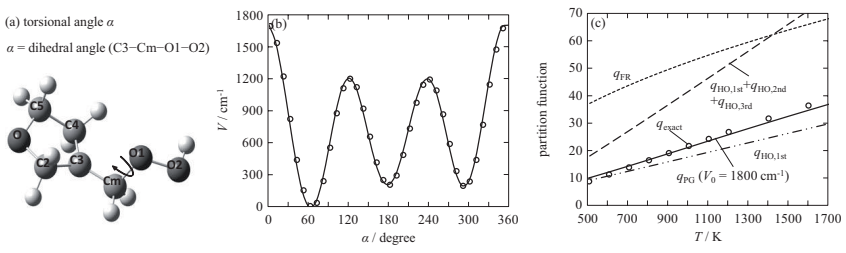


Figure A51. Hindered rotor analysis for the OOH rotor attached to the Cm atom in the side chain

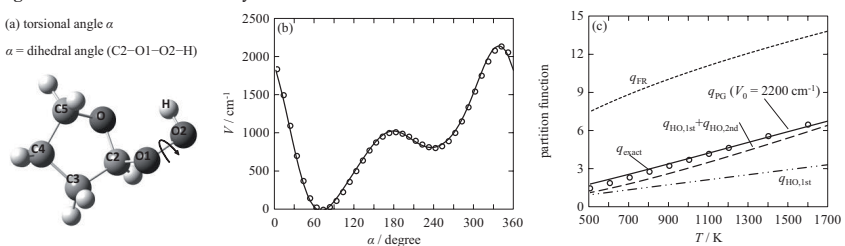


Figure A52. Hindered rotor analysis for OH rotor attached to the O1 atom in the side chain attached to C2 atom

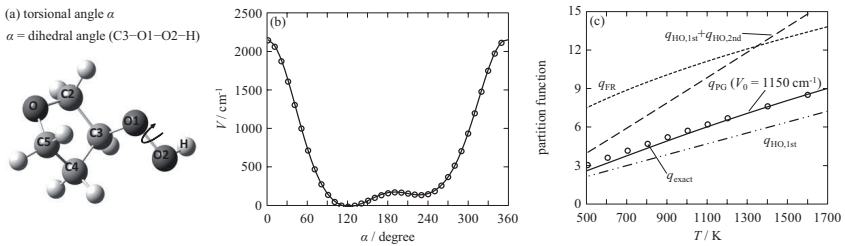


Figure A53. Hindered rotor analysis for OH rotor attached to the O1 atom in the side chain attached to C3 atom

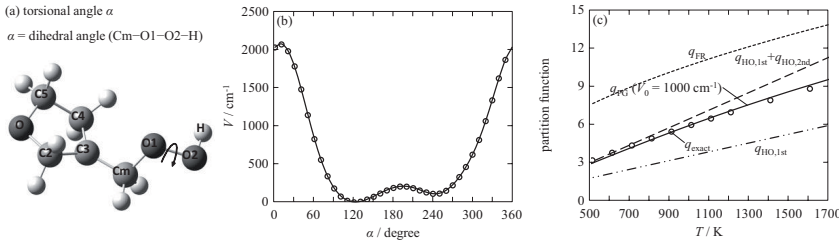


Figure A54. Hindered rotor analysis for OH rotor attached to the O1 atom attached to Cm atom

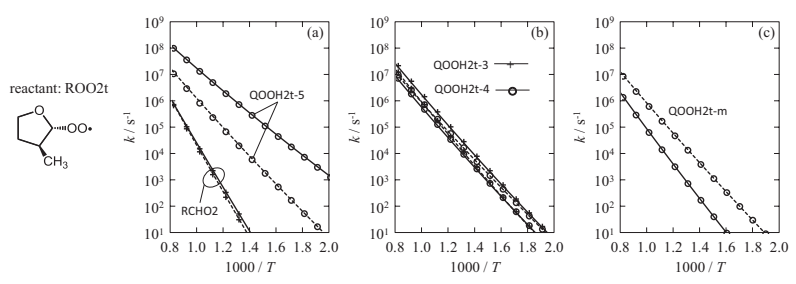


Figure A55. Comparison of rate constants ROO2t with methlcyclopentane, (a) hydrogen shift from C2 or C5, (b) hydrogen shift from C3 or C4, and (c) hydrogen shift from Cm. Solid and dashed lines denote 3-methyltetrahydrofuran and methylcyclopentane respectively.

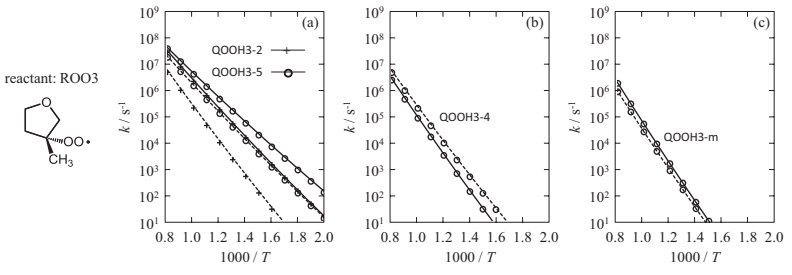


Figure A56. Comparison of rate constants ROO3 with methlcyclopentane, (a) hydrogen shift from C2 or C5, (b) hydrogen shift from C3 or C4, and (c) hydrogen shift from Cm. Solid and dashed lines denote 3-methyltetrahydrofuran and methylcyclopentane respectively.

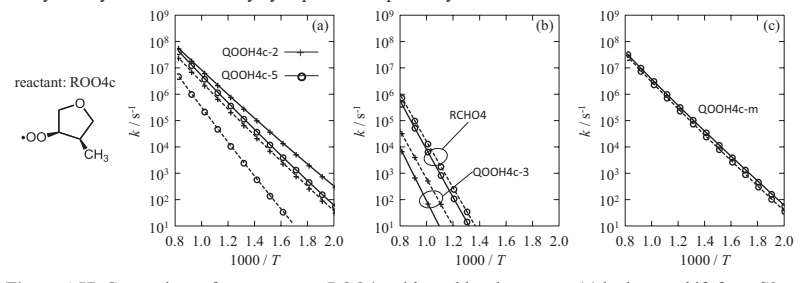


Figure A57. Comparison of rate constants ROO4c with methlcyclopentane, (a) hydrogen shift from C2 or C5, (b) hydrogen shift from C3 or C4, and (c) hydrogen shift from Cm. Solid and dashed lines denote 3-methyltetrahydrofuran and methylcyclopentane respectively.

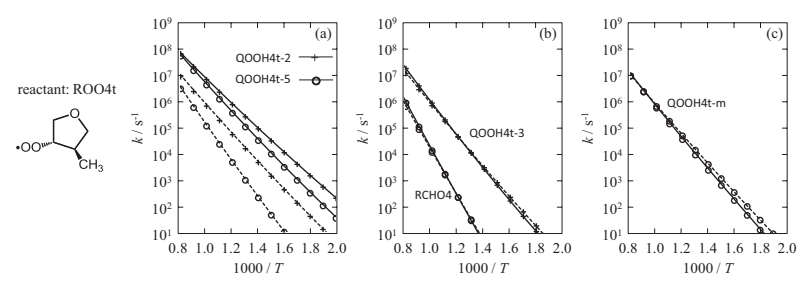


Figure A58. Comparison of rate constants ROO4t with methlcyclopentane, (a) hydrogen shift from C2 or C5, (b) hydrogen shift from C3 or C4, and (c) hydrogen shift from Cm. Solid and dashed lines denote 3-methyltetrahydrofuran and methylcyclopentane respectively.

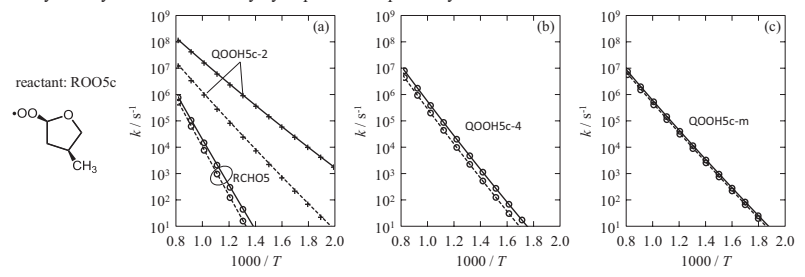


Figure A59. Comparison of rate constants ROO5c with methlcyclopentane, (a) hydrogen shift from C2 or C5, (b) hydrogen shift from C3 or C4, and (c) hydrogen shift from Cm. Solid and dashed lines denote 3-methyltetrahydrofuran and methylcyclopentane respectively.

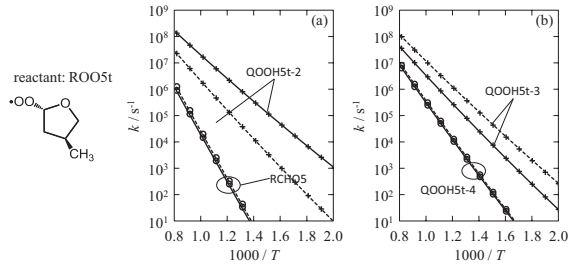


Figure A60. Comparison of rate constants ROO5t with methlcyclopentane, (a) hydrogen shift from C2 or C5, and (b) hydrogen shift from C3 or C4. Solid and dashed lines denote 3-methyltetrahydrofuran and methylcyclopentane respectively.

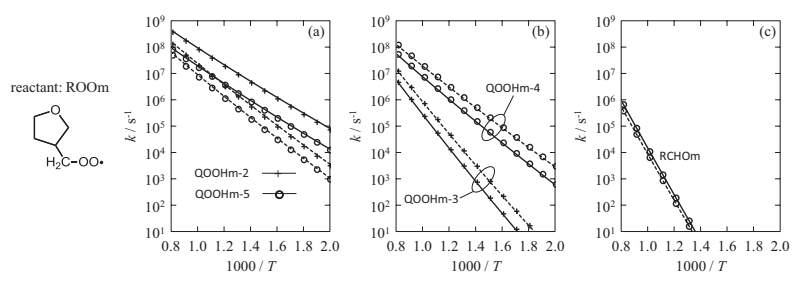


Figure A61. Comparison of rate constants ROOm with methlcyclopentane, (a) hydrogen shift from C2 or C5, (b) hydrogen shift from C3 or C4, and (c) hydrogen shift from Cm. Solid and dashed lines denote 3-methyltetrahydrofuran and methylcyclopentane respectively.

Table A3. Standard enthalpies of formation ($\Lambda_{\rm f}H^2_{298}$) and standard entropies (S^2_{298}) at 298.15 K, and heat capacity at constant pressure ($C_{\rm p}$) for temperatures between 300 and 1500 K for the reactants and products involved in the isomerization reactions in 3-MTHF.

Species	$\Delta_{\rm r} \overset{\circ}{H_{298}}$ (kJ mol ⁻¹)	S 298 (J mol K 1)	$C_p(I \text{ mol}^{-1} \text{ K}^{-1})$						
	calculated	calculated	300 K	400 K	500 K	600 K	800 K	1000 K	1500 K
ROO2c	-190.05	391.46	136.95	174.72	207.21	233.76	273.54	301.67	343.51
ROO2t	-187.52	397.31	136.37	174.38	207.02	233.64	273.49	301.64	343.50
ROO3	-178.71	394.72	138.84	176.70	208.94	235.20	274.54	302.40	343.90
ROO4c	-161.35	396.12	136.69	174.40	206.95	233.59	273.53	301.75	343.65
ROO4t	-162.26	391.52	136.05	173.98	206.69	233.43	273.51	301.80	343.73
ROO5c	-188.02	393.32	136.21	174.35	207.02	233.65	273.51	301.67	343.53
ROO5t	-191.96	391.53	136.70	174.62	207.19	233.78	273.60	301.75	343.58
ROOm	-147.36	404.87	130.51	169.91	204.92	233.72	276.42	305.89	348.48
QOOH2c-3	-159.64	403.94	139.58	177.49	210.55	237.63	277.87	305.90	347.05
QOOH2c-4	-145.74	398.37	146.06	184.29	216.75	242.94	281.53	308.41	348.16
QOOH2c-5	-160.91	393.13	144.79	183.19	215.74	242.01	280.70	307.67	347.63
QOOH2c-m	-134.03	400.36	143.59	181.58	214.17	240.57	279.51	306.66	346.96
QOOH2t-3	-159.64	403.88	139.58	177.49	210.55	237.63	277.87	305.90	347.05
QOOH2t-4	-148.11	402.71	145.96	184.34	216.85	243.04	281.58	308.41	348.12
QOOH2t-5	-163.29	393.73	145.01	183.53	216.13	242.38	280.98	307.86	347.72
QOOH2t-m	-135.56	403.48	143.54	181.62	214.25	240.67	279.63	306.79	347.06
QOOH3-2	-149.88	401.23	151.68	189.31	220.23	244.74	280.50	305.46	342.97
QOOH3-4	-118.60	402.54	150.95	188.83	220.06	244.83	280.96	306.10	343.62
QOOH3-5	-139.52	398.02	148.81	186.99	218.50	243.51	279.95	305.29	343.11

QOOH3-m	-106.12	410.83	148.40	185.99	217.42	242.48	279.09	304.56	342.64
QOOH4c-2	-124.72	401.70	147.25	184.95	216.63	241.94	278.94	304.63	342.85
QOOH4c-3	-120.48	412.98	142.48	179.67	211.81	237.91	276.43	303.18	342.52
QOOH4c-5	-136.49	401.86	147.48	185.33	216.90	242.09	278.89	304.49	342.69
QOOH4c-m	-97.03	412.67	144.85	182.71	214.68	240.30	277.78	303.81	342.47
QOOH4t-2	-139.90	404.27	149.75	187.19	218.44	243.34	279.69	304.99	342.85
QOOH4t-3	-120.03	414.08	142.89	179.93	212.00	238.06	276.54	303.26	342.56
QOOH4t-5	-129.88	410.44	148.92	186.29	217.61	242.66	279.32	304.84	342.90
QOOH4t-m	-96.62	413.39	146.60	183.80	215.44	240.86	278.11	304.00	342.49
QOOH5c-2	-158.33	400.29	143.69	182.36	215.10	241.52	280.43	307.52	347.60
QOOH5c-4	-145.68	417.93	145.59	184.11	216.63	242.82	281.35	308.19	347.95
QOOH5c-m	-138.01	403.20	143.57	181.69	214.30	240.70	279.62	306.75	347.01
QOOH5t-2	-162.15	398.54	145.48	183.81	216.28	242.45	280.99	307.86	347.70
QOOH5t-3	-158.72	409.67	139.25	177.13	210.29	237.51	277.99	306.16	347.37
QOOH5t-4	-144.83	399.23	145.36	184.16	216.79	242.98	281.41	308.17	347.86
QOOHm-2	-119.85	415.12	138.55	179.26	213.24	240.07	278.54	304.73	343.14
QOOHm-3	-103.82	415.54	142.45	179.50	211.24	237.11	275.82	303.19	344.06
QOOHm-4	-96.10	417.15	144.95	183.57	216.40	242.61	280.47	306.34	344.19
QOOHm-5	-120.20	415.42	140.61	180.67	214.26	240.89	279.17	305.29	343.54
RCHO2	-402.25	343.05	114.08	147.57	176.79	200.98	237.64	263.69	302.37
RCHO4	-320.41	347.04	116.64	149.74	178.64	202.58	238.91	264.74	303.04
RCHO5	-401.23	343.96	114.52	148.00	177.16	201.29	237.87	263.88	302.49
RCHOm	-292.70	362.86	110.69	144.15	173.94	198.79	236.52	263.21	302.45

Table A4. Arrhenius parameters for the hydrogen shift reactions in methylcyclopentane

reactant a	H atom	product a	rate constant b				
reactant	11 atom	product	A	n	E/R		
ROO1c	ROO1c H1t RCHO		9.92E+05	2.052	18906		
	H2c	QOOH1c-2	7.28E+02	2.656	12593		
	H2t	QOOH1c-2	2.79E+01	3.057	18924		
	H4c	QOOH1c-4	9.41E+04	1.906	10650		
	H5c	QOOH1c-5	1.48E+03	2.629	13428		
	H5t	QOOH1c-5	2.25E+01	3.063	18990		
	Hm	QOOH1c-m	2.96E+04	2.007	11065		
ROO1t	H1c	RCHO1 + OH	1.59E+06	2.065	18532		
	H2c	QOOH1t-2	3.32E+01	3.083	19392		
	H2t	QOOH1t-2	4.51E+02	2.801	12983		
	НЗ	QOOH1t-3	5.87E+05	1.794	9467		

	H4t	QOOH1t-4	1.37E+05	1.957	10870
	H5c	QOOH1t-5	3.86E+01	3.087	19043
	H5t	QOOH1t-5	3.42E+02	2.843	12599
ROO2c	H1c	QOOH2c-1	2.71E+02	2.771	12440
	H1t	QOOH2c-1	1.77E+01	3.079	18857
	H2t	RCHO2 + OH	7.55E+05	2.035	18072
	Н3	QOOH2c-3	1.67E+02	2.736	17790
	H4c	QOOH2c-4	1.01E+05	1.895	9976
	H5c	QOOH2c-5	6.29E+04	1.923	10427
	Hm	QOOH2c-m	1.57E+05	1.845	9929
ROO2t	H1c	QOOH2t-1	1.85E+01	3.079	18602
	Hlt	QOOH2t-1	7.72E+02	2.677	13392
	H2c	RCHO2 + OH	5.62E+05	2.038	17911
	H3	QOOH2t-3	2.00E+03	2.508	11394
	H4t	QOOH2t-4	4.51E+04	1.962	10725
	H5t	QOOH2t-5	5.38E+04	1.943	10641
	Hm	QOOH2t-m	5.79E+04	1.986	11091
ROO3	Hlt	QOOH3-1	1.08E+05	1.900	10431
	H2c	QOOH3-2	8.60E+00	3.103	19374
	H2t	QOOH3-2	4.45E+02	2.726	12619
	Hm	QOOH3-m	7.36E+01	2.935	14317
ROOm	H1c	QOOHm-1	9.52E+05	1.465	8023
	H2c	QOOHm-2	4.52E+06	1.367	7895
	H2t	QOOHm-2	8.69E+04	1.878	13295
	Н3	QOOHm-3	4.38E+04	2.134	11864
	Hm	RCHOm + OH	1.48E+06	1.883	18348

^aReactants abbreviations and their chemical structures are given in Figure 21 (Chapter IV.1). ^bRate constants are given by the Arrhenius expression, $k/s^{-1} = AT^n \exp(-E/(RT))$.

Hindered rotor analysis performed at the CBS-QB3 method for the internal rotations involved in the isomerization reactions in 2-MTHF

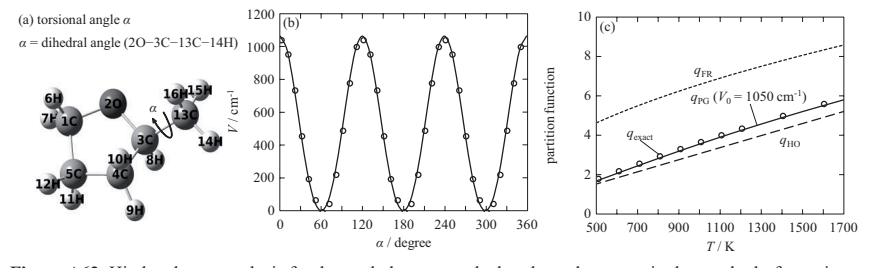


Figure A62. Hindered rotor analysis for the methyl rotor attached to the carbon atom in the tetrahydrofuran ring

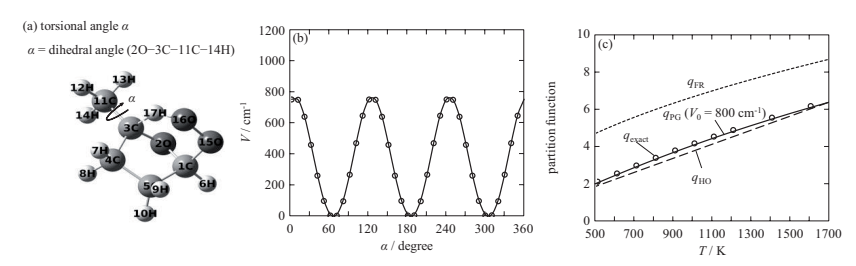


Figure A63. Hindered rotor analysis for the methyl rotor attached to the carbon atom where hydrogen atom is abstracted by peroxy group

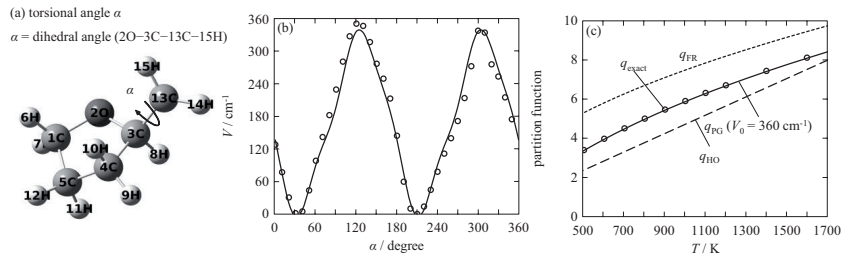


Figure A64. Hindered rotor analysis for the CH₂ rotor attached to the carbon atom in the tetrahydrofuran ring

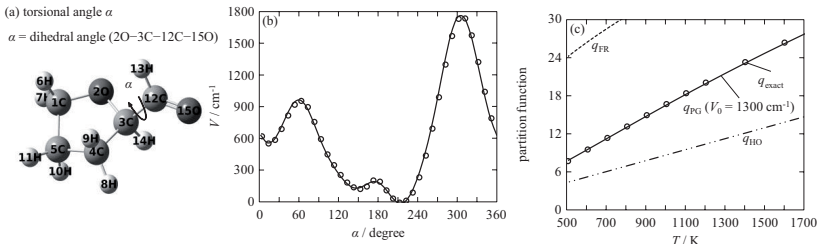


Figure A65. Hindered rotor analysis for the CHO rotor attached to the carbon atom in the tetrahydrofuran ring

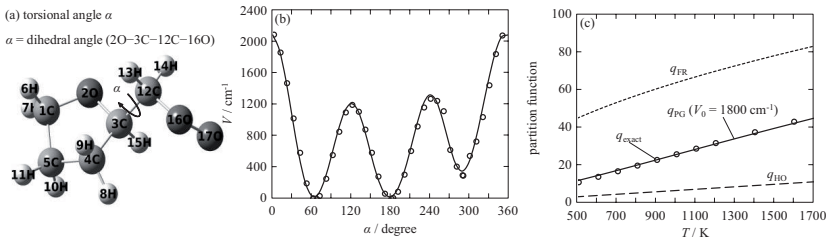


Figure A66. Hindered rotor analysis for the CH₂OO rotor attached to the carbon atom in the tetrahydrofuran ring

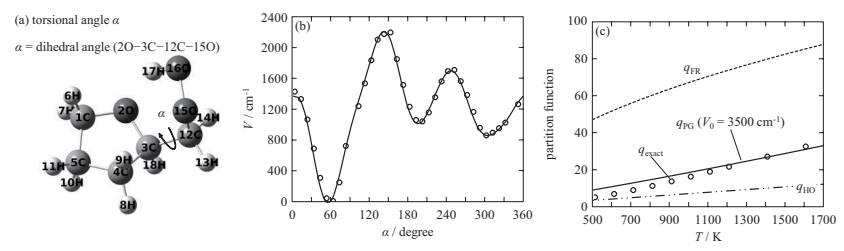


Figure A67. Hindered rotor analysis for the CH₂OOH rotor attached to the carbon atom in the tetrahydrofuran ring

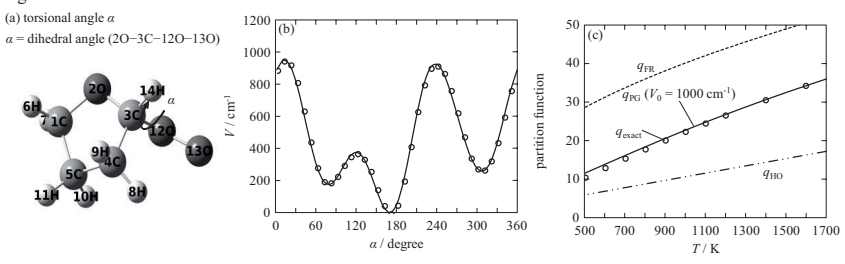


Figure A68. Hindered rotor analysis for the OO rotor attached to the carbon atom in the tetrahydrofuran ring

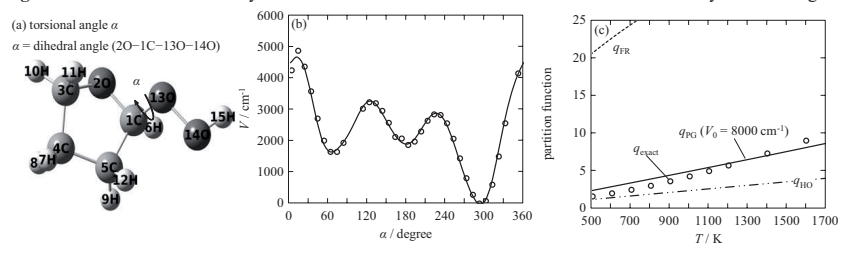


Figure A69. Hindered rotor analysis for the OOH rotor attached to the carbon atom in the tetrahydrofuran ring

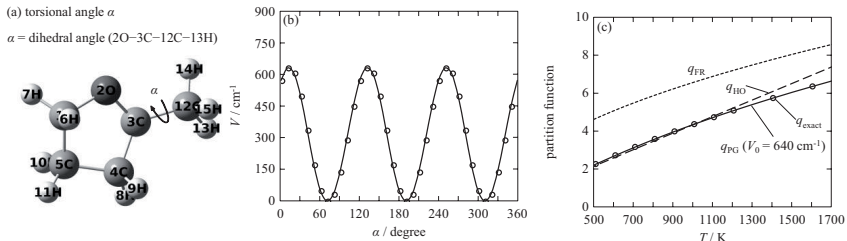


Figure A70. Hindered rotor analysis for the methyl rotor attached to the radical centered carbon atom in the tetrahydrofuran ring

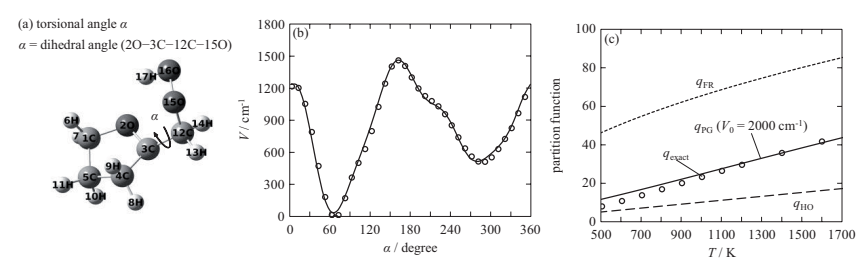


Figure A71. Hindered rotor analysis for the CH₂OOH rotor attached to the radical centered carbon atom in the tetrahydrofuran ring

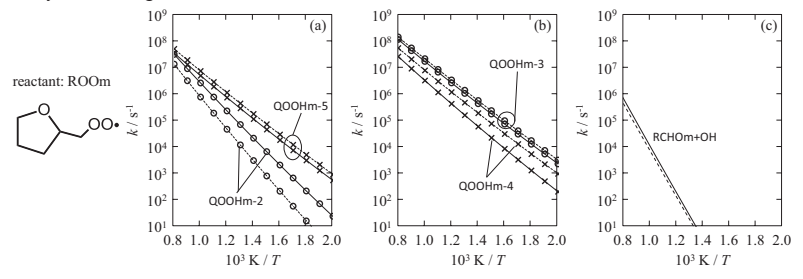


Figure A72. Comparison of rate constants ROOm with methlcyclopentane, (a) hydrogen shift from C2 or C5, (b) hydrogen shift from C3 or C4, and (c) hydrogen shift from Cm. Solid and dashed lines denote 2-methyltetrahydrofuran and methylcyclopentane respectively.

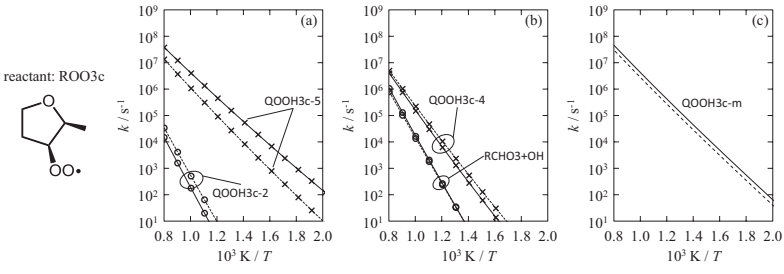


Figure A73. Comparison of rate constants ROO3c with methlcyclopentane, (a) hydrogen shift from C2 or C5, (b) hydrogen shift from C3 or C4, and (c) hydrogen shift from Cm. Solid and dashed lines denote 2-methyltetrahydrofuran and methylcyclopentane respectively.

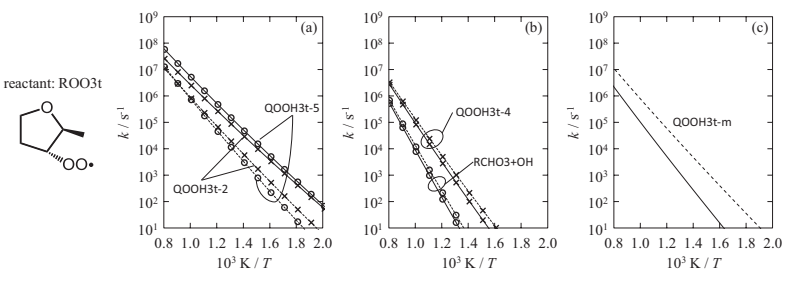


Figure A74. Comparison of rate constants ROO3t with methlcyclopentane, (a) hydrogen shift from C2 or C5,

(b) hydrogen shift from C3 or C4, and (c) hydrogen shift from Cm. Solid and dashed lines denote 2-methyltetrahydrofuran and methylcyclopentane respectively.

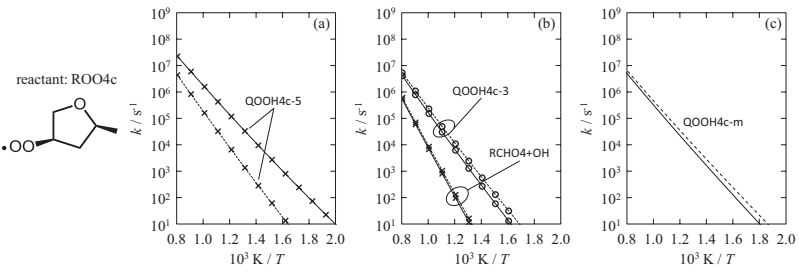


Figure A75. Comparison of rate constants ROO4c with methlcyclopentane, (a) hydrogen shift from C5, (b) hydrogen shift from C3 or C4, and (c) hydrogen shift from Cm. Solid and dashed lines denote 2-methyltetrahydrofuran and methylcyclopentane respectively.

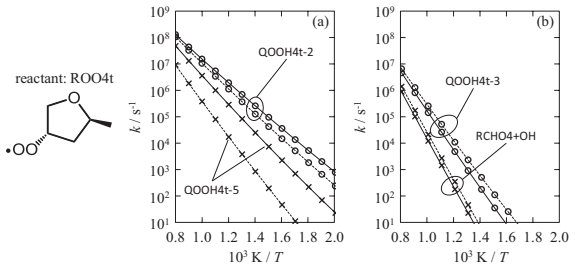


Figure A76. Comparison of rate constants ROO4t with methlcyclopentane, (a) hydrogen shift from C2 or C5, and (b) hydrogen shift from C3 or C4. Solid and dashed lines denote 2-methyltetrahydrofuran and methylcyclopentane respectively

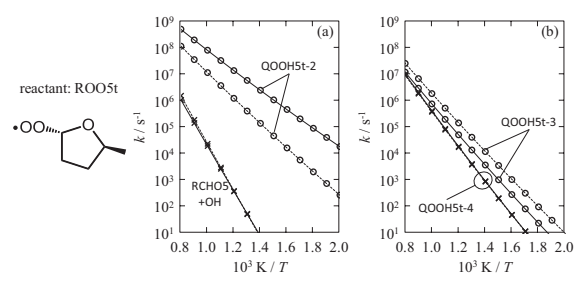


Figure A77. Comparison of rate constants ROO5t with methlcyclopentane, (a) hydrogen shift from C2 or C5, and (b) hydrogen shift from C3 or C4. Solid and dashed lines denote 2-methyltetrahydrofuran and methylcyclopentane respectively.

Table A5. Standard enthalpies of formation $(\Delta_t H^0_{298})$ and standard entropies (S^0_{298}) at 298.15 K, and heat capacity at constant pressure (C_p) for temperatures between 300 and 1500 K for reactants and products involved in the isomerization reactions in 2-MTHF.

Species	Δ _f H ²⁹⁸ / kJ mol ⁻¹	S ²⁹⁸ / J mol K 1				C_p / J mol 1 K	-1		
			300 K	400 K	500 K	600 K	800 K	1000 K	1500 K
ROO2	-213.91	391.45	139.48	177.47	209.63	235.74	274.77	302.41	343.75
ROO3c	-170.89	395.89	137.00	174.98	207.58	234.15	273.91	301.99	343.72
ROO3t	-175.96	397.83	136.78	174.97	207.65	234.26	274.01	302.07	343.76
ROO4c	-176.40	396.11	136.39	174.68	207.44	234.12	273.98	302.10	343.84
ROO4t	-176.79	392.73	136.92	175.04	207.69	234.28	274.05	302.13	343.83
ROO5c	-205.23	393.61	137.04	175.39	208.04	234.55	274.13	302.08	343.68
ROO5t	-201.41	391.96	136.93	175.13	207.75	234.28	273.93	301.94	343.62
ROOm	-156.31	401.15	130.54	170.70	205.82	234.44	276.64	305.77	348.14
QOOH2-3	-161.84	392.61	148.74	187.31	219.36	244.99	282.58	308.77	347.87
QOOH2-4	-165.82	394.25	148.66	187.17	219.30	245.03	282.78	309.07	348.19
QOOH2-5	-180.49	388.07	146.88	185.74	218.08	243.93	281.83	308.21	347.56
QOOH2-m	-143.26	401.25	144.43	182.67	214.80	240.70	279.19	306.47	347.91
QOOH3c-2	-154.47	407.40	147.56	183.74	214.83	240.06	277.40	303.49	342.30
QOOH3c-4	-116.71	407.55	149.24	187.16	218.71	243.82	280.43	305.85	343.60
QOOH3e-5	-136.19	401.44	147.67	185.69	217.40	242.65	279.47	305.02	343.04
QOOH3c-m	-101.94	411.41	144.80	183.15	215.32	240.97	278.35	304.26	342.72
QOOH3t-2	-154.67	411.37	146.12	182.40	214.02	239.94	278.48	305.42	345.33
QOOH3t-4	-117.46	409.32	149.73	187.30	218.72	243.79	280.42	305.87	343.66
QOOH3t-5	-138.77	406.48	147.74	185.77	217.49	242.74	279.51	305.03	343.03
QOOH3t-m	-105.85	414.86	147.26	184.85	216.55	241.88	278.83	304.47	342.67
QOOH4e-2	-145.41	411.41	145.48	182.19	213.75	239.36	277.16	303.49	342.46
QOOH4e-3	-118.63	408.62	148.93	187.05	218.67	243.79	280.34	305.70	343.44
QOOH4c-5	-145.71	409.28	149.29	187.02	218.39	243.32	279.67	304.96	342.81
QOOH4c-m	-103.96	416.74	146.84	184.55	216.30	241.68	278.72	304.41	342.65
QOOH4t-2	-143.96	406.60	145.66	182.19	213.70	239.30	277.14	303.52	342.51
QOOH4t-3	-115.15	404.81	148.99	187.15	218.77	243.86	280.34	305.66	343.37
QOOH4t-5	-151.70	403.90	149.82	187.51	218.79	243.66	279.94	305.19	342.97
QOOH4t-m	-106.90	414.69	147.26	184.80	216.47	241.80	278.76	304.42	342.65
QOOH5e-2	-180.64	397.16	142.54	179.96	212.46	239.09	278.71	306.39	347.18

QOOH5c-3	-159.75	398.35	146.26	185.04	217.61	243.73	282.06	308.74	348.26
QOOH5c-4	-155.80	395.73	145.71	184.74	217.39	243.54	281.89	308.57	348.12
QOOH5c-m	-143.98	410.90	143.47	182.01	214.76	241.16	279.97	306.99	347.12
QOOH5t-2	-176.56	405.52	142.43	179.72	212.19	238.83	278.52	306.25	347.12
QOOH5t-3	-160.30	399.03	146.27	184.89	217.42	243.55	281.95	308.67	348.24
QOOH5t-4	-159.23	397.00	146.09	184.81	217.34	243.46	281.84	308.56	348.15
QOOH5t-m	-145.11	399.49	143.59	182.07	214.81	241.21	280.04	307.06	347.18
QOOHm-2	-132.04	417.50	139.76	179.21	212.72	239.55	278.40	304.91	343.53
QOOHm-3	-109.29	413.83	141.23	181.00	214.46	241.26	280.45	307.48	346.55
QOOHm-4	-112.20	416.82	140.85	180.61	214.14	241.06	280.48	307.65	346.79
QOOHm-5	-127.76	411.60	140.12	179.98	213.55	240.46	279.82	306.96	346.20
RCHO3	-331.73	348.07	116.95	150.34	179.27	203.14	239.27	264.95	303.08
RCHO4	-332.61	347.65	117.36	150.82	179.72	203.55	239.60	265.22	303.26
RCHO5	-413.66	344.07	114.90	148.65	177.85	201.92	238.30	264.15	302.58
RCHOm	-297.06	369.19	113.09	146.84	176.52	201.09	238.17	264.38	303.00

Hindered rotor analysis performed at the CBS-QB3 method for the internal rotations involved in the H-atom abstraction reaction in 2-BT by $CH_3O\dot{O}$ radical.

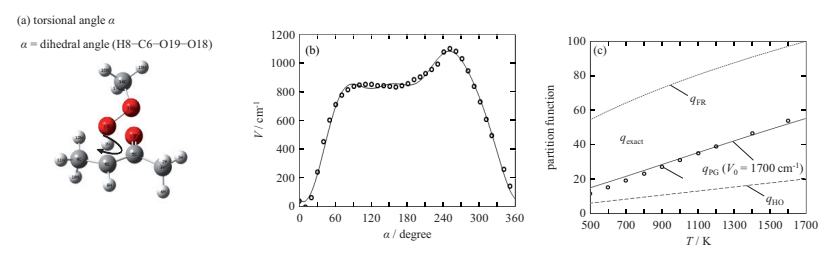


Figure A78. Hindered rotor analysis for H8-C6-O19-O18 in the TS for H-abstraction from 2-BT by $\mathrm{CH_3OO}$ radical

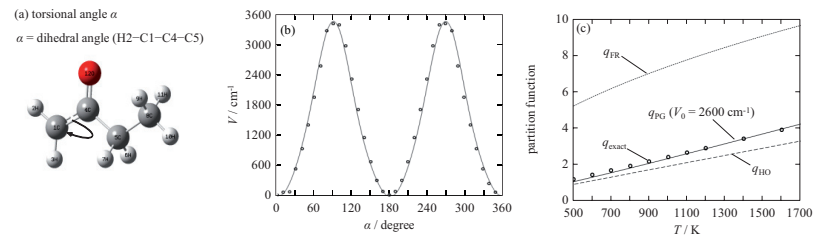


Figure A79. Hindered rotor analysis for H2-C1-C4-C5 in the product radical.

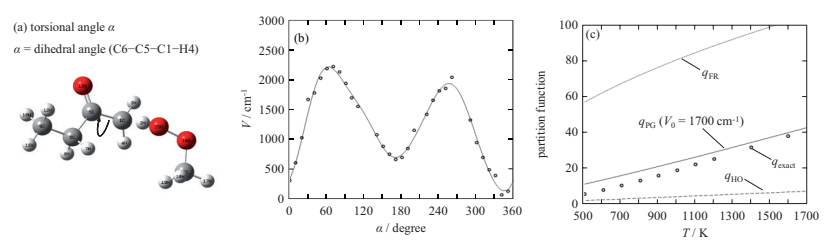


Figure A80. Hindered rotor analysis for C6-C5-C1-H4 in the TS for H-abstraction from 2-BT by CH₃OO radical.

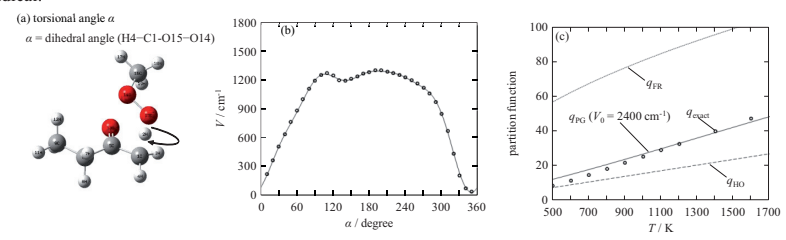


Figure A81. Hindered rotor analysis for C-C- - in the TS for H-abstraction from 2-BT by CH₃OO radical

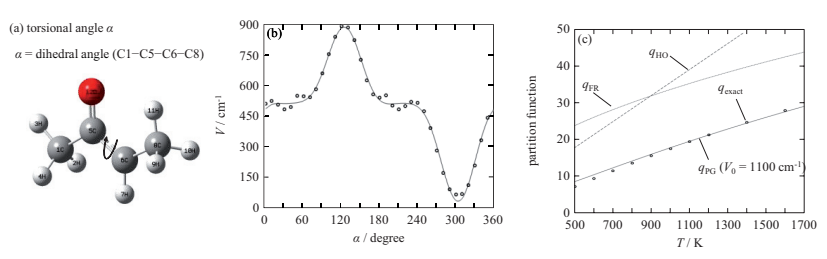


Figure A82. Hindered rotor analysis for C1-C5-C6-C8 in the TS for H-abstraction from 2-BT by CH₃OO radical

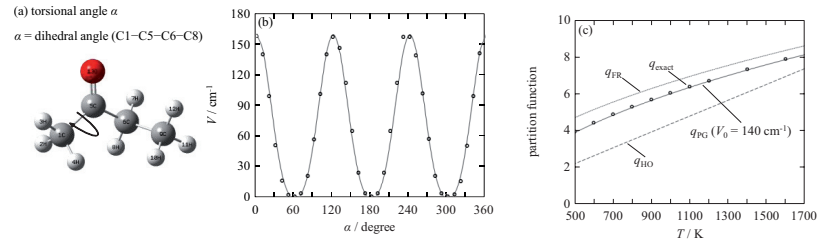


Figure A83. Hindered rotor analysis for H3-C1-C5-C6 in the TS for H-abstraction from 2-BT by $\mathrm{CH_3OO}$ radical

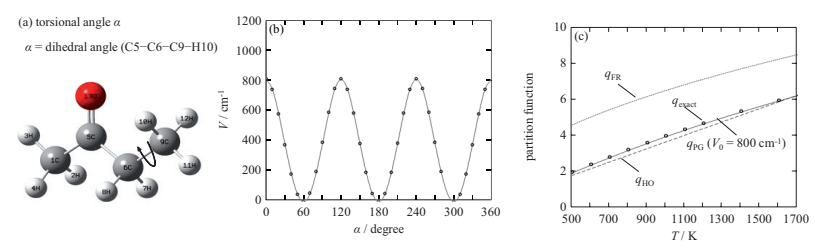


Figure A84. Hindered rotor analysis for C5-C6-C9-H10 in the TS for H-abstraction from 2-BT by CH₃OO radical

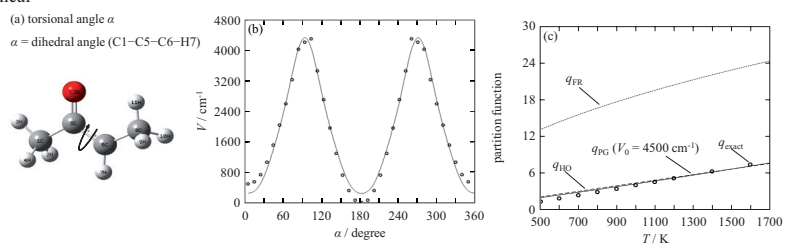


Figure A85. Hindered rotor analysis for C1-C5-C6-H7 in the TS for H-abstraction from 2-BT by CH₃OO radical

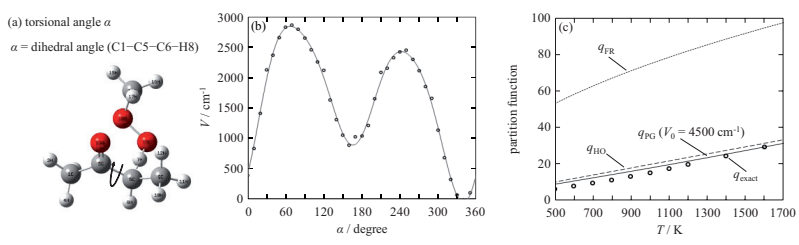


Figure A86. Hindered rotor analysis for C1-C5-C6-H8 in the TS for H-abstraction from 2-BT by CH₃OO radical

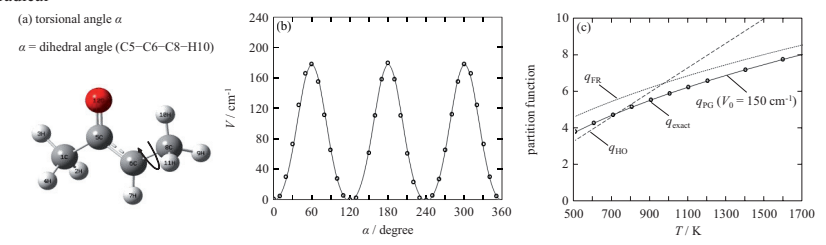


Figure A87. Hindered rotor analysis for C5-C6-C8-H10 in the product radical

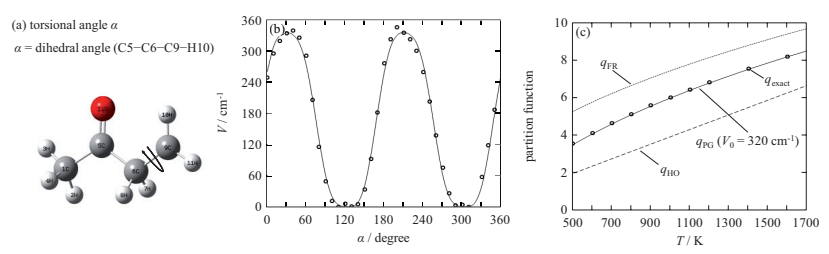


Figure A88. Hindered rotor analysis for C5-C6-C9-C10 in the TS for H-abstraction from 2-BT by $\mathrm{CH_3O\dot{O}}$ radical

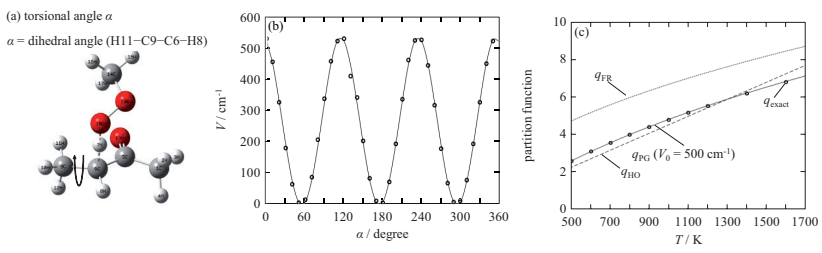


Figure A89. Hindered rotor analysis for H11-C9-C6-H8 in the TS for H-abstraction from 2-BT by $\mathrm{CH_3OO}$ radical

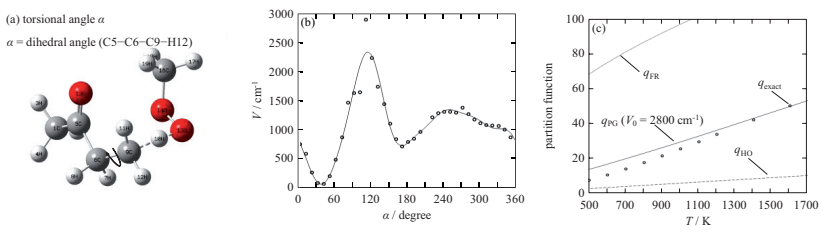
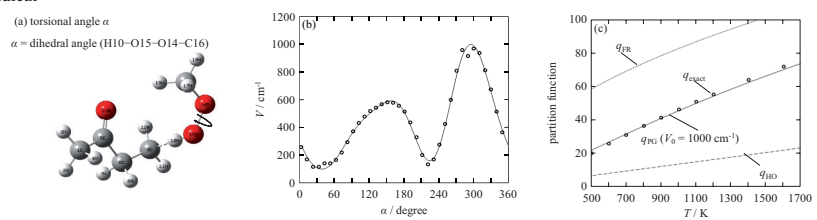


Figure A90. Hindered rotor analysis for C5-C6C9-H12 in the TS for H-abstraction from 2-BT by $\mathrm{CH_3O\dot{O}}$ radical



 $\textbf{Figure A91.} \ Hindered \ rotor \ analysis \ for \ H10-O15-O14-C16 \ in \ the \ TS \ for \ H-abstraction \ from \ 2-BT \ by \ CH_3OO \ radical$

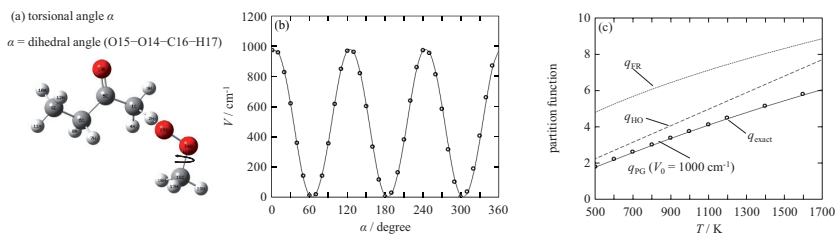


Figure A92. Hindered rotor analysis for O15-O14-C16-H17 in the TS for H-abstraction from 2-BT by CH₃OO radical

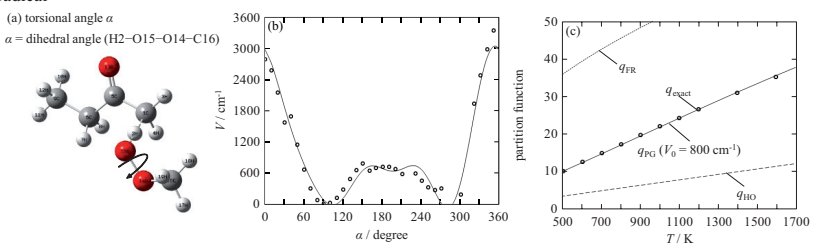


Figure A93. Hindered rotor analysis for H2-O15-O14-C16 in the TS for H-abstraction from 2-BT by $CH_3O\dot{O}$ radical

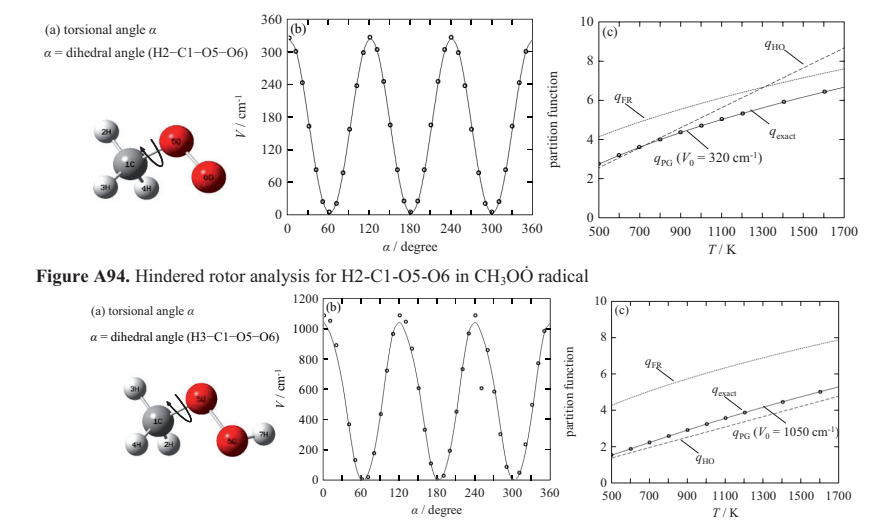


Figure A95. Hindered rotor analysis for H3-C1-O5-O6 in CH₃OOH.

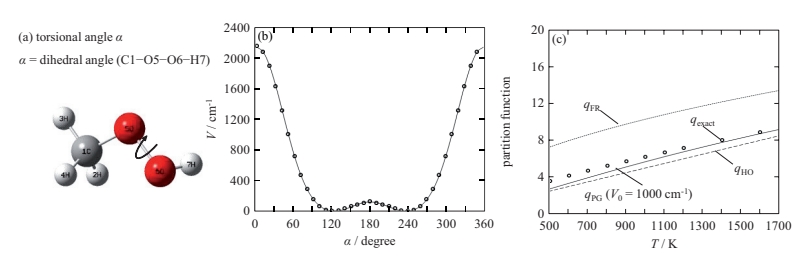


Figure A96. Hindered rotor analysis for C1-O5-O6-H7 in CH₃OOH

Table A6. Standard enthalpies of formation ($\Delta_{\rm f} H^2_{298}$) and standard entropies (\mathcal{S}^*_{298}) at 298.15 K, and heat capacity at constant pressure ($C_{\rm p}$) for temperatures between 300 and 2500 K for acetone species.

Species	Δ ₁ H 298 / kJ mol 1	S 298 / J mol 1 K 1				C_{p} J m	ol ⁻¹ K ⁻¹			
			300 K	700 K	1000 K	1200 K	1500 K	1700 K	2000 K	2500 K
CH ₃ _CBS-QB3	151.05	194.7	39.522	51.198	58.716	62.916	67.872	70.392	73.29	76.44
CH ₂ CO_ CBS-QB3	-50.42	241.1	51.324	74.382	84.21	88.914	94.038	96.516	99.288	102.186
CH ₃ COCH ₃ _CBS- QB3	-214.14	315.5	73.164	132.678	160.482	173.502	187.446	194.082	201.348	209.034
CH ₃ COCH ₂ _CBS- QB3	-31.94	306.8	74.214	129.15	152.418	162.96	173.838	178.878	184.212	189.63
CH ₃ COCH ₂ OO_ CBS-QB3	-137.73	371.8	105.462	169.722	193.242	203.952	215.292	220.668	226.59	232.89
CH ₃ _G3	144.72	197.6	40.95	50.274	57.414	61.614	66.654	69.3	72.324	75.726
CH ₂ CO_G3	-52.35	241.1	48.384	71.694	81.942	86.898	92.4	95.088	98.112	101.346
CH ₃ COCH ₃ _G3	-215.12	313.1	68.628	125.286	154.056	167.916	182.952	190.176	198.24	206.808
CH ₃ COCH ₂ _G3	-32.57	304.3	70.518	124.32	148.176	159.138	170.73	176.106	181.986	188.034
CH ₃ COCH ₂ OO_G3	-132.61	367.5	98.952	161.07	186.27	197.988	210.63	216.72	223.44	230.664
CH ₃ _G4	147.04	195.1	39.816	51.198	58.632	62.832	67.788	70.308	73.206	76.356
CH ₂ CO_G4	-50.34	241.2	51.366	74.298	84.084	88.788	93.954	96.432	99.204	102.144
CH ₃ COCH ₃ _G4	-213.53	315.6	73.29	132.678	160.398	173.418	187.32	193.998	201.264	208.992
CH ₃ COCH ₂ _G4	-34.70	306.9	74.298	129.108	152.334	162.834	173.754	178.752	184.128	189.588
CH ₃ COCH ₂ OO_G4	-135.80	371.8	105.462	169.638	193.158	203.826	215.208	220.584	226.548	232.806
CH3_CBS-APNO	146.61	196.4	40.488	50.484	57.75	61.95	66.99	69.594	72.576	75.894
CH ₂ CO_ CBS- APNO	-52.44	238.9	48.426	71.988	82.236	87.192	92.652	95.34	98.28	101.514
CH ₃ COCH ₃ _ CBS- APNO	-221.55	313.2	69.132	126.462	155.19	168.882	183.792	190.932	198.828	207.27
CH ₃ COCH ₂ _ CBS- APNO	-37.96	304.5	70.98	125.202	149.016	159.936	171.36	176.694	182.448	188.412
CH ₃ COCH ₂ OO_ CBS-APNO	-139.67	367.6	99.288	161.91	187.11	198.744	211.26	217.266	223.902	231.0

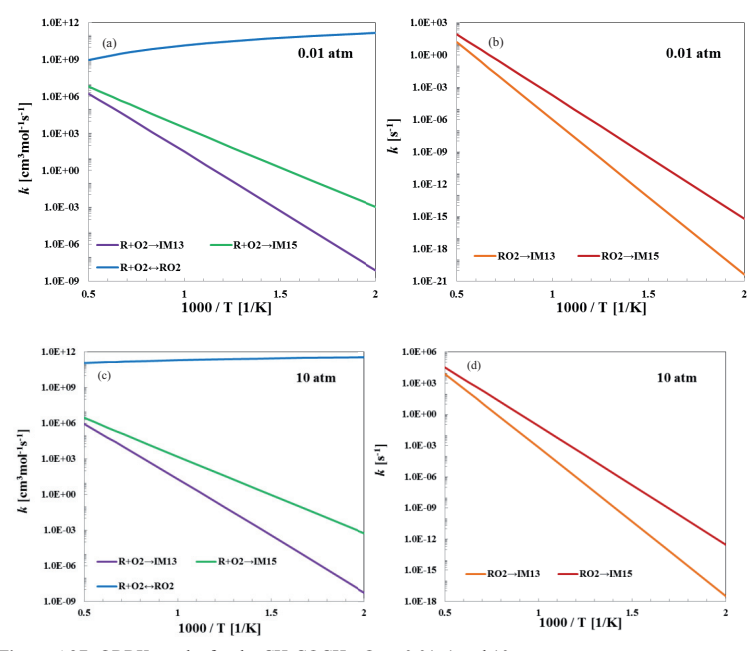


Figure A97: QRRK results for the CH₃COCH₂+O₂ at 0.01, 1 and 10 atm

Table A7: The complete set of the rate coefficients for the O₂ + CH₃COCH₂ reactions in a CHEMKIN-compatible PLOG format, with the modified Arrhenius parameters at 0.001, 0.01, 1, 10, and 100 atm.

```
CH3COCH2+O2<=>IM13
                                         +1.0000000E+000 +1.0000000E+000 +1.0000000E+000 ! QRRK/MSC ANALYSIS WITH CHEMDIS
                          +1.0000000E-003 +4.4800000E+001 +2.7700000E+000 +3.9198000E+004 /
PLOG
                          +1.0000000E=002 +4.5100000E+001 +2.7700000E+000 +3.9199000E+004 /
PLOG
PLOG /
                          +1.0000000E+000 +8.6300000E+001 +2.6800000E+000 +3.9300000E+004
                          +1.0000000E+001 +1.1000000E+003 +2.2800000E+000 +3.9735000E+004
PLOG /
                          +1.0000000E+002 +1.0500000E+004 +1.8000000E+000 +4.0324000E+004 /
PLOG /
CH3COCH2+O2<=>IM15
                                         +1.0000000E+000 +1.0000000E+000 +1.0000000E+000 ! QRRK/MSC ANALYSIS WITH CHEMDIS
                          ±1.0000000E=003 ±1.7100000E=005 ±4.3200000E±000 ±2.1978000E±004
PLOG
                          +1.0000000E-002 +1.7100000E-005 +4.3200000E+000 +2.1979000E+004 /
PLOG /
PLOG /
                          +1.0000000E+000 +1.9800000E-005 +4.2800000E+000 +2.2106000E+004 /
PLOG
                          +1.0000000E+001 +5.4800000E-005 +4.0800000E+000 +2.2686000E+004
PLOG /
                          +1.0000000E+002 +1.3100000E-004 +3.7700000E+000 +2.3378000E+004 /
                                        +1 0000000E+000 +1 0000000E+000 +1 0000000E+000 | ! ORRK/MSC ANALYSIS WITH CHEMDIS
CH3COCH2+O2<=>CH3COCH2O2
                          +1.000000E-003 +1.9500000E+025 -5.2100000E+000 +1.2440000E+003
PLOG /
PLOG /
                          +1.0000000E-002 +8.3500000E+023 -4.4800000E+000 +1.5680000E+003
PLOG /
                          +1.0000000E+000 +1.2600000E+017 -1.9300000E+000 +8.4900000E+002
                          +1.0000000E+001 +1.5500000E+014 -9.4000000E-001 +2.2700000E+002
PLOG /
                          +1.0000000E+002 +2.0000000E+013 -6.4000000E-001 +2.9000000E+001
PLOG /
CH3COCH2O2<=>IM13
                                         +1.0000000E+000 +1.0000000E+000 +1.0000000E+000 !ORRK/MSC ANALYSIS WITH CHEMDIS
                          +1.0000000E-003 +1.2700000E-002 +2.7400000E+000 +6.0586000E+004
PLOG /
                          +1,000000E-002 +1,2800000E-001 +2,7400000E+000 +6,0588000E+004 /
PLOG /
PLOG /
                          +1.0000000E+000 +3.7600000E+001 +2.5800000E+000 +6.0739000E+004
                          +1.0000000E+001 +1.8900000E+004 +2.0000000E+000 +6.1307000E+004
PLOG
                          +1.0000000E+002 +7.8100000E+006 +1.3100000E+000 +6.2005000E+004 /
CH3COCH2O2<=>IM15
                                         +1.0000000E+000 +1.0000000E+000 +1.0000000E+000 + ORRK/MSC ANALYSIS WITH CHEMDIS
                          +1.0000000E-003 +1.2700000E-002 +2.5200000E+000 +4.6970000E+004
PLOG
                          +1.0000000E-002 +1.2800000E-001 +2.5200000E+000 +4.6972000E+004 /
PLOG /
                          +1.0000000E+000 +1.4800000E+001 +2.4700000E+000 +4.7064000E+004
PLOG /
                          +1.0000000E+001 +1.4800000E+002 +2.3700000E+000 +4.7403000E+004
PLOG.
PLOG /
                          +1.0000000E+002 +1.0200000E+003 +2.2000000E+000 +4.7829000E+004 /
```

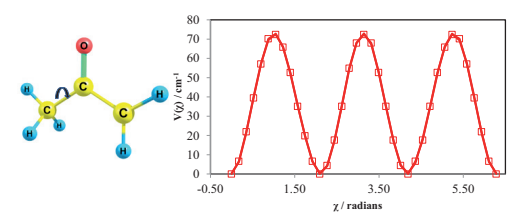


Figure A98. Scan of the CH₃ internal rotor in acetone performed at M062X/6-311++G(d,p) method.

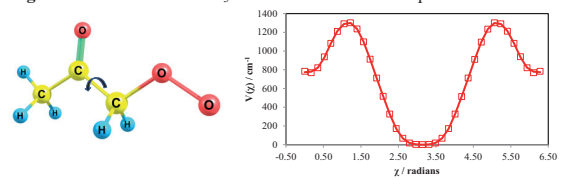


Figure A99. Scan of CH₂OO rotor in CH₃COCH₂OO performed at M062X/6-311++G(d,p) method.

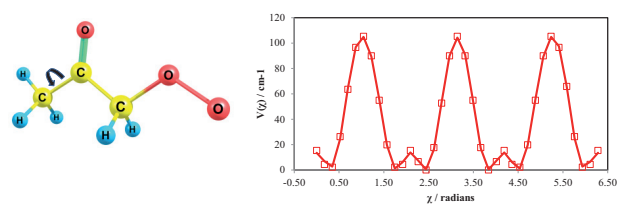


Figure A100. Scan of CH3 rotor in CH3COCH2OO performed at M062X/6-311++G(d,p) method.

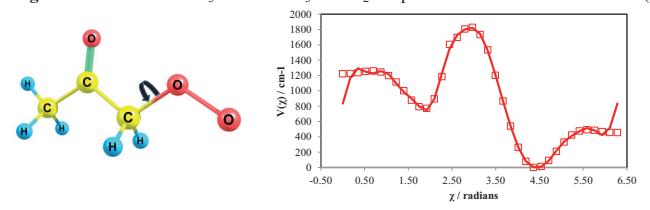


Figure A101. Scan of OO rotor in $CH_3COCH_2O\dot{O}$ performed at M062X/6-311++G(d,p) method.

Curriculum Vitae

Name: Prajakta Rajaram Parab

Date of birth: February 1st 1987

Place of birth: Goa, India
Parents: Rajaram Parab

Rupali Parab

Citizenship: Indian Marital status: Married

Husband: Dr. Gauresh Palav

Education

1996-2002 Secondary school education, Goa, India

2002-2004 Higher secondary school education, Goa, India

2004-2007 Bachelor of science (Chemistry), Goa University, India

2007-2009 Master of science (Physical Chemistry), Goa University, India

Since 2012 Scientific research associate at the Physico-Chemical Fundamentals of

Combustion, RWTH Aachen University, Germany